

Nanoscale multilayer Me-graphite coatings grown by combined steered cathodic arc/unbalanced magnetron sputtering.

KOK, Yin Nan.

Available from the Sheffield Hallam University Research Archive (SHURA) at:

<http://shura.shu.ac.uk/19926/>

A Sheffield Hallam University thesis

This thesis is protected by copyright which belongs to the author.

The content must not be changed in any way or sold commercially in any format or medium without the formal permission of the author.

When referring to this work, full bibliographic details including the author, title, awarding institution and date of the thesis must be given.

Please visit <http://shura.shu.ac.uk/19926/> and <http://shura.shu.ac.uk/information.html> for further details about copyright and re-use permissions.



Return to Learning Centre of issue
Fines are charged at 50p per hour

REFERENCE

ProQuest Number: 10697232

All rights reserved

INFORMATION TO ALL USERS

The quality of this reproduction is dependent upon the quality of the copy submitted.

In the unlikely event that the author did not send a complete manuscript and there are missing pages, these will be noted. Also, if material had to be removed, a note will indicate the deletion.



ProQuest 10697232

Published by ProQuest LLC (2017). Copyright of the Dissertation is held by the Author.

All rights reserved.

This work is protected against unauthorized copying under Title 17, United States Code
Microform Edition © ProQuest LLC.

ProQuest LLC.
789 East Eisenhower Parkway
P.O. Box 1346
Ann Arbor, MI 48106 – 1346

Nanoscale Multilayer Me-Graphite Coatings Grown by Combined Steered Cathodic Arc/Unbalanced Magnetron Sputtering

Yin Nan Kok

**A thesis submitted in partial fulfilment of the requirements of
Sheffield Hallam University for the degree of Doctor of Philosophy**



October 2005

Abstract

Low friction, nanoscale multilayer carbon/chromium (C/Cr) coatings were successfully deposited by the combined steered cathodic arc/unbalanced magnetron sputtering technique (also known as Arc Bond Sputtering or ABSTM) using a Hauzer HTC 1000-4 PVD coater. The work described in this thesis has been directed towards understanding the effect of ion irradiation on the composition, microstructure, and functional properties of C/Cr coatings. This has been achieved by varying the bias voltage, U_B , over a wide range between -65 V and -550 V.

C/Cr coatings were deposited in three major steps: (i) Cr^+ ion etching using a steered cathodic arc discharge at a substrate bias voltage of -1200 V, (ii) deposition of a 0.25 μm thick CrN base layer by reactive unbalanced magnetron sputtering to enhance the adhesion, and (iii) deposition of C/Cr coatings by unbalanced magnetron sputtering from three graphite targets and one chromium target at 260°C. The coatings were deposited at different bias voltages (U_B) from -65 V to -550 V in a non-reactive Ar atmosphere.

C/Cr coatings exhibit excellent adhesion (critical load, $L_c > 70$ N), with hardness ranging from 6.8 to 25.1 GPa depending on the bias voltage. The friction coefficient of C/Cr coatings was found to reduce from 0.22 to 0.16 when the bias voltage was increased from $U_B = -65$ to -95 V. The relevance of C/Cr coatings for actual practical applications was demonstrated using dry high-speed milling trials on automotive aluminium alloy (Al-Si8Cu3Fe). The results showed that C/Cr coated cemented carbide ball-nose end mills prepared at $U_B = -95$ V (70 at.% C, 30 at.% Cr) enhance the tool performance and the tool life compared to the uncoated tools by a factor of two, suggesting the potential for use in dry high-speed machining of “sticky” alloys such as aluminum. Different film morphologies were observed in the investigated bias voltage range between $U_B = -65$ and -550 V using XTEM. With increasing bias voltage from $U_B = -65$ to -95 V, the structure changed from columnar, with carbon accumulated at the column boundaries, to a dense structure which comprised randomly distributed onion-like carbon clusters. A novel nanostructure was observed within this bias voltage range, in which the basic nano-lamellae obtained as a result of substrate rotation in front of the C and Cr targets were modified by an ion-irradiation induced nanocolumnar structure. Further increases in the bias voltage to $U_B = -350$ V and $U_B = -450$ V led to segregation and self-organisation of the carbon atoms induced by the high energy ion bombardment and, finally, to the formation of a new type of self-organised multilayer structure. A coating growth model accounting for the influence of ion bombardment on the growing C/Cr film was introduced to explain the phase separation and formation of the self-organised layered nanostructure.

A novel experimental set-up for the investigation of tribocorrosion was built based on a modification of the conventional Scanning Reference Electrode Technique (SRET). The device comprises a ball on rotating cylinder contact configuration combined with a SRET electrochemical device. This combination may contribute significantly to the understanding of wear-corrosion synergism.

Acknowledgements

I am greatly indebted to my director of studies cum first supervisor Professor Papken Eh Hovsepian, for giving me invaluable supervision and support, knowledgeable comments, patience and encouragement throughout these research studies. I would like to express my gratitude to my second supervisor Professor Robert Akid for his dedication and excellent and knowledgeable supervision. I would like to thank my former director of studies Professor Dieter Münz for giving me the chance to carry out this research project.

I would like to thank Professor I. Petrov, Dr J.-G. Wen, and Dr R. Haasch of the Centre for Microanalysis of Materials at the University of Illinois for their invaluable discussions and comments, and for providing HRTEM, STEM-EELS, RBS, and XPS results. I want to thank all members of Nanotechnology Centre for PVD research at Sheffield Hallam University for valuable discussions, technical support, help and encouragement; specifically, Dr A. P. Ehasarian for plasma characterisation and Mr G. Robinson for building the tribocorrosion test rig and for technical support. Thanks also go to Dr S. Read from Corus Ltd. Sheffield, for SNMS measurements. I also like to thank all MERI staffs, in particular Mr S. Creasey for help within the XRD instrument, and Dr D. Greenfield for help with corrosion test instruments, the School of Engineering staff (Mac Jackson, Keith, Tim, and many others) for technical support and help. The same applies to all members of Bodycote SHU Coatings Ltd, who shared the same building in Matilda Street.

I would like to express my gratitude to my parents, sisters and brother for their unlimited support and encouragement. Last but not least, I would like to give my special thanks to my husband, his patient love enabled me to complete this work.

Advanced Studies

The following conferences were attended, and presentations were given during the course of this study.

1. 8th Sheffield ABS Day, July 2002, Sheffield, U.K
2. 9th Sheffield ABS Day, July 2003, Sheffield, U.K (oral)
3. 44th Corrosion Science Symposium, September 2003, University of Southampton, Southampton, U.K (poster)
4. 4th Asian-European International Conference on Plasma Surface Engineering (AEPSE), October 2003, Jeju Island, South Korea (oral)
5. MRI Research Day, January 2004, Sheffield Hallam University, Sheffield, U.K (poster and oral)
6. Materials Congress 2004, Young Researcher Lecture Competition (part of Surface Engineering Symposia), April 2004, London, U.K (oral)
7. 1st HIPIMS-ABS Day, July 2004, Sheffield, U.K (oral)
8. 45th Corrosion Science Symposium, September 2004, Sheffield, U.K (poster and oral)
9. 9th International Conference on Plasma Surface Engineering (PSE), September 2004, Garmisch-Partenkirchen, Germany (oral)
10. Research student event, May 2005, Leeds Metropolitan University, Leeds, U.K
11. 2nd HIPIMS-ABS Day, July 2005, Sheffield, U.K (oral)

Publications

- 1) Y.N. Kok, P.Eh. Hovsepian, Q. Luo, D.B. Lewis, J.G. Wen, I. Petrov, "Influence of the Bias Voltage on the Structure and the Tribological Performance of Nanoscale Multilayer C/Cr PVD Coatings", *Thin Solid Films* 475 (1-2) (2005) 219-226.
- 2) Y.N. Kok, P.Eh. Hovsepian, R. Haasch, I. Petrov, "Raman Spectroscopy study of C/Cr Coatings deposited by the combined steered cathodic arc/unbalanced magnetron sputtering technique", *Surface and Coatings Technology* 200 (1-4) (2005) 1117-1122.
- 3) Y.N. Kok, R. Akid, P.Eh. Hovsepian, "Tribocorrosion testing of stainless steel (SS) and PVD coated SS using a modified scanning reference electrode technique", *Wear* 259 (7-12) (2005) 1472-1481.
- 4) Y.N. Kok, J.G. Wen, I. Petrov, P.Eh. Hovsepian, "Influence of ion bombardment on the Structure and Tribological Performance of Nanoscale Multilayer C/Cr PVD Coatings", 2005, submitted to *Surface Engineering*. (*Runner-up prize in Bodycote Prize Paper Competition, Toronto, Canada*).
- 5) P.Eh. Hovsepian, Y.N. Kok, A.P. Ehasarian, A. Erdemir, J.-G. Wen, I. Petrov, "Structure and tribological behaviour of nanoscale multilayer C/Cr coatings deposited by the combined steered cathodic arc/unbalanced magnetron sputtering", *Thin Solid Films* 447-448 (2004) 7-13.
- 6) P.Eh. Hovsepian, D.B. Lewis, C. Constable, Q. Luo, Y.N. Kok, W.-D. Münz, "Combined steered cathodic arc/unbalanced magnetron grown C/Cr nanoscale multilayer coatings for tribological applications", *Surface and Coatings Technology*, 174-175 (2003) 762-769.
- 7) P. Eh. Hovsepian, Y. N. Kok, A.P. Ehasarian, R. Haasch, J.-G. Wen, I. Petrov, "Phase separation and formation of the self-organised layered nanostructure in C/Cr coatings in conditions of high ion irradiation", *Surface and Coatings Technology*, 2005, article in press.
- 8) Y.N. Kok, P.Eh. Hovsepian, "Resistance of Nanoscale C/Cr PVD Coatings against Environmental Attack", to be submitted for publication.

Paper not directly related to this thesis

- 9) Q. Luo, P.Eh. Hovsepian, D.B. Lewis, W.-D. Münz, Y.N. Kok, J. Cockrem, M. Bolton and A. Farinotti, "Tribological properties of unbalanced magnetron sputtered nano-scale multilayer coatings TiAlN/VN and TiAlCrYN deposited on plasma nitrided steels", *Surface and Coatings Technology* 193 (1-3) (2005) 39.

Table of Contents

Abstract	I
Acknowledgements.....	II
Advanced Studies	III
Publications	IV
Table of Contents	V
List of Figures and Tables	VII
 CHAPTER 1 Introduction	 1
1.1 Motivation.....	1
1.1.1 Limitations of existing carbon-based coatings.....	2
1.1.2 Research opportunities.....	3
1.2 Aims and objectives.....	6
1.3 Methods of approach	6
1.4 Structure of thesis	8
 CHAPTER 2 Review of Literature	 9
2.1 Physical Vapour Deposition (PVD) coatings technology.....	9
2.1.1 Introduction to plasma	10
2.1.2 Sputtering	13
2.1.3 Cathodic Arc Evaporation Technique.....	18
2.1.4 Arc Bond Sputtering (ABS™) Technique	22
2.2 Coating growth and microstructure evolution.....	23
2.3 Nanocomposite structure	30
2.4 Carbon-based Coatings	35
2.4.1 Background of carbon.....	36
2.4.2 Types of carbon-based coatings.....	42
 CHAPTER 3 Experimental Methodology	 51
3.1 Materials, specimen preparation and coating deposition.....	51
3.1.1 Materials and specimen preparation prior to coating deposition.....	51
3.1.2 Principle process sequence of ABS™ technology	53
3.1.3 Deposition procedures and process parameters setting.....	56
3.2. Modification of conventional Scanning Reference Electrode Technique (SRET) rig for tribocorrosion testing	58
3.2.1 Principle and design of the tribocorrosion test rig.....	58
3.2.2 Experimental setup and tribocorrosion calibration.....	59
3.3. Characterisation techniques	61
3.3.1 Tribological test.....	61
3.3.2 Scratch test and Rockwell-C indentation test.....	62
3.3.3 Nano-hardness test.....	64
3.3.4 Ball-cratering thickness measurement	65
3.3.5 Stress measurement by disc deflection method.....	66
3.3.6 Plasma characterisation.....	68
3.3.7 Secondary neutral mass spectrometry (SNMS).....	69
3.3.8 Rutherford backscattering spectroscopy	69
3.3.9 X-ray diffraction (XRD).....	70
3.3.10 X-ray Photoelectron Spectroscopy (XPS).....	72

3.3.11	Raman Spectroscopy.....	72
3.3.12	Scanning electron microscope (SEM).....	74
3.3.13	Transmission electron microscope (TEM).....	75
3.3.14	Scanning TEM-Electron energy loss spectroscopy (STEM-EELS).....	77
3.3.15	Oxidation test.....	78
3.3.16	Corrosion test.....	79
3.3.17	Dry high-speed milling test	85
CHAPTER 4 Results		87
4.1	Plasma characteristics during C/Cr deposition process	87
4.2	Influence of bias voltage on the deposition parameters.....	89
4.3	Compositional analysis	91
4.3.1	Secondary Neutral Mass Spectrometry (SNMS).....	91
4.3.2	Rutherford backscattering spectroscopy (RBS)	94
4.4	Mechanical and tribological properties.....	95
4.4.1	Adhesion scratch and Rockwell-C indentation	96
4.4.2	Tribological test.....	99
4.4.3	Ball-cratering thickness measurement	102
4.4.4	Nano-hardness test.....	103
4.4.5	Stress measurement.....	104
4.5	Structure and microstructure analyses	105
4.5.1	X-ray diffraction (XRD).....	105
4.5.2	Chemical bonding analysis by X-ray Photoelectron Spectroscopy (XPS) 107	
4.5.3	Raman spectroscopy	109
4.5.4	Scanning electron microscope (SEM).....	115
4.5.5	Transmission electron microscope (TEM).....	120
4.5.6	Scanning TEM (STEM) - electron energy loss spectroscopy (EELS) .	132
4.6	Oxidation tests.....	137
4.6.1	Thermogravimetry analysis (TGA)	137
4.6.2	Isothermal heat-treatment.....	144
4.7	Corrosion tests.....	156
4.7.1	Potentiodynamic polarisation test.....	156
4.7.2	Tribocorrosion test.....	162
4.8	Performance in dry high-speed milling test.....	188
CHAPTER 5 Discussion		202
5.1	Ion bombardment induced microstructure evolution and the proposed coating growth model	202
5.2	Mechanical and tribological behaviour.....	213
5.3	Oxidation behaviour	217
5.4	Corrosion behaviour	221
5.5	Dry high speed machining	223
CHAPTER 6 Conclusions		225
Further Research		228
References		230
Appendix: Papers Published in Refereed Journals		249

List of Figures and Tables

List of Figures

- Figure 1.1 Carbon-chromium phase diagram
- Figure 2.1 PVD techniques (Note: RF = radio frequency; e-beam = electron beam)
- Figure 2.2 Schematic illustration of the DC glow discharge, (a) plasma regions, (b) voltage characteristics, and (c) net space charges
- Figure 2.3 Current-voltage relation for various types of plasma discharge
- Figure 2.4 Sputtering mechanism
- Figure 2.5 Interactions which occur at and near the target surface during the sputtering process: Weissmantel model (after [44])
- Figure 2.6 Schematic diagram of rectangular planar magnetron showing the arrangement of magnets, the electric and magnetic fields, and the plasma (shaded area)
- Figure 2.7 Plasma localisation and confinement for (a) conventional magnetron and
- Figure 2.8 Schematic illustration of the magnetic field and plasma distribution on target surface, and the erosion track on the sputtered target
- Figure 2.9 Schematic of (a) Cathodic Arc Evaporation, (b) generation of macroparticles, (c) growth defect initiated at a droplet
- Figure 2.10 Schematic cross-section of ABSTM coater
- Figure 2.11 Coating growth process
- Figure 2.12 Thornton's microstructure zone diagram of sputtered deposited films (after [8])
- Figure 2.13 Messier's model for thin film microstructure (after [9])
- Figure 2.14 Molecular dynamic computer simulations of a Si film growth under (a) without ion bombardment, (b) at $-V_s = 50$ V, $J_i/J_n = 0.04$, (c) at $-V_s = 50$ V, $J_i/J_n = 0.16$ (after [70])
- Figure 2.15 (a) Structure zone model relating to the closed-field unbalanced magnetron sputtering system, (b) slices through structure zone model at constant bias voltages V_1 and V_2 ($V_2 > V_1$) (after [71])
- Figure 2.16 Coating structures produced by the ABSTM
- Figure 2.17 Hardness as a function of superlattice period
- Figure 2.18 Hardness as a function of grain size
- Figure 2.19 Schematic of sp^3 , sp^2 , and sp^1 bonding type of carbon atoms
- Figure 2.20 Three-dimensional representation of sp^3 covalent bonding (shaded regions) in diamond structure [101]
- Figure 2.21 Schematic of the sp^2 structure of graphite showing the sigma bond and pi bond (above and below the sigma orbital plane) [101]
- Figure 2.22 Carbon phase diagram (after [101])
- Figure 2.23 Crystal structure of graphite (where a is the lattice parameter)
- Figure 2.24 Characteristic Raman spectra for the various carbon-based materials: carbyne (sp bonded carbon), graphite, disordered graphite (sp^2 bonded carbon), fullerene C60, carbon nanotubes, and diamond (sp^3 bonded carbon) [108].
- Figure 2.25 Types of carbon-based coatings
- Figure 2.26 Ternary phase diagram of carbon-based coatings
- Figure 3.1 (a) HTC 1000-4 ABSTM PVD coater and (b) schematic cross-section of the chamber

Figure 3.2	(a) Schematic of target arrangement, (b) Process sequence and parameter settings for C/Cr coating deposition
Figure 3.3	Schematic outline design of the tribocorrosion test rig (not to scale)
Figure 3.4	Schematic of SRET experimental set up including probe geometry
Figure 3.5	Pin-on-disc test
Figure 3.6	(a) CSEM Revertest Scratch tester, (b) Schematic of scratch generated
Figure 3.7	HRc adhesion failure mechanisms. Number corresponds to acceptable grade, with 1 the best and 6 the poorest
Figure 3.8	Nano-hardness instrumented calculations
Figure 3.9	Schematic of the calottes
Figure 3.10	Stress measurement (a) schematic of sample before and after coating deposition, (b) outline of radius of curvature calculation
Figure 3.11	X-ray diffraction from crystal planes
Figure 3.12	Schematic of Bragg-Brentano geometry
Figure 3.13	Schematic of glancing angle geometry
Figure 3.14	Schematic of (a) Raman spectroscopy and (b) Raman scattering
Figure 3.15	Schematic of SEM and interaction volumes
Figure 3.16	Schematic outline of a Transmission Electron Microscope
Figure 3.17	Arrangement of samples glue on glass plate
Figure 3.18	Cahn TG 131 microbalance
Figure 3.19	PIS calibration output signal in tap water and in 0.01% NaCl solution
Figure 3.20	Potentiodynamic polarisation test apparatus
Figure 3.21	Experimental setup for tribocorrosion test
Figure 3.22	Schematic of milling test
Figure 4.1	Influence of unbalancing coil current and substrate bias on the ion saturation current and ion-to-neutral ratio during film growth
Figure 4.2	Ion saturation current and ion-to-neutral ratio as a function of the substrate bias voltage. The dark squares represent conditions at which C-Cr films were deposited
Figure 4.3	Influence of bias voltage on the substrate temperature induced by ion bombardment during coating deposition
Figure 4.4	Bias current as a function of the bias voltage
Figure 4.5	Compositional depth profiling of (a) $U_B = -75$, (b) $U_B = -350$ V, (c) $U_B = -75/350$ V, (d) $U_B = -450$ V samples
Figure 4.6	RBS spectrum of C/Cr coating
Figure 4.7	Critical load as a function of bias voltage
Figure 4.8	(left) Adhesion scratch and (right) Rockwell-C indent for films deposited at various bias voltages (scale bar = 200 μ m)
Figure 4.9	Average friction coefficient as a function of the bias voltage
Figure 4.10	Friction curves of C/Cr coatings as a function of the sliding distance and the bias voltage
Figure 4.11	(a) Sliding wear coefficient as a function of the bias voltage, and (b) wear track profiles after pin-on-disc tests
Figure 4.12	Coating thickness as a function of bias voltage
Figure 4.13	Optical images of craters used for thickness measurement as a function of the bias voltage
Figure 4.14	Hardness and Young's modulus of C/Cr coatings as a function of bias voltage
Figure 4.15	Compressive stress of C/Cr coatings as a function of the bias voltage
Figure 4.16	(a) $\theta/2\theta$ and (b) Glancing angle X-ray diffraction patterns of C/Cr coatings deposited at various bias voltages

- Figure 4.17 XPS spectra taken after 2 min and 4 min Ar⁺ etching of: (a) U_B = -75 V, and (b) U_B = -350 V samples
- Figure 4.18 Raman spectra of C/Cr coatings deposited at various bias voltages
- Figure 4.19 Raman spectra of graphite target material, the wear track generated after pin-on-disc test, and the pure cemented carbide sample
- Figure 4.20 Raman spectrum curve fitting result (D-band at 1380 cm⁻¹, G-band at 1572 cm⁻¹)
- Figure 4.21 D-band shift as a function of the bias voltage
- Figure 4.22 ID/IG ratio as a function of the bias voltage
- Figure 4.23 Raman spectra of as deposited coatings and the wear tracks generated on U_B = -65 V and -95 V samples
- Figure 4.24 SEM micrographs of C/Cr coatings deposited at the bias voltage indicated (note the different scale on U_B = -95 V and -350 V samples)
- Figure 4.25 Surface morphology of C/Cr coating deposited at U_B = -75 V and U_B = -350 V
- Figure 4.26 EDX analysis of C/Cr coatings deposited at U_B = -75 V and U_B = -350 V
- Figure 4.27 (a) XTEM image of growth defect found in U_B = -95 V sample, (b) SEM image of growth defects on U_B = -350 V sample
- Figure 4.28 SEM images of the wear tracks of coatings deposited at the bias voltage indicated
- Figure 4.29 BF-XTEM micrographs of C/Cr coatings deposited at (a) U_B = -75 V, (b) U_B = -95 V, (c) U_B = -120 V, (d) U_B = -350 V, and SAD pattern of (i) C/Cr coating, (ii) CrN base layer (note the different scale)
- Figure 4.30 Low magnification HAADF image of the films deposited at U_B = -95 V
- Figure 4.31 BF-XTEM of the coating near-surface region for (a) U_B = -75 V and (b) U_B = -95 V samples
- Figure 4.32 Z-contrast XTEM, showing both nanolayers and nanocolumns
- Figure 4.33 High-resolution BF-XTEM image of U_B = -95 V sample
- Figure 4.34 (a) BF-XTEM image of coating deposited at U_B = -120 V, (b) magnified image of dotted box region (rotated 90° clockwise) showing the artificial multilayer structure (arrowed)
- Figure 4.35 Dark field image of C/Cr coating grown at U_B = -350
- Figure 4.36 HAADF image of C/Cr coating grown at U_B = -350 V
- Figure 4.37 (a) BF-XTEM image of U_B = -350 V sample, (b) lattice resolution bright field image of the dotted box region
- Figure 4.38 Lattice resolution image of coating grown at U_B = -350 V
- Figure 4.39 BF-XTEM image of U_B = -75/350 V sample
- Figure 4.40 ADF STEM image of C/Cr coating grown at alternative bias voltage of U_B = -75 V (columnar) and U_B = -350 V (multilayer)
- Figure 4.41 (a) ADF STEM image, (b-c) Electron energy loss spectra of CK (~286 – 294 eV) and CrL (~575 – 595 eV) for point 1 to point 4
- Figure 4.42 (a) CK-edge data of U_B = -75 V and U_B = -350 V layers, (b) CK-edge and CrL_x data of the clusters and matrix within U_B = -350 V layer
- Figure 4.43 Jump ratio maps of C and Cr in U_B = -75/350 V sample
- Figure 4.44 TGA results for C/Cr coating deposited at various bias voltages (TiN coating was taken for reference)
- Figure 4.45 Glancing angle XRD patterns after TGA tests for C/Cr coatings deposited at various bias voltages
- Figure 4.46 SEM surface morphology of the (a) as deposited coating, and oxidised surface after TG tests of coating deposited at (b) U_B = -65 V, (c) U_B = -75 V, (d) U_B = -95 V, (e) U_B = -120 V, (f) U_B = -350 V, after TGA tests. Arrows show initiation of diffusion processes at growth defects

- Figure 4.47 SEM/EDX analysis after TGA tests of coating deposited at (a) $U_B = -65$ V, (b) $U_B = -95$ V, (c) $U_B = -350$ V
- Figure 4.48 SEM image of the oxidised surface of coating deposited at $U_B = -95$ V, (b) EDX analysis of the bright particles marked with "X"
- Figure 4.49 SEM images (top) and EDX/elemental mapping of oxidised surfaces of $U_B = -65$ V and $U_B = -350$ V samples
- Figure 4.50 High magnification SEM surface morphology of chromium oxide formed on the oxidised surface after TGA tests: (a) $U_B = -65$ V, (b) $U_B = -75$ V, (c) $U_B = -95$ V, (d) $U_B = -120$ V, (e) $U_B = -350$ V
- Figure 4.51 XRD patterns of (a) as deposited C/Cr coatings, and coating grown at (b) $U_B = -75$ V, (c) $U_B = -95$ V, (d) $U_B = -120$ V, and (e) $U_B = -350$ V, after heat treated at the indicated temperature
- Figure 4.52 Surface morphology for coating deposited between $U_B = -65$ V and $U_B = -350$ V after heat treatment at 350°C for 1 hour
- Figure 4.53 Surface morphology for coating deposited between $U_B = -75$ V and $U_B = -120$ V after heat treatment at 410°C for 1 hour
- Figure 4.54 Surface morphology for coating deposited between $U_B = -65$ V and $U_B = -350$ V after heat treatment at 450°C for 1 hour
- Figure 4.55 Surface morphology for coating deposited between $U_B = -65$ V and $U_B = -350$ V after heat treatment at 700°C for 1 hour; the -350 V-edge shows the surface around the edge of coating deposited at $U_B = -350$ V after heat treatment
- Figure 4.56 (a-c) Initiation and growth of spiky iron oxide globule; (d) EDX analysis, and (e) elemental mapping analysis of the spiky globule
- Figure 4.57 Raman spectra of coating deposited at (a) $U_B = -75$ V, (b) $U_B = -95$ V, (c) $U_B = -120$ V, (d) $U_B = -350$ V, heat-treated at the indicated temperature
- Figure 4.58 Potentiodynamic polarisation curves for uncoated (316SS) and C/Cr coated samples
- Figure 4.59 Comparison of anodic current density at a working electrode potential of +300 mV against the substrate bias voltage for C/Cr coated samples
- Figure 4.60 SEM images after potentiodynamic polarisation tests of C/Cr films deposited at the indicated bias voltage
- Figure 4.61 SEM surface morphology after potentiodynamic polarisation tests for C/Cr coated samples prepared at the indicated bias voltage
- Figure 4.62 Pitting mechanisms: surface morphology of (a) $U_B = -65$ V, (b) $U_B = -75$ V, (c) $U_B = -350$ V, and cross-section of the polarised samples (d) $U_B = -65$ V, (e) $U_B = -95$ V, (f) $U_B = -350$ V (note: cracking of the coating was the consequence of poor cross-section sample preparation)
- Figure 4.63 Tribocorrosion calibration results in air and tap water for SS sample
- Figure 4.64 Tribocorrosion calibration results in tap water for SS and C/Cr coated samples
- Figure 4.65 Influence of loading and unloading on the open circuit potential of SS in 0.01% NaCl
- Figure 4.66 Influence of loading and unloading on the open circuit potential of SS in 0.01% NaCl
- Figure 4.66 E_{corr} versus time for C/Cr coated SS at a load of 1 N in 0.01% NaCl
- Figure 4.67 SRET line scan under various applied loads for identical contact times (30 s per load) for (a) SS and (b) C/Cr coated samples (note that portion negative values relate to anodic activity and positive values to cathodic activity)

- Figure 4.68 Equivalent total volume of metal loss (mC/cm^2) calculated from SRET line scans shown in Figure 4.6
- Figure 4.69 Uncoated SS sample (a) SRET line scan under various applied loads for 5 min contact time per load at new position for each load, (b) the corresponding wear track generated at the load indicated, (c) Area under the wear tracks and equivalent total volume of metal loss (mC/cm^2) calculated from SRET line scan shown in (a) as a function of load
- Figure 4.70 C/Cr coated sample (a) SRET line scan under various applied loads for 5 min contact time per load on same contact point, (b) Equivalent total volume of metal loss (mC/cm^2) calculated from SRET line scan shown in (a)
- Figure 4.71 Damage (area under SRET line scan) generated at various loads as a function of loading time for (a) stainless steel, and (b) C/Cr coated samples
- Figure 4.72 Line displacement versus time scan upon unloading and loading
- Figure 4.73 SRET line scan for C/Cr coated sample subjected to repeated loading and unloading sequence at (a) 0.5 N, (b) 1 N, (c) 3 N, (d) 5 N
- Figure 4.74 Unloading line scan after 1 hr sliding showing the corrosion activity after 45, 60, 75, and 90 s following unloading at 3 N (C/Cr sample). No corrosion activity was observed after approximately 2 min of unloading.
- Figure 4.75 (a) Typical wear track profiles and (b) wear coefficients determined for various test environments after 1hr testing
- Figure 4.76 SEM/EDX elemental mapping of the wear track generated on C/Cr coated samples after 1 hr testing in (a) air, and 0.01% NaCl at (b) E_{corr} , and (c) cathodic protection
- Figure 4.77 Optical images of the wear scar (arrow shows the sliding direction) of uncoated SS sample and alumina ball counter part tested (a-b) in air, (c-d) at E_{corr} , and (e-f) under cathodic polarisation. All markers: 200 microns.
- Figure 4.78 SEM images of the wear scar of C/Cr coated sample tested (a) in air, (b) at E_{corr} , and (c) under cathodic protection (images on the right represent the magnified picture of the centre of the wear tracks in (a) to (c))
- Figure 4.79 Optical images of the counter part of C/Cr coated samples tested (a) in air, (b) at E_{corr} , and (c) under cathodic polarisation
- Figure 4.80 Flank wear versus volume removed for uncoated and C/Cr coated samples prepared at various bias voltages
- Figure 4.81 Amount of volume removed for uncoated and C/Cr coated end mills deposited at various bias voltages
- Figure 4.82 SEM images of uncoated and C/Cr coated ($U_B = -65, -95, -120 \text{ V}$) end mills after milling 135720 mm^3 AlSi alloy
- Figure 4.83 SEM surface morphology of the flank and the EDX analysis of the built-up material of uncoated sample
- Figure 4.84 SEM surface morphology of the flank and the EDX analysis of the built-up material of $U_B = -65 \text{ V}$ sample
- Figure 4.85 $U_B = -95 \text{ V}$ sample (a) SEM surface morphology of the flank, (b) magnified image of built-up edge highlighted with yellow, (c) backscattered electron image (BSE) of built-up material highlighted with red, (bottom) EDX analysis of the area indicated with A, B and built-up material
- Figure 4.86 $U_B = -120 \text{ V}$ sample: SEM surface morphology of the flank and the EDX analysis of the area indicated with A and B shown in (a)

Figure 4.87	SEM-EDX Elemental mapping of endmill coated with C/Cr at $U_B = -120$ V
Figure 4.88	(a) Optical image showing the flank of end mill where a Raman spectrum was taken, (b) Raman spectra of the flank for uncoated and C/Cr coated ($U_B = -65, -95, -120$ V) end mills. Note that the green spectrum is for reference which was taken from uncoated end mill before the milling test
Figure 4.89	(a) Optical image of the flat end swarf/chip of removed workpiece material, (b) Raman spectra of the flat end of the chip removed after milling tests using uncoated and C/Cr coated ($U_B = -65, -95, -120$ V) end mills. The spectrum of bulk AlSi workpiece material shown in purple is taken for reference
Figure 4.90	(a) Optical image of the sharp end swarf/chip of removed workpiece material, (b) Raman spectra of the sharp end of the chip removed after milling tests using uncoated and C/Cr coated ($U_B = -65, -95, -120$ V) end mills. The spectrum of bulk AlSi workpiece material shown in red is taken for reference
Figure 5.1	Figure 5.1 XTEM micrograph and SAD pattern of film deposited at (a) $U_B = -450$ V, (b) $U_B = -550$ V
Figure 5.2	BF-XTEM image and SAD pattern of film grown at temperature of 450°C at $U_B = -75$ V
Figure 5.3	BF-XTEM image and SAD pattern of film grown at temperature of 260°C , at $U_B = -75$ V, and Cr target power of 3 kW
Figure 5.4	Schematic of the microstructures formed between $U_B = -65$ and -350 V
Figure 5.5	BF-XTEM views of the various types of structures developed in the C/Cr coatings deposited at bias voltages between $U_B = -75$ V and $U_B = -550$ V with their corresponding temperature induced by ion bombardment
Figure 5.6	Schematic diagram of formation of nanoscale multilayer structure in the C-Me system due to irradiation induced self-organisation mechanism.
Figure 5.7	XTEM image showing the substrate-CrN base layer interface, and C/Cr coatings
Figure 5.8	D-band shift and stress as a function of bias voltage for C/Cr coatings
Figure 5.9	I_D/I_G ratio and friction coefficient as a function of bias voltage for C/Cr coatings
Figure 5.10	Corrosion mechanisms of coatings in the presence of solution

List of Tables

Table 1.1	Summary of the recent research trend of carbon-based coatings produced using magnetron sputtering technique
Table 2.1	Sputtering yield of elements at 500 eV ions
Table 2.2	Properties of various forms of carbon [105]
Table 3.1	Dimensions and materials used for various tests and analytical methods
Table 3.2	Substrate cleaning procedure prior to coating deposition (Note: DECOSPRAY N and GALVEX are commercial cleaning solutions)
Table 3.3	Principle deposition sequence of ABSTM
Table 4.1	Coating area density and film bulk density against the bias voltage
Table 4.2	Summary of the properties of C/Cr coatings
Table 4.3	Areas under the peaks for C-C and Cr-C bonds expressed as a % of total area under these peaks obtained from the XPS curve fitting for the indicated etch time of samples deposited at $U_B = -75$ V and the $U_B = -350$ V

CHAPTER 1

Introduction

1.1 Motivation

New trends in today's industries are leading to more stringent demands on machining tools, machine components and design of machinery, to reduce friction. Reduction in friction could result in better efficiency and service life of tools and motors, improve the reliability of gears and roller bearings, and reduce the use of hazardous liquid lubricants, such as coolants. However, the requirements on higher loads, closer tolerances or the prohibition of lubricant on components can lead to adhesive wear of surfaces, as a result of high tribological stresses. Therefore, lubricants are indispensable in most cases. Although lubricants could effectively reduce friction, they fail under extreme service conditions, such as under vacuum, at very low or high temperatures and in corrosive environments. In addition, lubricants are detrimental to the environment as they are released during machining in an ecologically and economically undesirable situation. According to Sreejith [1], the use of lubricants costs approximately 16-20% of the total manufacturing cost as a result of subsequent steps for degreasing, surface cleaning, lubricant handling and recycling, and treatment of by-products or waste.

As a result, alternative lubrication methods are sought to replace liquid lubricants in machining. One possible way of reducing or even avoiding of liquid lubricants is by using solid lubricant materials or tribologically active coatings which possess high thermal stability and chemical inertness, increased wear and adhesion resistance, improved toughness and a lower coefficient of friction, and that can take over some of the functionality of the lubricant. Solid lubricants of great technological interest are graphite and molybdenum disulfide (MoS_2), because of their low friction coefficient ranging from 0.05 to 0.25. MoS_2 offers an extremely low friction coefficient of ~ 0.01 in vacuum. However, the susceptibility of such lubricants to degradation when

exposed to a humid environments and vulnerability to oxidation [2] have limited their use to more conventional applications. In comparison, carbon-based coatings are well-known and widely used in many industrial applications under ambient conditions. Carbon has been known for decades as a key element in reducing friction of thin films, due to its layered-lattice structure that allows easy shearing between contacting surfaces [3]. For this reason, solid carbon (more specifically a graphite target) and/or carbon containing gas, such as methane (CH_4) and acetylene (C_2H_2), have attracted considerable research interest and have been widely used in conjunction with other metals to synthesis carbon-based coatings, such as diamond-like carbon (DLC), metal-DLC, and metal-graphite coatings. Among the current technologies, physical vapour deposition (PVD) is the most promising technique to produce carbon-based coatings. The PVD process produces DLC films that offer a smoother surface and use a significantly lower deposition temperature (generally between 100 and 450°C) than the chemical vapour deposition (CVD) technique (approximately 600°C is needed, to give the required combination of properties [4]. The PVD process is also an ideal deposition technique for temperature sensitive tribological materials, such as low carbon steels (< 0.2 %C, where typical uses are in automobile body panels and wire products), low-alloy carbon steels (e.g. bearing steels), and martensitic grades of stainless steel (0.1-0.65 %C, 11-17 %Cr; e.g. springs, surgical blades, knives and cutting edges). From the advantages offered by the PVD process, and the availability of this technique at Sheffield Hallam University, PVD was chosen as the coating deposition method to be used in this research study.

1.1.1 Limitations of existing carbon-based coatings

DLC-coating is the most commonly used carbon-based coating due to their excellent tribological characteristics, for example high hardness (5-70 GPa), low friction coefficient (≤ 0.1) and good wear resistance ($\sim 10^{-17} \text{ m}^3\text{N}^{-1}\text{m}^{-1}$). However, the major drawbacks for DLC coatings use for machining and component-wear applications are their poor adhesion to the substrate, the high compressive stress (0.5-6 GPa), the brittleness (less toughness) and the low load-bearing capacity [see Table 2.3 in Chapter 2]. Because of the high compressive stress, DLC coatings are limited to a very thin thickness ($\leq 1 \mu\text{m}$ [5]), so that good adhesion can be produced between the coating and the substrate. This in turn limits their applications as protective coatings, because

thicker films are usually preferred to prolong coating wear life [6]. To overcome the limitations of DLC films, the two methods are commonly used. The first method is to deposit a metal transition layer between the substrate and the coating to reduce the effect of the difference in the coefficient of expansion of the film and the substrate upon cooling down from the deposition temperature. The incorporation of metal transition layers has been found to reduce the compressive stress, and to have adhesion promoting, coating strengthening and higher load bearing functions. The second method is to incorporate a metal, such as tungsten (W), chromium (Cr), titanium (Ti), into the carbon-based coating to reduce the intrinsic stress. Inclusion of a small amount of these metals could lead to stabilisation of the coating structure by reduction of the internal stress, improve film toughness, and allow growth of thicker and better adherent films [7]. A coating produced by this second method is commonly known as either metal-DLC (Me-DLC) or metal-Graphite (Me-Graphite).

1.1.2 Research opportunities

A number of techniques have been used to grow carbon-based coatings. More detailed information is presented in Chapter 2 of this thesis. Until recent years, investigations have been carried out to study the properties of these coatings under different process parameters and/or testing conditions. This is summarised in Table 1.1, which shows the recent research trend of carbon-based coatings produced using the PVD technique, specifically the magnetron sputtering technique (this is discussed in Chapter 2). Table 1.1 clearly shows that attention has focused on the investigation of the mechanical properties and tribological performance. Although a structure zone model of PVD coatings has been available [8-9], and substantial studies have been carried out to gain a better understanding of the effects of process parameters, such as temperature, pressure, ion flux and ion energy, on the evolution of the film microstructure [10-12], particular attention has so far focussed on titanium-nitride (TiN) based coatings [13-14], and fullerene-like carbon nitride coatings [15-16]. The understanding of the relationship between the influences of process parameters on the structure, microstructure, mechanical and tribological behaviour of carbon-based coatings, typically Me-Graphite coatings is rather limited. Therefore, this research is aimed at closing this gap. This is carried out by investigating Me-Graphite i.e. C/Cr coatings deposited using the combined steered cathodic arc/unbalanced magnetron sputtering available in the

Parameters	Carbon-based coating	Properties		Structure	Microstructure	Ref
		Mechanical	Tribological			
Coil current (control plasma density)	Me-DLC	X	X			[17]
*General study	Me-Graphite (C/Cr)	X	X		Brief	[18]
*Current on Cr target	Me-Graphite (C/Cr)	X	X		Brief	[19]
*Pin-on-disc test environments	Me-Graphite (C/Cr), Me-DLC	X	X		X	[20]
*Pin-on-disc test environments	Me-Graphite (C/Cr), Me-DLC		X			[21]
Acetylene flow rate	DLC	X	X			[22]
Target materials	Me-DLC		X			[23]
Bias voltage	DLC			X		[24]
Bias voltage and ion current density	Me-DLC	X	X		X	[25]
Bias voltage	DLC	X	X	X		[26]
Sputtering power	DLC	X			X	[27]
Bias voltage and argon pressure	Me-Graphite (Cr/C)	X			X (SEM)	[28]
General study (40 at.% C)	Me-Graphite (Cr/C)			X	X	[29]
*Bias voltage, frequency of pulse applied to the substrate bias	Me-Graphite (sputtered carbon)	X	X		Brief	[30]

* Carried out by the same research group

Table 1.1 Summary of the recent research trend of carbon-based coatings produced using magnetron sputtering technique

1.2 Aims and objectives

The major aims of this research are first, to study the effects of ion irradiation on the composition, microstructure, and functional properties of C/Cr coatings grown by the combined steered cathodic arc/unbalanced magnetron sputtering method (also known as ABSTM). A second aim is to open up a new area of application for the ABSTM technique by establishing new coatings deposited using this process.

The objectives are:

- 1) To deposit C/Cr coatings at bias voltage ranging from -65 V to -550 V, using the combined steered cathodic arc/unbalanced magnetron sputtering (or the ABSTM) technique.
- 2) To select the best techniques for coating characterisation.
- 3) To build a tribocorrosion test rig by modifying a conventional Scanning Reference Electrode Technique (SRET).
- 4) To study the influence of bias voltage on the coatings properties, their microstructure and the actual practical cutting performance of C/Cr coatings, based on the characterisation methods identified in (2).

1.3 Methods of approach

This research work contains two parts. The first part, which is the core of this research, is devoted to the development and investigation of low friction C/Cr coatings deposited by the combined steered cathodic arc/unbalanced magnetron sputtering (also known as Arc-Bond Sputtering, ABS) technique, using an industrial size Hauzer HTC 1000-4 PVD coater. Production of C/Cr coatings by this type of deposition process has never been previously investigated. This research focused on the influence of process parameters. Of particular importance in this respect is the substrate bias voltage (U_B), which controls the ion bombardment energy on the growing film and plays a crucial role in determining the properties and the microstructure/structure of the coating. The bias voltage range investigated within this project was between $U_B = -65$ V and $U_B = -550$ V. The effects of bias voltage on the mechanical properties, tribological behaviour, structure, microstructure, oxidation and corrosion performance, and the actual practical cutting performance of C/Cr coatings were studied.

In this research, chromium (Cr) was incorporated into the carbon-based coatings system due to its high sputtering yield, low cost, good corrosion-, oxidation-, and wear-resistances [31]. Cr is also used in a wide range of industrial applications as both a

The diagram is a phase diagram for the Cr-C system. The y-axis represents Temperature in °C, ranging from 400 to 2400. The top x-axis represents Weight % C, ranging from 0 to 100. The bottom x-axis represents Atom % C, ranging from 0 to 100. The diagram shows several phase regions and reaction lines. Key features include:

- Cr₂₃C₆ phase:** A solid solution phase that exists at low carbon concentrations (below ~15.69 wt% C). It has a maximum solubility of 1.3 wt% C at 1569°C.
- Cr₇C₃ phase:** A phase that exists between ~15.69 wt% C and ~30 wt% C. It has a maximum solubility of 17.65 wt% C at 1765°C.
- Cr₃C₂ phase:** A phase that exists between ~30 wt% C and ~40 wt% C. It has a maximum solubility of 32.4 wt% C at 1725°C.
- Liquid (LIQ) phase:** The liquid phase region, which is bounded by a liquidus line that starts at 1860°C (melting point of pure Cr) and curves upwards as carbon content increases.
- Carbon (C) phase:** The carbon phase, which is a solid solution of carbon in iron, represented by a horizontal line at 1805°C.
- Other phases:** The diagram also shows regions for (Cr) + Cr₂₃C₆, Cr₂₃C₆ + Cr₇C₃, and Cr₇C₃ + Cr₃C₂.

7

The second part of this research work is focused on the modification of the conventional Scanning Reference Electrode Technique (SRET), which aims to provide a novel method for characterising the real-time localised tribocorrosion behaviour of uncoated and Physical Vapour Deposited (PVD) coated samples. A tribocorrosion test rig has been constructed using a ball-on cylinder contact configuration, and was used in a preliminary study of uncoated and C/Cr ($U_B = -75$ V) coated stainless steel. If successful, the modified SRET will provide a novel tribocorrosion test rig that can be used to study the tribocorrosion behaviour of other materials and coatings.

1.4 Structure of thesis

Chapter 2 is the review of literature, which was divided into four sub-sections. Section 2.1 gives a brief introduction to the selected Physical Vapour Deposition (PVD) techniques mainly focused on unbalanced magnetron sputtering and cathodic arc evaporation, which are the principle of the Arc Bond Sputtering (ABS) technique. The growth and development of thin films and the influence of process parameters on microstructure evolution are given in Section 2.2. Section 2.3 gives a brief introduction to nanocomposite structure, which is further divided into nanolayered or superlattice, nanocrystalline and self-organised structure. Section 2.4 gives a general introduction to carbon and its allotropes, the properties, deposition methods, and applications of the three major groups of carbon-based coatings, such as diamond-like carbon (DLC), metal-DLC, and metal-graphite.

Chapter 3 describes the experimental details of this research. Section 3.1 presents the materials used, procedures for substrate preparation prior to coating deposition, procedures for coating deposition and the process parameters used to grow C/Cr coatings. Section 3.2 focuses on the modification of the conventional Scanning Reference Electrode Technique (SRET) to provide a tribocorrosion test method. This includes the design, experimental set-up, and tribocorrosion calibration procedures. The analytical techniques used for characterising C/Cr coatings are presented in Section 3.3. Some of the analysis work was performed with the support from members of Centre for Microanalysis of Materials at University of Illinois, USA, and Corus in Rotherham. These were mentioned in the acknowledgements.

The results of the experiments are presented in Chapter 4. The discussions and conclusions are given in Chapter 5 and Chapter 6, respectively.

CHAPTER 2

Review of Literature

This chapter aims to give fundamental knowledge to the selected physical vapour deposition (PVD) coating processes; these include magnetron sputtering, cathodic arc evaporation, and the combination of these two techniques which led to the development of the Arc Bond Sputtering (ABSTM) technique. The principle behind each of these deposition processes was studied in order to understand the importance of deposition parameters, such as substrate temperature, gas pressure, bias voltage, and ion-to-neutral ratio, on the film microstructure, properties and performance during real-life applications. The mechanisms during coating growth and the microstructure evolution were also studied as a function of deposition parameters to gain a better understanding of PVD coating growth. In this chapter, coating microstructures were classified into nanolayered or superlattice, nanocrystalline, and self-organised structure. The last section of this chapter covers the fundamental knowledge of the bonding configurations, structure, and properties of carbon allotropes, and categories, the current development, properties and applications of carbon-based coatings.

2.1 Physical Vapour Deposition (PVD) coatings technology

Physical Vapour Deposition is widely used to deposit coatings for various functional and decorative applications. It involves the creation of material vapour from the coating material target and its subsequent condensation onto a substrate to form a thin film. The process is discussed in more detail in the following sections. Figure 2.1 shows two of the most important methods for depositing thin films, these are sputtering and evaporation. In sputtering, atoms (neutral) are dislodged from the solid target surfaces through the impact of gaseous ions, whereas in evaporation, atoms are removed from the target surfaces by thermal means [35].

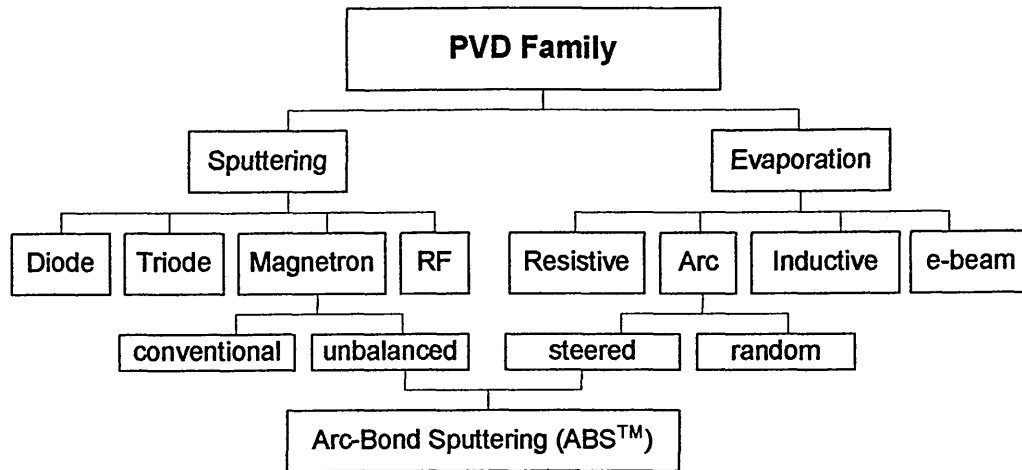


Figure 2.1 PVD techniques (Note: RF = radio frequency; e-beam = electron beam)

2.1.1 Introduction to plasma

The terms ‘glow discharge’ and ‘plasma’ are often used interchangeably used in thin film processing. Plasma is a conductive quasineutral (approximately equal numbers of electrons and ions) ionised gas, which can respond to local changes in potential. An external energy source, such as an electric field (acting directly on the charged particles only) is required to maintain the necessary equilibrium in the plasma. The dominant charge carriers in the plasma are electrons, which are generally much more energetic than the ions. This is due to the low mass of electrons which can respond much more quickly to electric fields than can the heavier ions [36]. To generate a plasma, generally argon is fed into the chamber while a high voltage is applied to two electrodes (cathode and anode). Argon is usually used as the preferred bombarding gas due to its low cost, higher atomic weight and because it is easier to ionise than the other two inert gasses, such as neon and helium. The discharge is usually maintained in an Ar atmosphere in the pressure range between $1 - 500 \times 10^{-3}$ mbar, and in the negative cathode voltage range between 0.3 – 5 kV [37]. Under the applied potential and an appropriate gas density, two processes may occur. These are: free electrons will be accelerated towards the anode and due to electron impact ionisation, further electrons and ions are produced. It is important to note that the gas density must not be too low (otherwise the electron will strike the anode without having a gas phase collision with a gas atom) or too high (otherwise the electron will not have gained sufficient energy by the time it strikes a gas

atom to cause ionisation). The positively charged ions (Ar^+) will strike the cathode and, if their energy is high enough, the emission of electrons known as secondary electrons (important for the initiation and further self-sustaining of the glow discharge due to their contribution in the intensive ionisation of the background gas by collisions with neutrals) will occur. These electrons will be accelerated across the sheath and will attain energies of the order of the discharge voltage.

Figure 2.2 is the classical architecture of a DC glow discharge [38], showing several distinct regions within the plasma between the cathode and the anode. These include:

- (i) Cathode glow region. The cathode glow region adjacent to the cathode is luminous due to neutralisation of both the positive and negative ions at the cathode surface. The emitted light is the characteristic of the target material and the sputtering gas.
- (ii) Cathode dark space or cathode sheath. An adjacent layer between the cathode surface and the plasma due to potential variation. Across this region, most of the voltage drop occurs, providing the accelerating force which drives the positive ions into the target.
- (iii) Negative glow region (an illuminated bright glow region). This is the region where intensive excitation and recombination occurs.

Beyond the negative glow region is another dark space (known as the Faraday dark space), the positive column, an anode dark space and the anode, which are essential for connecting electrically the negative glow to the anode but are not essential in the sputtering process because the negative glow usually fills the chamber.

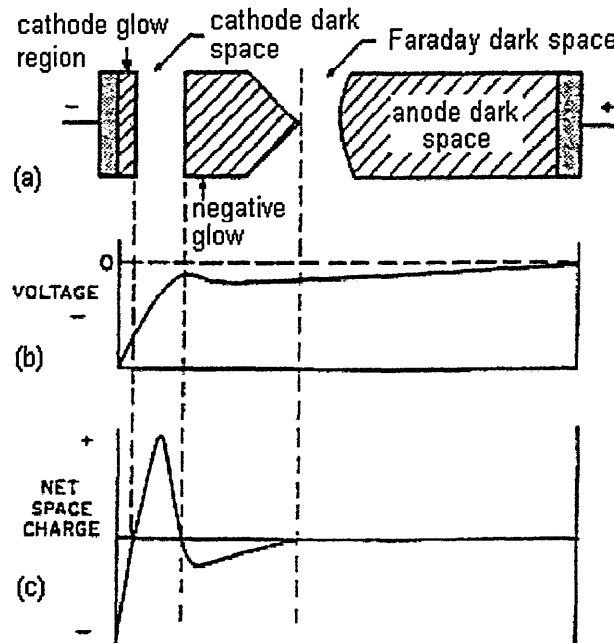


Figure 2.2 Schematic illustration of the DC glow discharge, (a) plasma regions, (b) voltage characteristics, and (c) net space charges

Figure 2.3 shows the current–voltage relation for various types of glow discharge [39]. The initial part of the curve shows the Townsend discharge (the current increase with a small increase in voltage) [40] and the transition zone. In the normal glow region, the discharge current increases significantly with a small increase in the voltage. The discharge is self-sustained by electron ionisation avalanches. As a consequence it increases the coverage of the cathode. When the entire cathode surface is covered, any subsequent increase in current requires much larger increases in voltage. This is known as the abnormal glow, typical of magnetron sputtering devices, which is the most often used mode in thin film deposition for processing plasmas. Further increase in the discharge current leads to the occurrence of an arc discharge (high current, low voltage discharge mode).

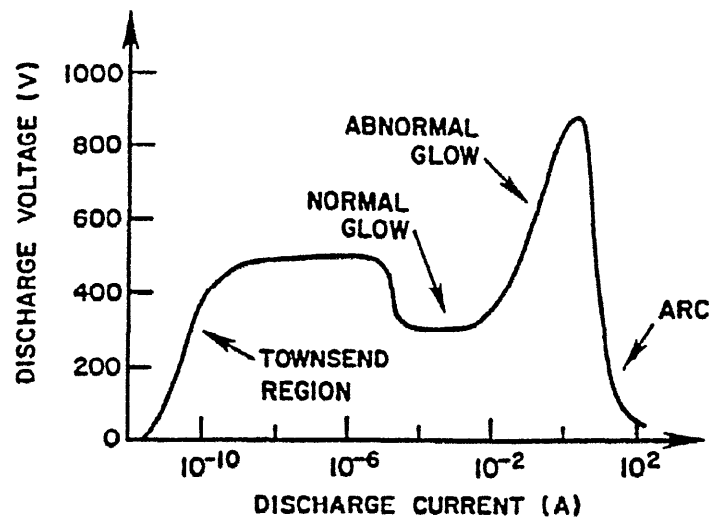


Figure 2.3 Current-voltage relation for various types of plasma discharge

2.1.2 Sputtering

Sputtering is one of the most versatile PVD techniques for applying coatings on metals, alloys, non-metals, intermetallic compounds and ceramics. It is a non-thermal vaporization process. The surface atoms of the target material are physically ejected by momentum transfer from energetic bombarding particles, usually gaseous ions accelerated from a plasma or ion gun. Most of the energy of the bombarding particle is converted to heat in the near-surface region.

In non-reactive sputtering, the positively charged gas ions are noble gas ions, which are generated when the free electrons collide with the gas (such as Ar) introduced into the chamber. These high-energy ionised Ar^+ particles are accelerate towards the target and eject neutral target surface atoms by momentum transfer. These atoms enter and travel through the discharge or plasma to eventually deposit on the negatively biased substrate, in a process called ion plating [41-42]. The sputtering process is schematically represented in Figure 2.4. The adsorbed atoms (adatoms) on the substrate surface will move to the lowest energy position to initiate or continue the coating growth process. The adatom life-time depends strongly on its kinetic energy and the thermodynamic conditions on the substrate surface, hence the deposition temperature and the gas pressure become the significant process parameters, which influence the growth and the structure of the coatings, and determine the probability of collisions in the plasma respectively (see Section 2.2 for coating growth and microstructure evolution).

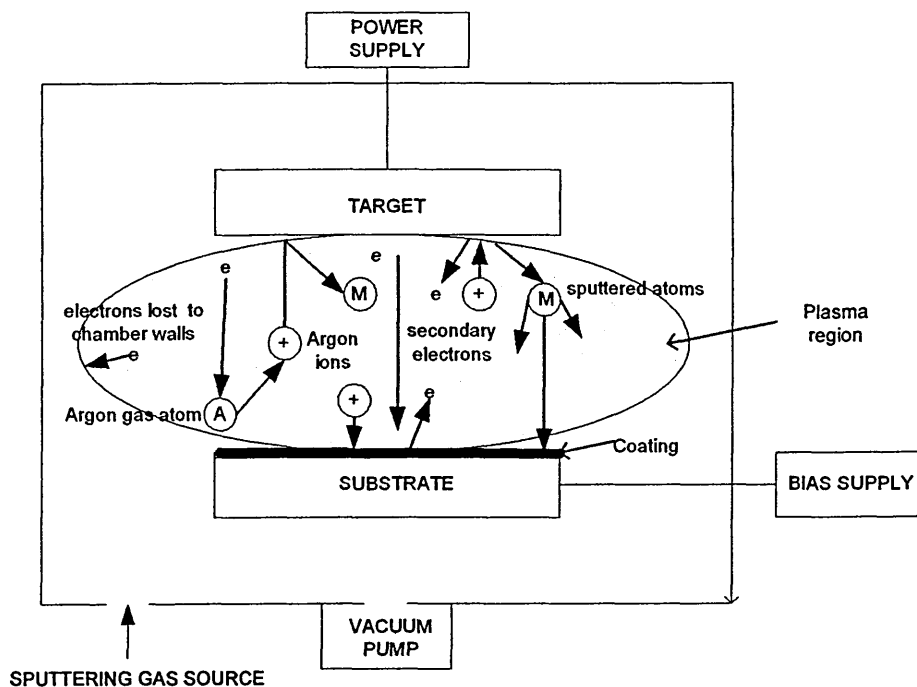


Figure 2.4 Sputtering mechanism

Sputtering can be quantified in terms of sputtering yield, Y , which is defined as the number of target material atoms that are sputtered for each incident energetic bombarding ion. The sputtering yield is dependent on the relative masses of the bombarding and target species, bombarding ion energy, the cohesive energy and the chemical bond strength of the target surface atoms. The sputtering yield can increase 2-3 times when the angle of incidence of the bombarding ions becomes off normal [43]. On the other hand, the sputtering yield can reduce substantially at high collision angle due to little momentum transfer. Table 2.2 [38] shows the sputtering yield of the elements commonly used for target materials. For 500 eV Ar^+ , carbon has the lowest sputtering yield of 0.12, which is about 10 times less than that of chromium i.e. 1.18.

Element	Ion				
	He	Ne	Ar	Kr	Xe
C	0.07	-	0.12	0.13	0.17
Cr	0.17	0.99	1.18	1.39	1.55
Nb	0.03	0.33	0.6	0.55	0.53
Al	0.16	0.73	1.05	0.96	0.82
Ti	0.07	0.43	0.51	0.48	0.43
V	0.06	0.48	0.65	0.62	0.63
Fe	0.15	0.88	1.1	1.07	1
Ni	0.16	1.1	1.45	1.3	1.22
Cu	0.24	1.8	2.35	2.35	2.05
Y	0.05	0.46	0.68	0.66	0.48
Zr	0.02	0.38	0.65	0.51	0.58
Mo	0.03	0.48	0.8	0.87	0.87
Ta	0.01	0.28	0.57	0.87	0.88
W	0.01	0.28	0.57	0.91	1.01
Au	0.07	1.08	2.4	3.06	3.01

Table 2.2 Sputtering yield of elements at 500 eV ions

2.1.2.1 Ion-surface interactions during sputtering

During bombardment of the target by positive ions, various interactions can occur on the target surface. This is illustrated in the Weissmantel model, shown in Figure 2.5 [44]. The interactions include liberation of ionised atoms, neutral atoms, secondary electrons, backscattered particles, x-ray emission, photon generation and gas desorption. Several other processes can occur in the target itself, which include the generation of collisional cascades (occurs when the surface atom that is struck attains enough energy to displace other atoms), the creation of point defects, compound formation, implantation, amorphisation, and local heating.

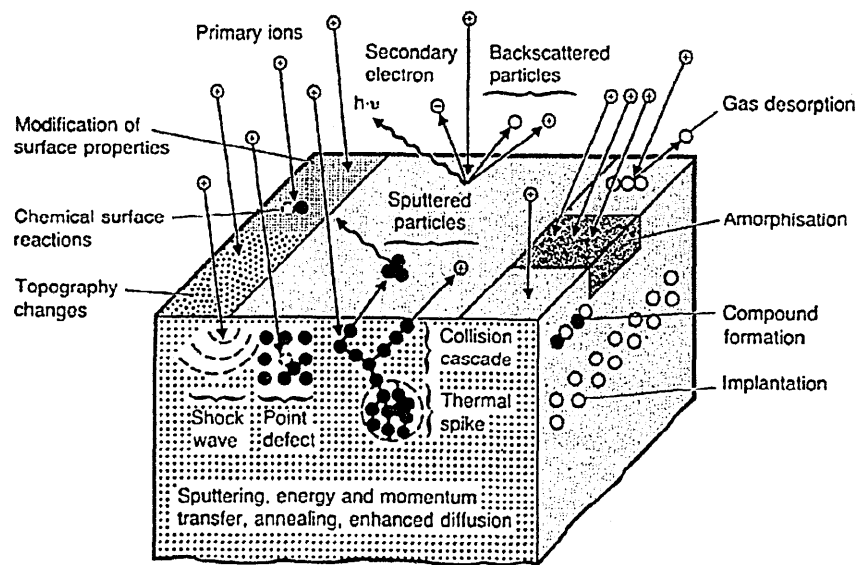


Figure 2.5 Interactions which occur at and near the target surface during the sputtering process: Weissmantel model (after [44])

2.1.2.2 Magnetron Sputtering

Magnetron sputtering is based on maintaining a glow discharge in a crossed electric (e) and magnetic field (B) [45]. When an electron is ejected from the target surface, it is accelerated away from the surface by the electric field but is trapped and forced to spiral around the magnetic field lines generated from the permanent magnets near the target (cathode) surface. The most common types of magnetron are circular and rectangular planar magnetrons, however, the use of a rectangular planar magnetron (Figure 2.6) is more practical for most applications.

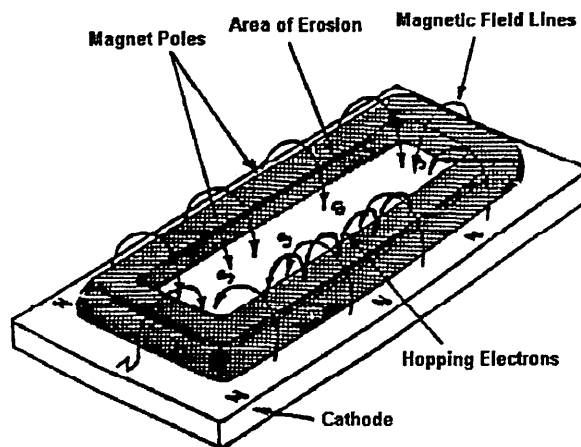


Figure 2.6 Schematic diagram of rectangular planar magnetron showing the arrangement of magnets, the electric and magnetic fields, and the plasma (shaded area)

In comparison to the conventional glow discharge, magnetron sputtering has additional ionisation as a result of the crossed electric and magnetic fields that confine the plasma near to the target surface. Therefore, the sputtering and the deposition rates are higher due to the increased ionisation and plasma density in the region adjacent to the target [37]. However, the major disadvantage of the use of the conventional magnetron (the magnetic field is equal in the centre and the periphery of the target, see Figure 2.7(a)) is that it is restricted by the sharp decrease in ionisation with increasing distance from the target to the substrate, because the high plasma density is confined to the vicinity of the target. To overcome this drawback, Window and Savvides [46] introduced the unbalanced magnetron concept where the magnetic field is stronger at the periphery than in the centre of the target. This is achieved by designing the magnetron array in such a way that the magnetic flux from one of the magnets is unequal to that from the other. As a result, the plasma glow expands outwards and ionisation and ion bombardment of the substrate is increased. The unbalancing effect can be precisely adjusted by the magnetic field generated by electromagnetic coils. Figure 2.7 shows the schematic representation of the plasma localisation and confinement for a conventional magnetron and an unbalanced magnetron. Figure 2.8 illustrates schematically the distribution of magnetic field, the plasma confinement region near the target surface during balanced magnetron sputtering and the resulting erosion track on the target surface. In order to further increase the ion flux, to prevent its loss to the chamber walls, and to maintain a dense plasma in the substrate region, closed-field unbalanced magnetron sputtering (CFUBMS) was introduced (an example is shown later in Figure 2.10).

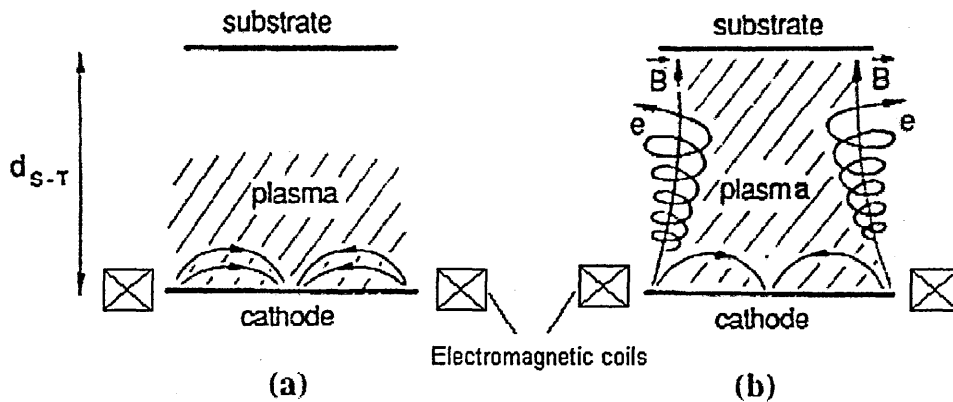


Figure 2.7 Plasma localisation and confinement for (a) conventional magnetron and (b) unbalanced magnetron; d_{S-T} is the distance between the substrate and the target

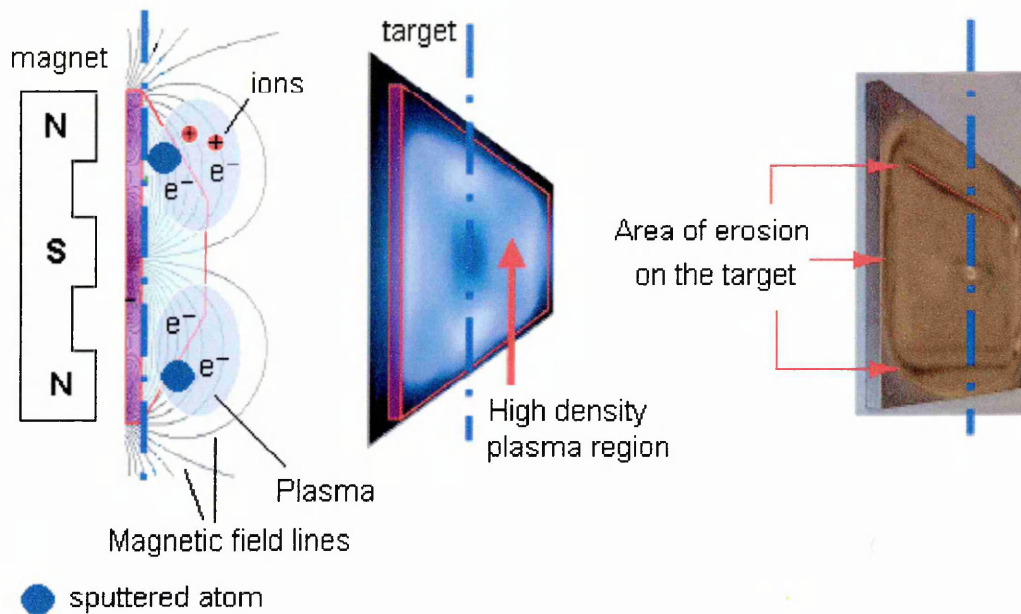


Figure 2.8 Schematic illustration of the magnetic field and plasma distribution on target surface, and the erosion track on the sputtered target

In magnetron sputtering, ions are extracted from the discharge surrounding the substrate by applying a negative potential of up to 500 V (usually 50 V) to the substrate [37]. The energy of ions incident at the substrate, and the ion-to-neutral ratio are the fundamental parameters that determine the structure and properties of the growing films. Ion energy can be estimated from the difference between the plasma potential and the substrate bias potential, and the incident ion-to-neutral ratio can be estimated from the ion current density and the deposition rate at the substrate. The effect of deposition parameters on coating growth will be discussed in Section 2.2.

2.1.3 Cathodic Arc Evaporation Technique

The arc deposition process is known to produce coatings that have high density, small grain size, and more importantly offer better coating to substrate adhesion strength [47]. A low-voltage and high-current power supply is essential to produce continuous cathodic arc sources and to maintain an arc discharge. The main characteristic features of arc discharges are [47]:

- A low discharge voltage close to the ionisation potential of the cathode or working gas atoms (30-80V),

- High current densities in the cathode spot, up to 10^8 - 10^{11} A/m²,
- High ion densities in the cathode region and electron density up to 10^{20} m⁻³
- Maximum temperatures of 4000 to 7000°C in the cathode spot

The arc evaporation process (see Figure 2.9(a)) begins when a high current, low voltage arc strikes on the surface of a cathode, and gives rise to a small (usually in a size of a few micrometers [48]) highly energetic emitting areas known as cathode spots (spots of plasma). Cathode spots are initiated at micro-protrusions (or tips) on the surface of the target, which may be located either at random points or the spot can be steered on the cathode surface. Steering of the arc can be achieved by using a magnetic field [49], the main challenge in this method is to reduce the amount of macroparticles (see next paragraph) deposited on the substrate. The continuous striking of electric arcs on the surface of the target (cathode) caused high local cathode surface temperatures (between 4000-7000°C) which evaporate the target materials from the cathode spots. The evaporated species are ionised and accelerated away from the cathode towards the substrate, because of the potential distribution and plasma expansion [50]. Theoretically, the arc is a self-sustaining discharge capable of sustaining large currents through electron emission from the cathode surface and the bombardment of the surface by positive ions under high vacuum conditions. The plasma generated in an arc discharge is dense and contains electrons, energetic ions, atoms (neutrals), and macroparticles in the form of droplets, these are schematically shown in Figure 2.9(b). The main drawback of the cathodic arc evaporation technique is the production of liquid droplets and macroparticles formed by the arc source during evaporation. It has been shown that target materials with higher melting point produce fewer droplets [51-53]. Macroparticles or droplets can lead to the initiation of growth defects, this is illustrated in Figure 2.9 (c) [54]. It was reported [54] that the film on top of the droplets grows under more intense ion irradiation and is deposited at higher rates than the material deposited near the lower part of the droplet, which is subjected to negligible ion-irradiation and is deposited at much lower rates due to the smaller acceptance angle. Therefore, the microstructure near the lower part of the droplet is of severely under dense as compared to the film grown on top of the droplet.

In PVD, the formation of macroparticles in the coatings has been shown to initiate corrosion and deteriorate the performance of the coating [55]. Therefore, great effort is concentrated on the suppression or elimination of macroparticles in the

coatings. This can be done by steering the arc using a magnetic field, reducing the temperature on the cathode surface near the cathode spots by providing effective cooling, and applying various filtering methods [56-57]. The commonly used filtering method is to insert a curved magnetic filter ('duct') between the source and the samples to guide the vacuum arc plasma from the source to the substrate by a curved magnetic field. This prevents the macroparticles from reaching the substrate because they move along nearly straight lines. The cathodic arc evaporation technique has been found to provide a useful tool in etching the substrate prior to coating deposition, due to its dense plasma and highly charged ions. The etching step has been proved to enhance the adhesion between the substrate and the subsequent coating [58]. In order to utilise the advantages of the arc and the magnetron sputtering techniques, the Arc Bond Sputtering (ABSTM) technique has been introduced [59-61].

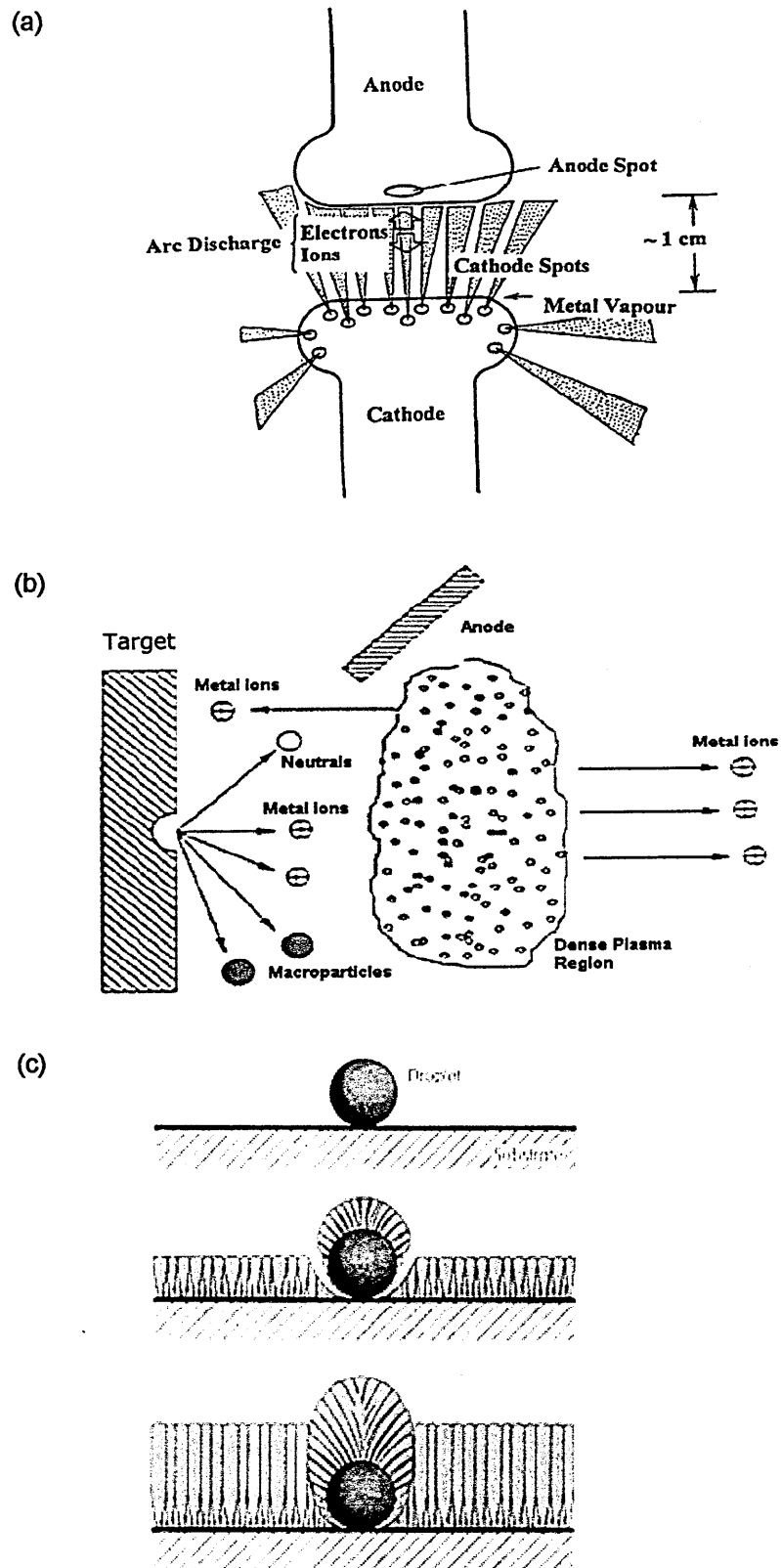


Figure 2.9 Schematic of (a) Cathodic Arc Evaporation, (b) generation of macroparticles, (c) growth defect initiated at a droplet

2.1.4 Arc Bond Sputtering (ABSTM) Technique

Arc Bond Sputtering (ABSTM) is the coating deposition technique used to produce C/Cr coatings in this research work. The ABSTM PVD coating technology has been available to the hard coating market since the first installation in 1991 [59-60]. This coating method combines two different coating techniques of steered cathodic arc and unbalanced magnetron technology in a single system, which offers substantial industrial advantages [61]. The idea behind the ABSTM technique was to combine the advantages of arc technology with the unbalanced magnetron technique, which aimed to combine the excellent adhesion offered by the arc technology with the versatility of material selection and reduced droplet formation offered by the magnetron source [59-60].

This technique allows the cathode to be used as an arc source by operating the cathode in a cathodic arc mode (see Figure 2.10) during simultaneous metal ion vacuum pre-cleaning (also known as ion-etching) of the substrate surface and metal-ion implantation prior to coating deposition. Coating deposition is then carried out in the unbalanced magnetron sputtering (UBM) mode. The schematic diagram of ABSTM coating chamber and the position of the magnetron array for alternative arc and unbalanced magnetron process modes are illustrated in Figure 2.10. The system comprises four rectangular cathodes, which have the advantage of operating either in steered cathodic arc or in unbalanced magnetron (UBM) mode by switching the power supplies and adjusting the magnetic field strength. The cathodes are surrounded by external electromagnetic coils which are magnetically coupled in a closed field manner to produce the unbalancing effect of the magnetrons and to increase plasma density in the vacuum chamber. The samples are mounted on a planetary rotating turntable in the centre of the chamber, which can be operated in 1, 2, or 3-fold rotation (τ) to ensure uniform coating thickness.

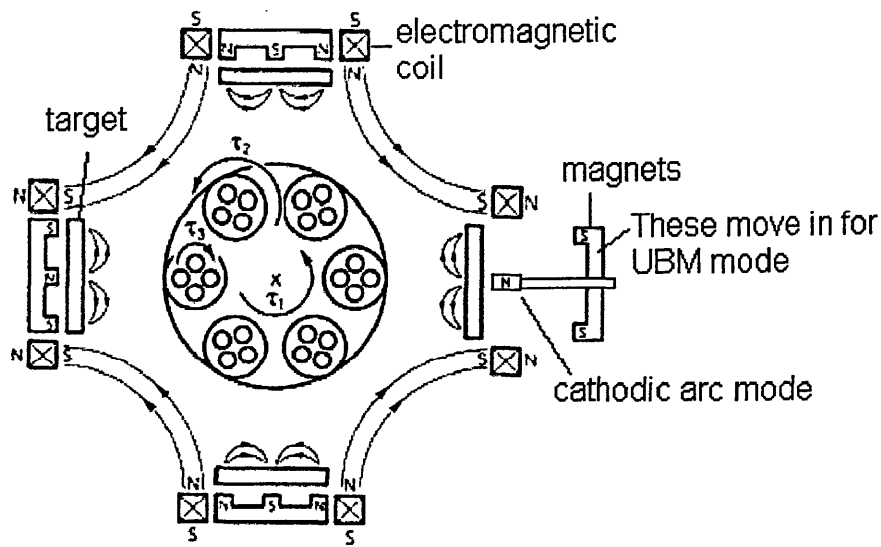


Figure 2.10 Schematic cross-section of ABSTM coater

2.2 Coating growth and microstructure evolution

The growth of PVD thin films proceeds through consecutive stages characterised by specific processes of microstructure evolution, which involves nucleation, island growth, impingement and coalescence of islands, formation of polycrystalline islands and channels, development of continuous structure and thickness growth [10, 62]. This is schematically shown in Figure 2.11 [63]. In general, PVD coating is grown following three general steps [8]:

- 1) transport of the coating species to the substrate,
- 2) adsorption of these species onto the surface of the substrate or the growing coating, their diffusion over this surface, and their incorporation into the coating or their removal from the surface by evaporation or sputtering,
- 3) migration of the coating atoms to their final position within the coating by bulk diffusion.

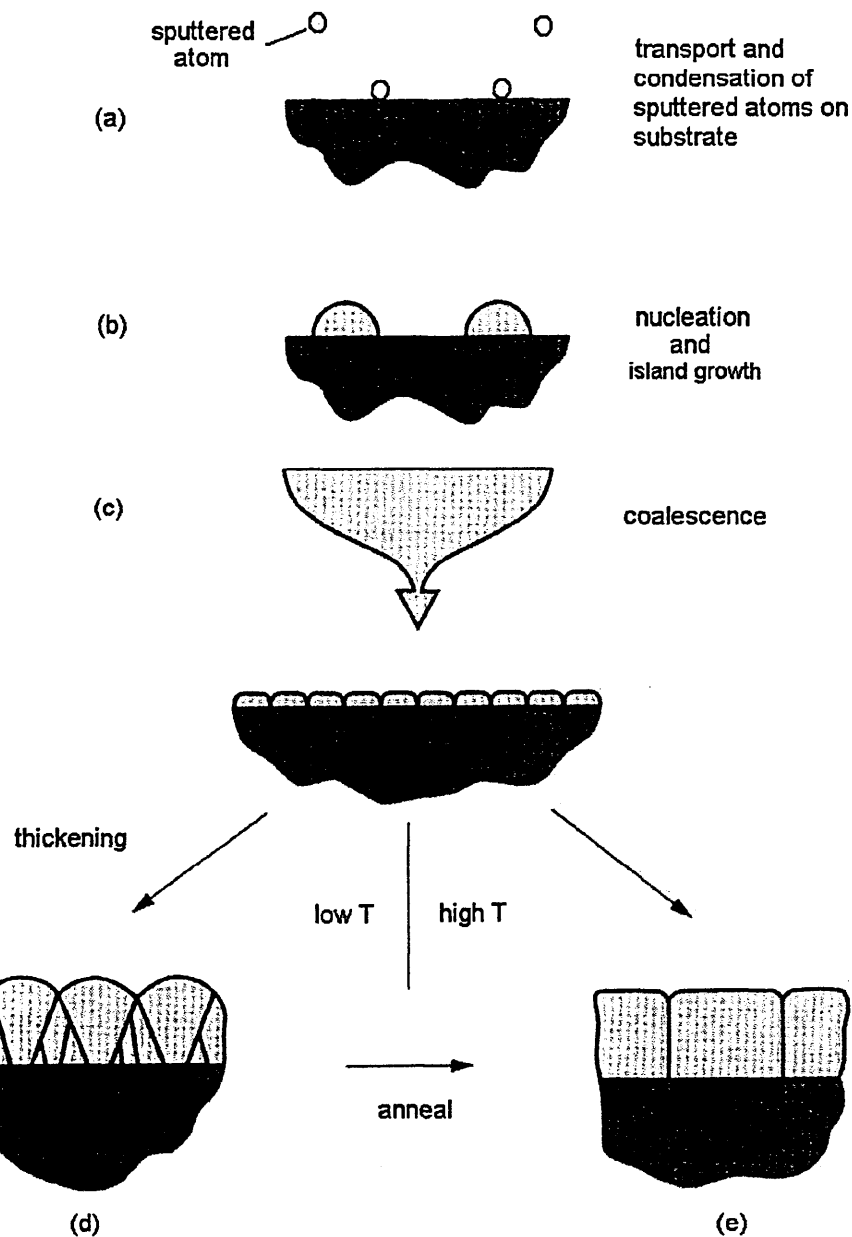


Figure 2.11 Coating growth process

It is known that deposition process parameters such as substrate temperature [64], gas pressure, bias voltage (energy of ion bombardment) [12] and ion-to-neutral ratio [65], play a dominant role within the growth of PVD films, influencing coating microstructure and properties of the coating. All of these parameters affect the energy delivered to the growing film, which, in turn, control the mobility of the deposited atoms that is crucial in determining the final coating microstructure. In addition to the process parameters, the presence of alloying or impurity elements (for example oxygen) and their segregation to surfaces and grain boundaries can also strongly affect the final structure by inhibiting or promoting the structure evolution [62]. A recent review on the

microstructural evolution during film growth as a function of deposition parameters can be found in [10].

The effects of the process parameters on coating microstructure are briefly discussed as follow:

Effects of substrate temperature, gas pressure, and bias voltage

During the PVD process, the working gas pressure controls the transport step of the coating atom, for example the coating atom arrival direction, while the substrate temperature controls the adatom diffusion step but this may be significantly influenced by the energetic ion bombardment. Figure 2.12 schematically presents the microstructure zone model introduced by Thornton in 1973 [8] illustrating the correlation between working gas pressure and substrate temperature. According to this model, at low T/T_m temperature (T = substrate temperature; T_m = coating material melting temperature), a pronounced columnar structure consists of tapered open voided growth boundaries, known as zone 1 (also shown in Figure 2.11(d)) is formed. This is due to atomic shadowing and low adatom mobility where incident atoms adhere where they impinge, in this zone. With increasing T/T_m , the structure transforms to the zone 2 structure (columnar grains structure, see also Figure 2.11(e)) via zone T (a transition state between zone 1 and zone 2, which consists of dense, poorly defined fibrous grains). Within zone 2, the width of the grain boundaries increases in accordance with activation energies or surface diffusion. At high T/T_m (zone 3), the structure consisted of equiaxed grains, for which the size increases in accordance with activation energies for bulk diffusion.

Messier et. al. [9] included an additional ion energy (E_i) contribution to the film growth model by replacing the pressure axis with a bias voltage (V_s) axis as shown in Figure 2.13. They found that at low T/T_m , an increase in the bias voltage (parameter that controls the ion bombardment energy) suppressed the formation of zone 1 and widened zone T (more densely packed structure), due to the increase in average energy of the bombarding ions which enhanced adatom mobility. Ion bombardment is a non-equilibrium process which provides energy to the growing film at an atomic level [66]. This process significantly differs from conventional heating due to the rapid transfer of the kinetic energy of the bombarding ions to a very small area of atomic dimensions and subsequent rapid cooling at the rate of about 10^{14} K/s [66]. Ar^+ ions are the dominant bombarding ions incident at the growing films with energy, E_i corresponding approximately to the applied negative substrate bias voltage, V_s , where $E_i = e(V_s - V_{pl}) \approx$

eV_s , since $V_{pl} \rightarrow 0$ (the plasma potential which is nearly the same as that of the grounded anode under conventional magnetron sputtering conditions [67]). Therefore, energetic ion bombardment influences the surface and bulk diffusion processes, and plays a crucial role in controlling the structure evolution during film deposition. It has been shown that an increase of the bias voltage changes the film microstructure from a porous to a dense structure due to increased adatom mobility. For example, it was found that, by varying the substrate bias voltage from -80 V to -160 V during TiN film deposition at 300°C, the film microstructure changed from a columnar structure with open column boundaries at $-V_s \leq 80$ eV, to a void-free dense columnar structure at $-V_s = 120$ eV, and finally to a fully dense structure at $-V_s = 160$ eV [68].

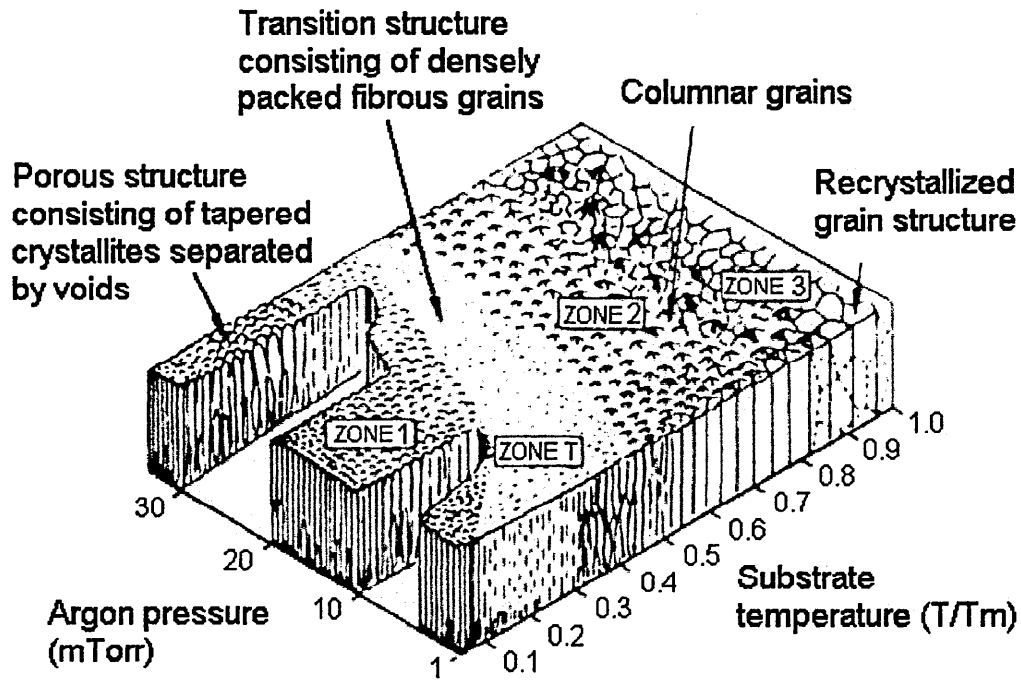


Figure 2.12 Thornton's microstructure zone diagram of sputtered deposited films (after [8])

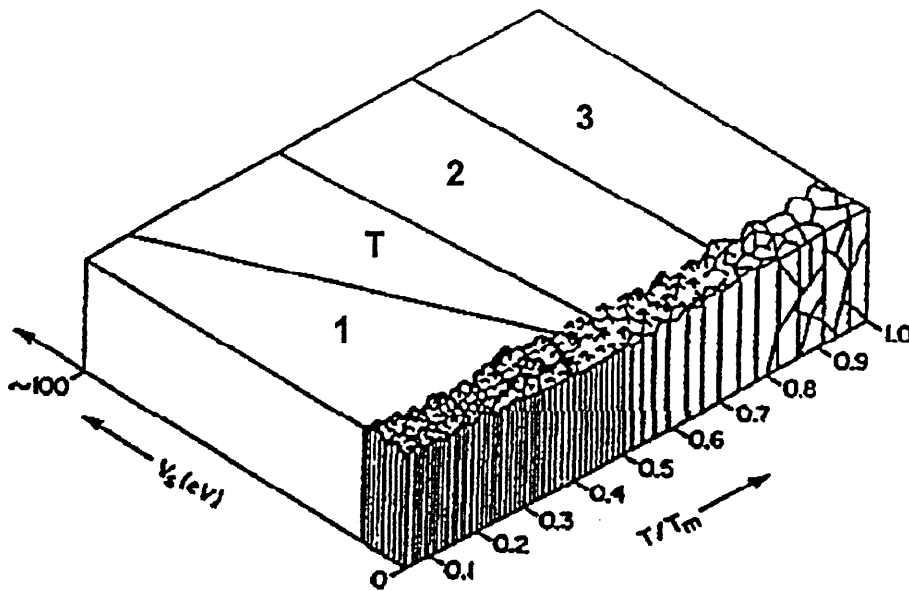


Figure 2.13 Messier's model for thin film microstructure (after [9])

The other effects of ion bombardment include [69]:

- modifying the substrate surface, such as cleaning (via ion etching), defect formation
- momentum transfer processes in the surface region, such as sputtering, desorption, recoil implantation, defect formation
- change in residual stress of film due to lattice defects and variation in film density
- addition of heat to the surface region
- formation of secondary electrons that can affect chemical reactions

However, by applying the correct deposition conditions, ion bombardment has been shown to give the following advantages [10]:

- increased nucleation rates and film density
- decreased in average grain size (finer grains)
- inhibition of the formation of columnar structures associated with high surface roughness
- changed defect density and orientation of coatings in a controllable manner

Effect of ion-to-neutral ratio (J_i/J_n)

The ion-to-neutral ratio determines the average energy carried by the arriving ions per condensing atom. A higher ion-to-neutral ratio (ion flux) at the substrate has been shown to result in grain refinement [68] and produce a dense film with more equiaxed grain structure [65]. The effects of ion-to-neutral ratio on the morphology of the growing film bombarded by Ar^+ has been shown using molecular dynamics computer simulation, see Figure 2.14 [70]. The model clearly demonstrated porous microstructure in the absence of ion bombardment (Figure 2.14(a)), which resulted from inhibition of surface diffusion. However, increased ion bombardment and/or J_i/J_n promote a dense structure as a result of enhanced adatom mobility and surface diffusion. This is shown in Figure 2.14(b) and (c), which presents the simulated microstructure formed at constant ion bombardment energy of 50 eV, and an increased J_i/J_n from 0.04 to 0.16, respectively. More recently, a novel structure zone model relating to the closed-field unbalanced magnetron sputtering (CFUBMS) system was developed [71]. This model takes into account the ion-to-neutral ratio (J_i/J_n) incident at the substrate, in addition to the homologous temperature (T/T_m) and the substrate bias voltage, to describe the coating microstructure, see Figure 2.15(a). According to the example given in the paper [71], for a constant bias voltage V_1 or V_2 (see Figure 2.15(b)), zone 2 or zone 3 structures defined by the previous models (Figure 2.12 and Figure 2.13) can be produced by varying the J_i/J_n ratio at any particular homologous substrate temperature.

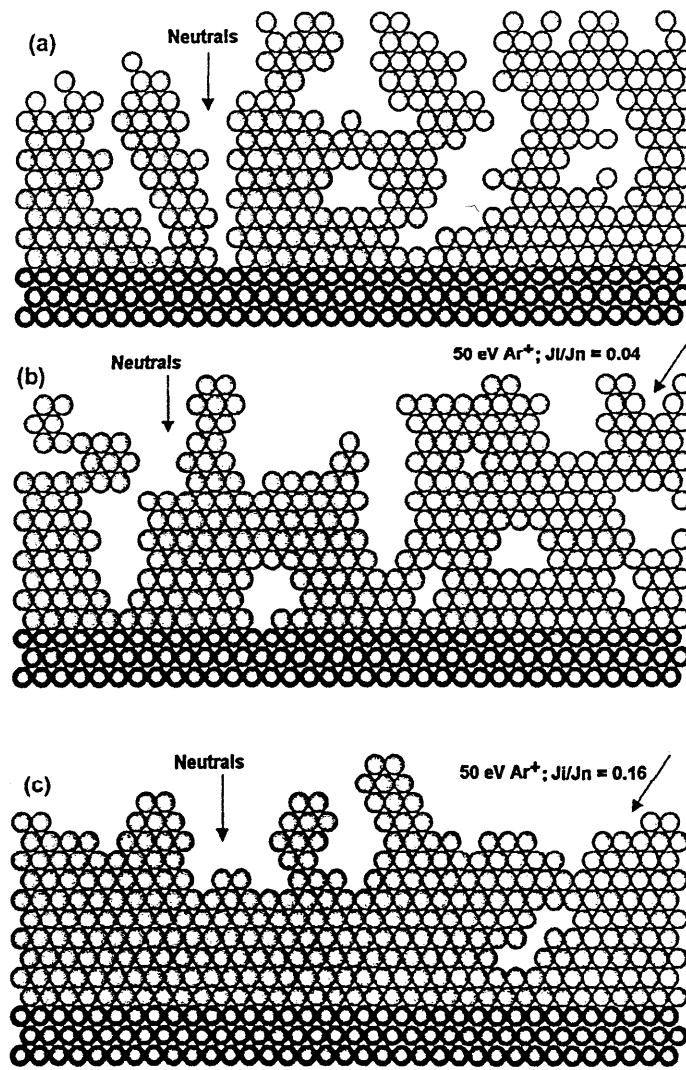


Figure 2.14 Molecular dynamic computer simulations of a Si film growth under (a) without ion bombardment, (b) at $-V_s = 50$ V, $J_i/J_n = 0.04$, (c) at $-V_s = 50$ V, $J_i/J_n = 0.16$ (after [70])

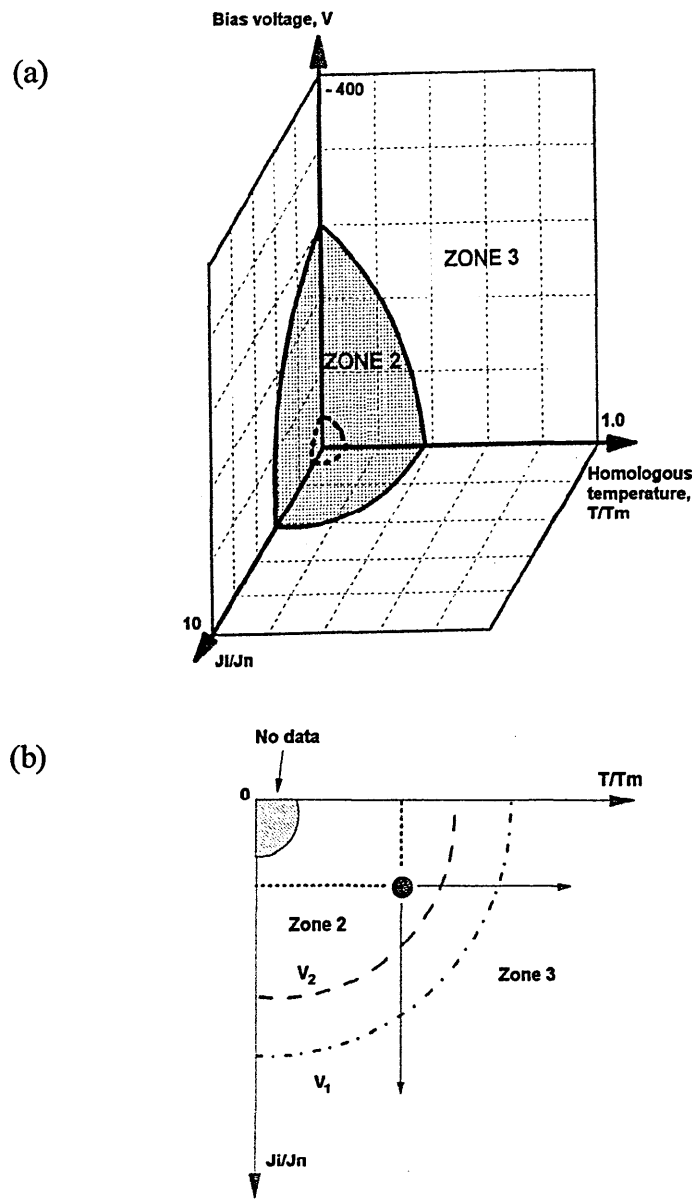


Figure 2.15 (a) Structure zone model relating to the closed-field unbalanced magnetron sputtering system, (b) slices through structure zone model at constant bias voltages V_1 and V_2 ($V_2 > V_1$) (after [71])

2.3 Nanocomposite structure

Nanostructure coatings are a novel class of materials. Nanotechnologies of the future will demand the creation of large arrays of nanoscale structures and morphologies due to the novelty of their physical and chemical properties [66]. In order to obtain a nanostructural features, the dimensions of morphological elements such as the average diameter of grains on thickness of layers, should be within the nanoscale range, usually between 2 and 100 nm [72].

Nanocomposite structures are two- or multicomponent systems containing additive(s) of varying concentration in addition to the film material and are normally composed of segregated phases [73]. The phases of nanocomposite thin films are determined primarily by the type and concentration of material constituents, the methods of preparation and process parameters [74]. A nanocomposite coating comprises of at least two phases either two nanocrystalline materials or a nanocrystalline material in combination with an amorphous phase. In general, nanocomposite structures can be classified into two groups [72]:

- (i) Nanolayered or superlattice, and
- (ii) Nanocrystalline

A brief section on self-organised structure is also included in this chapter.

(i) Nanolayered or superlattice structure

Nanolayered composite or superlattice structure is defined as a repeating layered structure of two different materials with nanometre scale dimensions [75]. The total thickness of the two successive pairs of layer, known as the bilayer thickness or superlattice period (Λ) depends on the substrate rotation speed and the deposition rate. The bilayer thickness of a film is in the nanometre scale normally within 5-25 nm [76]. Since the late 1980s, rapid progress in the early fundamental research on superlattice structured hard coatings has been achieved to produce nanoscale compositionally modulated coatings with hardness values exceeding 50 GPa [77-79]. Figure 2.16 shows the schematic structure of monolithic (which refers to first e.g. TiN and second e.g. TiAlCrN generation coatings) and superlattice coatings produced by the ABSTM technique, where the ion implantation zone was generated during the ion etching process.

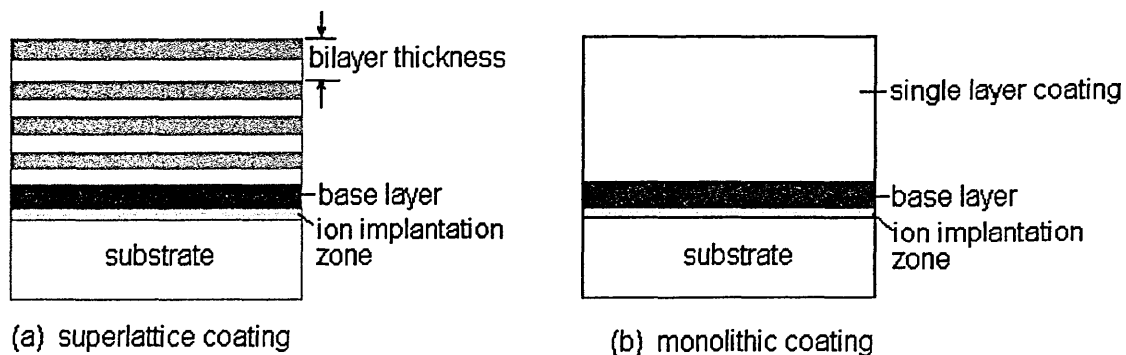


Figure 2.16 Coating structures produced by the ABSTM method

The interest in superlattice coatings, either isostructural (layered structure of two materials with the same crystal structure) or non-isostructural (layered structure of two materials with different crystal structure) originated from the possible generation of significant enhancements in mechanical and elastic/plastic properties (e.g. hardness, elastic modulus etc.) [75, 80]. These properties enhancements are believed to be due to the interfaces between the layers which provide energy barriers to the motion of dislocations (line defects that are mainly responsible for the plastic deformation of crystalline solids) and energy dissipation sites for crack propagation and deflection.

In the case of miscible and isostructural coatings (e.g. TiN/NbN), where the multilayer structure is made of two different materials with the same crystal structure either body-centered cubic (bcc), face-centered cubic (fcc), or hexagonal closed-packed (hcp), the property strengthening effects may due to the difference in elastic modulus between the two layers, E_A and E_B (where $E_A > E_B$). According to Koehler's model [81], the critical stress required to move a dislocation across an abrupt interfaces is proportional to $(E_A - E_B)/(E_A + E_B)$. If $(E_A - E_B)$ is large, greater critical stress is needed to move the dislocations, therefore the coating hardness is enhanced.

Figure 2.17 [77] shows the effect of superlattice period, Λ , on the hardness of superlattice coatings. It was noted that the hardness enhancement increases with increasing Λ until an optimal value is reached where further increases in Λ cause a decrease in hardness. At very small superlattice period, Λ (1-2 nm) the hardening effect of the interfaces is reduced owing to two main reasons [75]:

- Layers nearly interdiffuse and the elastic modulus of each layer becomes the same, thus no hardness enhancement can occur
- Very close interfaces can exert opposing forces on a dislocation at an interface, which lowers the stress needed to move the dislocations

However at larger superlattice period, Λ , the hardness decreases because the dislocations can move within the individual layers.

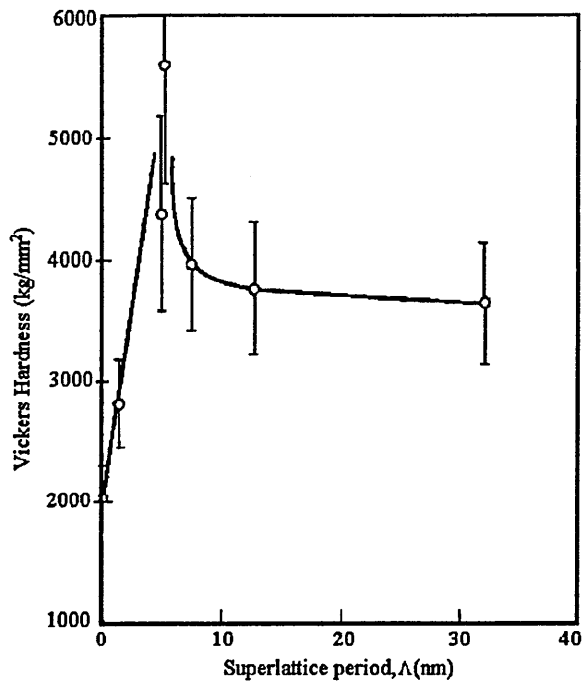


Figure 2.17 Hardness as a function of superlattice period

In comparison, immiscible, non-isostructural superlattices (e.g. combining bcc with fcc) such as Mo/NbN and W/NbN have substantial advantages over miscible and iso-structural superlattices especially in terms of strength/hardness. This is because of [75]:

- the formation of more abrupt interfaces, which lead to more stable structures at high temperature
- the formation of sharper and flat interfaces due to no intermixing of the interfaces (that is near zero width interfaces)
- the inhibition of motion of dislocations across interfaces because dislocation glide systems vary with varying material structures

Unfortunately, this type of superlattice is difficult to prepare due to poor crystal-lattice matching at the interfaces between non-isostructural materials.

(ii) Nanocrystalline structure

Nanocrystalline composite coatings are coatings that consist of nanocrystals or nanograins (e.g. TiN) embedded predominantly in the crystalline or amorphous matrix (e.g. DLC, a-Si₃N₄) of another material [72]. The dimensions of the nanocrystals or nanograins should be within a nanoscale range usually between 2 and 100 nm [72]. The

hardness of nanocomposites is related to a complex interplay of size of the nanocrystallites.

The concept for the design of hard ($H_V > 20$ GPa) or superhard ($H_V > 40$ GPa [66]) nanocomposites is based on the grain-boundary hardening described by the Hall-Petch relationship [82-83]:

$$\text{Hardness, } H = H_0 + kd^{-1/2}$$

where H_0 and k are material constants, and d is the average diameter of the crystallite. According to this equation, grain boundary hardening increases with decreasing crystallite size. This is due to blocking of grain boundary sliding by the formation of a strong interface between the two components in various nanocomposites [84]. One limitation of this relationship is that it is only prominent for crystallite size > 10 nm, because work hardening does not occur in small nanocrystals of ≤ 10 nm [85]. However, for nc-TiN/a-Si₃N₄ nanocomposites (nc stands for nanocrystalline), a maximum hardness was found between 40 and 60 GPa for mean crystallite sizes between 5 and 10 nm [86-87]. Figure 2.18 shows the relationship between the hardness and the grain size [88].

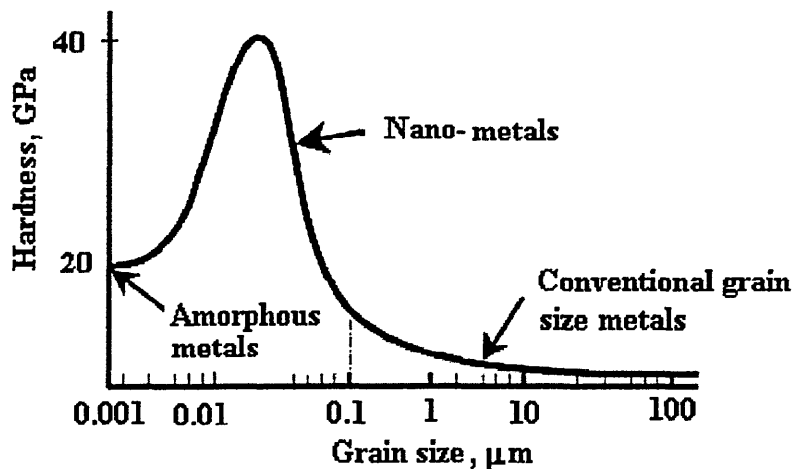


Figure 2.18 Hardness as a function of grain size

Self-organised structure

As the name implies, self-organised or self-assembled structural evolution is controlled by kinetically self-driven mutual segregation and surface diffusion of the condensing species to form pure or compound phases [89]. This structure evolves usually in multicomponent, multiphase thin films or films with artificial structures, for

example nanoscale multilayers or nanophase composites. According to Barna and co-workers [73], the structure evolution in a multicomponent composite follows the same phenomena as that of polycrystalline films. This includes nucleation, crystal growth, grain growth by grain-boundary migration, process-induced kinetic segregation of the species of insoluble minority components, and chemical interaction occurring on the growth surface, or within the uppermost layer of the developing film. Surface chemical reactions occur when the impinging species integrate themselves into the growing compound phase. The species that are not consumed and not dissolved in these reactions are segregated by the atomic processes, which results in an increased surface concentration of these species during growth and in the formation of new phase(s) either elemental or compound [73-74].

The theoretical study of the self-organised structure requires the investigation of two aspects [90]: (i) the mechanisms that drive the dynamics of the self-organised structure and (ii) the geometry i.e. the shape of the self-organised structure.

2.4 Carbon-based Coatings

The demand for high quality tribological coatings has led in the recent years to intensive research in further development of the carbon-based coating family. Carbon-based coatings, such as diamond-like carbon (DLC), metal-DLC, and metal-graphite are attractive in a wide range of applications due to the following reasons [91-93]:

- naturally low coefficient of friction combined with excellent chemical inertness
- excellent properties such as high hardness and good wear resistance [18-19, 30, 33, 94-96]
- the possibility of changing their properties by tailoring the microstructure, for example from graphite-like to diamond-like with an amorphous or crystalline structure
- the possibility of varying the sp^2/sp^3 ratio based on the deposition techniques and conditions used

The applications of carbon-based coatings include cutting tools, automotive components, precision parts, bearings [18, 30, 97-98], and recently exploiting the biomedical applications [20, 99-100]. In order to understand the properties of carbon-

based coatings, it is important to know the background of carbon, its structures and properties. These are discussed in the following sub-section.

2.4.1 Background of carbon

The word carbon is derived from the Latin “carbo” which means charcoal. The term “carbon” means only the element, because carbon has several material forms which are known as polymorphs or allotropes. There are four types of carbon allotropes, two allotropes of carbon are found on earth as minerals: natural graphite and diamond; the other two allotropes are fullerenes and nanotubes [101]. Recently, researchers have created a new form of carbon known as magnetic carbon or nanofoam, which is a spongy solid that is extremely light in weight, is attracted to magnets and could be used in medical applications, such as in treating cancer and enhancing brain scans [102]. Carbon (diamond) is one of the hardest materials known in its cubic structure but it is a relatively soft material, known as graphite, when it is in the hexagonal form. It is this hexagonal structure that gives the excellent lubricating characteristics of graphite. The following sections briefly discuss the bonding configurations of carbon and the general properties of its allotropes.

2.4.1.1 Bonding configurations of carbon

A carbon atom can adapt three different bonding configurations, which are sp^3 , sp^2 , and sp^1 , as shown in Figure 2.19 [103].

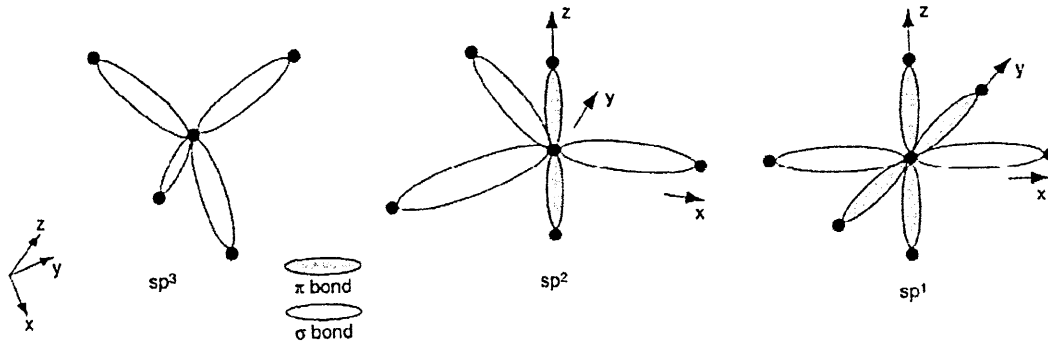


Figure 2.19 Schematic of sp^3 , sp^2 , and sp^1 bonding type of carbon atoms

- sp^3 (diamond): Each of the carbon's four valence electrons is assigned to a tetrahedrally (109.5° bond angles) directed sp^3 hybrid orbital (one s- and three p-orbitals), which then forms a strong covalent bond (also known as sigma, σ bond)

with an adjacent atom, shown schematically in Figure 2.20. This structure exists in diamond, and the strong bonding results in exceptionally high hardness and high thermal conductivity.

- sp^2 (graphite): Under ambient conditions, the graphite structure with strong in-plane sp^2 bonding is the most stable phase. Three of the four electrons are assigned to trigonally (120° bond angles) directed sp^2 hybrid orbital, which forms strong covalent bond (or σ bond) within the plane. The weak van der Waals bond (also known as π , π bond) between planes accounts for the layered structure of graphite, which is responsible for its high electrical conductivity, softness, and lubricity. See Figure 2.21 for the schematic representation of these bonds.
- sp^1 (hydrocarbons and certain polymers): Only two electrons form strong covalent bonds. This structure has linear geometry and exists in hydrocarbons and certain polymers.

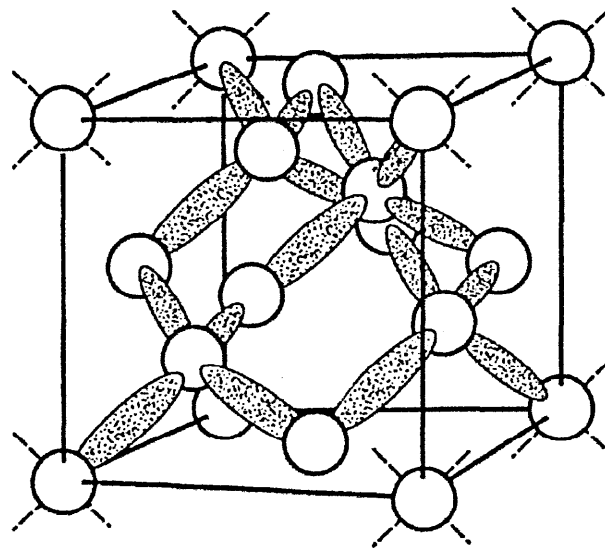


Figure 2.20 Three-dimensional representation of sp^3 covalent bonding (shaded regions) in diamond structure [101]

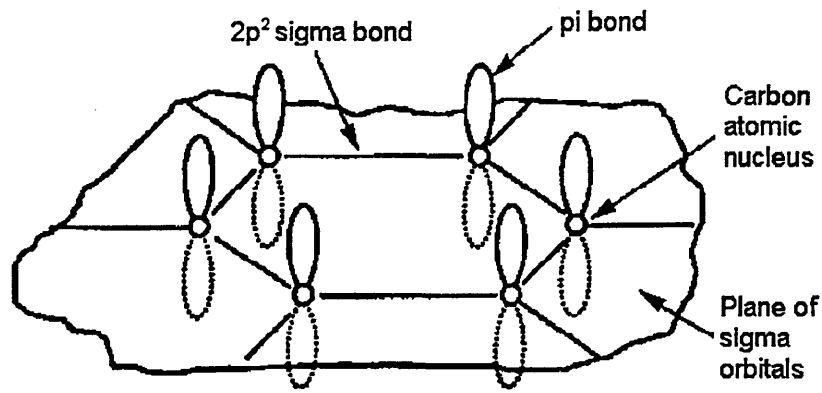


Figure 2.21 Schematic of the sp^2 structure of graphite showing the sigma bond and pi bond (above and below the sigma orbital plane) [101]

2.4.1.2 Properties and structure of carbon allotropes

Carbon has small atomic radius of 0.071 nm. Figure 2.22 illustrates the conditions for the production of diamond and graphite [101]. Graphite is stable at ordinary pressures and at all temperatures, whereas diamond is theoretically only stable at high pressures. The selected physical properties of various forms of carbon are shown in Table 2.2. Diamond has a hardness reaching 100 GPa. The properties and structure of diamond and graphite are now further explained.

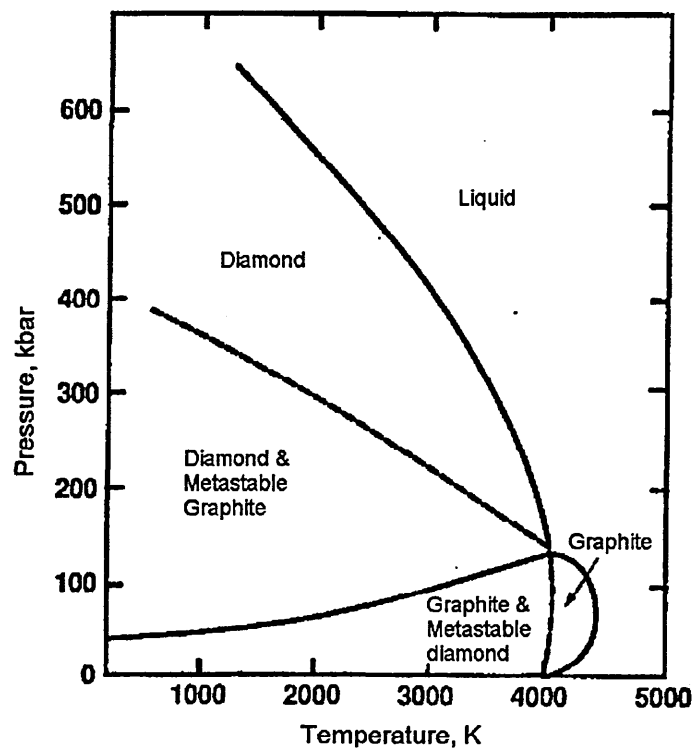


Figure 2.22 Carbon phase diagram (after [101])

Carbon form	Density, kg/m ³	Hardness (HV), GPa	Modulus of elasticity, GPa	Temperature limit in air, °C
*Diamond (100% sp ³)	3515	80-104	900-1050	1000
**Graphite (100% sp ²)	2267	very soft	9-15	425
Amorphous/ black carbon	1600-2000	soft	11-15	260

* Poisson's ratio = 0.1-0.16

* Coefficient of friction = 0.05-0.1 (in air); ~ 1 (in vacuum)

** Coefficient of friction ~ 0.1 (in air) [104]

Table 2.2 Properties of various forms of carbon [105]

Diamond

There are four main sources of diamond [101]:

1. Natural diamond
2. High-pressure synthetic diamond
3. Chemical vapour deposited (CVD) diamond
4. Diamond-like carbon (DLC)

For a material to be recognised as diamond, it must possess the following characteristics [101]:

- A crystalline morphology visible by electron microscopy
- A single-phase crystalline structure detectable by X-ray or electron diffraction
- A clear diamond Raman spectrum with a sharp single peak at 1332 cm⁻¹

The properties of diamond can be summarised as follows:

- Lowest friction coefficients (< 0.1) of any solid in air. This low friction is dependent on the presence of oxygen and other adsorbed impurities. In high vacuum, the friction coefficients increase considerably (~1) due to the absence of the chemisorbed species [106].
- Chemically inert except to oxidation. The onset of oxidation starts at temperature as low as 250°C in pure oxygen, and ~500°C in air.
- Optically transparent
- Highly electrically insulating
- biocompatible

Graphite

Graphite is a crystalline carbon, which is soft and shiny. Graphite is well known for its excellent solid lubrication property in normal air atmosphere or even at elevated temperatures [2, 107], but not at high altitudes or in vacuum [2]. The key value of graphite as a self-lubricating solid is due to its layered-lattice structure and its ability to form strong chemical bonds with gases such as water vapour which weakens the interlayer bonding forces, resulting in easy shear and low friction [3, 107].

Graphite has two allotropic forms with different stacking arrangements, they are hexagonal and rhombohedral. Hexagonal graphite is thermodynamically stable, however the rhombohedral graphite is thermodynamically unstable. The crystal structure of hexagonal graphite is shown schematically in Figure 2.23, which has strong covalent bond within the hexagonal ring layers, but weak bonding (Van der Waals bond) between adjacent layers. Graphite has a c/a_0 ratio of more than 2 (c is the distance between adjacent planes which is 3.34\AA , and a_0 is the spacing between the atoms within the basal planes which is 1.42\AA [107]). The c/a_0 ratio determines the shear ability of a compound. For example, compounds with a high c/a_0 ratio exhibit very anisotropic shear properties with preferred shear parallel to the basal planes or perpendicular to the c -axis of the crystal structure [2]. The Raman spectra of various forms of carbon can be distinguished using Raman spectroscopy (this technique is described in Chapter 3). Figure 2.24 shows the characteristic Raman spectra which are normally found for various forms of carbon materials. In general, carbon contains a graphitic G-band that appears at $\sim 1582\text{ cm}^{-1}$ and a disordered induced D-band that exists at $\sim 1350\text{ cm}^{-1}$.

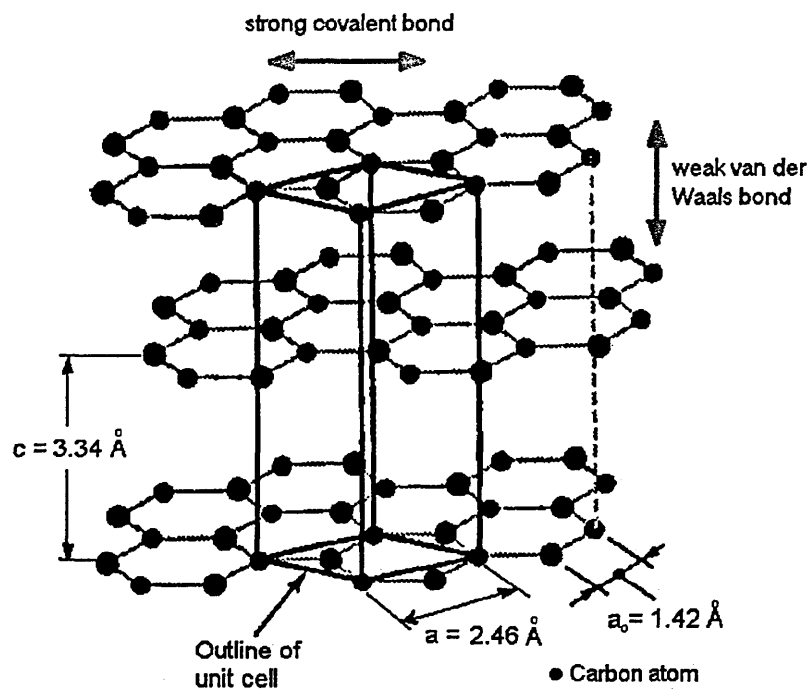


Figure 2.23 Crystal structure of graphite (where a is the lattice parameter)

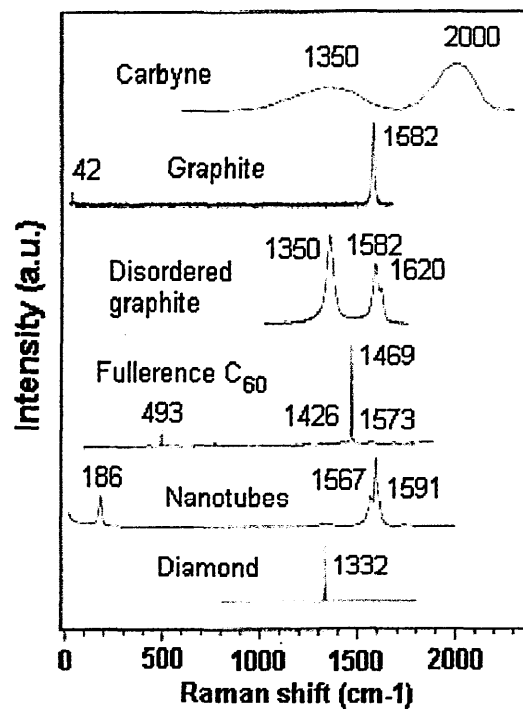


Figure 2.24 Characteristic Raman spectra for the various carbon-based materials: carbyne (sp bonded carbon), graphite, disordered graphite (sp^2 bonded carbon), fullerene C_{60} , carbon nanotubes, and diamond (sp^3 bonded carbon) [108].

The properties of graphite can be summarised as follow:

- Lattice parameter, $a = 2.46 \text{ \AA}$

- d-spacing, $d = 6.68 \text{ \AA}$
- Excellent corrosion resistance
- Electrical conductor ($1 \text{ to } 1000 \Omega^{-1}\text{cm}^{-1}$)
- Excellent thermal conductor
- High radiation capacity and good thermal conductivity
- Excellent chemical resistance, except to the elements of Group VI of the Periodic Table, particularly oxygen and oxygen compounds. Graphite begins to oxidise in air at approximately $350\text{-}400^\circ\text{C}$. The oxides formed by the oxidation of graphite are gaseous (CO and CO_2), which offer no protection to the surface [99].

2.4.2 Types of carbon-based coatings

The carbon based coatings can be classified into diamond-like carbon (DLC), metal-DLC (Me-DLC or Me-C:H) and metal-Graphite (Me-Graphite), as shown in Figure 2.25. DLC and Me-DLC possess diamond-like properties, which combine the properties of solid lubricating graphite structure and hard diamond crystal structure; whereas, Me-Graphite exhibits graphitic-like structure, and exhibits a mixture of properties from graphite, DLC and Me-DLC. Table 2.3 gives a general comparison of these coatings. It should be noted that the values shown in Table 2.3 may vary depending on the deposition and testing conditions. Figure 2.26 [109-110] shows the ternary phase diagram of carbon-based coatings. This diagram shows that DLC, such as ta-C (tetrahedral-carbon), ta-C:H (tetrahedral-hydrogenated carbon), and a-C:H (amorphous-hydrogenated carbon) have a significant fraction of sp^3 bonds, with ta-C and ta-C:H containing about 80-90% of sp^3 bonds.

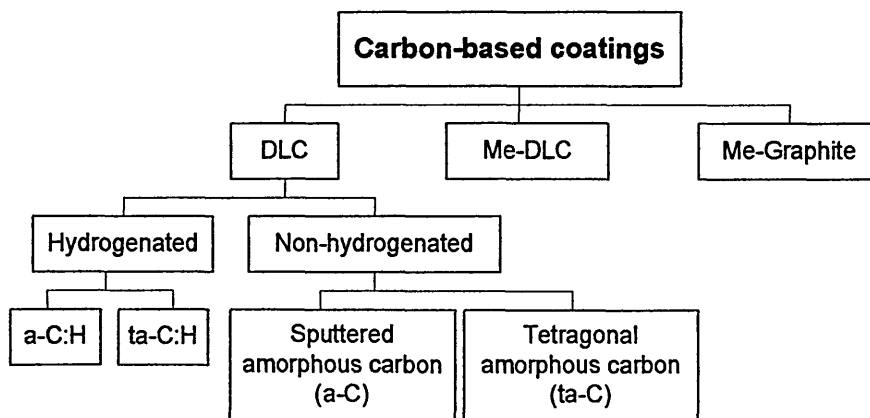


Figure 2.25 Types of carbon-based coatings

Properties	DLC	Me-DLC	Me-Graphite [18, 111-112]
Bonding (significant fraction of)	sp^3	n/a	sp^2
Friction coefficient in ambient	~0.1 [113]	0.1-0.2	0.1-0.2
Wear coefficient, $m^3N^{-1}m^{-1}$ in ambient	$\sim 10^{-17}$ [113-114]	$10^{-15} - 10^{-16}$ [17,97,115-116]	$\sim 10^{-17}$
Compressive stress, GPa	2-6 [5]	< 1 [117]	0.6-2.8 [112]
Hardness, GPa	5-70 [118] (brittle)	15-20 (tough)	8-25 (tough)
Young's modulus, GPa	300-750	100-300	180-320
Oxidation temperature, °C	450-550 [6]	n/a	< 650 [119]

Table 2.3 Comparison between DLC, Me-DLC and Me-Graphite (e.g. C/Cr)

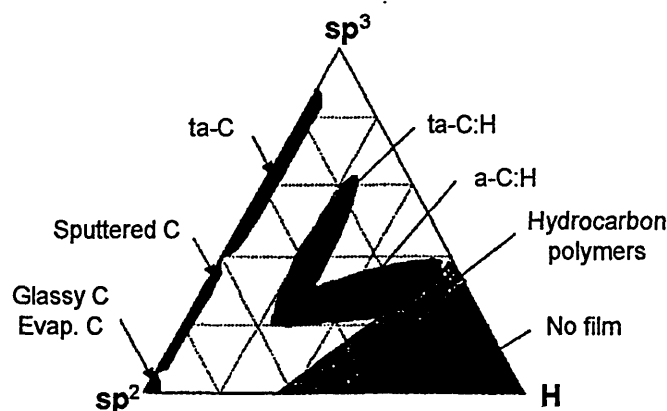


Figure 2.26 Ternary phase diagram of carbon-based coatings

Studies of carbon-based coatings have developed a wide variety of deposition techniques to grow this type of coating on various substrate materials, depending on the specific applications of the coatings. The following sections briefly discuss the methods for the production of pure DLC, metal-DLC and metal-graphite coatings, their properties and applications.

2.4.2.1 Diamond-Like Carbon (DLC)

The term DLC, which refers to diamond-like carbon, was first introduced by Aisenberg and Chabot in 1973 [120]. DLC is used to describe a range of carbon-based coatings including amorphous carbon materials which contain up to approximately 50% hydrogen (known as hydrogenated coatings) and materials which contain < 1% hydrogen (known as non-hydrogenated coatings, e.g. a-C) [21]. DLC is a very promising coating material because of its low friction, high hardness, good wear resistance, corrosion resistance, chemical inertness and biocompatibility.

Properties, limitations and applications

DLC can be considered as metastable carbon produced as a thin coating with a broad range of structures, primarily amorphous with a variable sp^2/sp^3 bonding ratio. DLC contains a significant fraction of sp^3 bonds and variable hydrogen concentration [101]. The hydrogen content and the relative amount of the sp^2 to sp^3 carbon hybridisation determine the structure and the properties of the DLC films [109]. Higher sp^3 to sp^2 ratio leads to diamond-like properties, higher hardness but also to higher residual stress, which results in cracking or delamination under high load applications [121]. Hydrogenated DLC shows a lower friction coefficient than hydrogen-free DLC film because the hydrogenated DLC surface is normally terminated with a layer of chemisorbed hydrogen and oxygen. This chemisorbed layer renders the surface relatively unreactive and prevents strong carbon-carbon bonding between the sliding interfaces. This chemisorbed hydrogen and oxygen passivate the dangling bonds on the films and permit only weak interactions between the film and the sliding partner [122]. This is why hydrogenated DLC films possess a lower friction coefficient and have a longer wear life than the film containing no hydrogen [123].

DLC-coatings are well known for their tribological characteristics, such as high hardness (5-70 GPa), good wear resistance ($\sim 10^{-17} \text{ m}^3\text{N}^{-1}\text{m}^{-1}$) and low friction coefficient (<0.1). The high wear resistance, low friction coefficients, chemical inertness and high-corrosion resistance of DLC have promoted the films as a good candidate for use as biocompatible and blood compatible coatings for biomedical devices and tools. However these properties are strongly affected by the films nature, which is controlled by the deposition process and tribotesting conditions [123]. The maximum operating temperature of a DLC coating is approximately 250°C [124]. The major drawbacks of DLC are their high internal stresses and poor adhesion that limit the

thickness of this coating to less than 1 μm [5]. It is difficult to grow thick adherent DLC films because they tend to delaminate and separate from the substrate due to the high internal stress. The high compressive residual stress in hard DLC films originates from the formation of sp^3 interatomic bonds.

The development of diamond-like coatings offer the potential for exploiting their unique properties in applications such as:

- wear resistant coatings, for example bearings, abrasives, and tools
- anti-reflection coatings, for example free-standing windows
- lenses, for example, visible and infrared (IR) transmission
- thin coatings as a heat sink for high temperature, high-power semiconductor devices
- nanometer thick films for use in wear- and corrosion-resistant coatings in thin-film magnetic rigid disks
- medical devices, such as hip and knee joints, coronary stents, heart valves, intraocular lenses implanted in the human body [125], orthopaedic implants [126]

Deposition methods

The basic process to produce thin films with DLC properties requires deposition using high energy carbon and argon ions impinging on the substrate [120]. Most DLC deposition techniques are non-equilibrium because the high energy deposited material and ions cause sudden increase and decrease in local energy on the growing surface. So, the properties obtained under these conditions will not be achieved by a normal equilibrium process [127]. The conversion of graphite to diamond requires a compression from the lower energy and density of graphite to the higher energy and density of diamond as the coordination shifts from sp^2 to sp^3 . This may happen under the impact of an energetic particle, such as argon or carbon itself, generated by an ion beam, laser or other means. The optimum C^+ kinetic energy range to grow DLC coatings using ion-beam deposition was found to be 30-175 eV [128]. The diamond-like structure cannot be attained at lower energy, however higher energy may drive the atom back to the sp^2 configuration unless the particle is rapidly quenched [101].

DLC coatings can be prepared by a wide variety of PVD and CVD techniques. However, PVD grown DLC films offer a smoother surface and significantly lower deposition temperature (generally between 100 and 450°C) than the CVD technique (generally at least 600°C to give the required combination of properties [4]). Therefore, CVD is not an ideal deposition technique for many temperature-sensitive tribological

materials. The PVD techniques use for preparation of DLC films normally involves the deposition of carbon during concurrent ion bombardment. The absence of ion bombardment during deposition results in the formation of soft carbon layers with no diamond-like properties [129]. A review covering diamond-like amorphous carbon including deposition methods has been published recently [6]. Below are some techniques used to grow DLC films:

- Ion beam deposition [120, 127]
- Magnetron sputtering [23, 27, 114, 129-130]
- Pulsed laser deposition (PLD) [131]
- Cathodic arc deposition [130]
- Plasma-enhanced CVD (PECVD) [132]

2.4.2.2 Metal-DLC (or Me-C:H)

The abbreviation Me-DLC or Me-C:H, has been used by researchers to name metal-containing DLC films. Me-DLC coatings contain mixtures of graphitic and diamond bonds [98].

Properties and applications

The tribological behaviour of DLC coatings can be largely influenced and stabilised by doping the films with metals [7, 133], or by the synthesis of super-hydrogenated DLC films reported recently by Erdemir and co-workers [132], who found that their films exhibit friction coefficients as low as 0.003 in dry N₂. The high compressive stress of DLC films can be overcome by inclusion of an intermediate metal layer interposed between the substrate and the DLC film [124], and/or incorporation of a small amount of transition metals, for example Cr [7, 18, 94], Ta, W [7, 23], Nb [23], or Ti [23, 134-135] into the C-based coatings. The reduction in compressive stress occurs because a small fraction of the sp³ bonds convert to sp² bonds. It was estimated that only about 2 % of sp³ bonds need to convert to sp² to reduce the stress [136]. As compared to the sp³ bond, the shorter sp² bond would reduce the strain in the film plane [136].

Me-DLC has a friction coefficient similar to that of DLC coatings, but its abrasive wear resistance is markedly lower than that of DLC by about a factor of 2 or more [23]. Generally, Me-DLC films which have a metal to carbon atomic ratios of up to approximately 0.3 have markedly lower compressive stress (< 1 GPa) than DLC

films. The reduction in the compressive stress leads to better adhesion and stabilisation of structure, and allows the growth of thicker and more adherent films [7, 17]. Me-DLC is mainly used for industrial applications such as components in fuel injection pumps, gearboxes, bearings, wrist pins and spur gears for motorbikes, and hydraulic compressor rotors [97]. In general, Me-DLC coatings are applied [98]:

- to prevent the galling which stainless steels often suffer from when in contact with other metallic materials
- in transmission components to counter a range of surface-related failures
- to conventional bearing steels, for example rolling element bearings. Me-DLC is an advantage when good lubrication is difficult to achieve, or there are variations in loading conditions, or, in high temperature operations
- to precision forming tools in the glass industry [137].

Deposition methods

The techniques used to grow Me-DLC coatings are very similar to those for the DLC coatings, except for the incorporation of other metals during deposition. Metal-DLC coatings are generally produced by decomposition of hydrocarbon gases such as methane (CH_4) or acetylene (C_2H_2). For example, tungsten-carbon (W-C) coatings have been deposited by reactive magnetron sputtering from a W target in $\text{Ar} + \text{CH}_4$ gas discharges [138], and W-C:H films, have been produced by the unbalanced magnetron sputtering technique using WC targets in an acetylene atmosphere [17]. Recently, the ABS method, has been used to grow Me-C:H films using graphite and metal (Ti, Nb, W) targets in an $\text{Ar} + \text{C}_2\text{H}_2$ atmosphere [23, 115]. A magnetron sputtering pulsed laser deposition (PLD) technique has also been used to deposit metal-containing, hydrogen-free amorphous carbon composite coatings, such as titanium carbide and tungsten carbide containing DLC films [139]. During pulsed laser deposition of DLC films, foreign atoms such as copper, titanium, and silicon were incorporated into the DLC films to improve the film adhesion [140].

2.4.2.3 Metal-Graphite

Metal-graphite or Me-Graphite coatings are graphite-like coatings which contain a significant fraction of sp^2 bonds. Until recently, research carried out on Me-Graphite coatings was very limited. The most recent publications have focused on

carbon/chromium (C/Cr) coatings [18, 94, 96, 111-112]. This section presents a brief discussion based on the available information on this type of carbon-based coating.

Properties and applications

The properties of the recently-developed sputtered graphite-like amorphous coatings combine the advantages of DLC and Me-DLC coatings. These include high hardness, good toughness, low friction coefficient (0.1-0.2), excellent wear resistance ($\sim 10^{-17} \text{ m}^3 \text{N}^{-1} \text{m}^{-1}$), high load bearing capacity, and low compressive stress (see Table 2.3). The combination of these properties promotes graphite-like carbon coatings as an excellent candidate for tribological applications [18, 30, 94, 111-112]. Me-Graphite coatings are graphitic in nature and contain mostly sp^2 bonds.

This new hard solid lubricant coating is expected to be used in a wide range of new applications that exploit its unique combined properties. These include in dry machining, metal cutting, sizing and forming tools, machine elements, for example, rolling or sliding bearings, seals, pistons, cylinder systems and valves, and in automotive engineering, where the need for coolant or lubricant is prohibited. This lubricious and non-stick coating can also be deposited as a top coat on other state-of-the-art coatings, such as TiAlCrYN, and has been shown to preserve better the cutting edge geometry, reduce the material transfer effects and increase the end mill life time [96]. Most recently, C/Cr coatings were tested for use in artificial hip joints, medical tools such as bone cutting saws and dental instruments [20].

Deposition methods

Although C/Cr coatings have been produced by direct magnetron sputtering of a chromium carbide (Cr_3C_2) target since 1994 [28], up to now, only two techniques of sputtering such as closed-field unbalanced magnetron sputtering (CFUBMS) [18-19] and Arc Bond Sputtering (ABSTM) [33, 95-96, 111-112] using chromium and graphite targets, have been reported as the most promising techniques for C/Cr coating deposition. The main difference between these two techniques is that the ion-cleaning step in CFUBMS sputtering is carried out by Ar^+ ion etching whilst the ABSTM technology utilises Cr^+ ions generated by a steered cathodic arc discharge, which allows intensive surface sputter cleaning and implantation of Cr ions to a depth, typically between 5-20 nm [141]. The atomically pre-cleaned and chemically modified surface provides appropriate conditions for local epitaxial growth resulting in excellent

adhesion of the successive coating deposited by magnetron sputtering [78]. Furthermore the use of Cr as an etchant metal minimises the number of macroparticles generated from the arc spot during evaporation and produces fewer growth defects and smoother surfaces [53]. The incorporation of a metal containing layer between the substrate and the C/Cr coating has been found to have adhesion promoting, coating strengthening and higher load bearing functions. Although formation of chromium carbides is possible under certain deposition conditions during C/Cr coating deposition, the complete immiscibility of C and Cr (under equilibrium conditions) and the relatively low deposition temperatures used, potentially allow for deposition of nano-scale multilayer structured or nanocomposite coatings with sharp interfaces [96]. Therefore it is believed that a precise tailoring of the structure of the C/Cr coatings may lead to further optimisation of their tribological behaviour.

The following two paragraphs briefly explain the most promising techniques used to grow C/Cr coatings:

- **Closed-field unbalanced magnetron sputtering (CFUBMS)**

State-of-the-art C/Cr (Graphit-iC) multilayer coatings have been produced using a Teer UDP450 unbalanced d.c. magnetron sputtering system (also known as Closed Field Unbalanced Magnetron Sputtering or CFUBMS) [18, 30, 94]. The system comprises four magnetrons furnished with one chromium and three graphite targets and a three-axis substrate rotation mechanism to produce uniform coatings on flat samples. The deposition procedure was carried out in an argon atmosphere. The power applied to the target was DC and the substrate was biased with pulsed DC. Prior to coating deposition, the substrates were cleaned in an argon atmosphere using a DC voltage of 300 V on the chromium target, and a pulsed DC voltage of 450 V with a frequency of 100 kHz on the substrate [30]. This was then followed by the deposition of a 0.2 μm thick chromium adhesive layer. Finally, the deposition of a graded C/Cr ramp layer was made by decreasing the sputtering power on Cr target and increasing sputtering power on C target, using DC unbalanced magnetron sputtering [18]

- **Arc Bond Sputtering (ABS)**

The Hauzer HTC 1000-4 ABS coater has been successfully used for depositing C/Cr multilayer coatings [33, 95-96, 111-112]. The system comprised four rectangular cathodes furnished with one chromium and three graphite targets (see section 2.1.4

for a detailed descriptions of the ABSTM technique). The samples were mounted on a three-fold planetary rotating turntable to improve coating thickness uniformity. The sputtering was carried out in an Ar atmosphere, and N₂ was introduced only for the CrN base layer deposition. The substrates in the chamber were first heated to the required deposition temperature (250-450°C) and pressure. During the metal ion-etching step, the substrates were negatively biased to 1200 V and were sputter cleaned by Cr⁺ ions generated by the steered arc discharge sustained on the Cr target. This step also resulted in a shallow ion implantation into the substrate which improved the adhesion between the substrate and the successive coating deposited by magnetron sputtering. This was then followed by deposition of 0.2 µm thick CrN base layer using unbalanced magnetron sputtering. The base layer functioned as a supportive layer to further enhance the adhesion strength and to reduce the residual stresses in the coating. Finally, a 1.6µm thick C/Cr multilayer coating (with approximately 2 nm bilayer repeat period) was deposited using unbalanced magnetron sputtering. It was found that the coatings deposited at 250°C exhibited the lowest coefficient of friction [96].

CHAPTER 3

Experimental Methodology

This chapter consists of three sections: (3.1) presents the materials used, the sample preparation procedures prior to coating deposition, the PVD process sequence and parameters used for C/Cr coating deposition; (3.2) explains the modification to the conventional Scanning Reference Electrode Technique (SRET) for use in the tribocorrosion test, which includes the design, experimental set-up, and system calibration; and (3.3) presents the characterisation techniques used to analyse the coatings.

3.1 Materials, specimen preparation and coating deposition

3.1.1 Materials and specimen preparation prior to coating deposition

M2 high-speed steel (HSS) (composition 0.68% C, 4% Cr, 14% W, 0.25% V) and 316 stainless steel (SS) (composition 0.08% C, 16-18% Cr, 10-14% Ni, 2.0% Mn, 1% Si) were used as the substrate materials for the purposes of different coating evaluation. Table 3.1 outlines the dimensions and the materials used for various tests and analytical techniques. Prior to coating deposition, all test coupons and the cylindrical samples were ground with 240, 320, 400, 800 and 1200 grit paper and then polished to mirror finish with 6 μm and 1 μm diamond paste. All specimens were cleaned in an industrial size automated ultrasonic cleaning line, following the sequence shown in Table 3.2, to remove surface impurities and contaminants. This was then followed by hot air drying in the vacuum dryer. After drying, the specimens were loaded into the PVD chamber immediately.

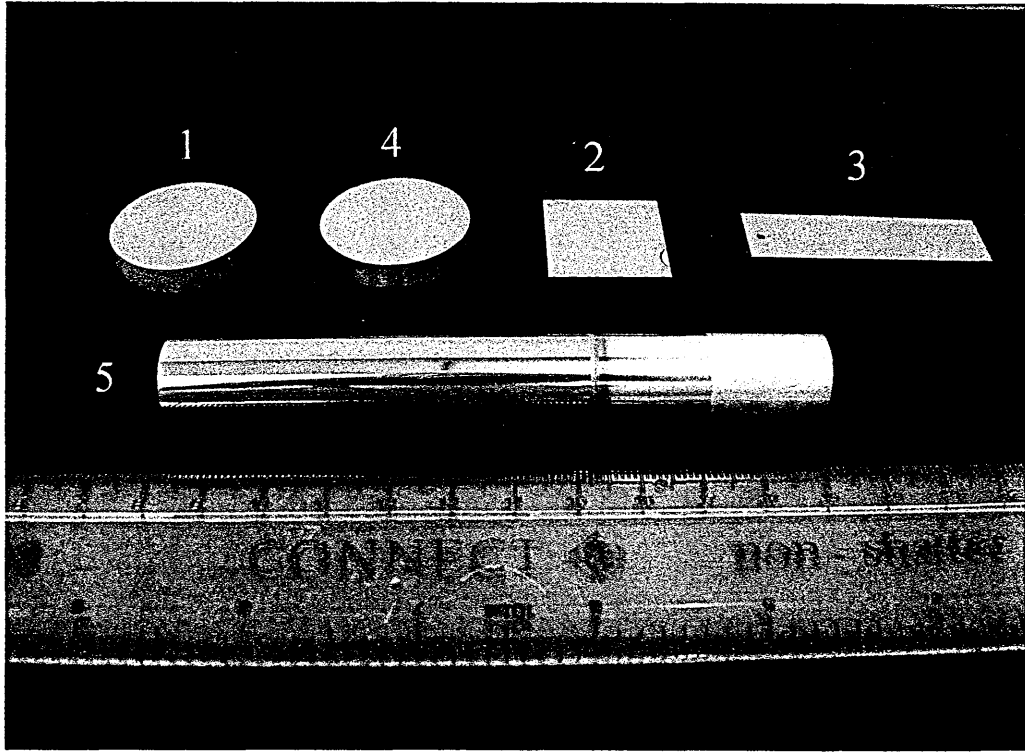
	
Tests	Dimensions
pin-on-disc, scratch, Rockwell C indentation (adhesion), nanohardness, Raman, SEM	Ø30mm x 6mm HSS coupon (Sample 1)
Stress measurement	0.1 × 10 × (50 ± 0.5) mm ³ rectangular steel substrate (E = 260 GPa, Ra = 0.078µm, composition: 0.17-0.23 %C, 99-99.5 %Fe) (not shown)
SNMS, RBS, XPS, TEM, EELS	25 × 25 × 0.8 mm ³ SS square plate (Sample 2)
Thermogravimetric (TG)	15 × 50 × 0.8 mm ³ SS (1 × Ø1.5mm hole) (Sample 3)
XRD	Ø30mm × 6mm SS coupon (Sample 4)
Corrosion:	
a) Potentiodynamic polarisation	Ø30mm × 6mm SS coupon (Sample 4)
b) Tribocorrosion	Ø15mm × 110mm solid cylinder (Sample 5)
Milling	8mm ball nose cemented carbide end mill (not shown)

Table 3.1 Dimensions and materials used for various tests and analytical methods

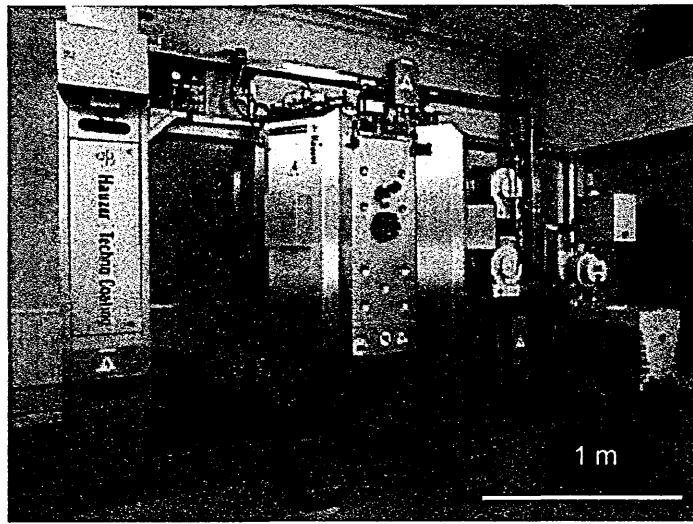
Step	Solutions	Temperature, °C	Time, s
1	De-Ionised water + 6 L DECOSPRAY N	75 °C	180
2	De-Ionised water + 3 kg GALVEX SU 93	75 °C	180
3	Tap water + 0.65 L GALVEX 17.30	50 °C	10
4	De-Ionised + 4.2 L GALVEX 17.30	65 °C	120
5	Tap water + 1.30 L GALVEX 17.30	35 °C	10
6	De-Ionised water	50 °C	10

Table 3.2 Substrate cleaning procedure prior to coating deposition (Note: DECOSPRAY N and GALVEX are commercial cleaning solutions)

3.1.2 Principle process sequence of ABSTM technology

The deposition process was carried out in an industrial sized HTC 1000-4 ABSTM PVD coater [61], as shown in Figure 3.1(a), using combined steered cathodic arc/unbalanced magnetron sputtering. This coater has a volume of 1 m³, is octagonal in cross-section and comprises four cathodes (targets), schematically shown in Figure 3.1(b). The samples are mounted on a turntable located in the centre of the chamber, which is rotated at a primary rotation speed of 7.5 rpm (55 %). The samples can be rotated in one-, two- or three-fold rotation (τ_1 , τ_2 , τ_3). The four cathodes have the flexibility to be operated individually either in cathodic steered arc mode (normally operated at 30 V, 100 A) or in unbalanced magnetron sputtering (UBM) mode (normally operated at 500 V, 20 A) by switching the power supply. The ABSTM coater is equipped with an excellent pumping system (further explained in Table 3.3), which provides optimum suitability for the reactive coating processes. The basic deposition steps and the objectives of each step are outlined in Table 3.3. The recipe of the process is programmed in the computer controlled ABSTM machine that allows a step-by-step process control.

(a)



(b)

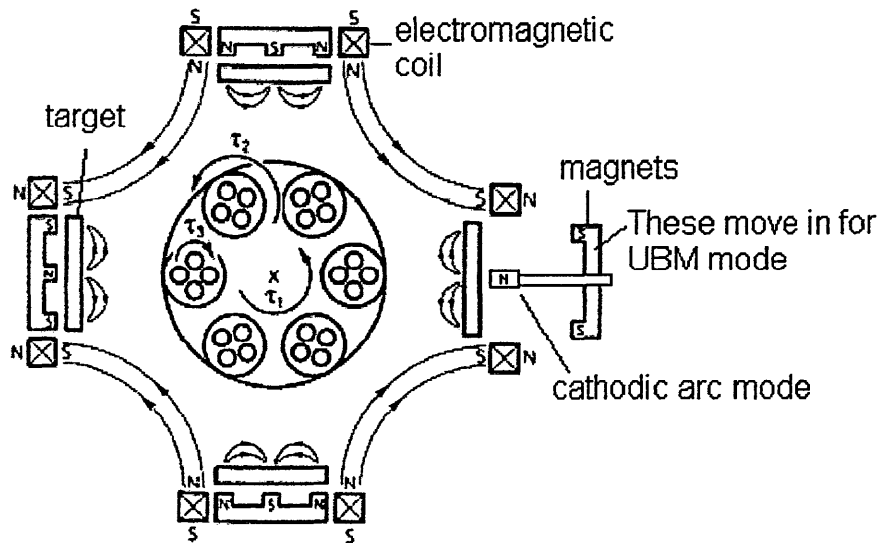


Figure 3.1 (a) HTC 1000-4 ABSTM PVD coater and (b) schematic cross-section of the chamber

Process step	Objectives/Descriptions
Pumping down	<p>To evacuate the coating chamber to a relatively low pressure of $< 7.9 \times 10^{-5}$ mbar, to minimise contamination or impurities trapped in the coating during deposition.</p> <p>The chamber is evacuated in two stages:</p> <p>(i) Rough pumping via 250 m³/h roots pump and 500 m³/h rotary vane pumps to a pressure of 8×10^{-2} mbar.</p> <p>(ii) Fine pumping via two Balzers TPH 2200 turbo molecular pumps with a total pumping speed of 4400 l/s to the lower pressure of $< 7.9 \times 10^{-5}$ mbar.</p> <p>Hot water flows around the chamber walls to prevent condensation of moisture on the chamber walls when the machine is vented.</p>
Heating	<p>To heat up the chamber and the substrates, to produce suitable temperature for coating deposition. In addition, heating enhances water desorption (outgassing) from the chamber and the substrate table. Heating is accomplished by one heater on each chamber wall and one heater under the turntable. Target cleaning is started when the required temperature is reached and the pressure is $< 7.9 \times 10^{-5}$ mbar.</p>
Target cleaning	<p>To remove impurities and contaminants on the target surface. Shutters are positioned in front of the targets during target cleaning to prevent substrate contamination.</p>
Metal ion etching	<p>Substrate pre-treatment prior to deposition. The cathode is operated in steered cathodic arc mode at a high current of 100 A. By applying a high bias voltage of -1200 V to the substrate, the ionised positive ions are accelerated towards the substrate and bombard the substrate surface, resulting in sputter cleaning and shallow metal ion implantation which enhances the adhesive strength of subsequent coatings.</p>
Base layer	<p>To provide a gradient layer and to further enhance the adhesion between the substrate and the coating.</p>
Coating	<p>To coat monolithic, multilayer or superlattice coating.</p>
Cooling	<p>Cooling down and venting.</p>

Table 3.3 Principle deposition sequence of ABS™

3.1.3 Deposition procedures and process parameters setting

This section presents the deposition procedures and process parameters used for C/Cr coatings, see Figure 3.2. The coating was deposited at 260°C, which is a relatively low temperature deposition process. Low temperature deposition has advantages over high temperature deposition, which would reduce the choice of substrate materials. Four rectangular targets, one 98% pure metal (Cr) and three graphite targets, each with dimension $600 \times 190 \text{ mm}^2$ were used for coatings deposition. The arrangement of the targets is shown in Figure 3.2(a). The samples experienced three-fold rotation to increase coating thickness uniformity. Prior to C/Cr coating deposition, a CrN base layer was deposited to provide a stress reduction graded layer between the substrate and the C/Cr coating. C/Cr coatings were deposited on various substrates for 4 hours at bias voltages, U_B of -65 V, -75 V, -95 V, -120 V, -350 V, -450 V, and -550 V respectively, following the deposition procedures and parameters presented in Figure 3.2(b). In addition, coatings were also deposited at two alternating bias voltage of -75 V and -350 V (labelled as -75/350 V), at 30 min interval per bias voltage, for a duration of 4 hours, to gain a better understanding of the effects of ion bombardment energy on the growth of the C/Cr coatings.

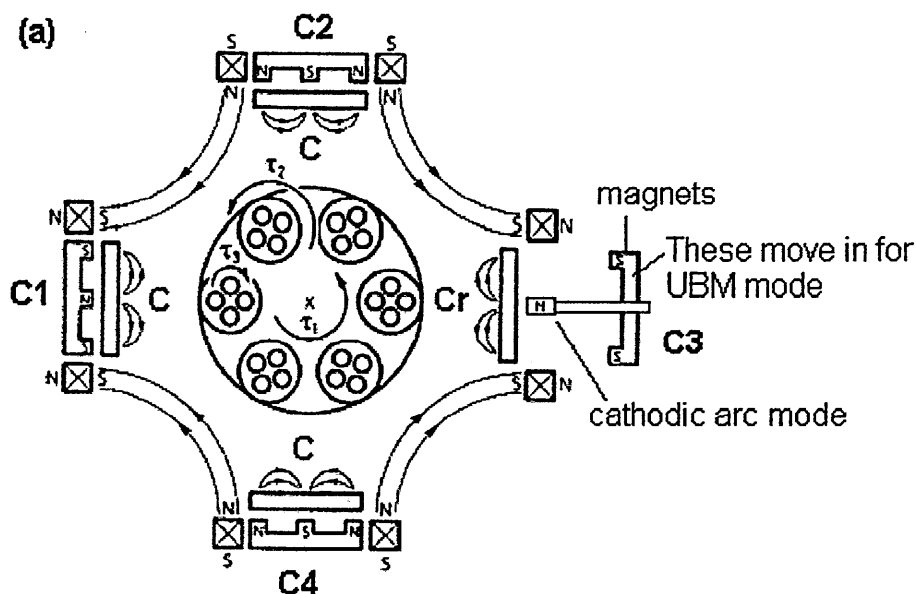
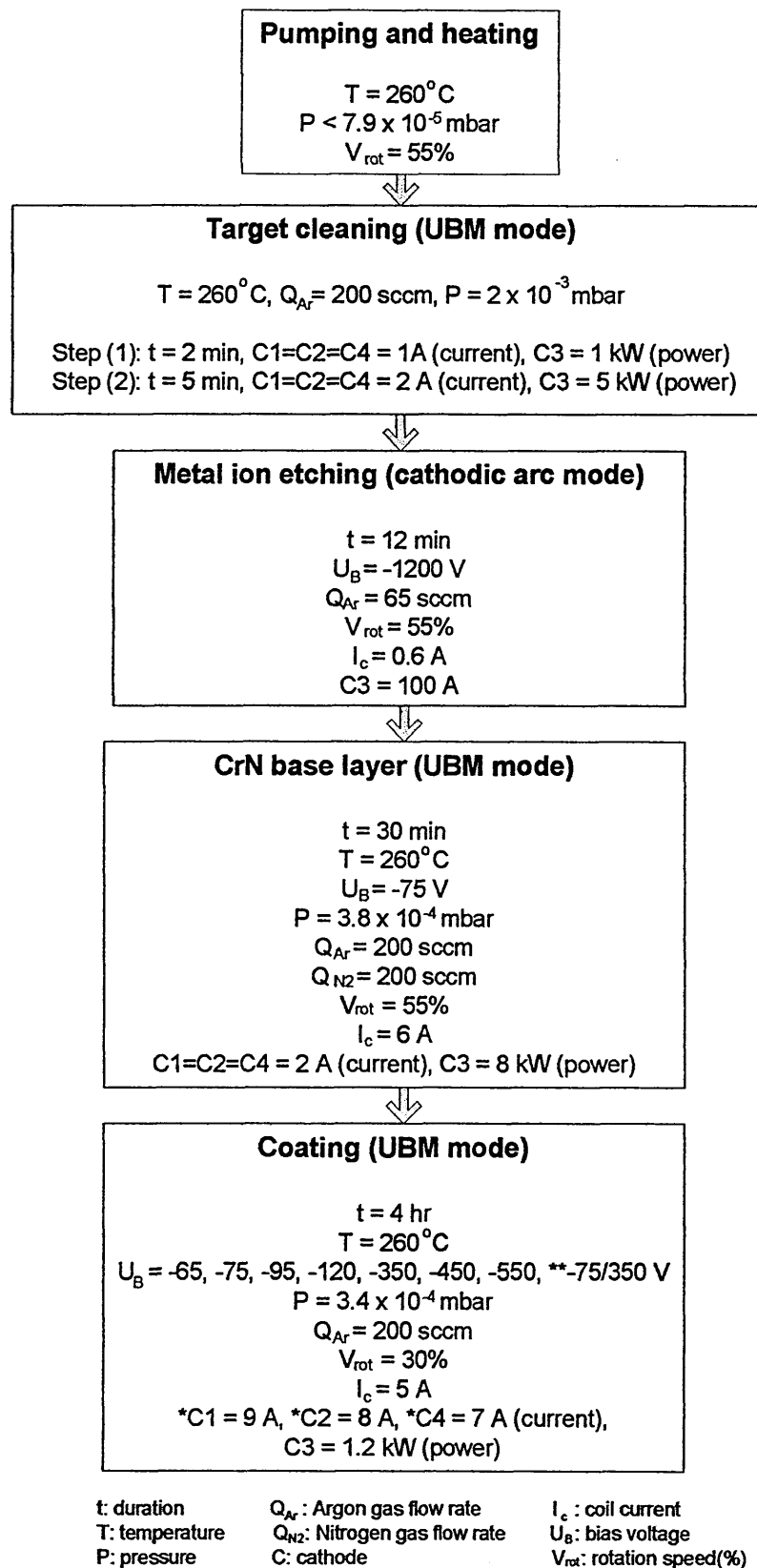


Figure 3.2 continues on next page

(b)



* The initial current on C1, C2, and C4 are 3 A each. The current was gradually increased by 1 A per minute until the current on C1 = 9 A, C2 = 8 A, and C4 = 7 A

** Bias voltage was applied alternatively at -75 V and -350 V at 30 min interval, with -75 V layer adjacent to CrN

Figure 3.2 (a) Schematic of target arrangement, (b) Process sequence and parameter settings for C/Cr coating deposition (Note: 100% $V_{\text{rot}} = 15 \text{ rpm}$)

3.2. Modification of conventional Scanning Reference Electrode

Technique (SRET) rig for tribocorrosion testing

As mentioned previously in Chapter 1 the purpose of modifying a conventional Scanning Reference Electrode Technique (SRET) was to provide a tribocorrosion test method which could be used to study the real-time localised tribocorrosion behaviour of specimens. The SRET was chosen for this experiment because it has been demonstrated to be a useful tool for the investigation of localised corrosion [142-148] due to its ability to provide quantitative information regarding local anodic and cathodic processes [149]. Furthermore, it is a non-invasive, highly sensitive, and reliable electrochemical method which can be used to image and quantify real-time localised electrochemical activity. SRET measures microgalvanic potentials existing close to the surface of the materials under investigation, using a pseudo reference electrode probe which scans over the surface. This non-intrusive technique provides dynamic information on corrosion activity by recording variations in ionic flux in the electrolyte, on a microscopic scale [143].

3.2.1 Principle and design of the tribocorrosion test rig

The modification of the SRET rig (Uniscan Instruments SP-100 Scanning Reference Electrode Technique) was carried out based upon the principle of a ball-on-cylinder contact. Figure 3.3 schematically presents the design of the modified SRET for tribocorrosion testing. The load is applied based on a cantilever approach, where a load cell is screwed to a ball bearing which is attached to the cantilever arm. The main purpose of the load cell is to allow the system to be calibrated when the load cell is connected to the strain gauge indicator, in which a strain gauge indicator provides an output signal (micro-strain, $\mu\epsilon$) when a load is applied. The output signal is then plotted versus the applied load and a calibration factor obtained. Assuming no plastic deformation of the ball or sample, a linear graph is expected. When a load (weight) is placed on the empty pan, it will exert a force causing the sliding probe to make contact with the sample. Negligible frictional forces exist on movement of the sliding probe towards the specimen, thereby ensuring that the load applied on the empty pan is proportional to the load applied on the sample. This has been confirmed by system calibration, as discussed in Chapter 4.

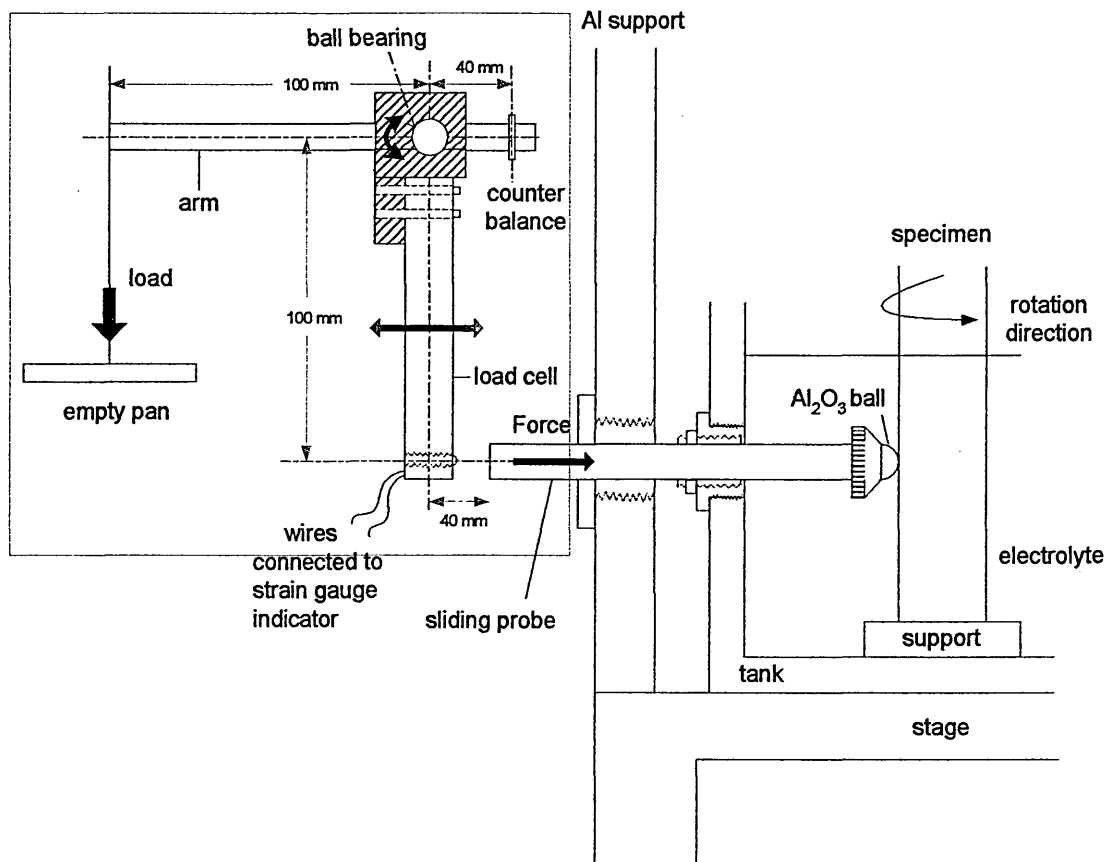


Figure 3.3 Schematic outline design of the tribocorrosion test rig (not to scale)

3.2.2 Experimental setup and tribocorrosion calibration

Figure 3.4 presents a schematic of the experimental set-up for conducting tribocorrosion tests using the modified SRET, where the sliding contact system highlighted with the box is given in Figure 3.3. Here, the sliding probe comprises a changeable 6 mm alumina ball, being positioned diametrically opposite a pseudo reference electrode probe (Pt probe) which is located 100-150 μm away from the surface of a cylindrical specimen which rotates at a 100 rpm (equivalent to ~ 0.08 m/s flow rate, see section 3.3.16.2 for detail of calculation). The wires of the Pt probe are sharpened to increase their sensitivity and measure respectively the local and bulk isopotential field associated with the surface corrosion activity. By convention the SRET activity is defined as follows; negative values (anodic) and positive values (cathodic). The contact probe, specimen and Pt probe are immersed in aqueous 0.01% NaCl, which has a very similar conductivity to that of tap water. The dynamic corrosion activity is monitored via the Pt probe by recording variations in ionic flux emanating at the surface of the corroding sample. The Pt probe can operate in three modes, namely

line scan (current versus displacement and current versus time), in which corrosion activity along a single position on the circumference of the specimen is measured, or map scan in which a 2D corrosion activity area map of the surface of the specimen is obtained.

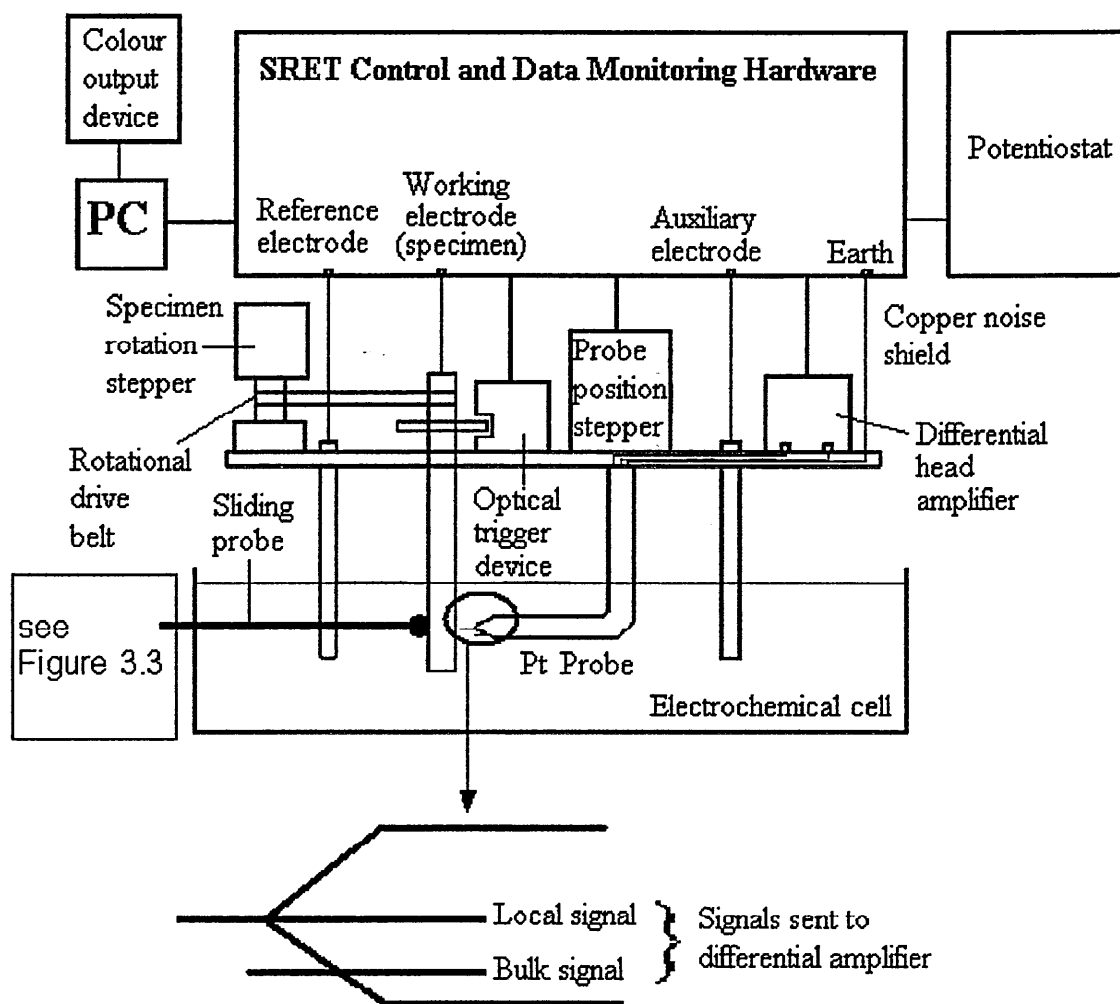


Figure 3.4 Schematic of SRET experimental set up including probe geometry

Calibration of the system was carried out using both uncoated 316 SS (SS) and C/Cr coated test specimens, which were rotated in air and in tap water (which has a very similar conductivity and viscosity to that of 0.01% NaCl solution). The use of coated and uncoated samples for calibration was aimed at assessing any effects of the coating on the calibration factor. The load cell (model SP02, max. load 50 N, gauge factor of 0.5) was connected to a P3500 strain gauge indicator, and the output reading ($\mu\epsilon$) was recorded each time a load was applied from 0 - 6 N. The empty pan (weight ~ 0.2 N)

was located at a constant position on the arm. The rotation speed of the sample was set to 100 rpm. The calibration results for the tribocorrosion test are given in Chapter 4.

3.3. Characterisation techniques

3.3.1 Tribological test

Pin-on-disc test

The tribological studies were conducted using a pin-on-disc (CSEM tribometer) apparatus. The tests have been carried out in an ambient atmosphere (RH: 13-34%, temperature: 25-28°C) under the testing conditions of 5 N normal load, 0.1 ms⁻¹ sliding speed, sliding distance of 1.3 km, using a 6 mm 100Cr6 steel ball as a counter part (see Figure 3.5 for the experiment set-up). In the majority of the industrial applications, the C/Cr coatings are expected to be in tribological contact with different types of steels. Therefore, the counter part material in the pin-on-disc tests was selected to be a 100Cr6 bearing steel ball (HRc = 62).

During testing, the stationary ball was pressed by a 5 N normal load on a rotating sample and the coefficient of friction was recorded by monitoring the tangential forces on the specimen as a function of the sliding distance. This test permits a qualitative interpretation of various topographical effects and changes in wear mechanism during tribological contact, based on the friction curve obtained. Friction coefficient can be expressed as:

$$\mu = F_t / F_N$$

where F_t = tangential force, and F_N = normal force

The cross-sectional area of the wear track (A) was measured using a laser profilometer, four measurements were taken on each sample at 90° apart. The values were then entered into a program to obtain the wear coefficient, K_c , which was calculated using Archard's equation:

$$K_c = V / (F_N \cdot d)$$

where V = wear volume (mm³) = $2 \pi R A$

R = radius of wear track (mm)

F_N = normal force (N)

d = sliding distance (m)

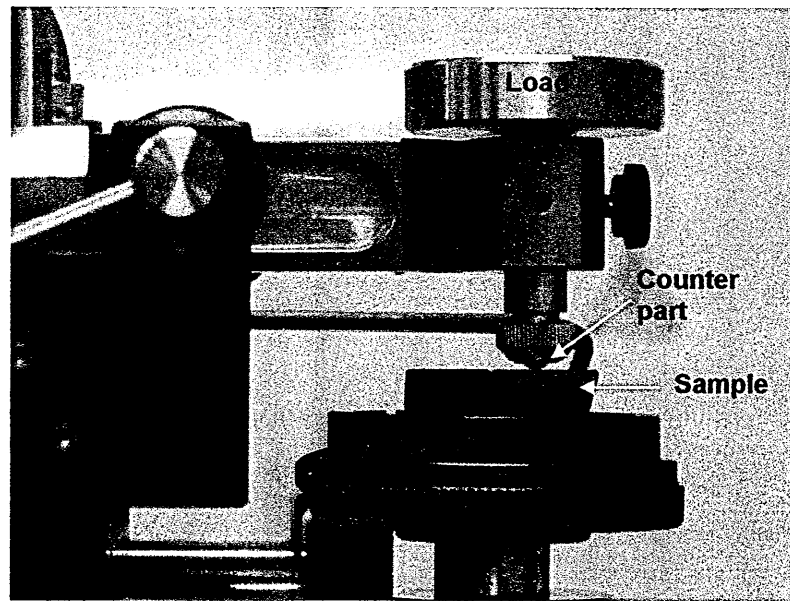


Figure 3.5 Pin-on-disc test

3.3.2 Scratch test and Rockwell-C indentation test

A sufficient level of coating/substrate adhesion is the minimum requirement for the acceptable performance of a coated component. These tests are important to determine how good the coating is bonded to the substrate.

Scratch adhesion test

The adhesion of the films was evaluated using a CSEM REVETEST scratch tester by measuring the critical load, L_c , at which coating failure occurs. A stylus, typically Rockwell C diamond (120° cone with a 0.2 mm radius hemispherical tip) is drawn over the coated surface with a gradually increasing normal load up to a set value. After testing, the scratch is examined under the microscope attached to the adhesion test machine, to determine the critical load, L_c at which coating detachment or spallation initiates. Figure 3.6 shows the CSEM Revertest scratch tester and the schematic of the scratch after test.

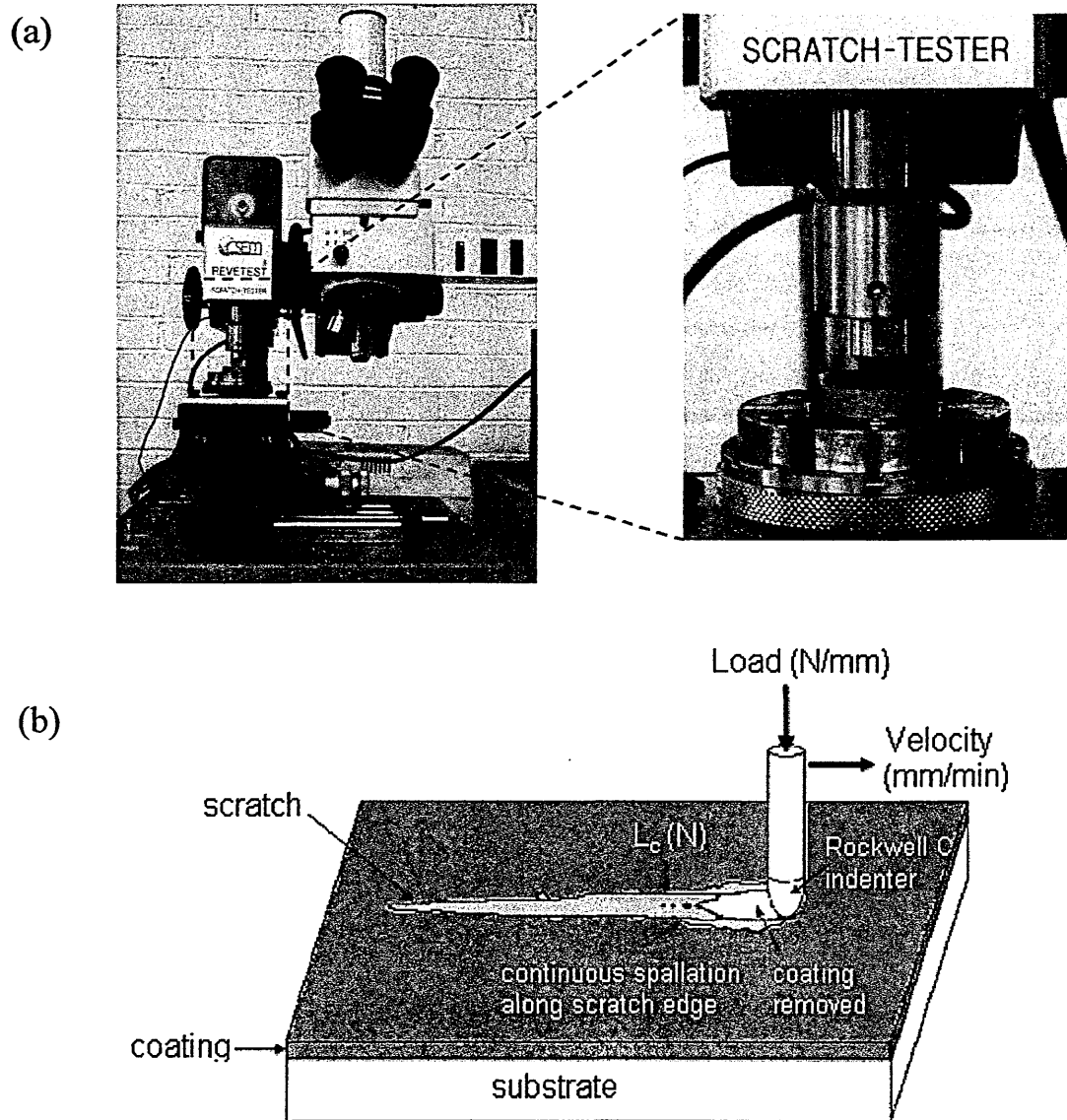


Figure 3.6 (a) CSEM Revertest Scratch tester, (b) Schematic of scratch generated

Rockwell C (HRc) Indentation method

A conventional Rockwell hardness test machine using a C-type diamond indenter is pressed into the coated sample by 150 kgf load. The indentation made through the coating and into the substrate is observed in an optical microscope and is categorised according to the six grades of indentations outlined by the Verein Deutscher Ingenieure (VDI) criteria, shown in Figure 3.7. The gradings, that is HF1 - HF4 (acceptable) and HF5 - HF6 (unacceptable), are dependent on the degree of cracking and/or spallation of the coating around the indentation (HF is the German abbreviation for adhesion strength). The test is limited to coated samples in which the substrate is harder than $HR_c = 54$ and the coating thickness is $< 5\mu\text{m}$.

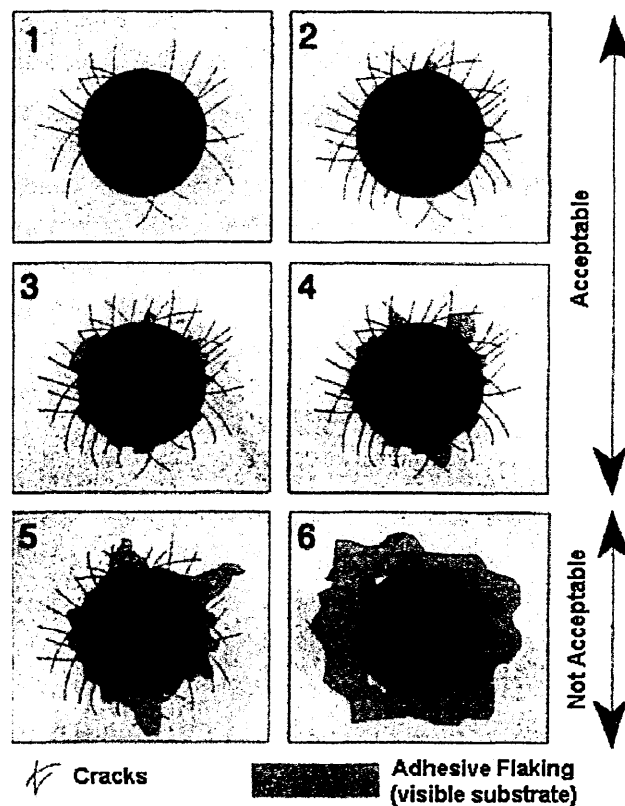
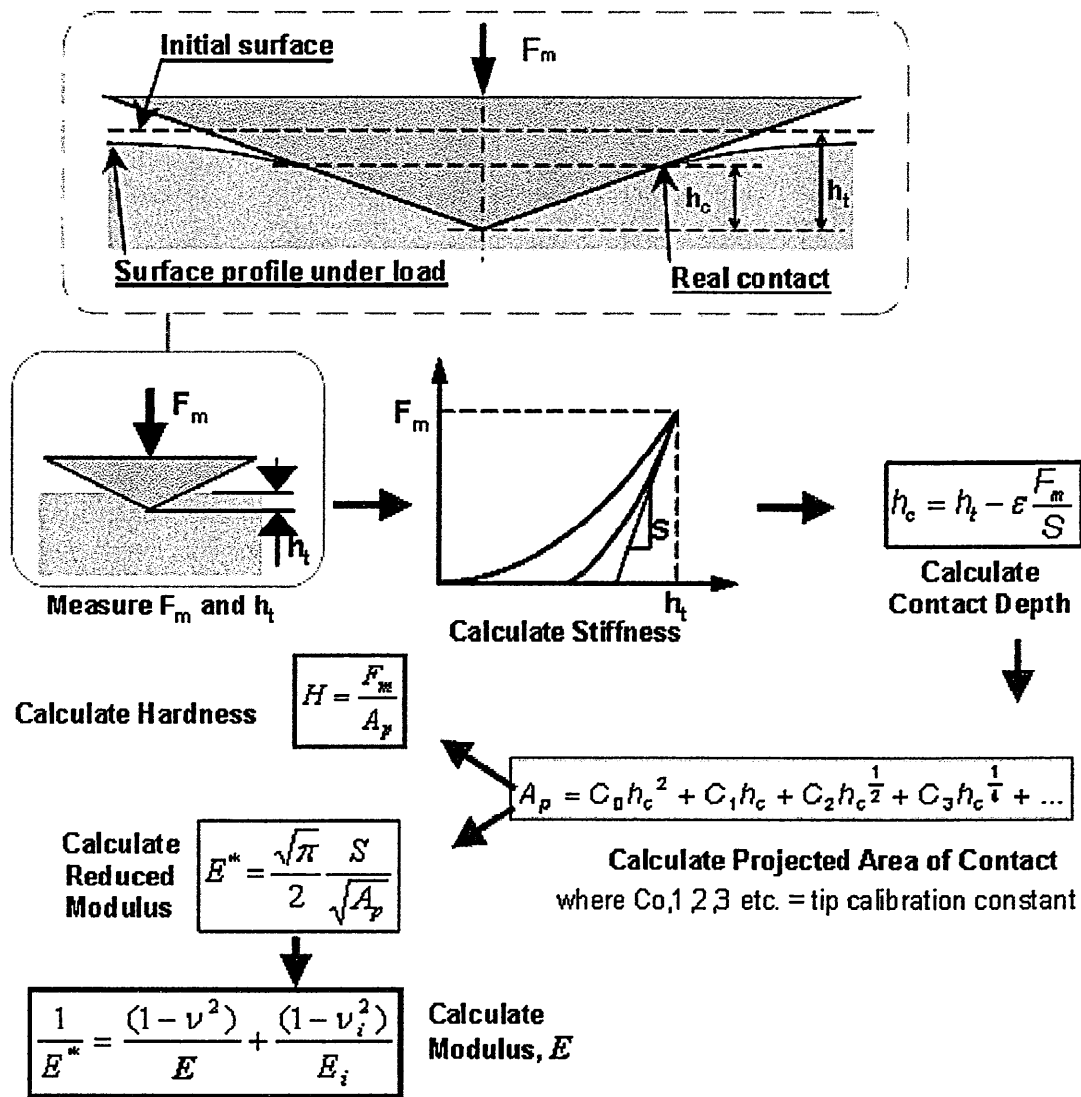


Figure 3.7 HRc adhesion failure mechanisms. Number corresponds to acceptable grade, with 1 the best and 6 the poorest

3.3.3 Nano-hardness test

The hardness and Young's modulus (E) of coatings was measured using the CSM indentation tester. An indenter tip (Berkovich) is driven into the sample normal to the sample surface, by applying an increasing load up to the preset value. To avoid substrate influence, the indentation depth should be $< 10\%$ of the coating thickness, a 10 mN load was used in this experiment. The load is then gradually removed until partial or complete relaxation of the material occurs. The applied force and depth are measured dynamically during a load-unload cycle. Hardness and Young's modulus are calculated directly from the resultant force-displacement curve, by the software based on the procedure and equations shown in Figure 3.8 [150]:



where F_m = maximum applied load

h_t = depth from the original surface

A_p = projected contact area which is determined from the contact depth, h_c

ε = strain obtained from stress-strain curve

S = contact stiffness (tangent to the unloading curve)

ν = Poisson ratio of measured material (0.3 was used in the experiment)

Figure 3.8 Nano-hardness instrumented calculations

3.3.4 Ball-cratering thickness measurement

The coating thickness was measured using the ball cratering technique (CSEM Calotest). The thickness was determined from the average of ten measurements. A rotating steel ball with 30 mm diameter (or radius $R = 15$ mm) wears a crater through

the coating, known as a calotte. During this test, a few droplets of diamond slurry (particle size 1 μm) were applied between the contacting surfaces. The calotte inner and outer diameter (see Figure 3.9) is measured using an optical microscope equipped with layer measurement software which enables the coating thickness to be calculated based on the following equation:

$$\text{Coating thickness, } h = (D^2 - d^2) / 8R$$

D = outer diameter of calotte

d = inner diameter of calotte

R = radius of ball

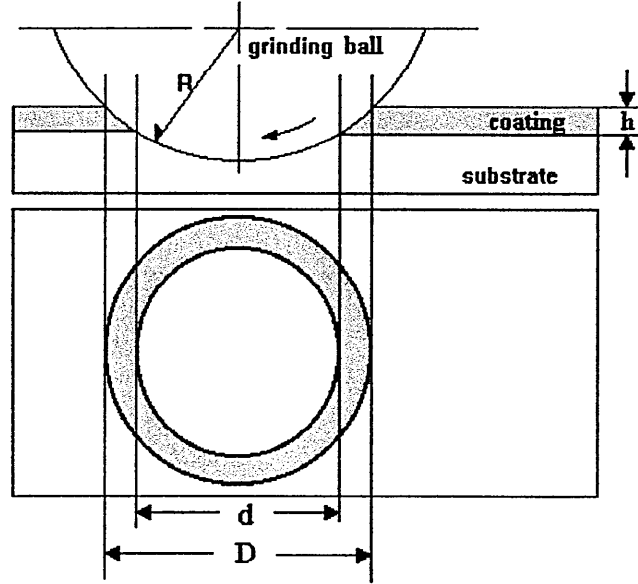


Figure 3.9 Schematic of the calottes

3.3.5 Stress measurement by disc deflection method

Because of the amorphous nature of the coatings investigated, the use of XRD for stress measurement is not possible. For this reason, the residual stresses in the coatings were determined using a disc deflection method [151], utilising Stoney's equation:

$$\sigma = (E_s d_s^2) / [6(1 - \nu_s) R d_c]$$

where E , is the Young's modulus, d is the thickness, ν is the Poisson ratio (0.3 was used in the calculation), and R is the radius of curvature of the coated substrate; subscripts s and c denote the substrate and the coating, respectively. The maximum deflection, H , see Figure 3.10(a), of the coated substrate was measured by optical microscopy (Society

Genevoise Optical Measuring Machine available in the School of Engineering). The H value minus the coating and the substrate thicknesses ($h = H - d_c - d_s$), was then used to calculate the radius of curvature, R using the following mathematical calculation (see Figure 3.10(b) for representation of the variables used).

$$\tan \theta = \frac{(L/2)}{h}$$

$$\lambda = 90^\circ - \theta$$

$$\tan(\theta - \lambda) = \frac{x}{(L/2)}$$

$$\therefore x = (L/2) \tan(\theta - \lambda)$$

and

$$R = x + h$$

where L = length of substrate after coating deposition

$$d_s = 0.1 \text{ mm}$$

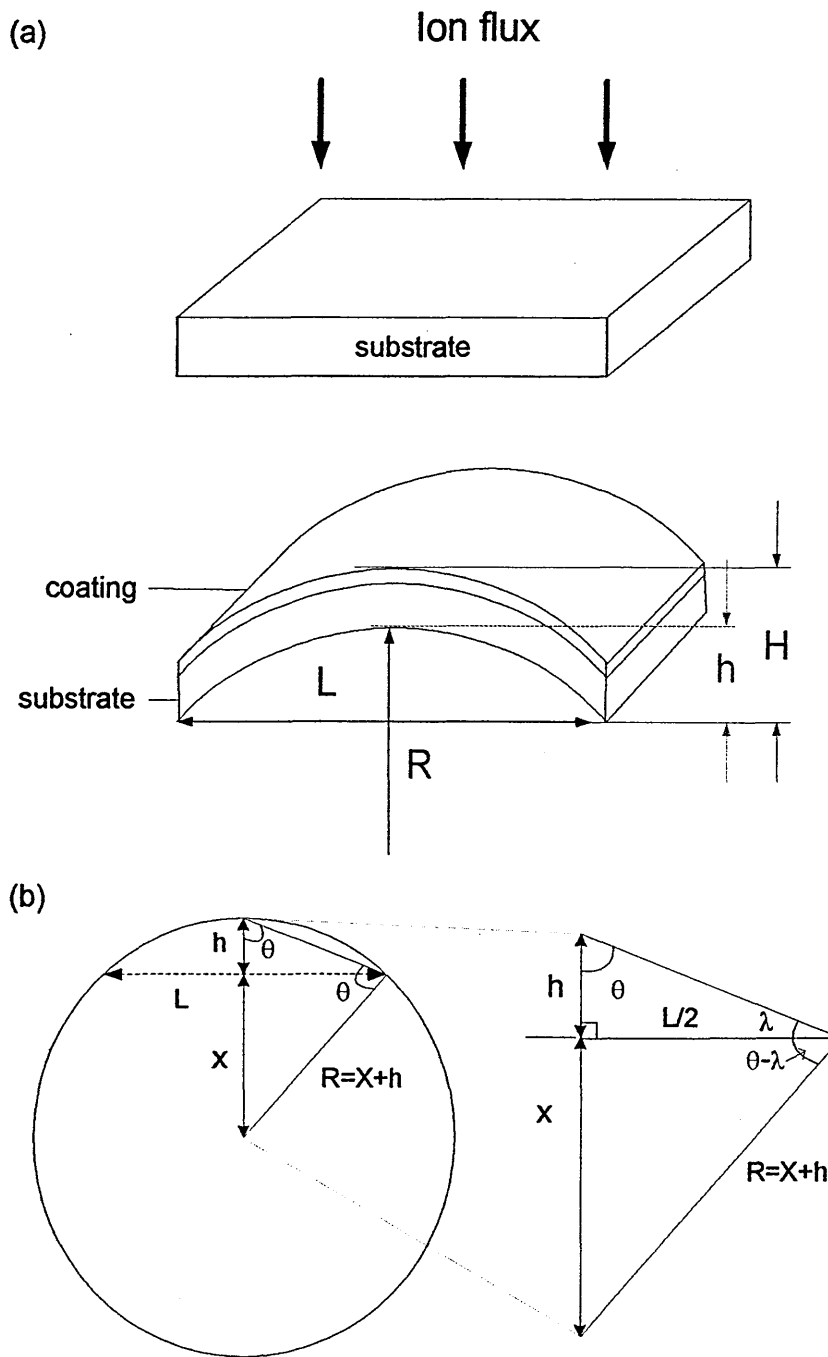


Figure 3.10 Stress measurement (a) schematic of sample before and after coating deposition, (b) outline of radius of curvature calculation

3.3.6 Plasma characterisation

The plasma conditions during C/Cr coating deposition were investigated using a flat electrostatic probe [152]. The probe consisted of a stainless steel disc with diameter of 20 mm. The probe was mounted stationary in front of a graphite target at a distance

of 300 mm, in close proximity to the position of the substrates. Plasma density and floating potential of the plasma were measured by sweeping the probe voltage from –150 V to –10 V. The floating potential, U_f measured for the ABSTM system was –30 V [152]. The values obtained for ion saturation current density, J_{sat} represent the peak ion bombardment received by the substrates when they are closest to the target. Based on previous results [61] the average ion bombardment over one full motion around the chamber is approximately 75% of the peak value measured with a stationary probe in front of the target. Therefore, the following expression was used to estimate the average ion flux during the deposition: $J_i = 0.75 * J_{sat}/e$, where $e = 1.6 \times 10^{-19}$ C is the elementary charge (or the charge of one ion) [111].

3.3.7 Secondary neutral mass spectrometry (SNMS)

Secondary Neutral Mass Spectrometry (SNMS) by a VG SIMSLAB was used to measure the composition of the films. The instrument uses an Ar-ion source at an acceleration voltage of 10 kV. The sample is placed in an ultra high vacuum chamber (about 5×10^{-9} mbar) and is bombarded using a specially designed ion gun. The sputtered flux from the sample consists of a mixture of neutrals and ions. The ions are stopped and neutrals ionised by an electron beam. The ratio between neutrals and ions is dependent on the elemental species. The ionised flux is accelerated through a series of filters and detected with a mass spectrometer.

3.3.8 Rutherford backscattering spectroscopy

Rutherford backscattering spectroscopy (RBS) utilises a beam of ions, usually He^+ , with high kinetic energy (typically 1-3 MeV) which is directed towards the sample. Upon collision, the incident ions are elastically scattered (backscattered) from the atoms of the sample. The mass of the target atom can be determined by measuring the scattered energy of the backscattered particles [153]. Hence, by detecting and analysing the backscattered ions from the sample using a solid-state detector, quantitative compositional information of the sample can be obtained. RBS is more sensitive for heavy elements than for light elements.

The composition of the coating x ($C_xCr_{(1-x)}$) and the coating area density N_a (in atoms cm^{-2}) were obtained using a 2 MeV H^+ (proton) beam with a scattering angle of 150° [111]. The Cr and substrate signals were fitted using the SIMNRA [154]

simulation software to obtain x and N_a . The neutral deposition rate was then calculated as the ratio of N_a and the deposition time while the film bulk density is given by the ratio of N_a and the coating thickness. The carbon and nitrogen signals, appear in the background and are mainly generated by different proton reactions.

3.3.9 X-ray diffraction (XRD)

XRD is based on the phase relationship of rays from an incident X-ray ($\text{CuK}\alpha$ with 1.5405 nm wavelength is used in this study) that have been scattered by periodically repeating planes of atoms (Figure 3.11). For any crystal, planes exist in a number of different orientations and each has its own specific 'd spacing'. X-rays are diffracted by crystalline materials when the Bragg condition is satisfied. Bragg's Law is expressed as:

$$n\lambda = 2d\sin\theta$$

where θ = Bragg angle; n = order of reflection; λ = wavelength of the radiation; and d = interplanar spacing

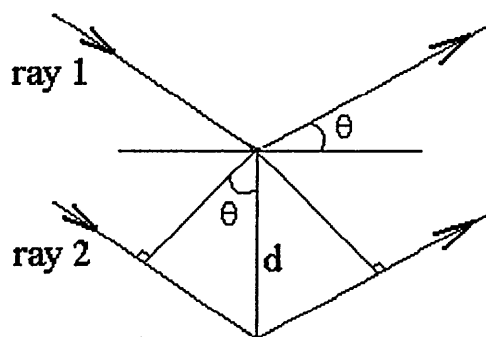


Figure 3.11 X-ray diffraction from crystal planes

The structure was investigated by X-ray diffraction (XRD) analysis utilising a Philips PW 1710 automated diffractometer, using glancing angle (fixed at 1° incidence angle) and Bragg-Brentano ($\theta/2\theta$) geometries, scanning from $2\theta = 10^\circ$ to 100° with a step size of 0.04° . The angles at which the peaks appeared were compared with the standard data from the JCPDS database to identify the structure and the phases present in the coatings.

3.3.9.1 Bragg-Brentano ($\theta/2\theta$) geometry

The specimen was irradiated with an x-ray beam incident at an angle θ to the sample surface and the diffracted beam intensity was detected using a counter at an angle 2θ relative to the incident beam to satisfy the Bragg condition (Figure 3.12). The only planes to diffract are those parallel with the surface.

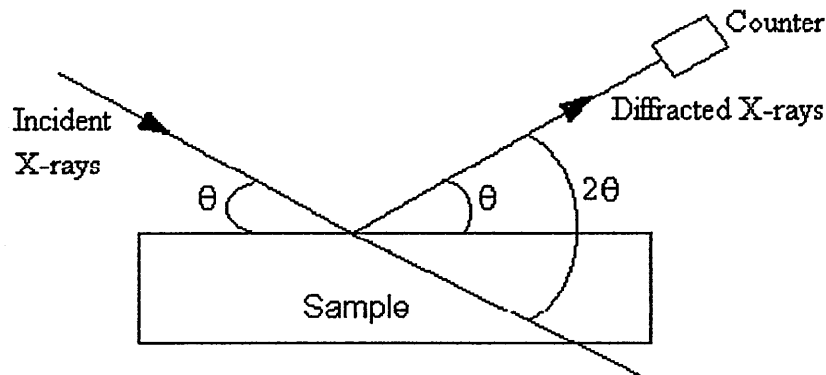


Figure 3.12 Schematic of Bragg-Brentano geometry

3.3.9.2 Glancing angle geometry

Glancing angle geometry was used to measure the structure and the phase presence in the near surface region of the sample. In this experiment, the angle of incidence γ was fixed at low angle of 1° and the counter was moved (Figure 3.13). The diffracting planes are at an angle $\theta - \gamma$ to the specimen surface. By varying the Bragg angle θ , the Bragg's Law condition is satisfied by different d-spacing of the materials.

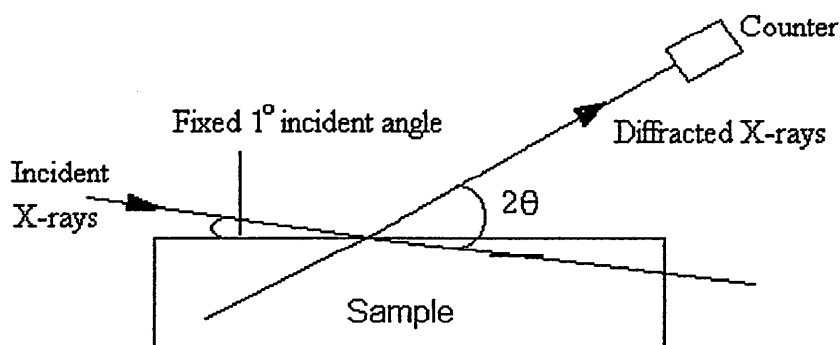


Figure 3.13 Schematic of glancing angle geometry

3.3.10 X-ray Photoelectron Spectroscopy (XPS)

X-ray Photoelectron Spectroscopy (XPS), also known as electron spectroscopy for chemical analysis (ESCA), is a widely used surface science technique capable of identifying elemental species present at a surface. The photoelectron phenomenon is based on Einstein's equation:

$$E_k = h\nu - E_b - E_w$$

where E_k is the kinetic energy of photoelectrons, $h\nu$ is the energy of the X-ray radiation, E_b is the electron binding energy, and E_w is the work function of the material. When a solid sample is exposed to X-rays, photoelectrons from a sample are excited, the emitted electron signal is then plotted as a spectrum of binding energies. Each chemical element has a set of characteristic photoelectron peaks corresponding to its electronic orbital energy levels [155]. Differing chemical states resulting from compound formation are reflected in the photoelectron peak positions and shapes. Hence XPS provides chemical bonding information. The peak areas can also be used to determine the composition of the material surface.

Photoelectron spectroscopic analysis was performed using a Physical Electronics model PHI 5400 X-ray photoelectron spectrometer using a Mg K_α source (300 W, 15 kV, 20 mA). Spectra were collected using a concentric hemispherical analyzer in constant pass energy mode (Fixed Analyzer Transmission or FAT). Survey wide scan spectra were taken using analyser pass energy of 178.95 eV and a 1 eV step size. Core level C 1s, O 1s and Cr 2p spectra were taken with pass energy of 35.75 eV and 0.1 eV step size. XPS depth analysis was performed by employing a 3 keV Ar^+ ion beam (beam current density = $8 \mu\text{A}/\text{cm}^2$) for 2, 4, and 6 minutes. The approximate sputter rate for SiO_2 under these conditions is 3 nm/min. The spectra were curve fitted using a mixed Gaussian/Lorentzian function to give quantitative binding energies and peak area ratios.

3.3.11 Raman Spectroscopy

Raman spectroscopy is widely used for the characterization of different forms of carbon, in both crystalline and amorphous forms and it is very sensitive to the nature of carbon bonding. In Raman spectroscopy (shown schematically in Figure 3.14), the sample is irradiated by intense laser beams in the UV-visible region (10^4 - 10^6 cm^{-1}) and the scattered light is usually observed in the direction perpendicular to the specimen, see

Figure 3.14(b). The scattered light consists of two types: Rayleigh scattering (having the same frequency as the incident beam, ν_0) and Raman scattering (having frequencies $\nu_0 + \nu_m$ and $\nu_0 - \nu_m$, where ν_m is a vibrational frequency of a molecule). The $\nu_0 - \nu_m$ and $\nu_0 + \nu_m$ lines are called the Stokes and anti-Stokes lines, respectively. The Stokes scattering (Raman effect) is produced when energy extracted from the light beam causes the crystal to vibrate, while the anti-Stokes scattering results from the annihilation of the existing thermally excited vibration [156]. Raman spectroscopy measures the vibrational frequency (ν_m) as a shift from the incident beam frequency (ν_0), and the vibrational modes are dependent on the atomic bonding in the solid.

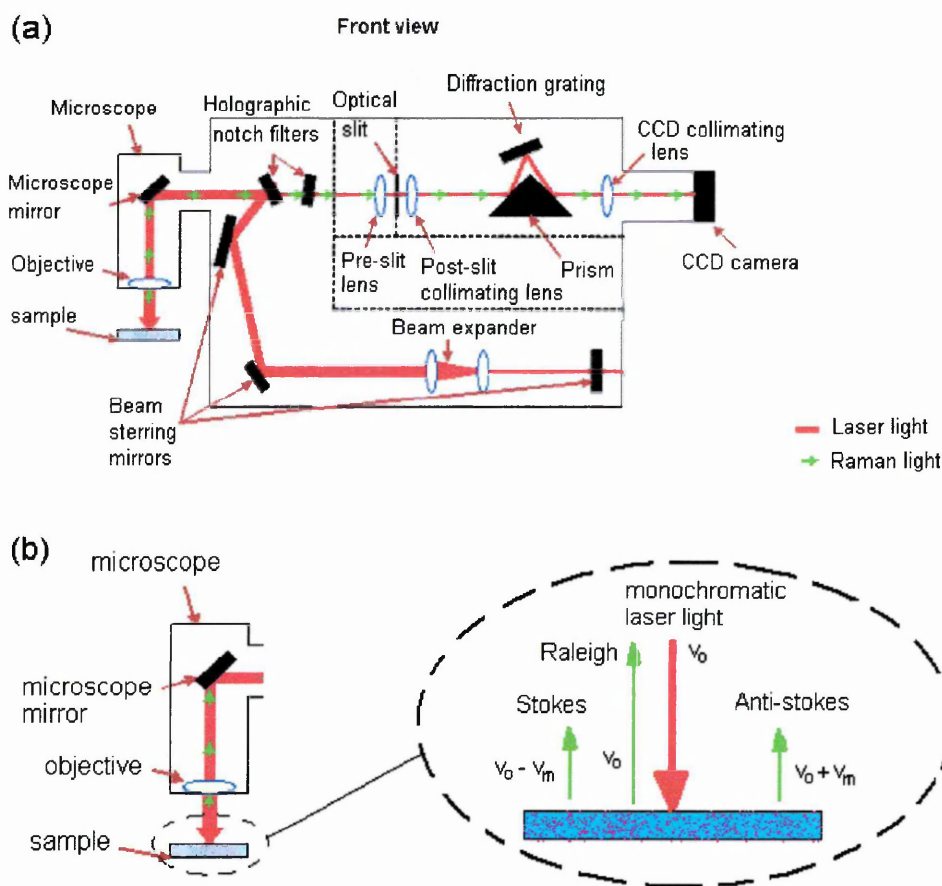


Figure 3.14 Schematic of (a) Raman spectroscopy and (b) Raman scattering

The Raman measurements were performed using a Renishaw Raman System 1000 spectrometer to obtain structural information on the graphitic character of free carbon within the coatings and the wear tracks. The excitation wavelength used was 632.8 nm (25mW laser) from a HeNe red laser. The laser was focused at the sample in a 2 μm diameter spot through a standard 50 \times microscope objective. Raman spectra were

measured at 6.25-12.5 mW (~25-50 % of the total laser power), to avoid thermal decomposition of the samples. Spectra were recorded from 1000-1800 cm^{-1} and fitted by two Gaussian peaks, where the peak positions and the area of D (1350 cm^{-1}) and G (1580 cm^{-1}) peaks were obtained. I_D/I_G ratios were calculated from the ratio of the area of D peak to G peak, which signifies the sp^2/sp^3 ratio in the films.

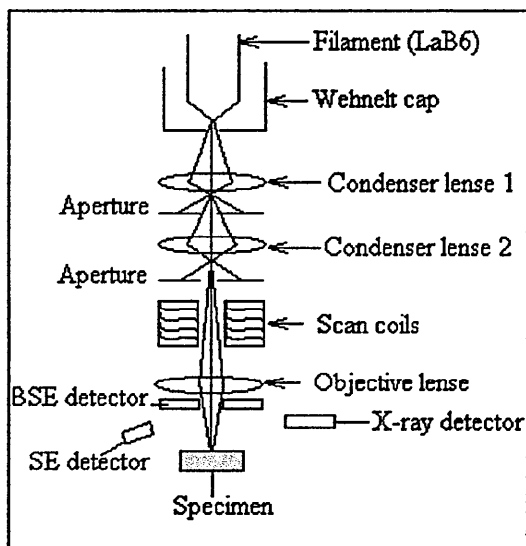
3.3.12 Scanning electron microscope (SEM)

A fully computerised SEM, Philips XL 40 microscope, equipped with energy dispersive X-ray (EDX) analysis, was used to investigate the microstructure and the elements present in the specimens. The accelerating potential used was 20 kV. The specimens must be conductive in order to be examined using a conventional SEM. Non conductive specimens will result in poor imaging due to accumulation of electrons in the sample and hence charging effects.

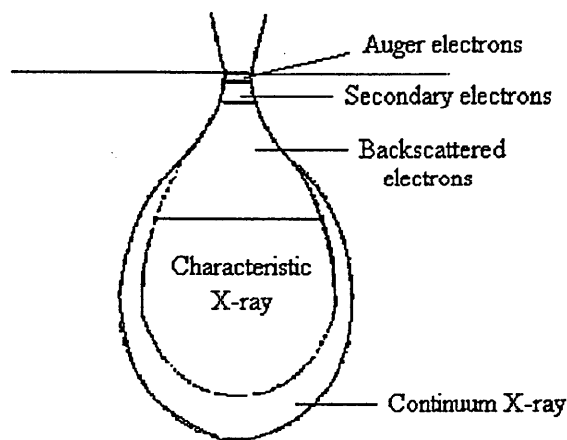
Two detectors are attached with the microscope:

- (i) Secondary electron (SE) detector: most widely used because it gives an excellent impression of surface morphology of the specimen (for topographical imaging).
- (ii) Backscattered electron (BSE) detector: Backscattered electrons are produced when an incident electron collides with an atom in the specimen which blocks the incident electron path (see Figure 3.15(b) for the interaction volumes). The incident electron is then scattered "backward" by 180 degrees. It is used for imaging surface compositional variations of the specimen. The production of backscattered electrons varies directly with the specimen's atomic number. In this imaging mode, higher atomic number elements appear brighter than lower atomic number elements.

Qualitative elemental analysis by means of energy dispersive X-ray (EDX) can be obtained by measuring the energy levels of the elements from the resulting X-rays collected by the X-ray detector. Figure 3.15 outlines the schematic and the interaction volumes of SEM, which show the escape depth of the electrons that can be detected by the SE or BSE detectors.



(a) Schematic of SEM



(b) Interaction volumes

Figure 3.15 Schematic of SEM and interaction volumes

3.3.13 Transmission electron microscope (TEM)

A Philips CM20 TEM microscope equipped with a Tungsten (W) filament, operated at 200 kV, was used to investigate the microstructure and to obtain crystallographic information (the arrangement of atoms in the specimen and their degree of order) of C/Cr coatings. An electron transparent sample was illuminated by an electron beam, which was generated in an electron source equipped with a tungsten filament. In TEM, when a direct beam is selected, the resultant image is called a bright-field (BF) image, and if scattered electrons are selected, the image is called a dark-field (DF) image. The way to choose which electrons form the image is to insert an aperture into the back focal plane of the objective lens, thus blocking out most of the diffraction pattern except that which is visible through the aperture. External drives were used to move the aperture so that either the direct electrons or some scattered electrons go through it. Figure 3.16 shows a schematic of a transmission electron microscope, which consists of a condenser lens, objective lens, intermediate lens, projector lens and apertures. Two optional apertures, namely objective and selected area apertures, can be used to restrict the beam. The objective aperture enhances contrast by blocking out high-angle diffracted electrons. The selected area aperture enables the examination of the diffraction of electrons (elasticity scattered electrons), which is called the selected area diffraction pattern (SAD). Each spot is corresponding to a specific atomic spacing (a plane).

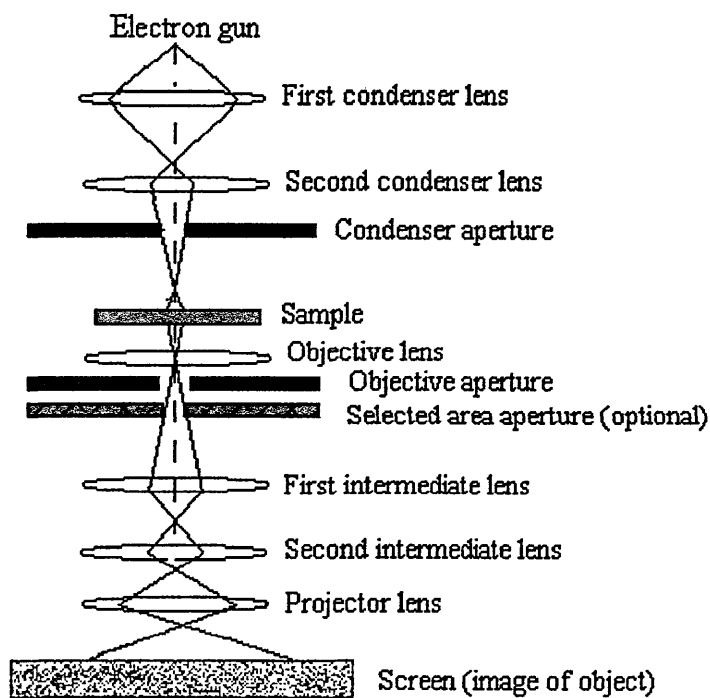


Figure 3.16 Schematic outline of a Transmission Electron Microscope

The following shows the procedures for preparing electron transparent (~100 nm) cross-sections samples:

1) Cutting:

- a) The coated sample (coating face up) was cut to a dimension $\sim 2.5 \times 2.0 \text{ mm}^2$ with a high speed SiC cutting wheel.
- b) Two cut samples with the coatings facing each other (to protect the coating surface) were glued with wax on a glass plate as shown in Figure 3.17.

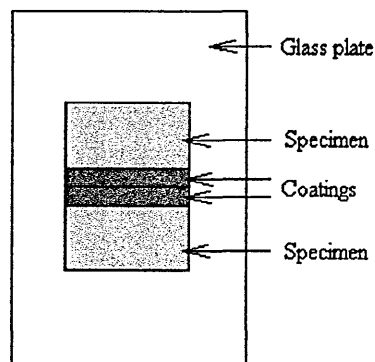


Figure 3.17 Arrangement of samples glue on glass plate

2) Grinding and polishing

- a) The samples were ground evenly by 240, 320, 400 and 600 grit papers, to half the sample thickness on one side and then polished with 5 μm diamond paper.

- b) The samples were turned over to the other side and were ground to $\sim 30\text{-}60\ \mu\text{m}$ following step (a).
- c) Finally, the sample was glued with epoxy resin on a copper grid with a slot hole and ready for ion beam thinning to electron transparent thickness.

3) PIPS (Precision Ion Polishing System-Ion beam milling)

A GATAN PIPS 691 system was used to thin the sample to the electron transparent thickness of $\sim 50\text{-}100\ \text{nm}$ by Ar ion beam milling. The parameters used were:

- a) Ion gun accelerating voltage: 5.5 keV
- b) Rotation speed: $\sim 1.5\ \text{rpm}$
- c) Incident angles: $\pm 8^\circ$

The sample was thinned until a small hole appeared on the coating region of the sample. The sample was then ready for investigation under TEM. Due to the limitation of CM20 to resolve nanoscale features in amorphous films, samples were also investigated at the Center for Microanalysis of Materials (CMM) at the University of Illinois, using high-resolution TEM (HRTEM) and scanning TEM (STEM-see section 3.3.14). The coatings were studied utilising a JEOL 2010F instrument operated at 200 keV using selected area electron diffraction (SAD), bright-field (BF), dark-field (DF), high-angle annular dark field (HAADF) and lattice resolution imaging techniques. HAADF images were obtained by using a HAADF detector attached to the STEM instrument. The contrast of HAADF images gives information about the average atomic number of the material encountered by the incident probe.

3.3.14 Scanning TEM-Electron energy loss spectroscopy (STEM-EELS)

Scanning TEM is a microscopy technique which enhances the analytical capabilities of conventional TEM. The main difference between STEM and TEM is that STEM uses a scanning beam which is rastered across an area of interest but TEM uses a stationary beam which is transmitted through a specimen. STEM can be coupled with analytical tools such as electron energy loss spectroscopy (EELS) which measures the amounts of energy lost by an electron. The incident electrons interact with specimen atoms in an inelastic fashion (inelastically scattered electrons), losing energy during the interaction. The inelastic loss of energy by the incident electrons is characteristic of the elements that were interacted with. These energies are unique to each bonding state of

each element and thus can be used to extract both compositional and bonding information on the specimen region being examined.

STEM-EELS analysis of C/Cr coatings was carried out at University of Illinois, using a VG HB501 STEM (100kV, 0.7nm Probe). Jump ratio images were recorded using Hitachi HD2300 STEM at Pleasanton, CA Demo facility 200kV 60eV Elemental Windows.

3.3.15 Oxidation test

3.3.15.1 Thermogravimetric (TG) analysis

The thermogravimetry tests were conducted using a Cahn TG 131 microbalance, Figure 3.18, with specifications: 10 $\mu\text{g}/^\circ\text{C}$ temperature drift stability, $\pm 3^\circ\text{C}$ temperature repeatability and 1 μg mass sensitivity. TGA allows the determination of onset point of oxidation and the extent of weight gain. Oxidation of C/Cr was assessed dynamically from room temperature by TGA in a linear-temperature-ramp mode (400–1000 $^\circ\text{C}$ at 1 $^\circ\text{C}/\text{min}$) mode. The total duration of the continuous measurements was 10.5 hrs. The gas flow rate in the furnace of the TG was 7.5 ml/min. The substrates used for the TGA test were coated on both sides, including the hole drilled for fixing the sample in the TG furnace, so that the oxidation would only occur in the coating, and the substrate would only become oxidized when the coating failed.

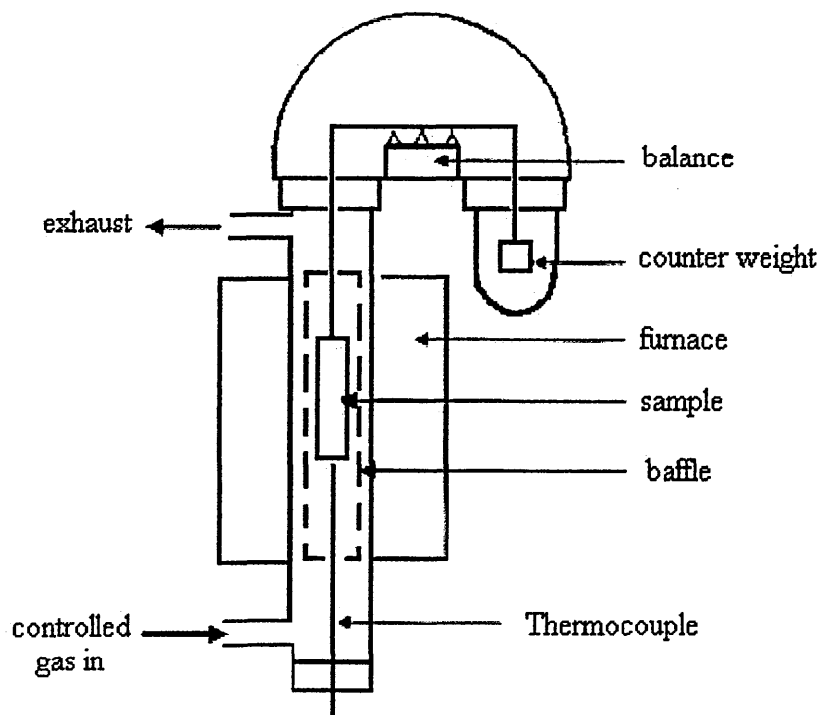


Figure 3.18 Cahn TG 131 microbalance

3.3.15.2 Heat treatment (Annealing)

C/Cr coatings were annealed in isothermal condition at 350 °C, 410 °C, 450 °C and 700 °C (temperatures selected based on the TG traces) for 1 hr each, in a conventional air atmosphere furnace in order to relate the TG traces with phase transformations on the coating surfaces. After heating, the samples were cooled in the furnace to room temperature before being examined using XRD, SEM and Raman spectroscopy.

3.3.16 Corrosion test

The electrolyte used in this study was 0.01% NaCl solution (0.1g NaCl in 1000ml deionised water). Its conductivity $\sim 200 \pm 10 \mu\text{S/cm}$, being similar to that of the conductivity of the tap water ($\sim 196 \pm 10 \mu\text{S/cm}$). The conductivity of the solution was measured using a conductivity meter. The solution was further validated by plotting the output signal (mV) versus the applied current (μA) for both the tap water (as a reference solution) and the 0.01% NaCl solution using the SRET Point-In-Space (PIS) calibration method [157], using the Saturated Calomel Electrode (SCE) as a reference electrode. The distance between the PIS specimen (as a working electrode) and the Pt probe was set at $\sim 100\mu\text{m}$. Current was applied to the PIS specimen by gradually increasing it from

0.1 to 1.0 μA . The output signal (mV) for both testing solutions was shown in Figure 3.19. For both calibration environments, such as tap water and 0.01% NaCl solution, the output signals increased linearly with increasing applied current and were close to each other. Thus, the conductivity of 0.01% NaCl is assumed equivalent to the conductivity of tap water.

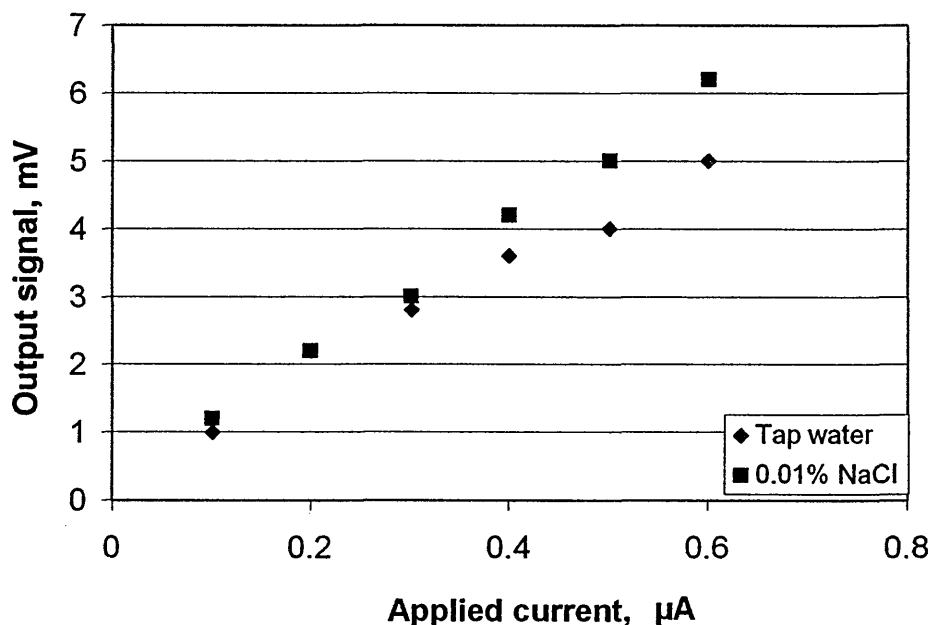


Figure 3.19 PIS calibration output signal in tap water and in 0.01% NaCl solution

3.3.16.1 Potentiodynamic polarisation

Potentiodynamic polarisation tests were conducted using an ACM Gill AC instrument, to measure the corrosion resistance of the coated substrates. The schematic diagram of the experiment setup is shown in Figure 3.20. The apparatus comprises one working electrode, a reference electrode and an auxiliary Platinum (Pt) electrode to supply current (I) to the working electrode (sample). Before testing, the coated sample was masked with a 3:1 mixture of beeswax and resin leaving a circular area of 1 cm diameter on coated surface (exposed area of $\sim 0.7855 \text{ cm}^2$). The test was carried out in a 0.01% NaCl solution. The potential, E of the working electrode was measured with respect to the reference electrode (SCE). The potential was increased gradually and the current density was recorded as the dependent variable. Before each measurement, the sample was cathodically cleaned at a potential of -1500 mV, and then allowed to equilibrate at the rest potential (E_{corr}) or open circuit potential (OCP) for 20 min. The

voltage was scanned from -100 to $+1500$ mV (offset to the rest potential, E_{corr}) and the scan rate was 0.5 mV/s.

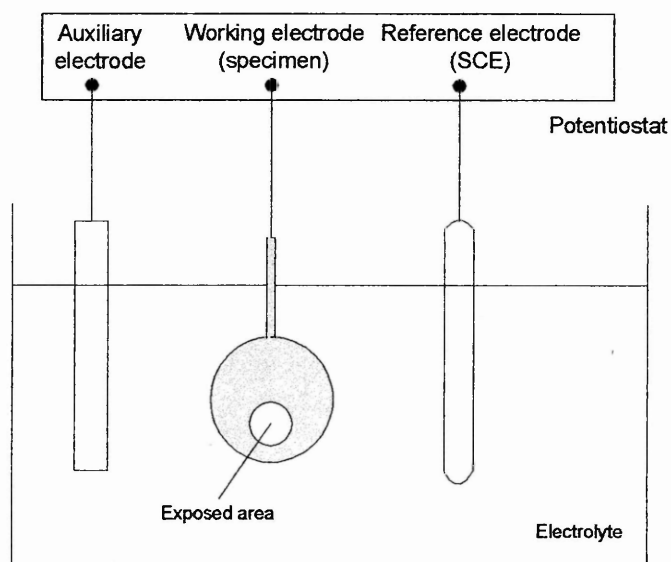


Figure 3.20 Potentiodynamic polarisation test apparatus

3.3.16.2 Tribocorrosion test

The following tribocorrosion tests (Experiment 1 to 5) were carried out using the same experimental conditions and procedures for system calibration as described in Section 3.2.2. Figure 3.21 presents the experimental setup for tribocorrosion tests. The details of the parameters setting for Experiment 1 to Experiment 5 are given in Table 3.4.

- Test 1.* Calibration of the system
- Test 2.* Effects of applied load on E_{corr}
- Test 3.* Effects of applied load on localised corrosion activity
- Test 4.* Effects of loading and unloading on sample recovery (repassivation)
- Test 5.* Effects of coating on tribocorrosion damage in different environments



Figure 3.21 Experimental setup for tribocorrosion test

The results for the tribocorrosion tests are presented in Chapter 4. The damage presented in the graphs being equivalent to the total volume of metal loss (mC/cm^2), and this was calculated based on the area under the anodic portion of the SRET line scan curve using Simpson's rule [158]. The area under the anodic portion of the SRET line scan curve in Figure 4.67 (shaded area) was also determined using Simpson's rule, being equivalent to the total volume of metal loss (mC/cm^2). The unit of the damage, mC/cm^2 is determined as follow:

$$1 \text{ revolution} = 2\pi R$$

R is the radius of sample, which is 7.5 mm

$$\text{Therefore, } 1 \text{ revolution} = 47.1239 \text{ mm}$$

$$= 4.71239 \text{ cm}$$

$$\text{Thus, } 100 \text{ rpm} = 100 * 4.71239 \text{ cm} / 60 \text{ s}$$

$$= 7.854 \text{ cm/s}$$

$$\approx 0.08 \text{ m/s}$$

$$= \text{velocity}$$

$$\text{Time} = \text{displacement} / \text{velocity}$$

$$1 \text{ cm} = 10000 \text{ microns}$$

$$\text{Current, } I \text{ (A)} = \text{charge passed per unit time (= Coulombs)}$$

$$1 \text{ Coulomb} = 1 \text{ A} \cdot \text{s}$$

Hence,

Area under curve of anodic portion of SRET line scan

$$= \text{current density} \cdot \text{time}$$

$$= \text{mA/cm}^2 \cdot \text{time}$$

$$= (\text{mA} \cdot \text{time})/\text{cm}^2$$

$$= \text{mC/cm}^2$$

where time is in seconds

Test	*Sample	Load, N	Loading mode	Test duration	Potential, mV	Environment	Results
1 Calibration of system	SS & C/CrSS	0-6	Increasing	N/A	N/A	Tap water	Output strain via load cell as a function of applied load
2 Effect on E_{corr}	SS	1 and 3	Loading and unloading	Up to 6 hours	E_{corr}	0.01 % NaCl	E_{corr} as a function of applied load and time
3 Effect of applied load	SS	0-4	Increasing	30 s per load	E_{corr}	0.01 % NaCl	SRET current density line scan (real-time tribocorrosion activity), line displacement scan and calculated active anodic area
	C/CrSS	0-6	Increasing and unloading				
4 Effect of loading and unloading	C/CrSS	0.5, 1, 3, 5	Loading and unloading (on same area)	1 hr per load	E_{corr}	0.01 % NaCl	SRET current density line
5 Effect of coating on TC# response in different environments	SS & C/CrSS	1 N	Constant	1 hr	a) N/A	air	Measured worn area, wear coefficient, E_{corr} vs time, SRET current density line scan, and microstructure
					b) E_{corr}	0.01 % NaCl	
					c) Cathodic potential (-500 mV below E_{corr})	0.01 % NaCl	

* 316 stainless steel was also used as the substrate material for C/Cr coated samples: # TC - tribocorrosion

Table 3.4 Test conditions for tribocorrosion tests using the modified SRET

3.3.17 Dry high-speed milling test

Dry high-speed milling tests, shown schematically in Figure 3.22, were carried out using a Mazak FJV-25 high-speed CNC machine to evaluate the actual practical cutting performance of C/Cr coated tools. The cutting tools were commercially available 8 mm cemented carbide ball nose end mills (Hydra-Marwin; produced by submicron grain of WC in cobalt matrix) which were coated with C/Cr coatings deposited at various bias voltages. The tests were performed using the following conditions: cutting speed, $V_c = 603$ m/min (corresponds to a spindle speed of 24000 rpm, calculated using the equation below), feed rate, $V_f = 0.2$ mm/rev, cut depth or axial feed, $A_p = 4$ mm, radial feed, $A_e = 0.5$ mm, using automotive aluminium alloy (Al-Si8Cu3Fe) as the work piece material.

$$\text{Cutting speed, } V_c = \pi dN/1000 \quad (\text{m/min})$$

where, $N = 24000$ rpm

Diameter of tool, $d = 8$ mm

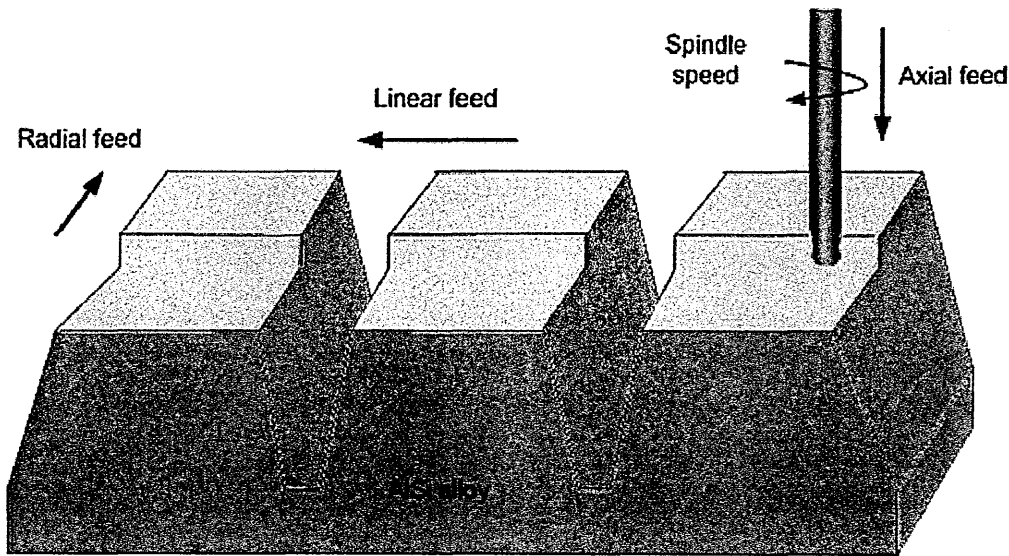


Figure 3.22 Schematic of milling test

Two tests were carried out for uncoated endmills and endmills coated with C/Cr coatings deposited at $U_B = -65$ V, -75 V, -95 V, and -120 V:

Test 1: The samples were tested until the coating failed. This experiment was aimed to determine the flank wear and the total volume of material removed by uncoated and C/Cr coated samples.

Test 2: The samples were used to remove the same volume ($135,720 \text{ mm}^3$, which is *1.5 passes) of material. This experiment was aimed to compare the worn morphology of the flanks and to identify the possible oxides formed on the end mills and the chips of the removed work piece material, against various bias voltages.

The chemical compositions of the work piece material (Al-Si8Cu3Fe) are shown in Table 3.5.

Work piece material (Al-Si8Cu3Fe)
Copper: 3-4 %,
Magnesium: 0.3% Max.
Silicon: 7.5-9.5%
Iron: 1.3% Max.
Manganese: 0.5% Max.
Nickel: 0.5% Max.
Zinc: 3% Max.
Lead: 0.2% Max.
Tin: 0.2% Max.
Titanium: 0.2% Max.
Aluminium: Remainder

Table 3.5 Chemical composition of work piece material

* Each pass is the removal of a layer of material from the work piece (Al-Si8Cu3Fe) which is 4mm thick. However, as the test pieces are tapered towards the top (see Figure 3.22), each pass removes a larger volume of material. Therefore, pass 1 is $88,000 \text{ mm}^3$ and pass 2 is $95,440 \text{ mm}^3$, so each tool has removed $88,000 + (95,440 / 2) = 135,720 \text{ mm}^3$.

CHAPTER 4

Results

This chapter presents the results of C/Cr coatings deposited at various bias voltages between $U_B = -65$ and -550 V. These results include the effects of substrate bias voltage on the plasma, the deposition parameters (temperature and bias current) during coating deposition, the microstructure and the functional properties of C/Cr coatings. The coatings were grown at $U_B = -65, -75, -95, -120, -350, -450$, and -550 V, which were equivalent to the ion energy of 65, 75, 95, 120, 350, 450 and 550 eV respectively. Higher bias voltages of $U_B = -450$ and -550 V were studied only to obtain a better understanding of the microstructure and the growth mechanism of C/Cr coatings. Therefore, only selected characterisation techniques were used to analyse these high bias coatings in order to support the interpretation and discussion of the results presented in Chapter 5.

4.1 Plasma characteristics during C/Cr deposition process

The characteristics of the plasma during C/Cr coating deposition was investigated as a function of the bias voltage, to gain a better understanding of the effect of ion bombardment on the properties and the structure of coatings. The results presented in Figure 4.1 show that the plasma density was influenced strongly by the unbalancing coil current in the system [111]. The ion saturation current, J_{sat} , at the position of the substrates, increased by an order of magnitude, from 0.1 to 1.3 mAcm⁻², as the coil current increased from 0 to 6 A. During coating deposition, a coil current of 5 A was used in order to increase the ionisation. For the deposition conditions, where a current of 5 A was used on all four unbalancing coils, J_{sat} was measured to be about 1.2 mAcm⁻² for bias voltage between $U_B = -65$ and -95 V, thus the corresponding average ion flux J_i was thus 5.6×10^{15} ions cm⁻² s⁻¹.

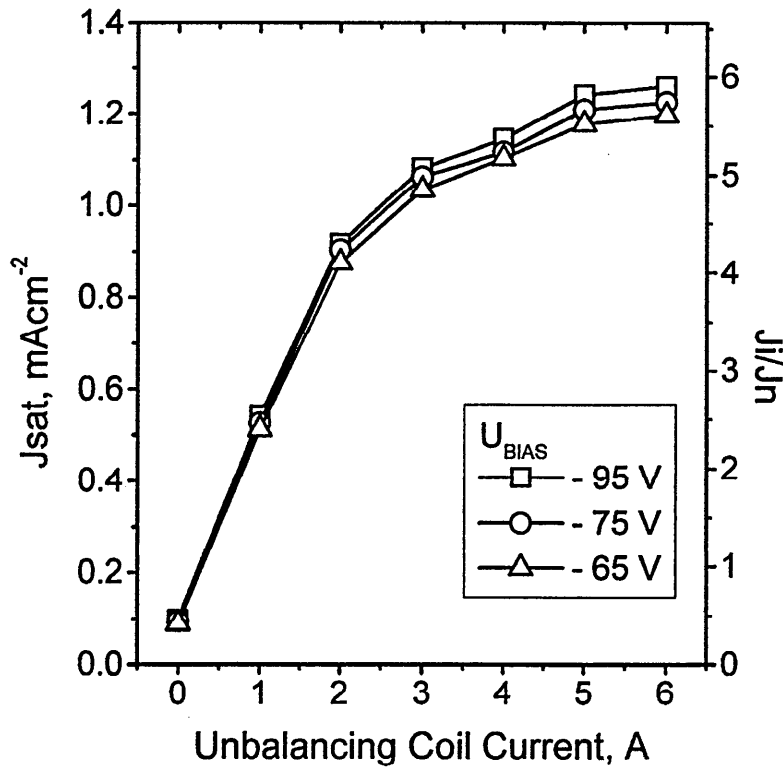


Figure 4.1 Influence of unbalancing coil current and substrate bias on the ion saturation current and ion-to-neutral ratio during film growth

Figure 4.2 shows that as the bias voltage increased from -65 V to -450 V, the ion saturation current density increased slightly from 1.2 mAcm⁻² to 1.6 mAcm⁻² (so, J_i varied from 5.6×10^{15} to 7.5×10^{15} ions cm⁻² s⁻¹), which was a factor of 1.3 [159]. This increase may be attributed to additional ionization by secondary electrons caused by the substrate bias. The effect on the ion-to-neutral ratio J_i/J_n was a small increase from 5.2 to 6.9 (where J_n was calculated using a constant $N_a = 1.55 \times 10^{19}$ atoms cm⁻²). The most significant influence was on the energy per neutral atom $W = J_i/J_n E_i$, which increased by a factor of approximately 9 from $W = 338$ eV atom⁻¹ to 3150 eV atom⁻¹, for $E_i = 65$ to 450 eV respectively.

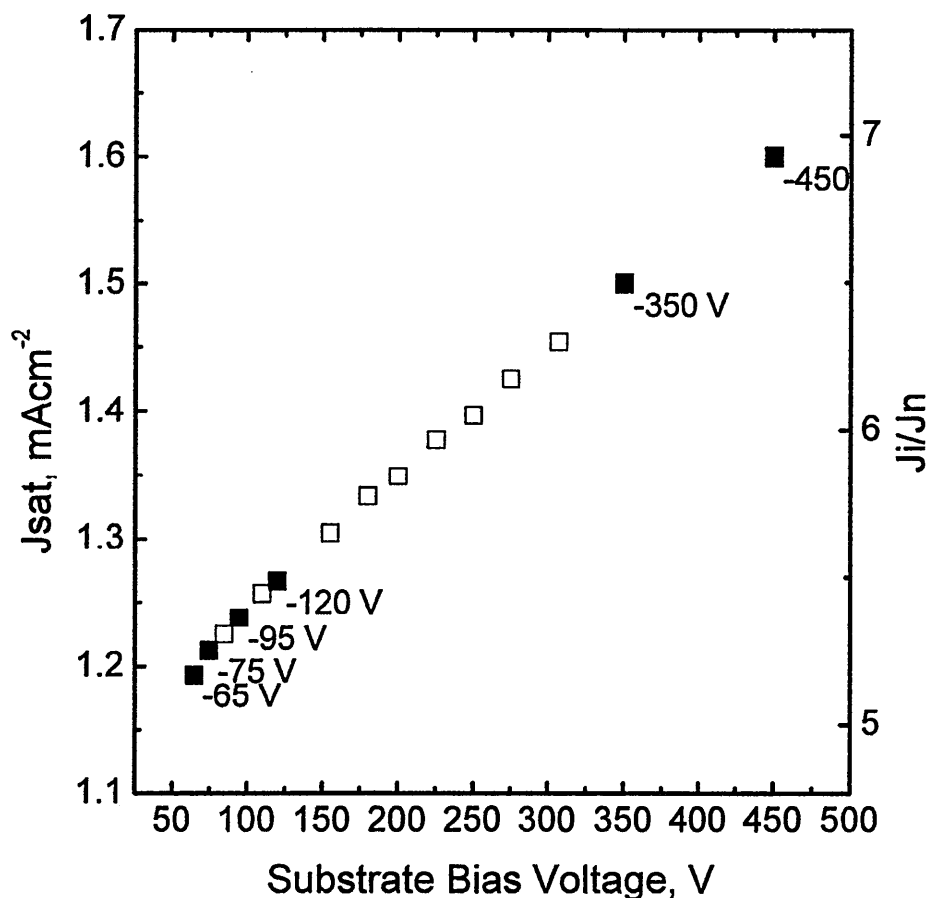


Figure 4.2 Ion saturation current and ion-to-neutral ratio as a function of the substrate bias voltage. The dark squares represent conditions at which C-Cr films were deposited

4.2 Influence of bias voltage on the deposition parameters

The variation in the bias voltage during C/Cr coating deposition was found to influence the following parameters:

Substrate temperature

The temperature during C/Cr coating deposition was set to 260°C before changing the applied bias voltages. The temperature in the chamber was monitored during deposition at different bias voltages between $U_B = -65$ V and -550 V. During bombardment with increasing ion energy from 65 eV to 550 eV, the substrate temperature rose from 260 to 530°C. Figure 4.3 shows the variation in temperature induced by ion bombardment as a function of the deposition time, for bias voltages

applied between $U_B = -65$ V and -550 V. From the results obtained, low bias voltages of $U_B = -65$ and -75 V show negligible effect on the substrate temperature. However, at $U_B = -95$ V, the substrate temperature was observed to increase slightly to 270°C , and at a higher bias voltage of $U_B = -550$ V the temperature reached 530°C . The increase in the substrate temperature was due to heating as a result of bombardment by energetic ions or neutrals, which transfer their kinetic energy to thermal energy in the bombarded material. The effect of ion bombardment on the substrate temperature was clearly seen during deposition of coating in one deposition run by applying alternatively, (in four cycles) low ($U_B = -75$ V) and high ($U_B = -350$ V) bias voltages to the substrate. Each individual cycle was conducted for 30 min. In this experiment, the substrate temperature stayed constant at $\sim 265^\circ\text{C}$ for the first 30 min, and gradually rose to 410°C at $U_B = -350$ V, then gradually decreased to $\sim 285^\circ\text{C}$ when switching the bias voltage back to $U_B = -75$ V. This process was repeated for the rest of the cycles.

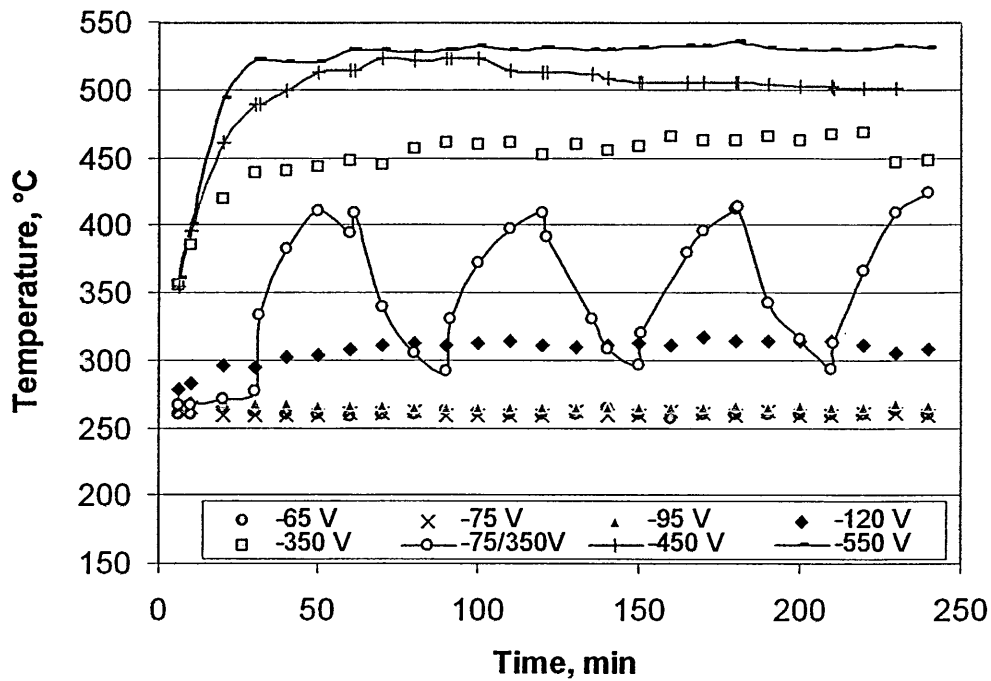


Figure 4.3 Influence of bias voltage on the substrate temperature induced by ion bombardment during coating deposition

Bias current

Bias current is the current induced on the substrate when a bias voltage was applied to the substrate. Figure 4.4 shows the effects of bias voltage on the bias current.

When the bias voltage was increased from $U_B = -65$ to -550 V, the bias current increased from 5.5 to 8.8 A. The bias current variation between 5.5 and 7.8 A may be equivalent to the current density change between 1.2 and 1.6 mAcm^{-2} (Figure 4.2) for bias voltage between $U_B = -65$ and -450 V. This means that the number of bombarding ions increased with the ion energy which was controlled by the bias voltage, this is in agreement with the increased ion-to-neutral ratio as discussed in Section 4.1. A similar effect has been observed by Hurkmans [32] during CrN_x coating deposition where the bias current was found to increase from 0.5 to 1.15 A, representing an increase in bias current density of 1.5 to 3.6 mAcm^{-2} , when the bias voltage was increased from -25 to -200 V.

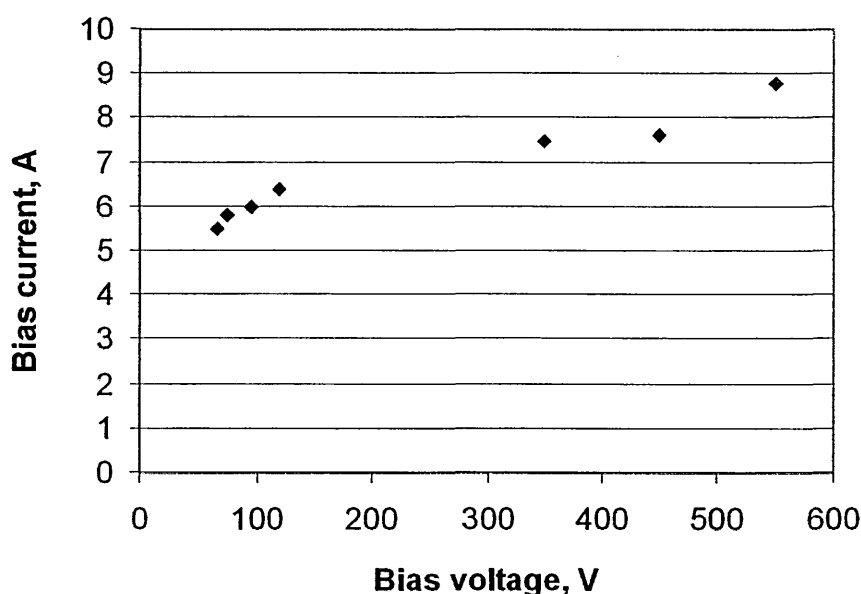


Figure 4.4 Bias current as a function of the bias voltage

4.3 Compositional analysis

The quantitative composition of the deposited films is often of crucial importance for the quality of the coatings. The composition of C/Cr coatings deposited at various bias voltages was determined using secondary neutral mass spectrometry (SNMS) and Rutherford backscattering spectroscopy (RBS).

4.3.1 Secondary Neutral Mass Spectrometry (SNMS)

The SNMS depth profiling through across the coatings to the substrate, for coatings deposited at different bias voltages are shown in Figure 4.5. The results show

that, for the applied bias voltages between $U_B = -65$ and -120 V (see Figure 4.5(a) for the result of $U_B = -75$ V sample, which is also representative for $U_B = -65$ and -120 V samples), the concentration of carbon and chromium in the films remained constant at ~ 68 at.% and ~ 32 at.% respectively. However, at $U_B = -350$ V (Figure 4.5(b)), the carbon content decreased by ~ 15 at.%, which gave a film concentration of 53 at.% C and 47 at.% Cr, resulting in a C to Cr ratio of nearly 1:1, this suggests the formation of metal-carbides. The decrease in the carbon content could be due to preferential resputtering (a process where the growing film is sputter-etched by energetic particles) of species from the growing film surface, especially the weakly bonded carbon adatoms, caused by the high energy ion bombardment [160]. This is typical of the weak binding characteristics of Cr with carbon due to the fact that carbon has a small single bond radius of 0.077 nm as compared to 0.125 nm for a Cr atom. Preferential sputtering may also occur depending on the bond strength between the different bombarding species, where the bond strength is lower for migrating adatoms [161]. This is why the lighter carbon is preferentially resputtered because of its lower bond strength compared to the heavier chromium. A similar effect was reported for (Ti,Al)N coatings, where the aluminium concentration in the coatings was found to decrease with increasing bias from 0 to -900 V due to resputtering of the aluminium [162]. The effect of ion bombardment on the composition of the growing film was clearly seen on coatings deposited at alternating low ($U_B = -75$ V) and high ($U_B = -350$ V) bias voltages ($U_B = -75/350$ V sample), as shown in Figure 4.5(c). From the results obtained, on average, the $U_B = -75$ V layers have an almost constant concentration of 58 at.% C and 38 at.% Cr, and the $U_B = -350$ V layers contained approximately 53 at.% C and 42 at.% Cr. As the bias voltage was increased further to $U_B = -450$ V, the C content in the film was ~ 40 at.% near the surface but rose to 50% near the film/substrate interface, see Figure 4.5(d).

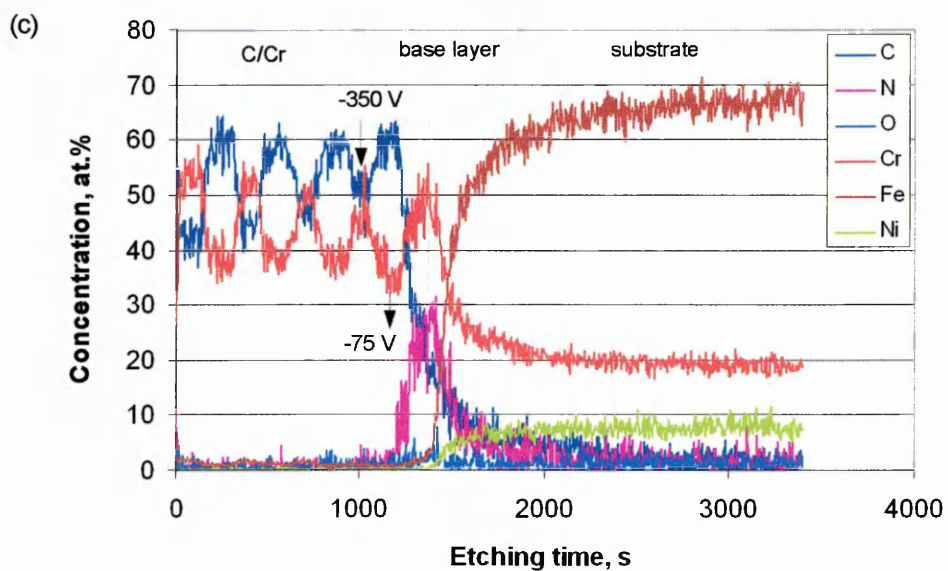
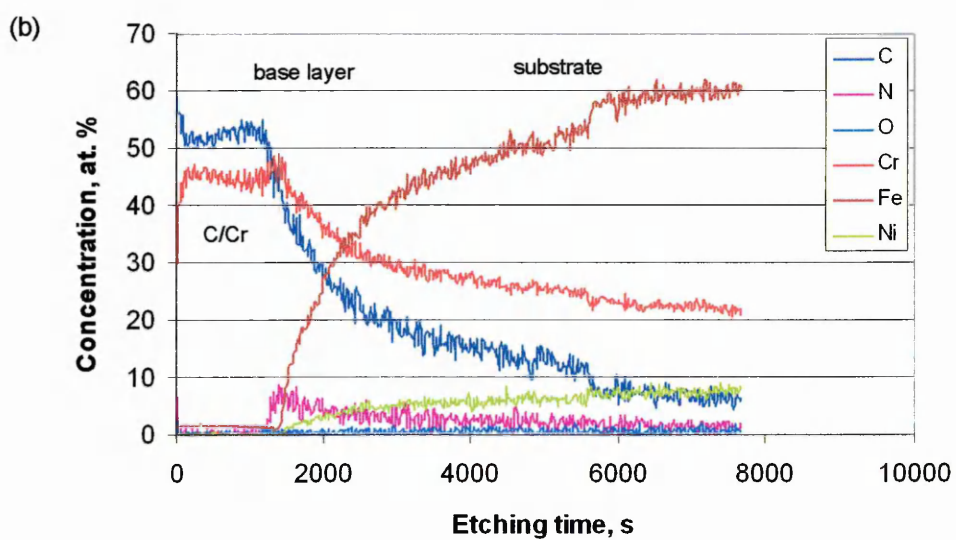
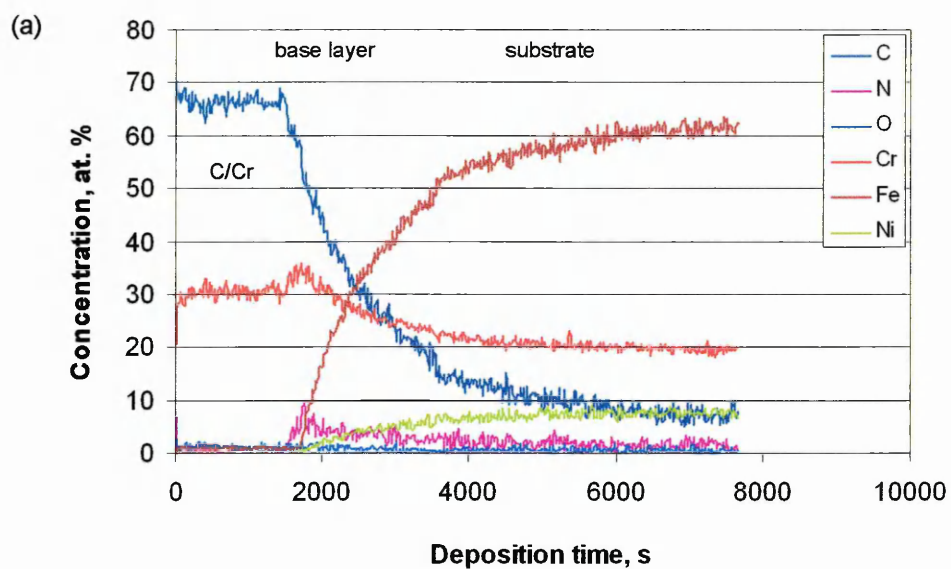


Figure 4.5 continues on next page

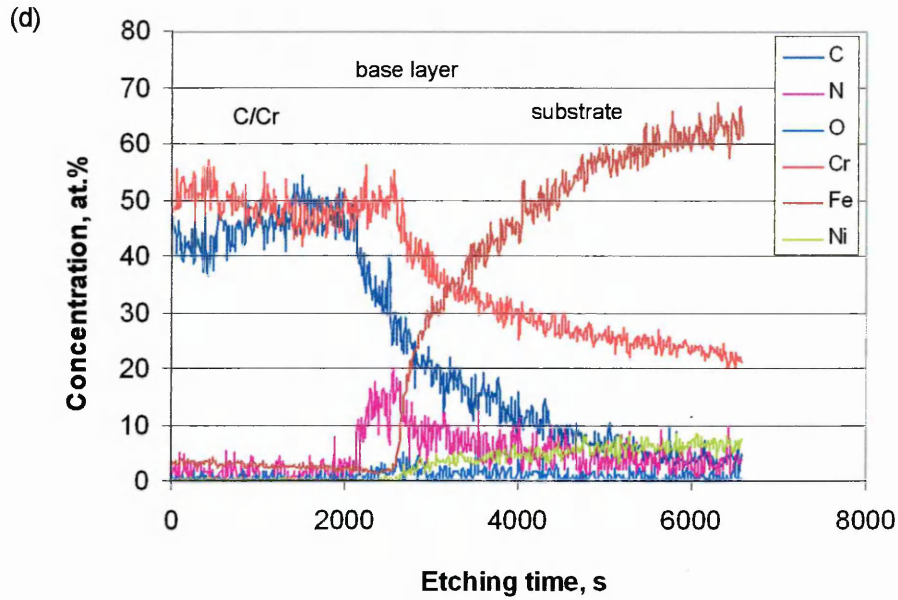


Figure 4.5 Compositional depth profiling of (a) $U_B = -75$, (b) $U_B = -350$ V, (c) $U_B = -75/350$ V, (d) $U_B = -450$ V samples

4.3.2 Rutherford backscattering spectroscopy (RBS)

The composition of the coating x ($C_xCr_{(1-x)}$) and the coating areal density N_a were determined by Rutherford backscattering spectroscopy (RBS) [111]. Figure 4.6 shows the RBS spectrum for a C/Cr coating. The blue line is the fitting result from the metal peaks because scattering from light elements, such as C and N gives a signal superimposed on Rutherford scattering signal. The composition of the films deposited between $U_B = -65$ V and -120 V was determined to be $C_{0.7}Cr_{0.3}$ and $C_{0.5}Cr_{0.5}$ for the $U_B = -350$ V sample (see Table 4.1). The C content is strongly affected by the ion energy. C seems to be resputtered as the ion energy was increased from 65 eV to 350 eV, where the incorporation of C into the C/Cr coating reduced by about 20 at. %.

Table 4.1 shows the coating areal density, N_a and the estimated film bulk density as a function of the bias voltage. The areal density, N_a decreased from 1.55×10^{19} to 1.03×10^{19} atoms cm^{-2} with increasing bias voltage from $U_B = -65$ to -350 V, due to increased resputtering. The film bulk density was estimated by dividing N_a by the coating thickness.

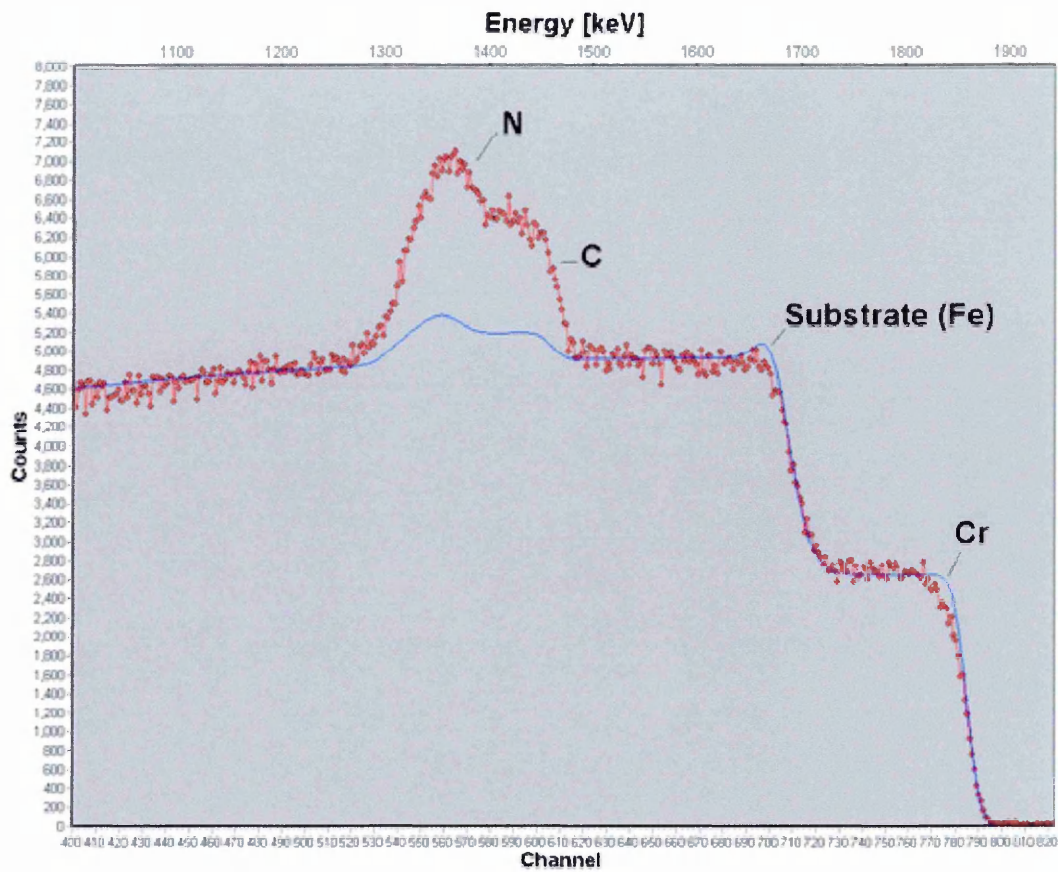


Figure 4.6 RBS spectrum of C/Cr coating

Bias voltage, V	at.% C, at.% Cr	*Coating thickness, μm	Coating area density (N_a), $\times 10^{19} \text{ atomscm}^{-2}$	Film bulk density, $\times 10^{22} \text{ atomscm}^{-3}$
-65	70%, 30%	1.96	1.55	7.91
-75	70%, 30%	1.82	1.32	7.25
-120	70%, 30%	1.53	1.18	7.71
-350	50%, 50%	1.48	1.03	6.96

* refer Figure 4.12

Table 4.1 Coating area density and film bulk density against the bias voltage

4.4 Mechanical and tribological properties

Table 4.2 summarises the mechanical and the tribological properties of C/Cr coatings deposited at various bias voltages, which are further discussed in the following

sections. The results showed that the films properties are strongly dependent on the substrate bias voltage.

Bias voltage, V	μ	L_c , N	HF	Thickness, μm	Hardness, GPa	Young's modulus E, GPa	Residual stress, GPa
-65	0.22	48	2	~1.96	6.80	138	0.62
-75	0.21	75	1	~1.82	9.40	155	1.14
-95	0.16	75	1	~1.78	15.50	216	1.70
-120	0.19	50	2	~1.53	16.50	245	2.81
-350	0.31	20	6	~1.48	25.10	285	2.00

Table 4.2 Summary of the properties of C/Cr coatings

4.4.1 Adhesion scratch and Rockwell-C indentation

The adhesion of C/Cr coatings was determined using scratch adhesion and Rockwell-C indentation tests, which were evaluated by the critical load and categorised by the indentation grades (HF1-HF6) respectively. Figure 4.7 shows the critical load as a function of the bias voltage. The critical load, L_c increased from 48 N to 75 N as the bias voltage was increased from $U_B = -65$ to -95 V. Further increase in the bias voltage to $U_B = -350$ V led to a reduction in the L_c to 20 N. Coating deposited at an alternating bias voltage of $U_B = -75$ V and -350 V ($-75/350$ V sample) shows an improved adhesion compared to the $U_B = -350$ V sample. For all the applied bias voltages, no formation of microflakes and spalling of the coatings both inside and at the rim of the scratch respectively, have been observed particularly in the lower bias voltage range. This demonstrated excellent adhesion between the coating and the substrate. Figure 4.8 presents the optical images of the scratch (the black arrow shows the direction of scratching) and the Rockwell-C indent for coatings deposited at various bias voltages. The grade of the indents as a function of the bias voltage is shown in Table 4.2. As mentioned in Chapter 3, the acceptable adhesion strength of coating is graded between HF1 and HF4, and those grades greater than HF5 are classed as poor adhesion.

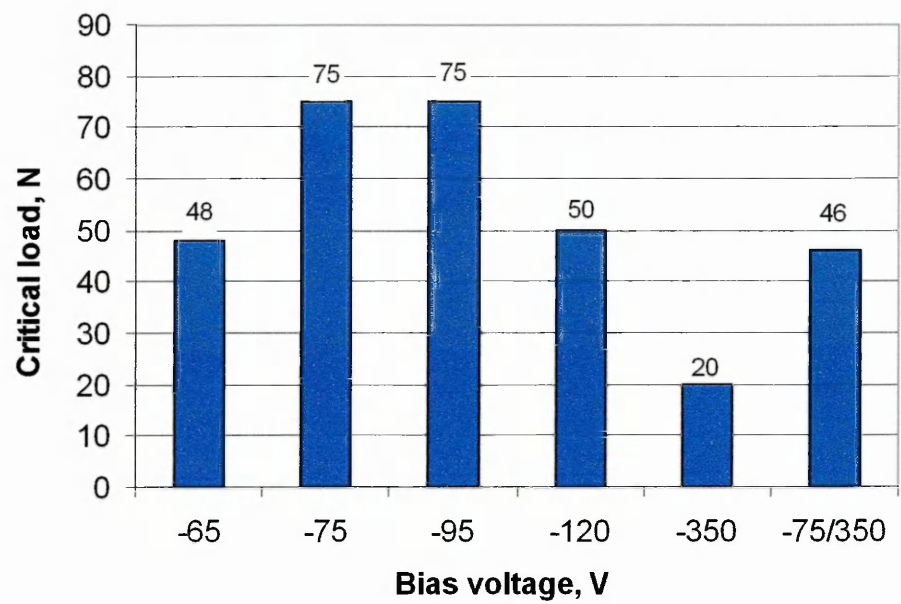


Figure 4.7 Critical load as a function of bias voltage

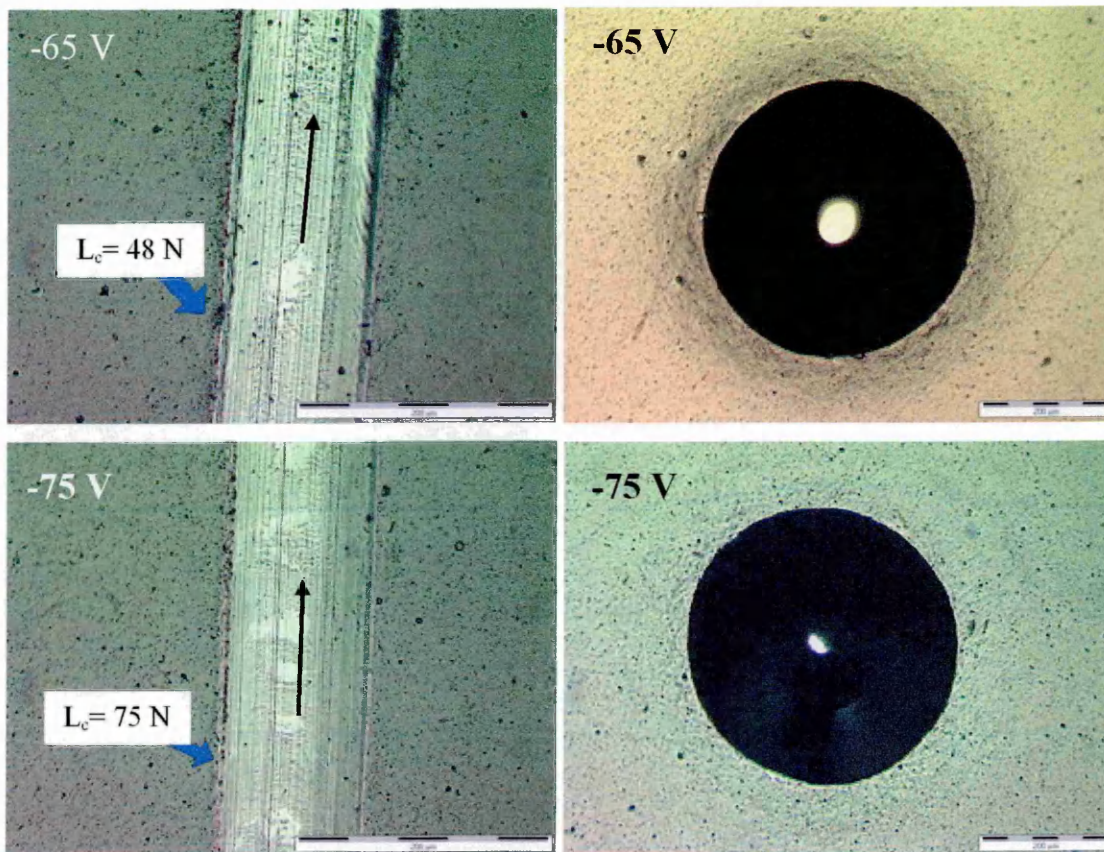


Figure 4.8 continues on the next page

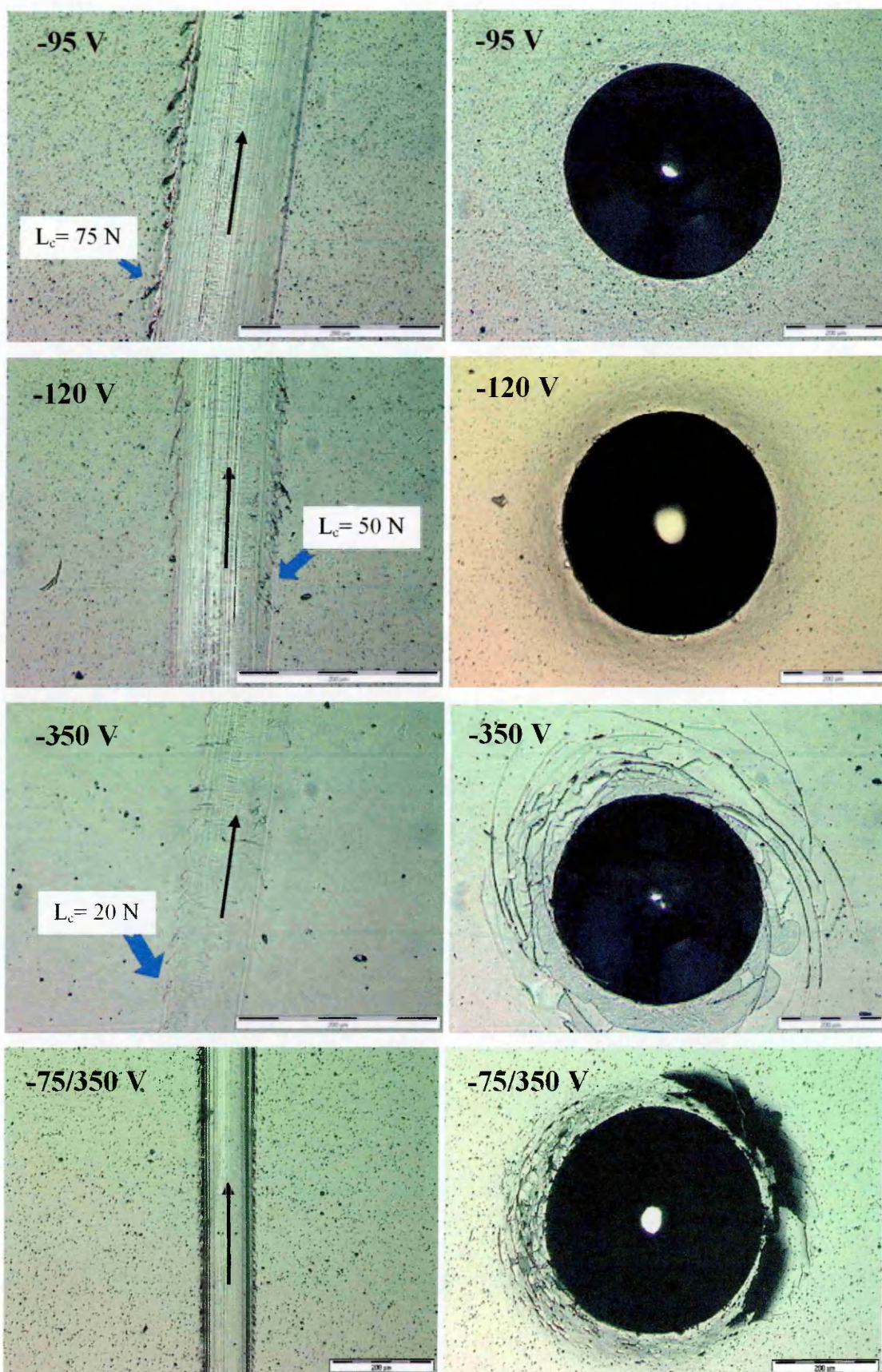


Figure 4.8 (left) Adhesion scratch and (right) Rockwell-C indent for films deposited at various bias voltages (scale bar = 200 μm)

4.4.2 Tribological test

A tribological test was carried out to determine the friction coefficient (resistance to sliding) and sliding wear resistance of C/Cr coatings as a function of the bias voltage. The tests were conducted using a pin-on disc tribometer as described in Chapter 3.

(a) Friction coefficient

Figure 4.9 shows the coefficient of friction of coatings deposited at a bias voltage between $U_B = -65$ and -350 V. The friction coefficient, μ , decreased from 0.22 to 0.16 when U_B was increased from -65 to -95 V. However, further increase in the bias voltage to $U_B = -350$ V led to an increase in the friction coefficient to 0.31. Figure 4.10 shows the friction curves as a function of the sliding distance for coatings deposited at various bias voltages. The running-in period (an instantaneous increase in the friction coefficient) was observed between the sliding distance of 0 and 40 m for all the applied bias voltages. Coatings deposited at $U_B = -95$ and -120 V possessed a smoother friction curve than coatings deposited at lower and higher bias voltages. The friction curve of the $-75/350$ V sample shows a strong dependence on the applied bias voltages, where the repetitive high and low friction coefficient resulted as the ball reached the $U_B = -350$ V and $U_B = -75$ V layers, respectively. The sudden increase in the friction coefficient after sliding distance of about 250 m, 520 m, and 750 m as seen in Figure 4.10 indicated that the ball has reached the $U_B = -350$ V layer.

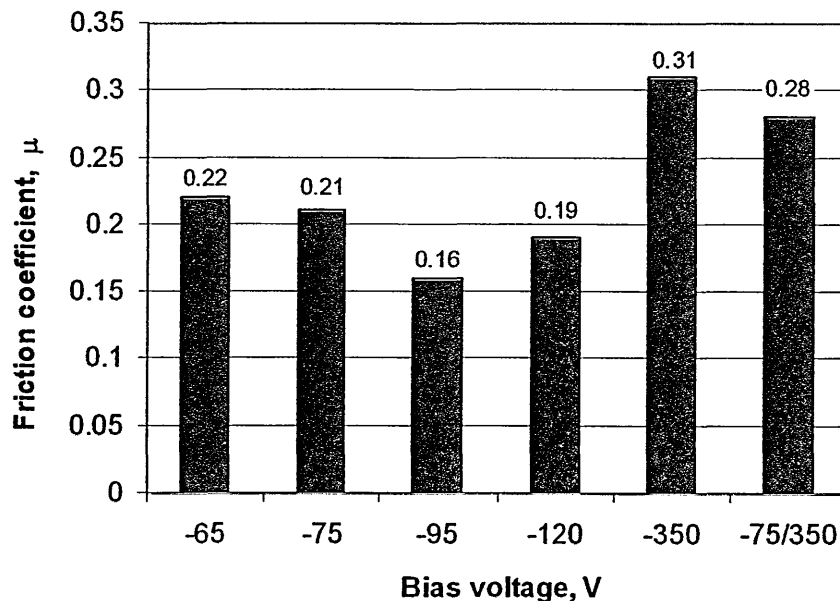


Figure 4.9 Average friction coefficient as a function of the bias voltage

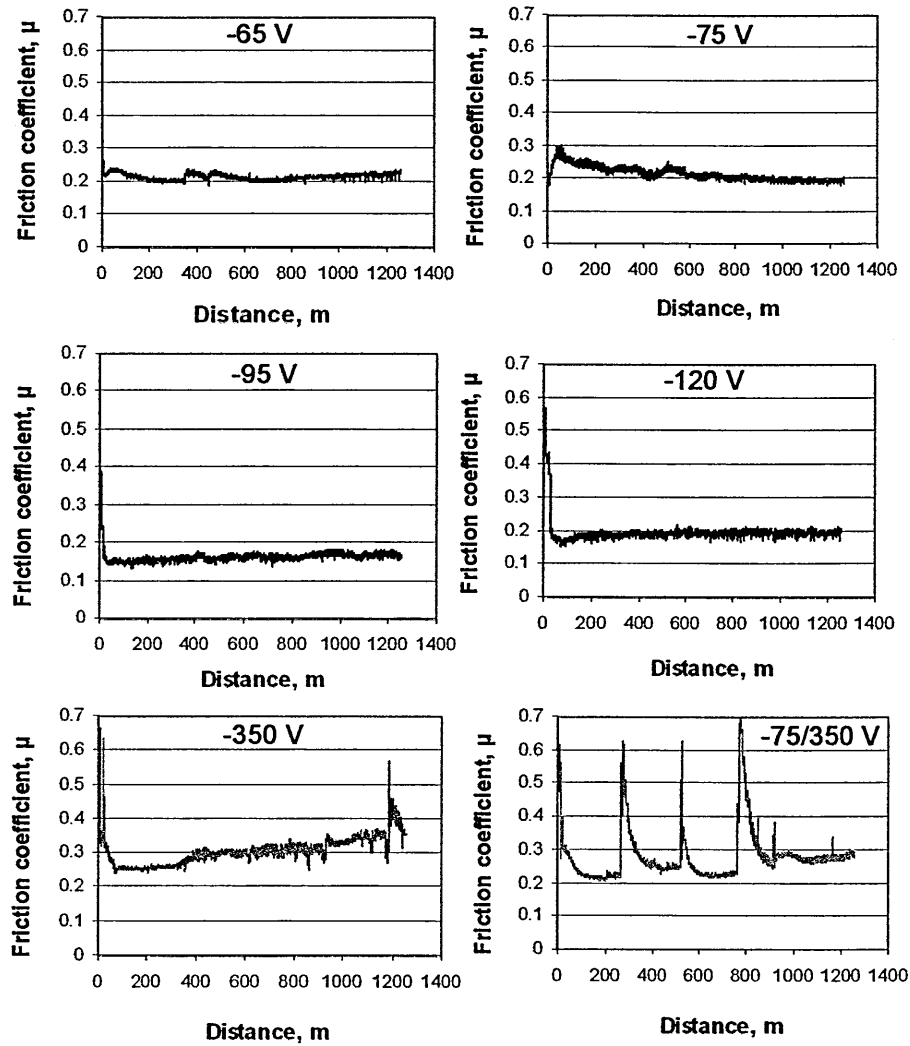


Figure 4.10 Friction curves of C/Cr coatings as a function of the sliding distance and the bias voltage

(b) Sliding wear coefficient

The wear resistances of C/Cr coatings were evaluated from their sliding wear coefficients determined by Archard's equation as shown in Chapter 3. Figure 4.11(a) and (b) show the sliding wear coefficient of C/Cr coatings and their corresponding wear track profiles after pin-on-disc tests, respectively. The wear resistances of the coatings correlate well with their friction performance i.e. films with higher friction coefficient suffer higher wear rates. As the bias voltage increased from $U_B = -65$ to -120 V, the coating wear coefficient, K_c decreased from $\sim 2.9 \times 10^{-16} \text{ m}^3\text{N}^{-1}\text{m}^{-1}$ to $\sim 6.3 \times 10^{-17} \text{ m}^3\text{N}^{-1}\text{m}^{-1}$. Further increases in the bias voltage to $U_B = -350$ V increased the sliding wear coefficient, K_c to $\sim 3 \times 10^{-16} \text{ m}^3\text{N}^{-1}\text{m}^{-1}$. Figure 4.11(b) shows that coatings deposited at

$U_B = -95$ and -120 V show much smaller and shallower wear tracks, thus correlating with the observed lowest wear coefficient (Figure 4.11(a)).

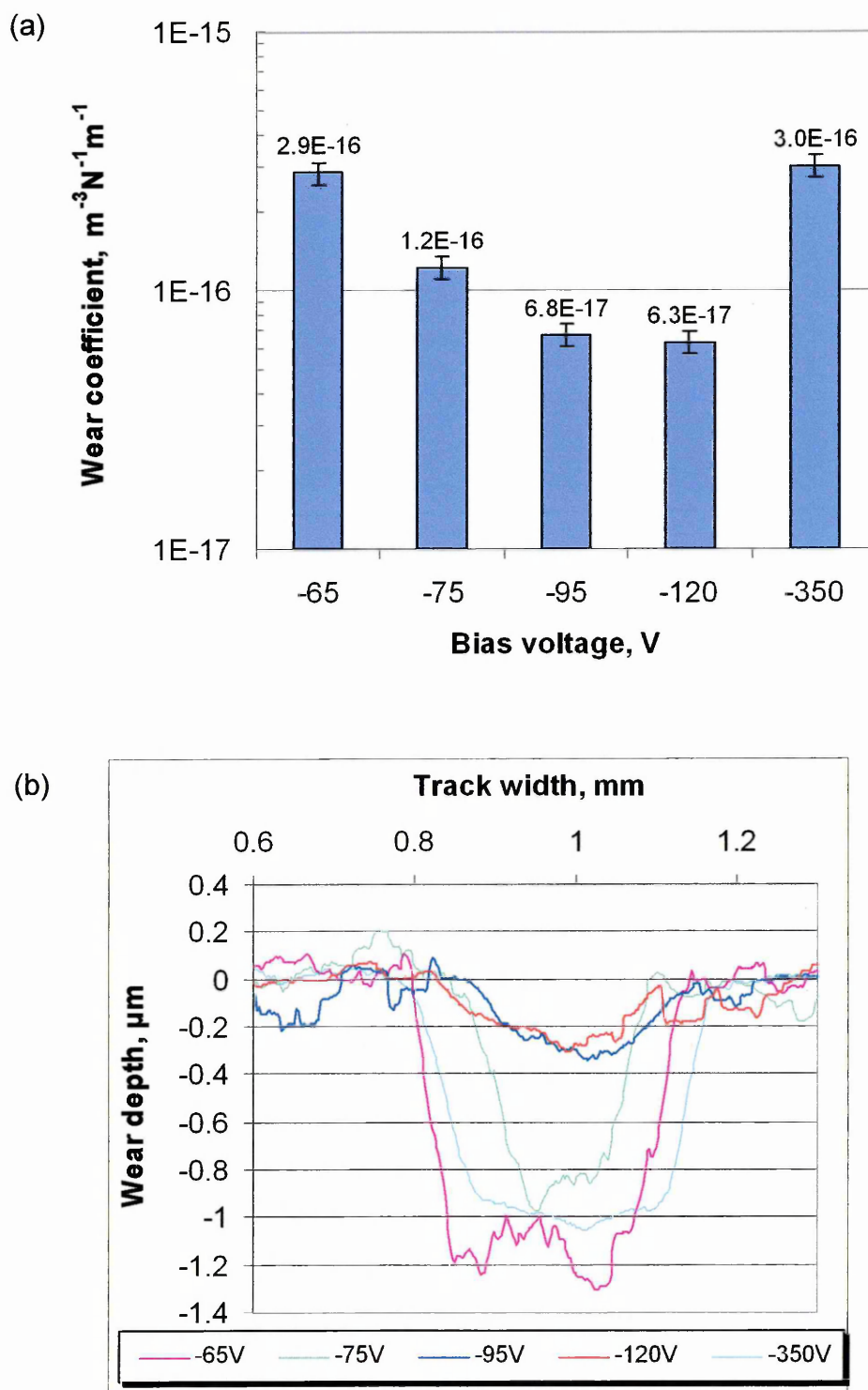


Figure 4.11 (a) Sliding wear coefficient as a function of the bias voltage, and (b) wear track profiles after pin-on-disc tests

4.4.3 Ball-cratering thickness measurement

The thickness of coating was calculated from the inner and the outer diameters of the calotte using the formula shown in Chapter 3. Figure 4.12 shows the coating thickness plotted as a function of the bias voltage. The thickness of C/Cr coatings decreases from 1.96 μm to 1.48 μm with increasing bias voltage from $U_B = -65$ to -350 V. This was due to increased resputtering activity of the growing film species resulting from high ion bombardment that effectively slows down the film growth rate [163]. Figure 4.13 shows the optical images of the wear craters (calottes used for measuring thickness) generated after ball cratering tests, for samples prepared at various bias voltages. Apart from the identified inner and outer diameters of the craters used for thickness measurements, two features can be observed in Figure 4.13. First, the interface between the substrate and the coating showed no sign of delamination which confirmed the effectiveness of the ion assistance process in promoting good adhesion. Secondly, the coating around the outer diameter of the crater seems to wear off. This is particular noticeable for the coating deposited at $U_B = -350$ V. This may indicate poor adhesion of the film deposited at $U_B = -350$ V and the result is in good agreement with the adhesion test results.

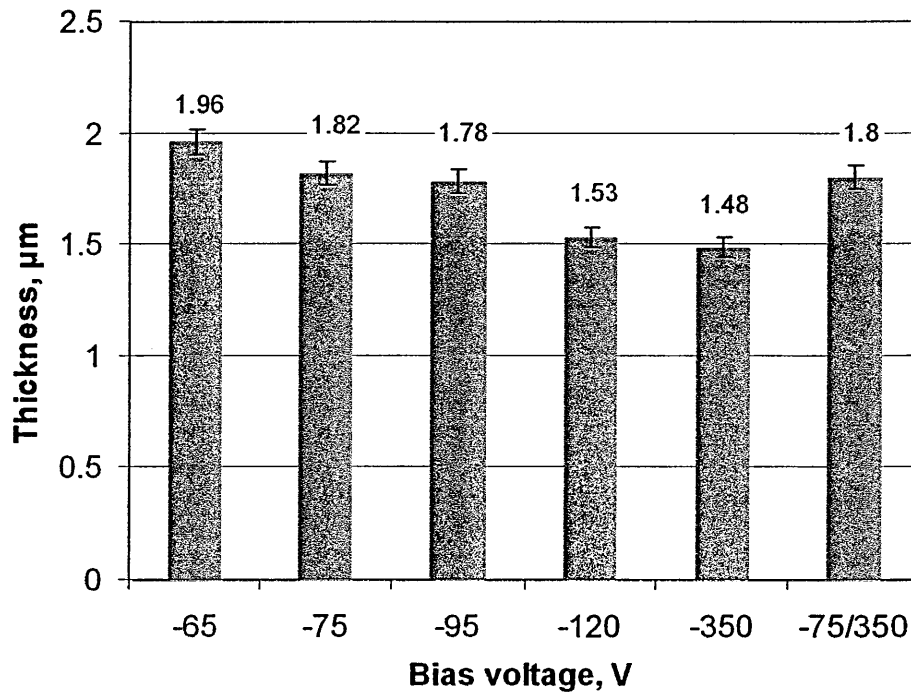


Figure 4.12 Coating thickness as a function of bias voltage

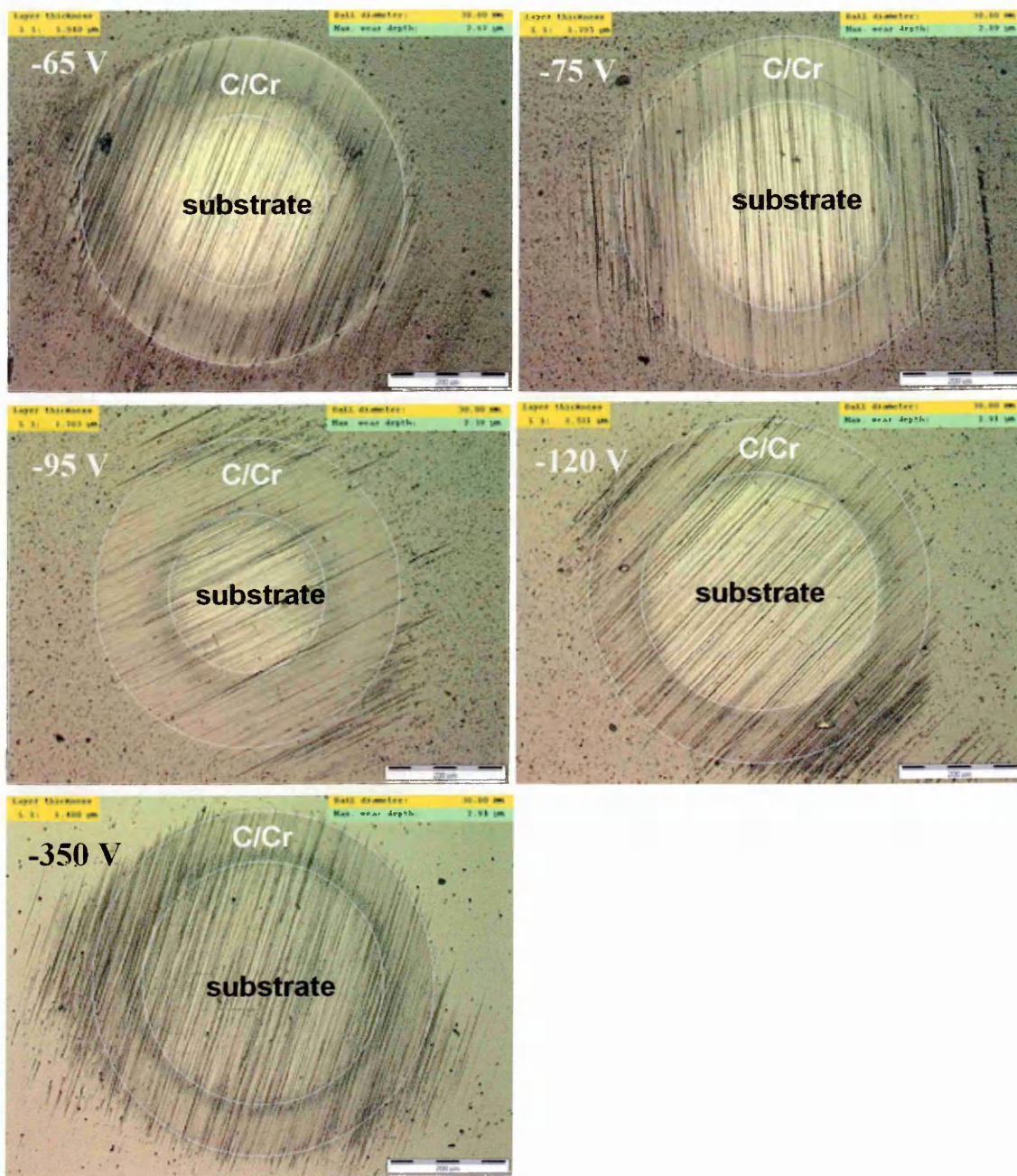


Figure 4.13 Optical images of craters used for thickness measurement as a function of the bias voltage (scale bar = 200 μm)

4.4.4 Nano-hardness test

The hardness and the Young's modulus of C/Cr coatings deposited at various bias voltages are shown in Figure 4.14. With increasing bias voltage from $U_B = -65$ V to -350 V, the hardness increased from 6.8 to 25.1 GPa, and the Young's modulus (E) increased from 138 to 285 GPa. Further increased in the bias voltage to $U_B = -550$ V resulted in a slight decrease in both the hardness and the Young's modulus to 21.9 GPa

and 272 GPa, respectively. The values and the trend of hardness as a function of the bias voltage obtained in this experiment are comparable with the results for magnetron-sputtered Cr-carbon composite coatings [30, 121] and metal-free a-C coatings [164], which were reported as being between 10 GPa and 22 GPa depending on the applied bias voltages (-50 to -200 V). The increase in the hardness with increasing bias voltage to $U_B = -350$ V may be attributed to the formation of a chromium carbide phase as suggested by the SNMS compositional analysis. The reduction in the hardness at $U_B = -450$ V and $U_B = -550$ V could be attributed to the annealing and softening of the structure at the high substrate temperature (see Section 4.2 for the temperature changes induced by ion bombardment) caused by ion bombardment. Some reports suggested that the reduction in hardness at high bias voltage may result from the reduction in the sp^3 fraction in the coating, for example the formation of ta-C:H [6] and a-C films [164]. This explanation can not be applied to these C/Cr coatings because of its graphitic nature.

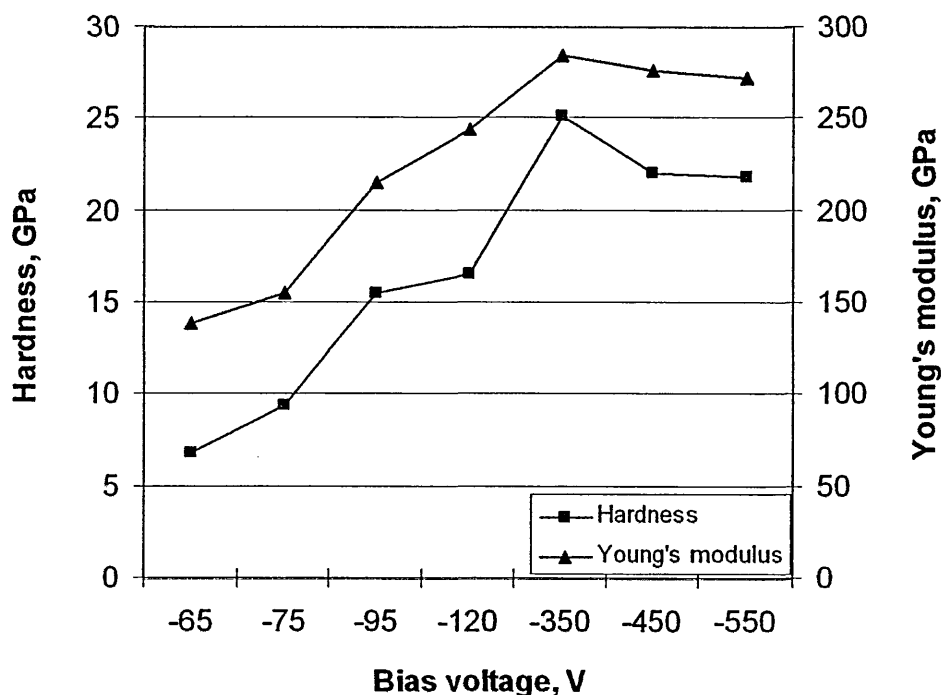


Figure 4.14 Hardness and Young's modulus of C/Cr coatings as a function of bias voltage

4.4.5 Stress measurement

The residual stress generated during coating deposition plays a crucial role in determining the adhesion and the properties of coating. Figure 4.15 shows the effect of

bias voltage on coating compressive stress. The stress increased from 0.62 to 2.81 GPa with increasing bias voltage from $U_B = -65$ to -120 V. As the bias voltage was further increased to $U_B = -350$ V, the stress in the coating reduced to 2 GPa. The $U_B = -75/350$ V sample has a compressive stress between that of $U_B = -75$ V and -350 V samples. The stress values shown in Figure 4.15 are in good agreement with values reported for other carbon-based coatings [165-166]. The decrease in the compressive stress at $U_B = -350$ V could be due to thermal relaxation of the structure and enhancement of the adatom mobility which contributes to the relaxation of the compressive stress in the film [165]. This will be discussed in Chapter 5.

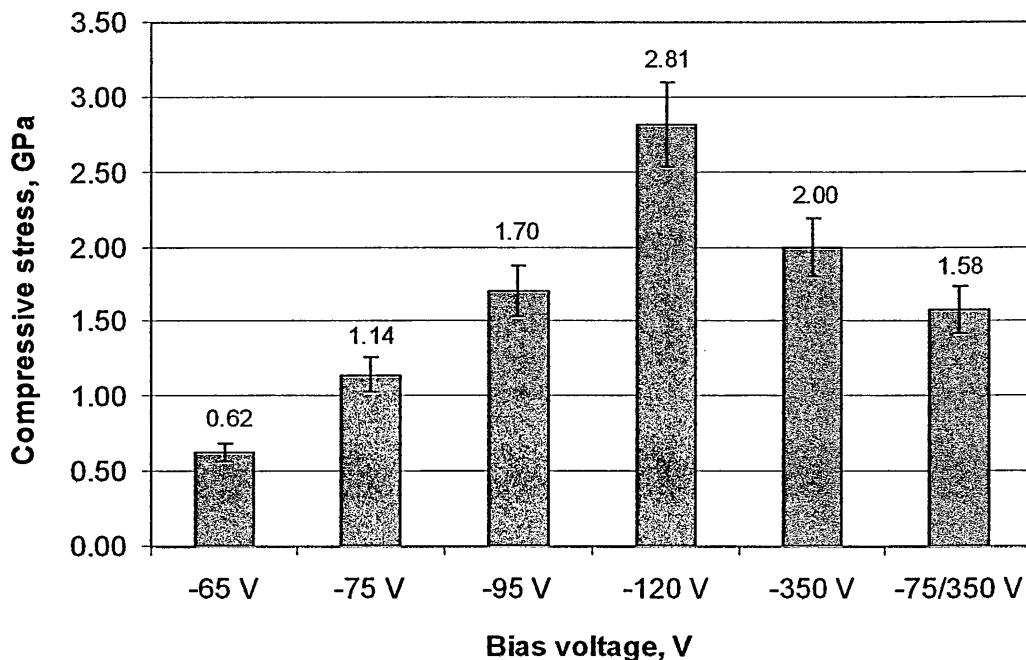


Figure 4.15 Compressive stress of C/Cr coatings as a function of the bias voltage

4.5 Structure and microstructure analyses

4.5.1 X-ray diffraction (XRD)

The structure of C/Cr coatings was investigated using Bragg-Brentano ($\theta/2\theta$) and glancing angle X-ray diffraction (XRD) analysis. The results are shown in Figure 4.16, plotted against various bias voltages. It was observed that the X-ray diffraction patterns of coatings deposited between $U_B = -65$ and -120 V were identical. Figure 4.16(a) is the $\theta/2\theta$ X-ray diffraction patterns of the specimens prepared at various bias voltages, showing the presence of (111), (200), and (220) peaks from the CrN base layer

and reflections from the substrate. It was noted for coatings deposited at $U_B = -350$ V and $U_B = -550$ V, that an additional peak of (011) Cr_3C_2 was present and the intensity of the (220) CrN peak increased substantially and was slightly shifted to a higher angle compared to the coatings deposited at lower bias voltages. To obtain the phases present in the coating only, and to reduce the signal from the substrate, a glancing angle scan was carried out. This is shown in Figure 4.16(b). The absence of the crystalline reflections and the broad diffuse peaks indicates that the film microstructure is essentially amorphous. For U_B between -65 V and -120 V, the diffuse peaks appear at 2θ values of $\sim 40^\circ$ and $\sim 80^\circ$ which correspond to the positions of the (110) and (211) reflections, respectively, from metallic chromium. In the conditions of more intensive ion irradiation ($U_B = -350$ to -550 V), the structure becomes more crystalline. A broad diffraction peak of the orthorhombic Cr_3C_2 phase can already be observed at about 32° , which corresponds to the (011) reflection. This tendency is even more pronounced with the $U_B = -550$ V sample, where clear separation between (011), (111) reflections of Cr_3C_2 and the (101) reflection of Cr_7C_3 can be detected. As no other peaks corresponding to Cr_3C_2 are present, it is not possible to unambiguously state that the carbide phase has been formed. Therefore, XPS analysis was carried out to identify and to further confirm the chemical bonding in C/Cr coatings. The results are presented in the next section.

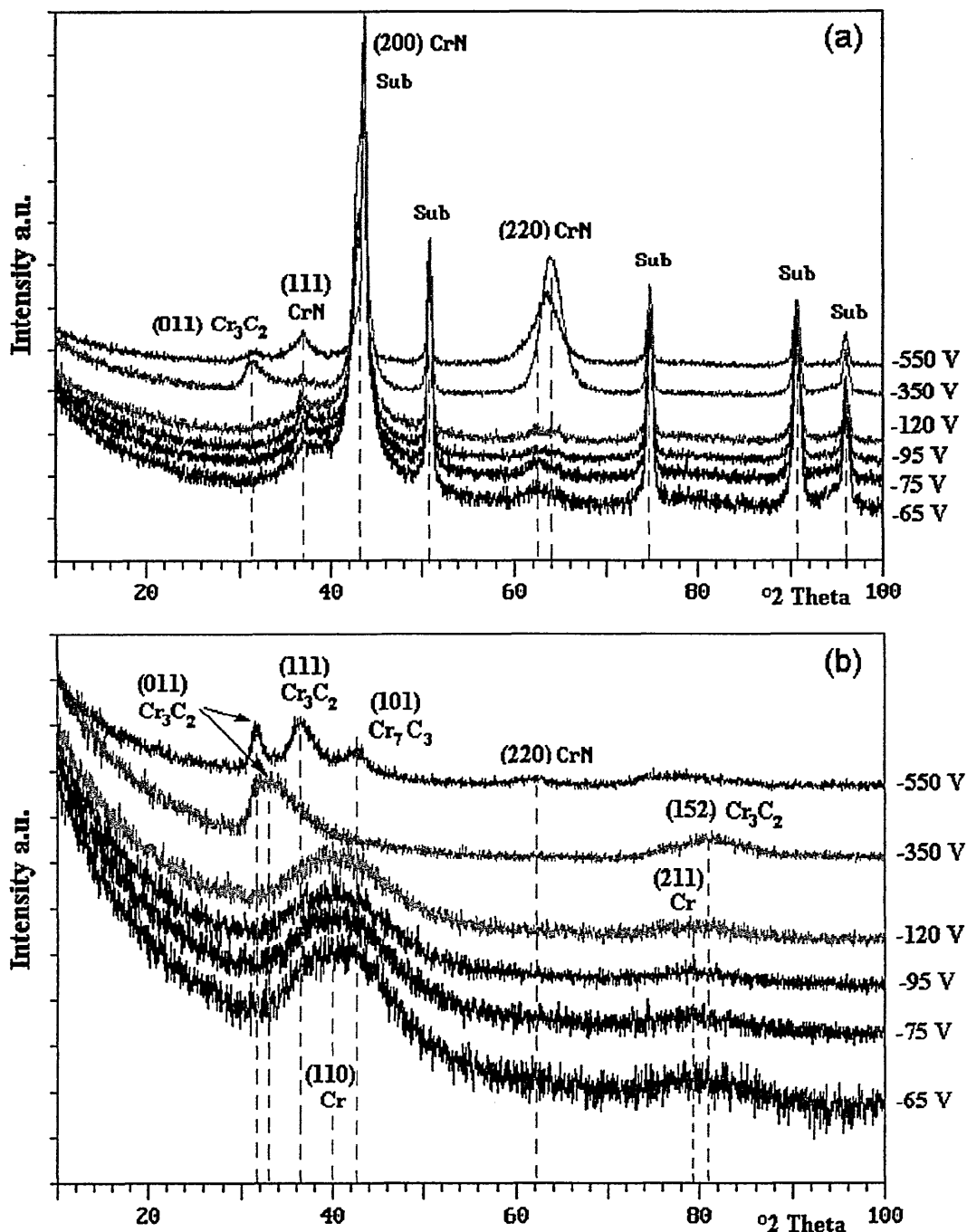


Figure 4.16 (a) $\theta/2\theta$ and (b) Glancing angle X-ray diffraction patterns of C/Cr coatings deposited at various bias voltages

4.5.2 Chemical bonding analysis by X-ray Photoelectron Spectroscopy (XPS)

Figures 4.17(a) and (b) show the XPS spectra of $U_B = -75$ V and $U_B = -350$ V samples, respectively, after 2 min and 4 min Ar^+ etching. The C 1s peak at 282.9 eV indicates Cr-C bonding, and the peak at 284.2 eV indicates free carbon (sp^2 C-C) [113, 167]. The peak at 282.9 eV can be attributed to the Cr_7C_3 phase (about 283 eV) [168] or

Cr_3C_2 phase (about 282.8 eV) [169]. However, the C 1s peak at 283 eV for the $U_B = -75$ V film does not necessarily indicate a chromium carbide phase, but does indicate some chromium-carbon bonding in the film. The C-C peak intensity reduces relative to the Cr-C peak after 4 min sputter time. One reason for this is that all air-exposed samples contain carbon on the surface, which is then removed in the initial stages of sputter cleaning. The situation however, is more complicated than this as the coatings contain an amorphous mixtures of Cr-C. The decrease of the C-C peak intensity relative to the Cr-C peak can be attributed to the preferential sputtering of the light carbon atoms during the Ar^+ etching used in XPS analysis. A similar decrease of the C-C peak intensity with respect to the Cr-C peak also occurs and is much better pronounced in the $U_B = -350$ V sample. In this case however, the Cr-C peak intensity is clearly greater, which indicates more Cr-C bonding relative to free carbon and therefore, suggests formation of Me-carbide phases in the coating. Table 4.3 shows the relative concentrations of C-C and Cr-C bonds after different sputter times determined by curve fitting.

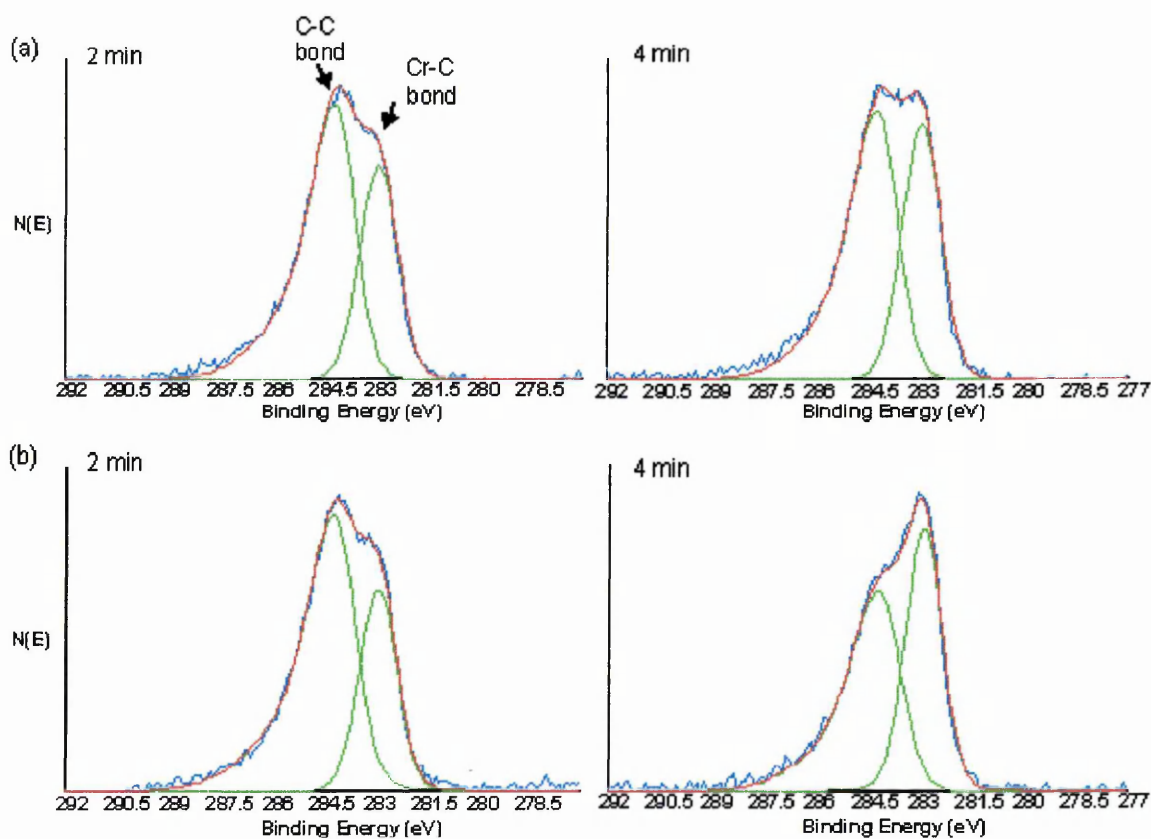


Figure 4.17 XPS spectra taken after 2 min and 4 min Ar^+ etching of: (a) $U_B = -75$ V, and (b) $U_B = -350$ V samples

Bias voltage, V	2 min		4 min		6 min	
	C-C	Cr-C	C-C	Cr-C	C-C	Cr-C
-75 V	64.8	35.2	59.8	40.2	59.1	40.9
-350 V	68.6	31.4	54.1	45.9	49.4	50.6

Table 4.3 Areas under the peaks for C-C and Cr-C bonds expressed as a % of total area under these peaks obtained from the XPS curve fitting for the indicated etch time of samples deposited at $U_B = -75$ V and the $U_B = -350$ V

4.5.3 Raman spectroscopy

Raman spectroscopy was employed to investigate the effect of ion irradiation on the bonding structure and the I_D/I_G ratio which, in this work, was used to represent the estimated amount of sp^2/sp^3 bonding in C/Cr coatings. This work has been published [170]. Figure 4.18 shows the Raman spectra of C/Cr coatings, which consist of two main Raman features on a strong photoluminescence background: broad bands around ~ 1380 cm^{-1} and ~ 1572 cm^{-1} , which are designated to D (disorder) and G (graphitic), peaks respectively. The Raman spectra show better resolved D and G peaks for samples deposited at low bias voltage ($U_B = -65$ V to $U_B = -75$ V). However, these peaks become more diffuse and difficult to resolve (featureless), and the intensity decreases with increasing applied bias voltage to $U_B = -350$ V, which suggests formation of chromium-carbides in the matrix. This agrees well with the XRD and the XPS results. In parallel to the coatings, the structure and the tribological behaviour of the bulk graphite material used for sputtering has also been investigated for completeness and comparisons. Figure 4.19 shows the strongly disordered spectra of the graphite target material, the spectra of the wear track produced on the target material during pin-on-disc test, and the spectra of a pure cemented carbide sample taken for reference. In the spectra of the target material, three lines can be resolved namely the G band at 1582 cm^{-1} , the strong defect induced D band at 1332 cm^{-1} and a weak defect band near 1616 cm^{-1} [171]. The spectra of the wear track contains two lines namely the D band at 1330 cm^{-1} and the G band at 1601 cm^{-1} . The Raman spectrum of chromium carbides is featureless and no carbon signals can be detected (no D and G bands). One reason could be due to the fact that carbides do not have any pair of free C-C bonds that dominate the sp^2 sites, which is essential for dominating the D and G bands. It was realised that the spectrum from the sample

produced at $U_B = -350$ V looks very similar to the spectrum from the reference carbide sample. This observation brings further evidence for the Me-carbide character of the C/Cr coatings produced under the conditions of intensive ion bombardment. The decrease in intensity of the D and G bands for $U_B = -95$ V and higher as well as their complete disappearance at $U_B = -350$ V shows the progression of the carbidisation process taking place in the coating.

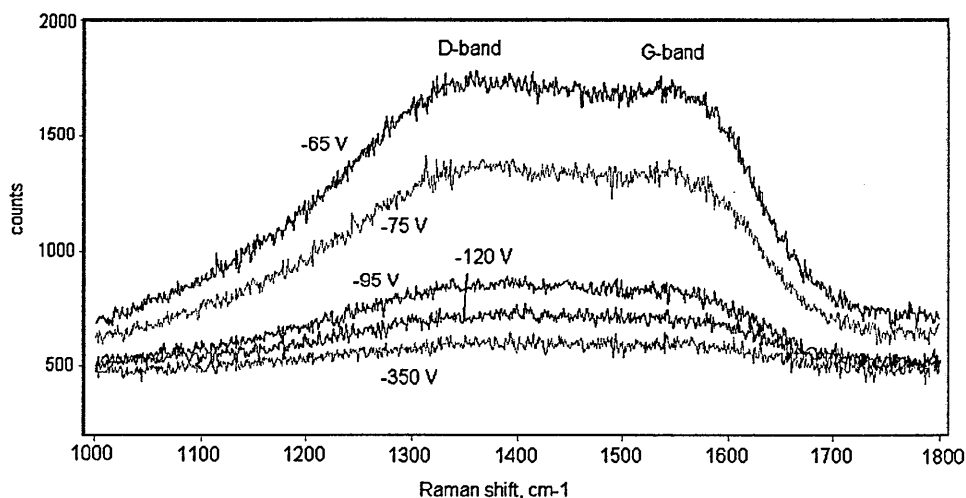


Figure 4.18 Raman spectra of C/Cr coatings deposited at various bias voltages

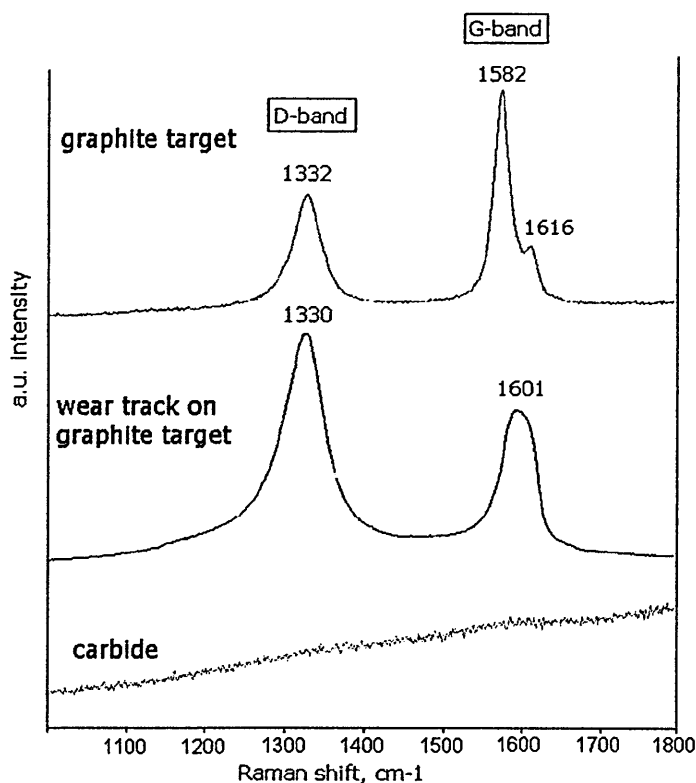


Figure 4.19 Raman spectra of graphite target material, the wear track generated after pin-on-disc test, and the pure cemented carbide sample

The Raman spectra in Figure 4.18 were deconvoluted into two bands with Gaussian line shapes (see Figure 4.20 for the fitted curve) to determine the D and G band positions and the I_D/I_G ratio, which relates to the sp^2/sp^3 content of the films. The results are shown in Table 4.4. It was noted that the D band shifted towards higher wave-numbers and the G band shifted towards lower wave-numbers as compared to the wave-numbers measured for the target material (D band: 1332 cm^{-1} , G band: 1582 cm^{-1}). Some researchers suggested that the downshift of both D and G peaks could be attributed to the change in the bond angle disorder [172] or to an increase in 4-fold coordination (diamond) [169], while others support the view that the downshift of the G-peak from the position 1582 cm^{-1} is due to the influence of shell curvature [173]. A specific Raman band at 1572 cm^{-1} was reported for onion-like carbon [173]. In this study, from the results shown in Table 4.4, the G-band of the coatings was downshifted by $\sim 2\text{-}10\text{ cm}^{-1}$ from the planar graphite value (1582 cm^{-1}). It can be speculated that this could result from the occupancy of dangling bonds by Cr atoms that caused bond angle disorder and led to shell curvature of the carbon plane.

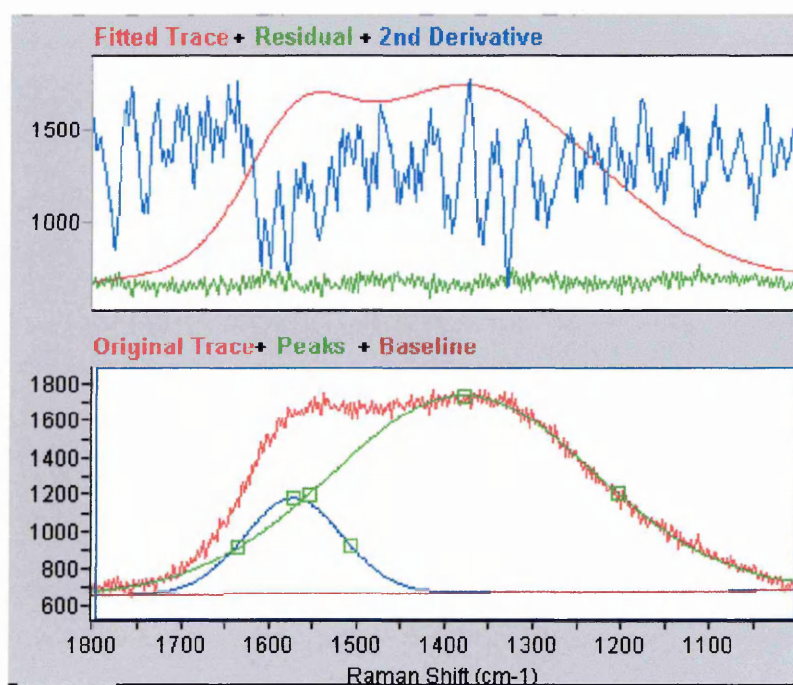


Figure 4.20 Raman spectrum curve fitting result (D-band at 1380 cm^{-1} , G-band at 1572 cm^{-1})

Bias voltage, V	D-band, cm^{-1}	G-band, cm^{-1}	I_D/I_G ratio
Graphite target	1332	1582	n/a
-65	1380	1572	5.56
-75	1381	1572	5.53
-95	1389	1572	7.37
-120	1393	1580	6.85
-350	1390	1580	6.41

Table 4.4 Summary of the curve fitting results showing D and G bands position, and the I_D/I_G ratio as a function of the bias voltage

Figure 4.21 shows the D-band shift as a function of bias voltage. The D-band shifted to a higher wave-number from 1380 to 1393 cm^{-1} as the bias voltage increased from $U_B = -65$ to $U_B = -120$ V, and downshifted by approximately 3 cm^{-1} when the bias voltage increased further to $U_B = -350$ V. It was found that the D-band shift follows the trend of the compressive stress in the coating as a function of the bias voltage. As shown in the preceding section, the bias voltage increased from $U_B = -65$ V to $U_B = -120$ V the compressive stress increased from 0.62 to 2.81 GPa, respectively, and decreased to 2 GPa when the bias voltage increased further to $U_B = -350$ V. This observation is consistent with a recent publication, which reported that Raman peak shift provides a direct relationship between processing conditions and the residual stresses [174]. Figure 4.22 shows the influence of bias voltage on the I_D/I_G ratio. Initially, the I_D/I_G ratio increases from 5.5 to 7.4 as the bias voltage increases from $U_B = -65$ to -95 V, then reduces to 6.4 when the bias voltage was further increased to $U_B = -350$ V. It has been reported that an increase in the I_D/I_G ratio indicates an increase in the sp^2 bonding [92, 175-176]. Thus, the results presented in Figure 4.22 tentatively suggest that the $U_B = -95$ V sample contains the highest amount of sp^2 bonding.

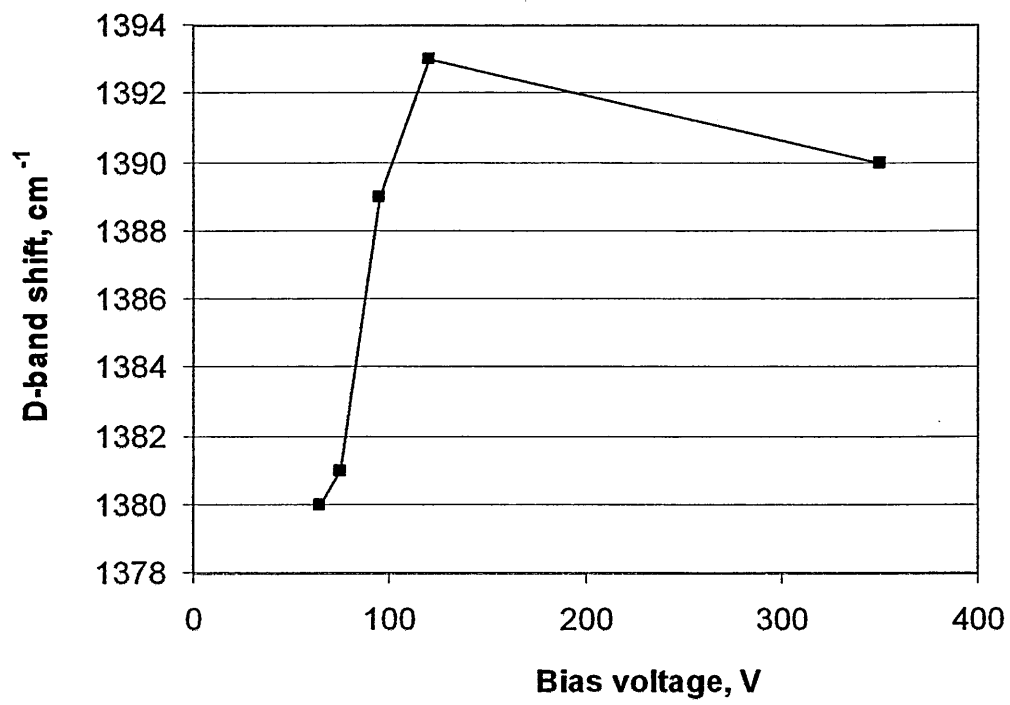


Figure 4.21 D-band shift as a function of the bias voltage

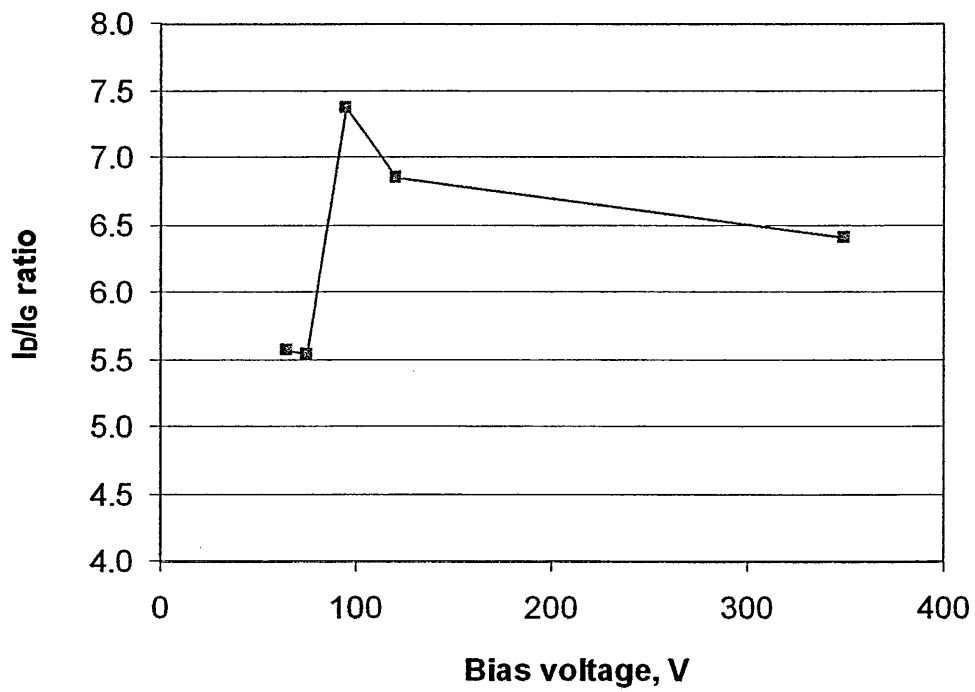


Figure 4.22 I_D/I_G ratio as a function of the bias voltage

The wear tracks generated after pin-on-disc tests for coatings deposited at $U_B = -65$ V and -95 V were investigated using Raman spectroscopy, see Figure 4.23. From Figure 4.23, the intensity ratio changes mainly due to an increase in the intensity of the G band of the material in the wear track, which indicates that, during sliding, the carbon transforms to a more ordered state. This revealed that a graphitisation process occurred at the sliding contact point due to the high contact temperatures which were estimated to be between 500 and 700 °C for the binary and multicomponent coating systems [177]. This temperature range is sufficiently high to cause this transformation. Several reports state that the wear track contains an sp^2 -rich transfer layer, which is responsible for the low friction coefficient of the DLC coatings [113, 131], however, others report no distinct difference between the film and the wear track, which suggests that structural changes occur only during the test and the film reverts back to its original structure after testing [114]. The Raman spectra obtained in this research suggest that C/Cr films undergo structural changes during sliding, transforming from a more disordered state to a more ordered graphitic structure indicated by the increase in the intensity of the G band line in the Raman spectra. The generation of a more lubricious graphitic carbon type within the wear region during service is expected to result in a more favourable tribological performance.

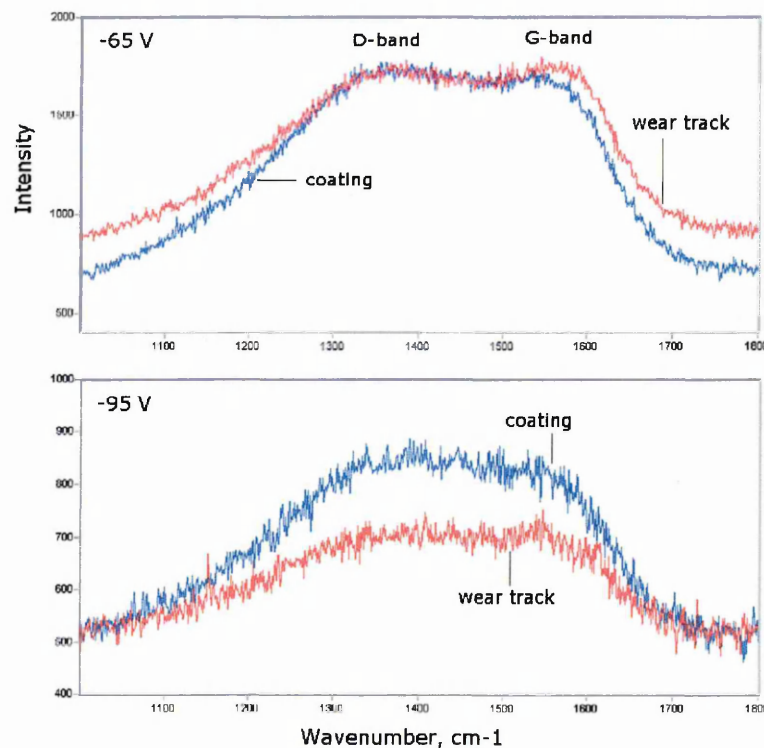


Figure 4.23 Raman spectra of as deposited coatings and the wear tracks generated on $U_B = -65$ V and -95 V samples

4.5.4 Scanning electron microscope (SEM)

Within this research work, the scanning electron microscope was used to study the surface topography of C/Cr coatings and the EDX detector attached to the SEM was used for elemental analysis of the coatings. Figure 4.24 shows the SEM micrographs of the surface morphologies of C/Cr coatings deposited at various bias voltages. The number of coating growth defects (white contrast particles) decreased with increasing bias voltage from $U_B = -65$ to $U_B = -350$ V, this could be due to the removal of loosely bonded droplets with increasing ion bombardment energy. A similar observation was reported for (Ti,Al)N coatings grown with pulsed bias voltages varying from 0 to -900 V [162]. Figure 4.25 shows that a coating deposited at the low bias voltage of $U_B = -75$ V exhibited a discernibly rougher surface (typically columnar) as compared to the coating deposited at a higher bias voltage of $U_B = -350$ V, which shows a significantly smoother surface and denser coating. EDX analysis on these surfaces ($U_B = -75$ and -350 V samples), see Figure 4.26, revealed the presence of Cr, C, Fe, O and Ar. The Fe peak may result from contamination or be due to the substrate; the oxygen peak was present due to exposure of samples to ambient atmosphere after coating deposition; and the Ar peak result from Ar incorporation during the deposition process. The coating microstructures were investigated in more detail using TEM, and the results are shown in the next section (4.5.5).

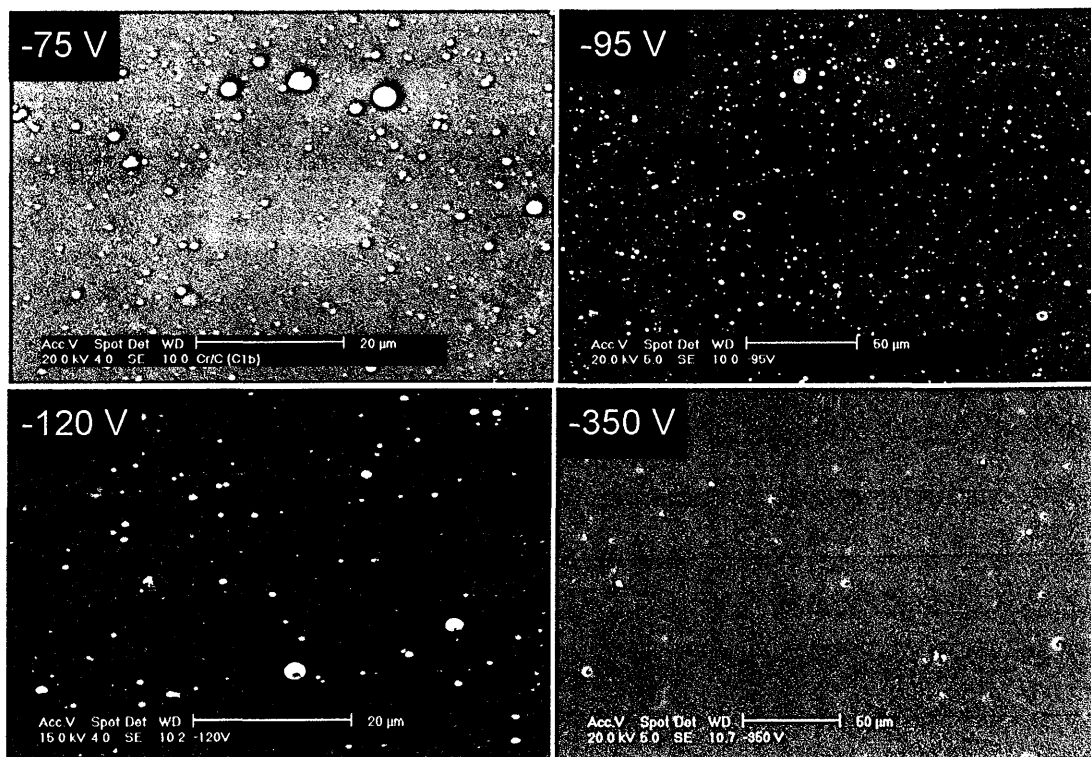


Figure 4.24 SEM micrographs of C/Cr coatings deposited at the bias voltage indicated (note the different scale on $U_B = -95$ V and -350 V samples)

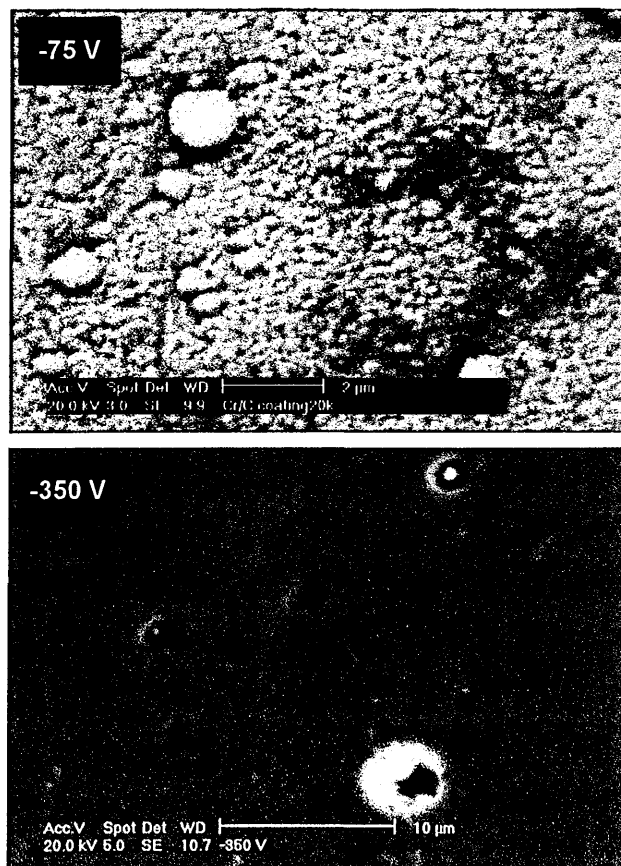


Figure 4.25 Surface morphology of C/Cr coating deposited at $U_B = -75$ V and $U_B = -350$ V

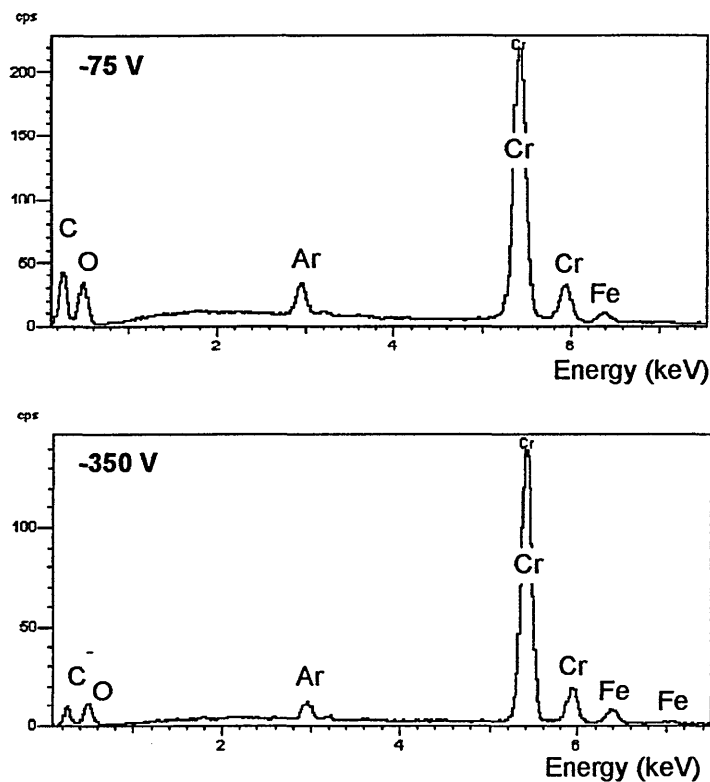


Figure 4.26 EDX analysis of C/Cr coatings deposited at $U_B = -75$ V and $U_B = -350$ V

It is not surprising that coatings deposited using the combined steered cathodic arc/unbalanced magnetron sputtering contained growth defects generated from the droplets/macroparticles deposited on the substrate during the metal-ion etching process [54]. The growth defects were revealed as the bright contrast regions of the rounded top nodule, as can be seen in Figure 4.24. Figure 4.27(a) is the cross-sectional view of the transmission electron microscope (XTEM) image of a growth defect found in coating deposited at $U_B = -95$ V. This image clearly shows the initiation site of the growth defect from a droplet which was deposited on the substrate, and the rounded top nodular geometry of the growth defect. The surface topography of the growth defects generated on a $U_B = -350$ V sample is shown in Figure 4.27(b). The discernible voided boundary/groove (observed only in the $U_B = -350$ V sample) between the growth defect and the unperturbed area of the coating is considered to result of an atomic shadowing effect [178]. Imagine if this image was a cross-section and viewed in the direction of the arrow shown in Figure 4.27(b), the growth defect may look like the schematic cross-section presented in Figure 2.9(c) (middle image, see page 20, Chapter 2). However, no direct correlation between the dimension of the voided boundary and the ion bombardment energy was previously reported.

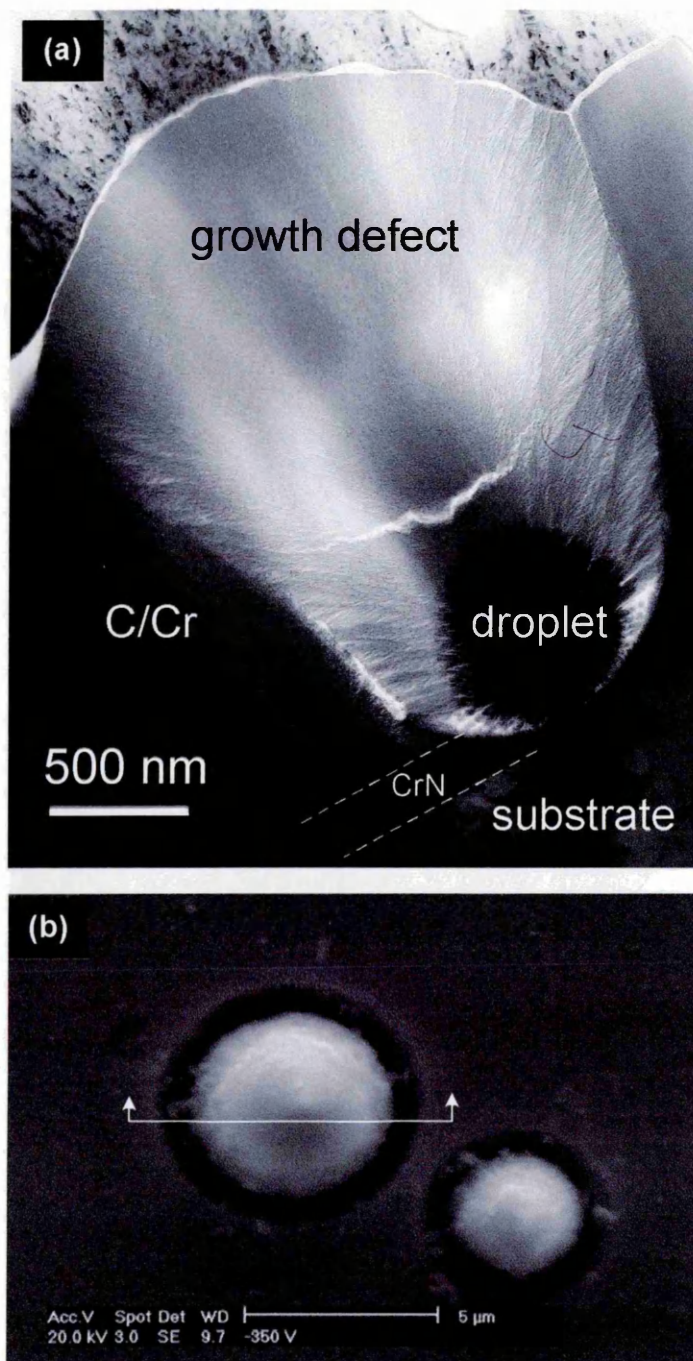


Figure 4.27 (a) XTEM image of growth defect found in $U_B = -95$ V sample, (b) SEM image of growth defects on $U_B = -350$ V sample

The surface morphologies of the wear tracks generated after pin-on-disc tests, for coatings deposited at various bias voltages were investigated using SEM. The results are shown in Figure 4.28. The SEM pictures of the wear tracks clearly show the excellent wear behaviour of the coatings produced at $U_B = -95$ V compared to that produced at either lower ($U_B = -65$ and -75 V) or higher ($U_B = -120$ and -350 V) bias voltages. Although the wear resistance of coatings grown at $U_B = -95$ V and $U_B = -120$

V were almost similar, which was within the range of $10^{-17} \text{ m}^3\text{N}^{-1}\text{m}^{-1}$ (see Figure 4.11 (a)), the high compressive stress (2.81 GPa) of the $U_B = -120 \text{ V}$ sample may contribute to the higher friction coefficient (see Figure 4.9) and the wider wear track (track width = $345 \text{ }\mu\text{m}$) as compared to the $U_B = -95 \text{ V}$ ($295 \text{ }\mu\text{m}$) sample. As can be seen in Figure 4.28, the wear track of the $U_B = -95 \text{ V}$ sample is very smooth and narrow, which indicated an efficient performance of the coating as a solid lubricant. In contrast, the wear track of the $U_B = -65 \text{ V}$ sample is wider (track width = $360 \text{ }\mu\text{m}$) and the coating is obviously worn out as the substrate has been exposed, imaged as a narrow band in the middle of the track. On the other hand, although the wear track of the $U_B = -350 \text{ V}$ sample appears smooth, it is much wider (track width = $420 \text{ }\mu\text{m}$) suggesting high wear of the coating but also more wear on the counter part. This can be expected as the hardness of the coating produced at $U_B = -350 \text{ V}$ is higher due to the presence of Me-carbide phases [170]. Generally, hard surfaces were expected to produce smaller wear particles with a weaker tendency to agglomerate as compared to soft surfaces which produced larger wear particles with a stronger tendency to agglomerate [179]. The SEM morphology of the wear tracks complement the friction coefficient measurements and well correlate with the XPS and Raman findings. This will be discussed in Chapter 5.

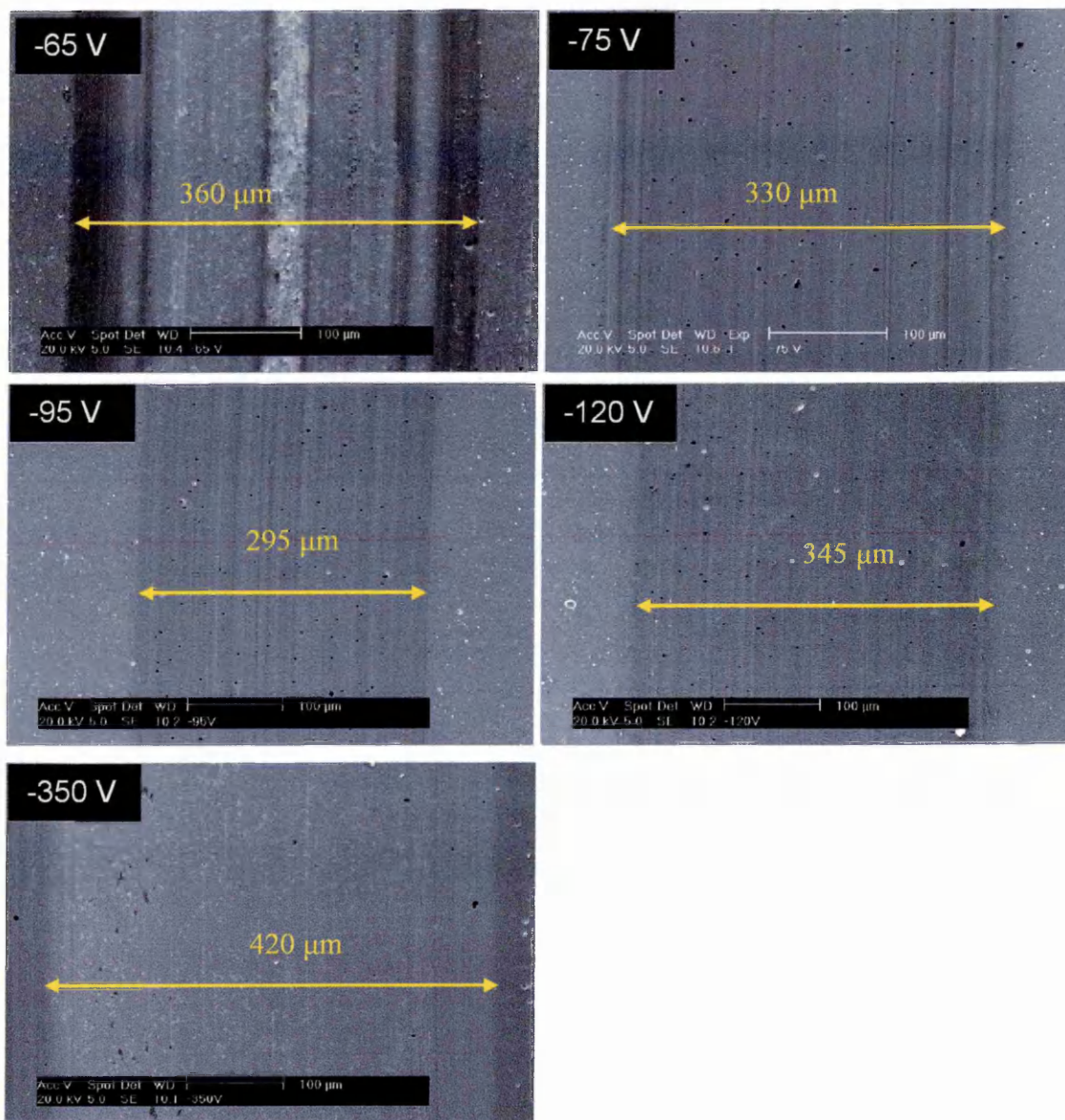


Figure 4.28 SEM images of the wear tracks of coatings deposited at the bias voltage indicated

4.5.5 Transmission electron microscope (TEM)

The microstructure of the as-deposited coatings was examined utilizing cross-sectional transmission electron microscopy (XTEM) using selected area electron diffraction (SAD) and bright-field (BF), dark-field (DF), high-angle annular DF (HAADF) and lattice resolution imaging techniques. Figure 4.29 gives the XTEM bright field micrographs of the sample deposited at $U_B = -75$ V, -95 V, -120 V, and -350 V, showing an overview of the coating architecture, which is composed of a Cr-ion irradiated substrate, $0.25\ \mu\text{m}$ CrN base layer and C/Cr coating. The coating appears overall brighter than the substrate and the base layer due to its lower average atomic

number. It is obvious that ion bombardment substantially influences the structure of C/Cr films as can be seen in Figure 4.29. The coating deposited at $U_B = -75$ V ostensibly does not appear fully dense, as column boundaries, outlined as weak-phase objects, are evident above film thickness of ~ 0.3 μm . This is particularly obvious in Figure 4.29(a). The coating becomes smoother and the structure changes from columnar to a self-organised multilayer structure with increasing bias voltage from $U_B = -75$ to -350 V. The selected area diffraction patterns (SAD) from the C/Cr layer (shown as inset in Figure 4.29(b)i – (c)i) present broad halo-like rings of uniform intensity and no diffraction contrast, indicating the amorphous nature of the coating. The analysis of the diffraction pattern revealed that the coating contains graphitic carbon and metallic chromium. The SAD pattern of the CrN base layer (Figure 4.29(b)ii) reveals a B1-NaCl structure with a weak 002 texture in the growth direction. It is worth commenting that the crystallinity of the coatings increased with increasing bias voltage, as can be seen by careful observation of the SAD pattern for the $U_B = -120$ V sample where crystalline diffraction arcs (reflections from Cr) can be seen around the most intense diffuse ring as shown by arrows in Figure 4.29(c)i. At $U_B = -350$ V, a rather complex diffraction pattern (Figure 4.29(d)i) was observed, which showed pronounced crystalline reflections from graphitic carbon, chromium crystallites, and chromium carbides (this could be a mixture of Cr_{23}C_6 , Cr_7C_3 and Cr_3C_2) in the amorphous structure. From the equilibrium C-Cr phase diagram shown in Figure 1.1, for a C/Cr film containing approximately 50 at.%C and 50 at.%Cr (see compositional analysis in section 4.3), at substrate temperatures $< 500^\circ\text{C}$, Cr_3C_2 carbide phase and excess carbon were expected to form.

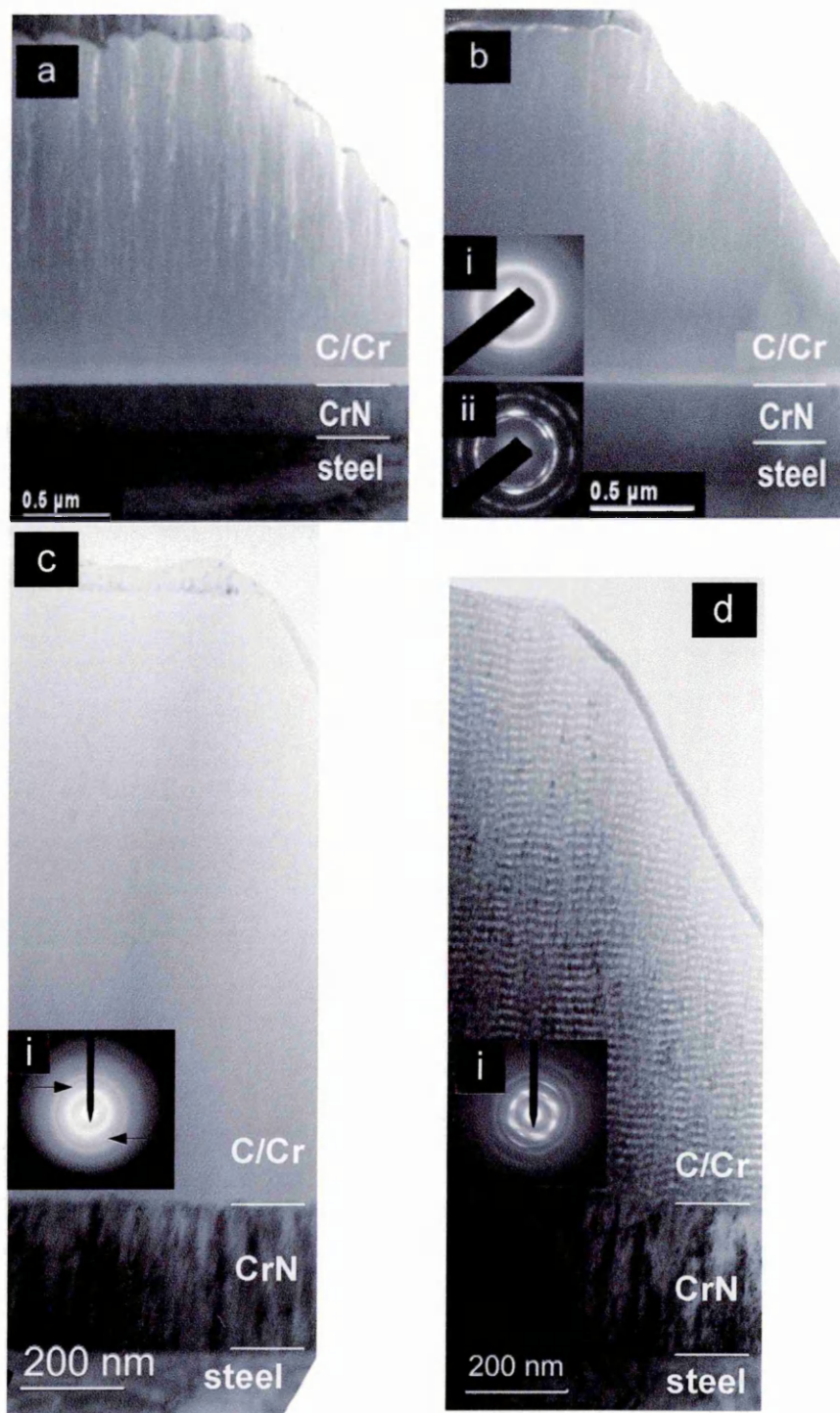


Figure 4.29 BF-XTEM micrographs of C/Cr coatings deposited at (a) $U_B = -75$ V, (b) $U_B = -95$ V, (c) $U_B = -120$ V, (d) $U_B = -350$ V, and SAD pattern of (i) C/Cr coating, (ii) CrN base layer (note the different scale)

A low-magnification high-angle annular dark field (HAADF) image of a film deposited with a bias voltage of $U_B = -95$ V is presented in Figure 4.30 [111]. This type

of imaging is obtained by scanning a sub-nanometer diameter beam across the sample. The signal in each pixel is proportional to the inelastic scattering events, which in turn are proportional to the atomic number Z of the atoms in the path of the beam. In addition, the signal magnitude is proportional to the total number of scattering atoms, which relates to the thickness and atomic density of the sample in that area. The brighter contrast thus increases with film thickness, which is the general variation of the signal from the upper right (the dark area occurs because of the hole in the sample) to the lower left area (bright area for the large thickness). In any given localized area of the sample foil, where the thickness variations are small, the contrast is dominated by variations of the average atomic number of the material. The base layer of CrN is thus outlined in darker contrast compared to the steel substrate, in agreement with the lower average atomic number because of the presence of nitrogen. The C/Cr coating in turn is darker than both the substrate and the base layer in agreement with the larger atomic percentage of the lighter carbon atoms. There are significant variations of the contrast within the C/Cr coating, which are worth comment. For bias voltages between $U_B = -65$ and -95 V, there is a dark band in the coating immediately adjacent to the base layer visible across the length of the micrograph shown in Figure 4.30 for $U_B = -95$ V sample. This is clearly due to atomic number contrast, which is evidence that, at the onset of the C/Cr deposition the coating is carbon rich and that the Cr concentration increases gradually to the value of ~ 32 at.% within a coating thickness of ~ 200 nm. This can be explained by the poisoning of the Cr target during the reactive sputter deposition of the CrN base layer, which is gradually being cleaned in the Argon discharge used for the C/Cr deposition [111].

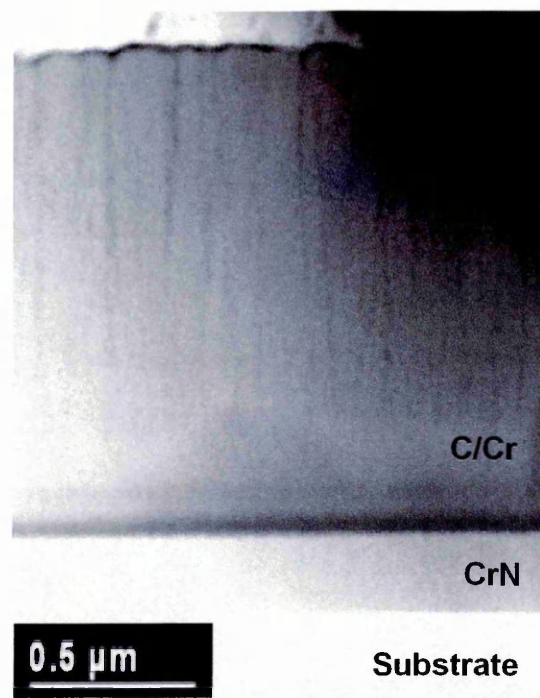


Figure 4.30 Low magnification HAADF image of the films deposited at $U_B = -95$ V

In addition to the dark interface band, the HAADF image (Figure 4.30) of the coating further reveals darker contrast lines in the growth direction, which have one to one correspondence with the weak-phase column boundaries seen in the BF image shown in Figure 4.29(b). The dark contrast in this case can be attributed to lower overall atomic density of the column boundaries, suggesting accumulation of carbon atoms in these regions of the coating. The accumulation of carbon at the column boundaries is further illustrated by the BF-XTEM micrograph of the sample deposited with $U_B = -75$ V, Figure 4.29(a). The overall C/Cr microstructure is similar to that of the C rich region near the interface and low atomic density column boundaries, both showing in brighter contrast. However, the width of the column boundaries in this sample is markedly larger compared to the sample deposited at $U_B = -95$ V (Figure 4.29(b)), and the top surface is considerably rougher. The surface roughness estimated from XTEM decreased from 140 nm, to 95 nm, to 45 nm as the bias voltage is increased from $U_B = -65$, to -75 , to -95 V due to the smoothening effect of ion-irradiation [111]. In agreement with the general observations in the literature [8], the effect of the increased ion energy during the deposition is to produce a smoother coating surface and, associated with that, a denser coating.

Figure 4.31 shows higher magnification BF-XTEM images of the near surface region of the C/Cr coating deposited at $U_B = -75$ and $U_B = -95$ V. The nanostructures for the films were very similar in size and appearance. These micrographs further confirm that the weak phase column boundaries are not completely open voids. The amorphous matrix is continuous between columns, although the overall atom density (especially the local Cr concentration) appears to be lower compared with the interior of the column. The multilayer nanostructure of the C/Cr coating is not readily apparent. It is revealed by careful investigation, as exemplified in the inset in Figure 4.31(b), of areas of the sample with appropriate sample thickness. The multilayers have an average periodicity of ~ 2 nm which is consistent with that calculated based on the total deposition thickness and the period of sample rotation. Figure 4.32 shows a Z-contrast image outlining essentially the artificial layered distribution of C and Cr in the film due to the substrate rotation in front of the Cr and C targets. Cr-rich regions tend to form, which are surrounded by a C-rich matrix. Cr-rich (brighter contrast) networks can be seen to align in nanocolumns (dashed lines) with width of 1–4 nm parallel to the growth direction. The artificial multilayer structure is heavily distorted by a network of these Cr-rich nanocolumns extending in the growth direction, which dominate the nanostructure. This is further discussed in Chapter 5. Lattice resolution bright field imaging presented in Figure 4.33 reveals a dense amorphous structure in the $U_B = -95$ V sample. The Cr-rich regions, which in this imaging mode appear with slightly darker contrast, exhibit a higher concentration of curved graphite planes indicating that Cr may act to cross-link and bend the graphite planes.

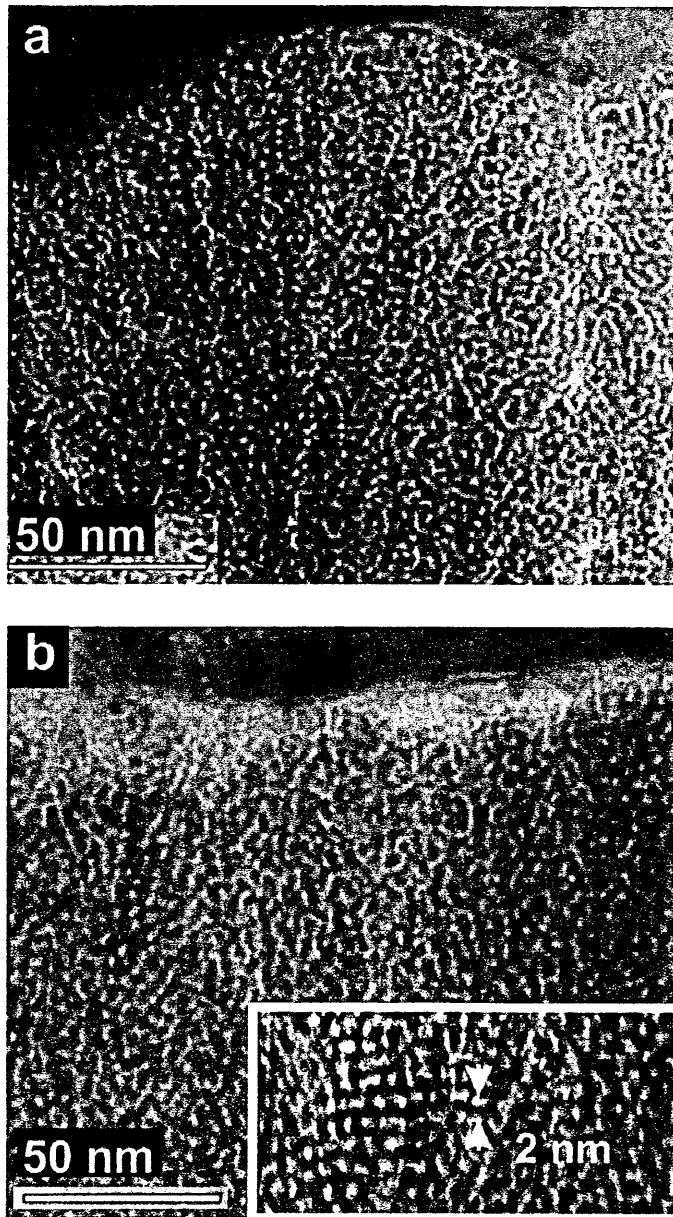


Figure 4.31 BF-XTEM of the coating near-surface region for (a) $U_B = -75$ V and (b) $U_B = -95$ V samples

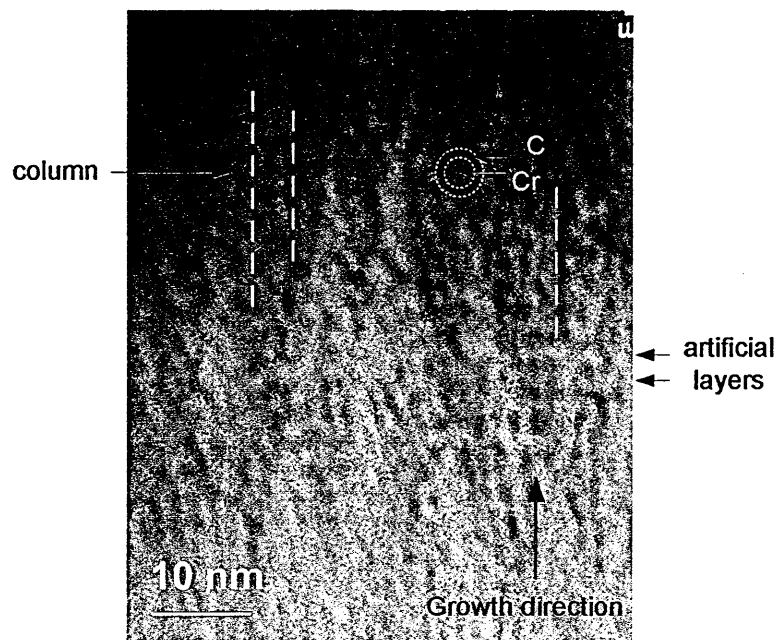


Figure 4.32 Z-contrast XTEM, showing both nanolayers and nanocolumns

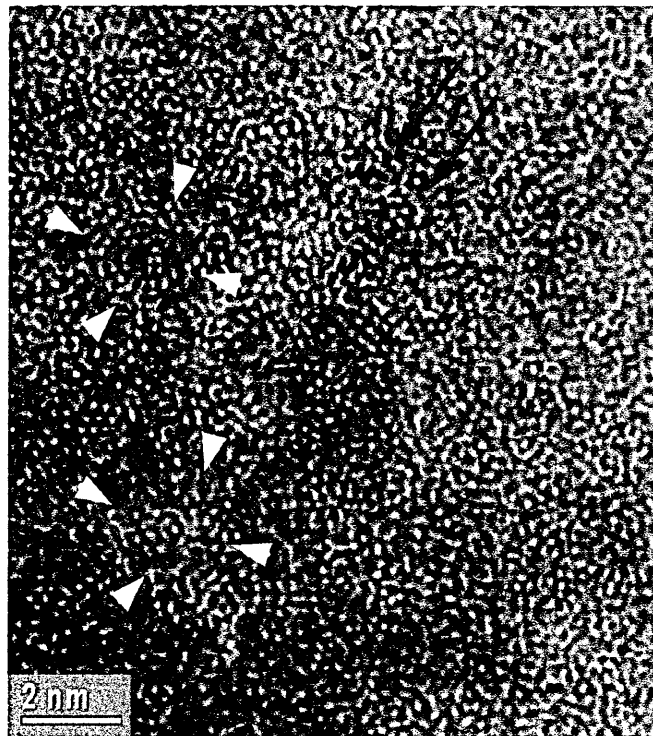


Figure 4.33 High-resolution BF-XTEM image of $U_B = -95$ V sample

Figure 4.34 shows the higher magnification bright field images of the coating deposited at $U_B = -120$ V [112]. The artificial multilayer structure with an estimated

periodicity of ~ 1.6 nm was highlighted in the dotted box region and is shown in Figure 4.34(b) (the image has been rotated through 90° clockwise to give a better representation of the layer structure). The structure seems to become slightly aligned in the growth direction (shown by arrows in Figure 4.34(a)) in comparison to the coating deposited at lower bias voltages (see Figure 4.31).

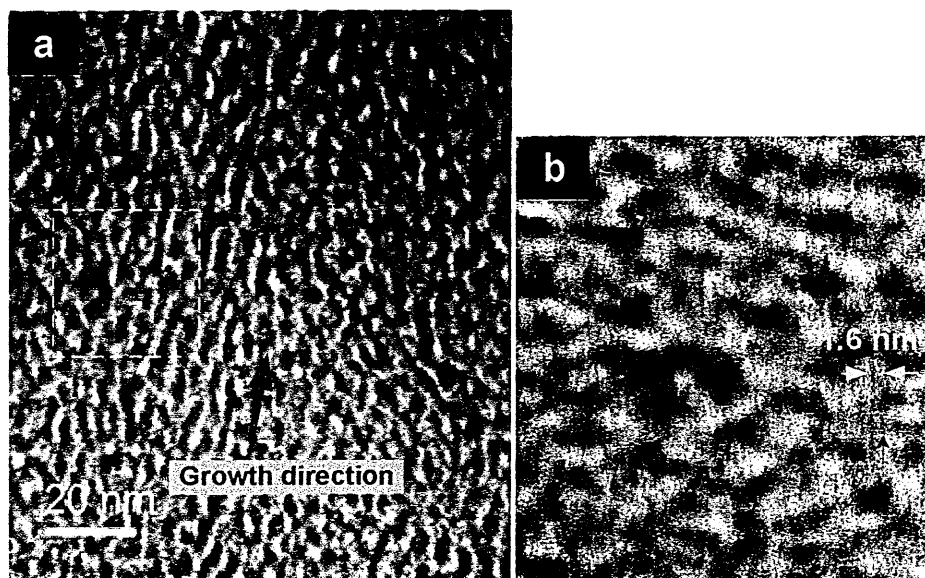


Figure 4.34 (a) BF-XTEM image of coating deposited at $U_B = -120$ V, (b) magnified image of dotted box region (rotated 90° clockwise) showing the artificial multilayer structure (arrowed)

Figure 4.35 and Figure 4.36 show the dark field and HAADF images of the C/Cr coating grown at $U_B = -350$ V, respectively. Under these imaging modes, the darker contrast layers indicated the areas occupied by C (lower atomic number). Figure 4.37 shows the higher magnification bright field images of this pronounced multilayer structure. The bilayer period of this new structure reached approximately 20 nm, which is almost one order of magnitude larger than that for the coatings deposited between $U_B = -65$ V and -95 V (bilayer thickness of about 2 nm). In these images, the bright contrast layers are the areas occupied by C, which is built up of onion-like carbon (Figure 4.37(b)). Upon closer examination of a coating grown at $U_B = -350$ V, using HRTEM and STEM-EELS analysis (presented in the following section), it was found that the onion-like carbon clusters are highly disordered, and are embedded in a more ordered matrix, see Figure 4.38.

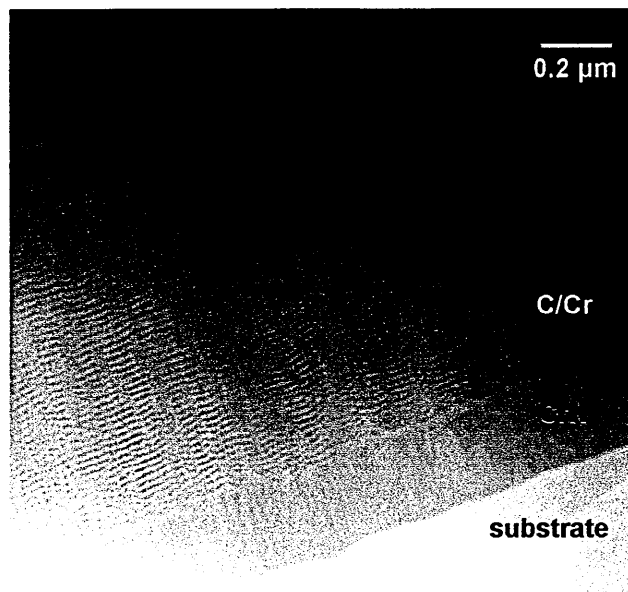


Figure 4.35 Dark field image of C/Cr coating grown at $U_B = -350$

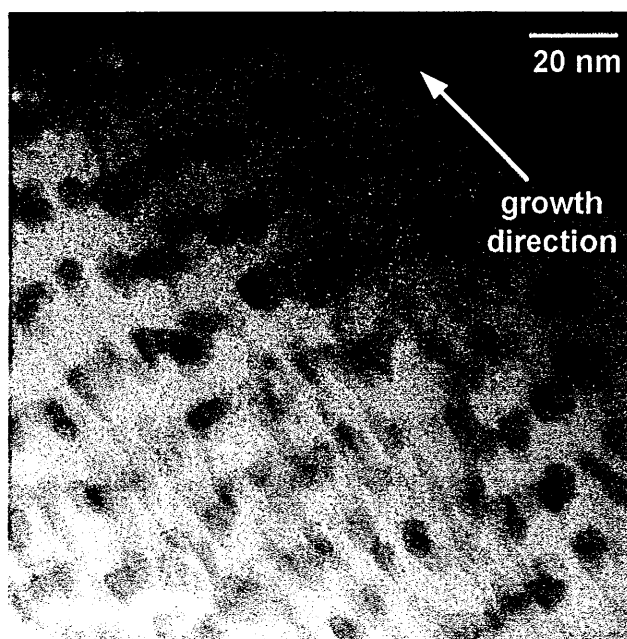


Figure 4.36 HAADF image of C/Cr coating grown at $U_B = -350$ V

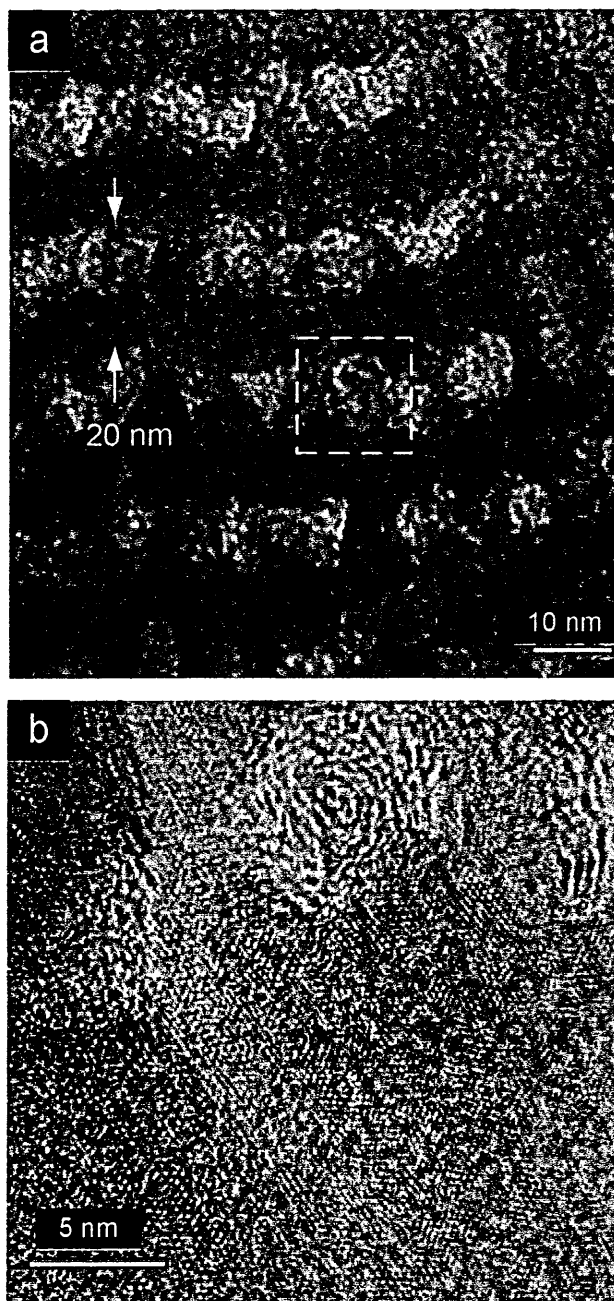


Figure 4.37 (a) BF-XTEM image of $U_B = -350$ V sample, (b) lattice resolution bright field image of the dotted box region

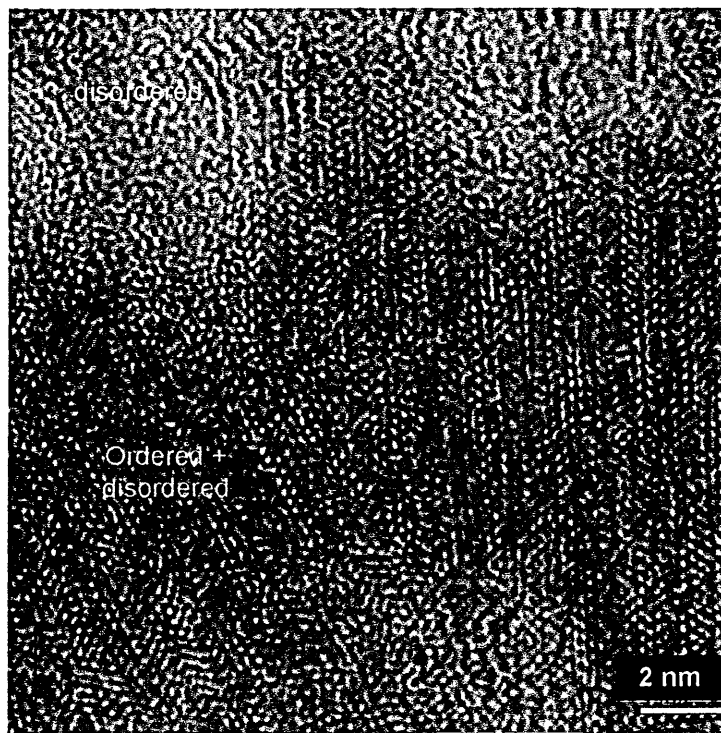


Figure 4.38 Lattice resolution image of coating grown at $U_B = -350$ V

To test the reproducibility of the structure observed in the $U_B = -350$ V sample, a coating was deposited in one deposition run by applying alternately in four cycles, low ($U_B = -75$ V) and high ($U_B = -350$ V) bias voltages, during the 4 hr deposition process. Figure 4.39 shows a BF-XTEM image of the C/Cr coating produced under these conditions. The layer adjacent to the base layer was deposited at $U_B = -75$ V and the top surface layer was grown at $U_B = -350$ V. The BF-XTEM image clearly shows the reproducibility of the multilayer structure at $U_B = -350$ V. It is interesting to note that, when switching the bias voltage from $U_B = -75$ V to $U_B = -350$ V, the interface between $U_B = -75$ V (columnar) and $U_B = -350$ V (multilayer) is wavy and rough as compared to the interface between $U_B = -350$ V and $U_B = -75$ V which is sharp and smooth, when switching the bias voltage back to $U_B = -75$ V from $U_B = -350$ V.

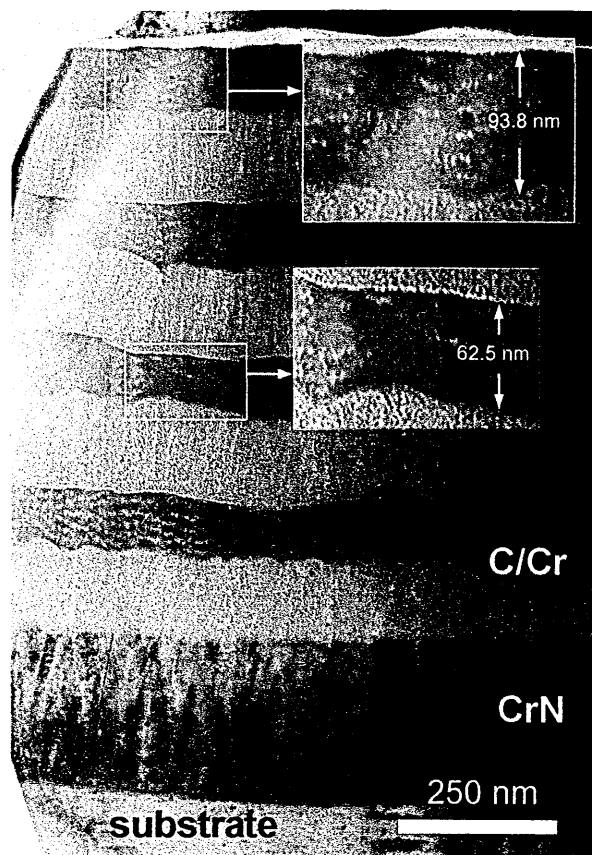


Figure 4.39 BF-XTEM image of $U_B = -75/350$ V sample

4.5.6 Scanning TEM (STEM) - electron energy loss spectroscopy (EELS)

Quantitative electron-energy loss spectroscopy (EELS) analysis was carried out to determine the composition locally within the various phases observed. Figure 4.40 is the annular dark field (ADF) STEM image of the $U_B = -350$ V sample shown in Figure 4.39. The quantitative EELS analysis and their corresponding electron energy loss spectrum of the -75 V and -350 V layers are shown in Figure 4.41(a) and (b-c) respectively. From Figure 4.41(a), in the $U_B = -75$ V layer (amorphous layer), the overall density and thickness of the film remains constant. There are C-rich regions accumulated typically along column boundaries (Point 1: 95.32 at.% C, 2.81 at.% Cr, 1.87 at.% O) as compared to the matrix (Point 2: 74.71 at.% C, 21.15 at.% Cr, 4.14 at.% O). In the -350 V region, there are C-rich clusters (Point 3: 91.34 at.% C, 4.72 at.% Cr, 3.94 at.% O) which organized themselves in a mixture of carbon and chromium-rich material (Point 4: 48.16 at.% C, 41.88 at.% Cr, 9.96 at.% O). This was possibly a carbides matrix. In the coating growth direction, it was observed that the interface between the $U_B = -350$ V and -75 V layers appears like a nearly continuous layer of the precipitates seen in the $U_B = -350$ V layer. The peaks appearing between 286 and 294

eV in Figure 4.41(b) and (c) correspond to the carbon K-edge, and those peaks between 575 and 595 eV are chromium L₃ and L₂ respectively. To identify the bond configuration of the carbon in C/Cr coating, STEM was conducted to obtain the high-resolution carbon and chromium L₂, L₃ data from the U_B = -75/350 V sample, this is shown in Figure 4.42. From Figure 4.42(a), the carbon edges look very different in the clusters (Point A) and the matrix (Point B). The clusters look very much like amorphous carbon (pi* at 285 eV followed by larger broad sp³ band) while the matrix has a much stronger pi* peak followed by a rapid fall off in intensity of the sp³ band, which is graphite like. The C-edge spectrum of the U_B = -75 V layer (Figure 4.42(a) point C) looks like a linear combination of the two and it is ascribed as a graphite-like structure. The inset in Figure 4.42(a) is the K-ionization region (K-edge) of the EELS of two allotropes of carbon taken for reference from [180]. As can be seen from Figure 4.42(b), the carbon edges between the clusters (Point D) and the matrix (Point E) are very different, and comprise amorphous and graphite-like carbon, respectively. The Cr edge, on the other hand looks almost the same in the two cases. This suggests that the Cr signal from the clusters might be from the surrounding C/Cr matrix. Figure 4.43 shows the jump ratio maps of C and Cr within the coating deposited at alternating bias voltage of U_B = -75 V and -350 V. This image clearly shows the distribution of carbon and chromium within the film, and further supports, the TEM-SAD and EELS findings (the clusters are carbon rich).

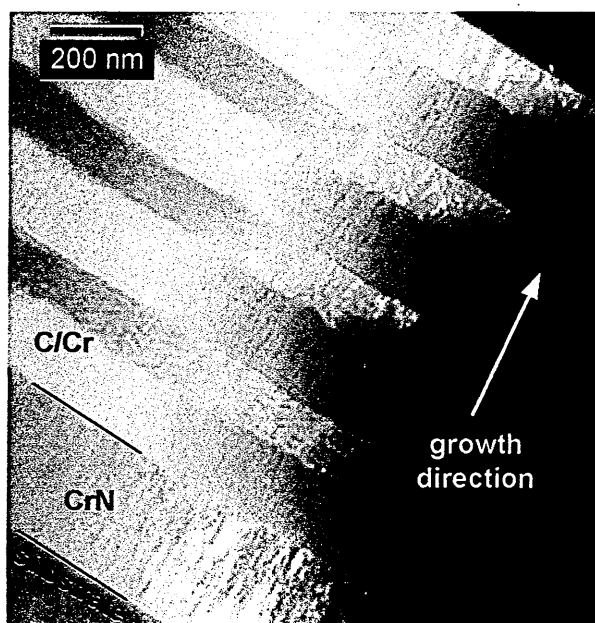


Figure 4.40 ADF STEM image of C/Cr coating grown at alternative bias voltage of U_B = -75 V (columnar) and U_B = -350 V (multilayer)

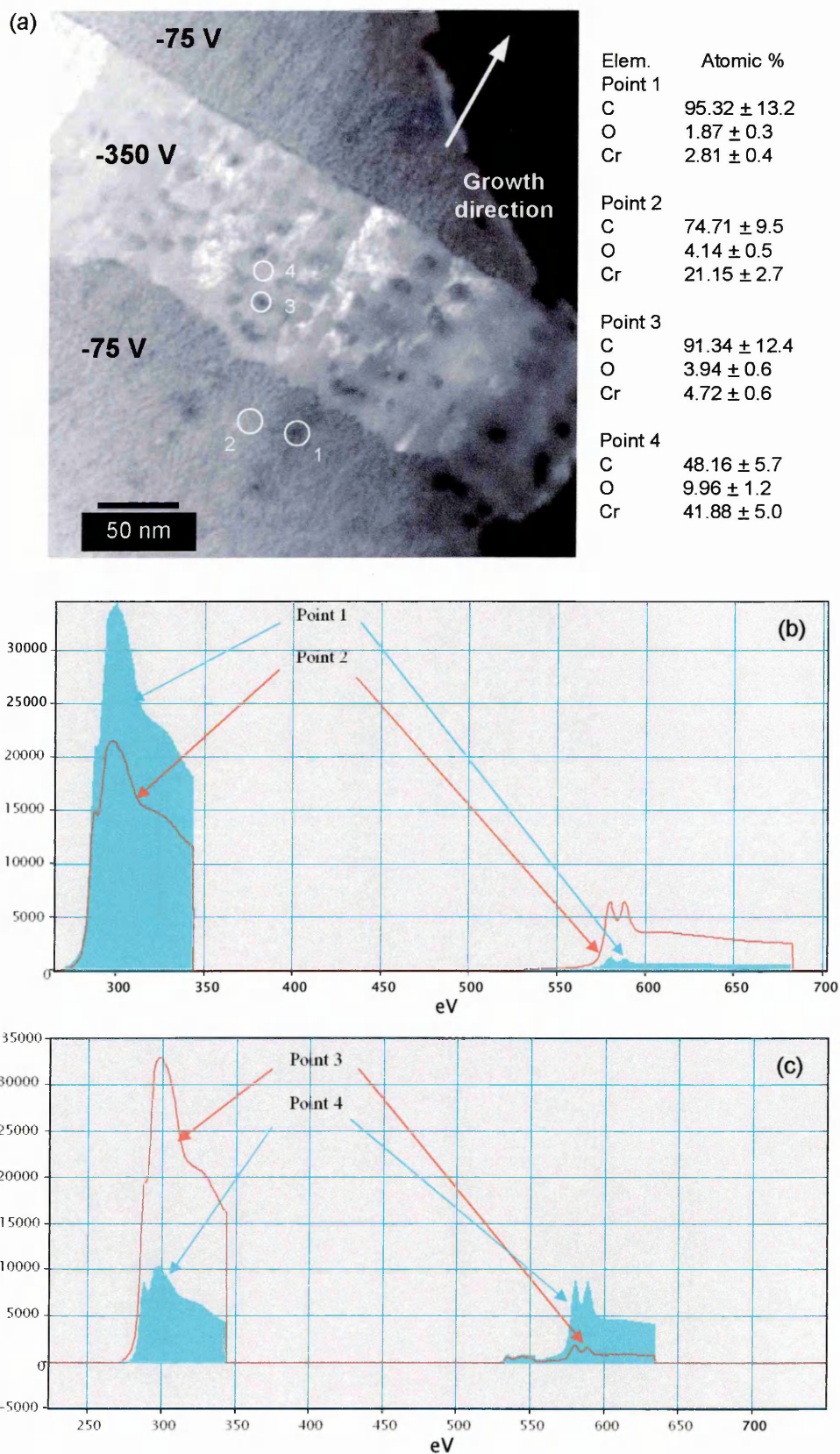


Figure 4.41 (a) ADF STEM image, (b-c) Electron energy loss spectra of CK (~286 – 294 eV) and CrL (~575 - 595 eV) for point 1 to point 4

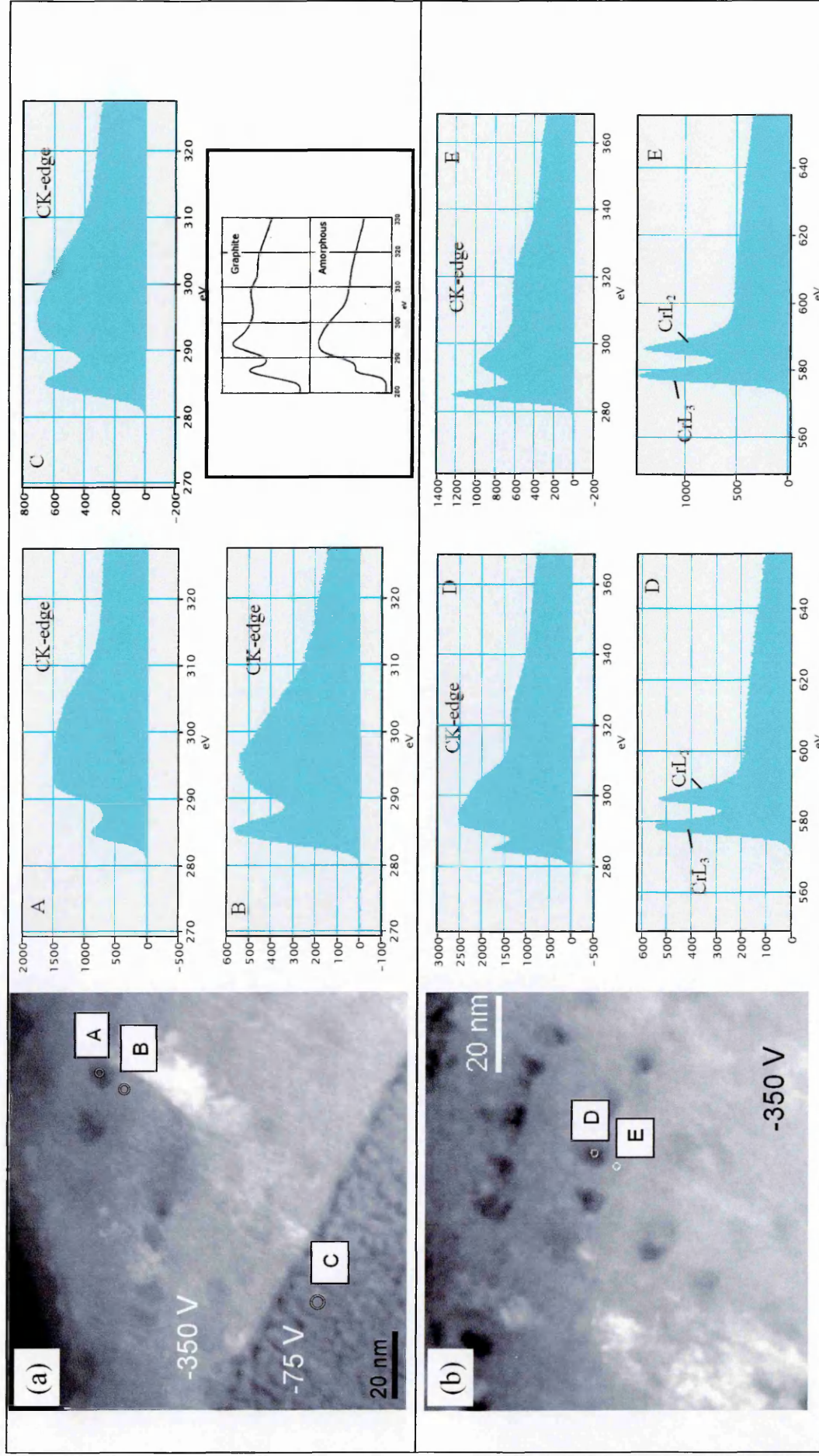
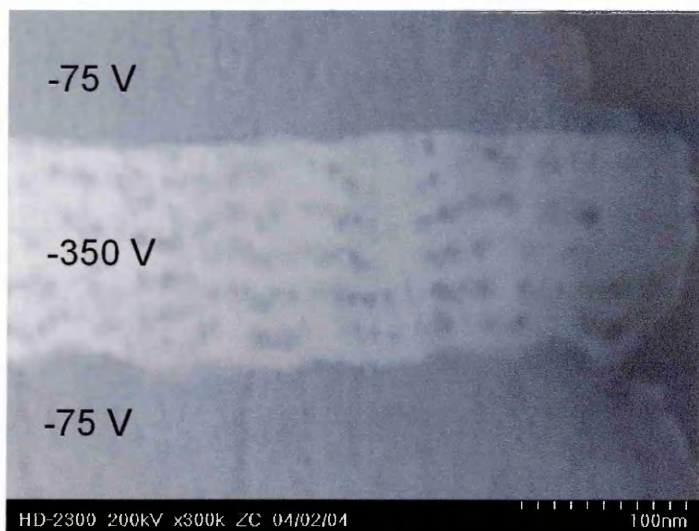
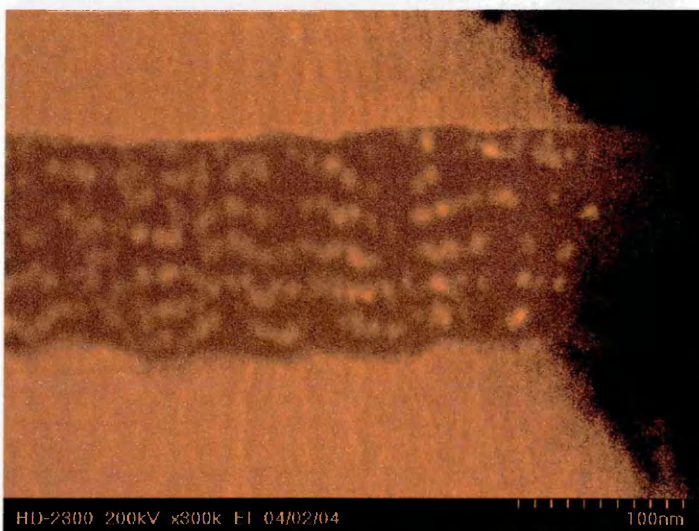


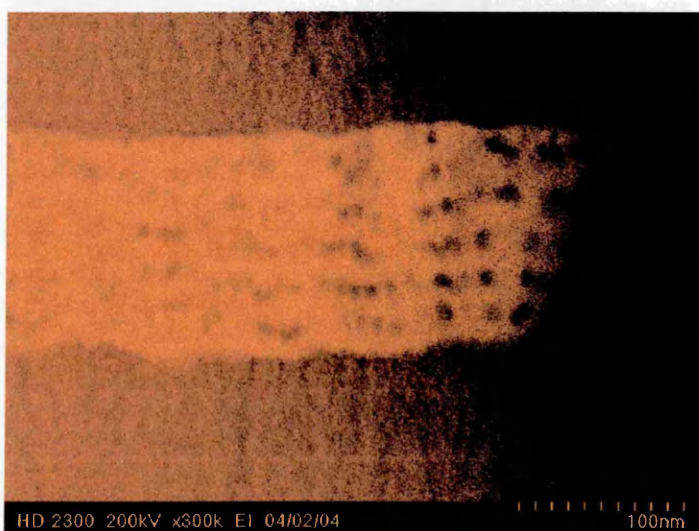
Figure 4.42 (a) CK-edge data of $U_B = -75$ V and $U_B = -350$ V layers, (b) CK-edge and CrL_x data of the clusters and matrix within $U_B = -350$ V layer



Z-Contrast
Image



Carbon Jump-Ratio
Map



Chromium Jump-
Ratio Map

Figure 4.43 Jump ratio maps of C and Cr in $U_B = -75/350$ V sample

4.6 Oxidation tests

The oxidation behaviour of C/Cr coatings was investigated using thermogravimetric analysis (TG) and isothermal heat-treatment at temperatures selected based on the TG traces. The oxidized surfaces were examined using XRD, SEM, SEM/EDX and Raman spectroscopy for the investigated bias voltage ranging from $U_B = -75$ to $U_B = -350$ V. The results are presented in the following sections and the oxidation behaviour of C/Cr coatings is further discussed in Chapter 5.

4.6.1 Thermogravimetry analysis (TGA)

Figure 4.44 shows the TGA oxidation curves for C/Cr and TiN (taken for reference) coatings deposited on a stainless steel substrate. C/Cr coatings begin to oxidise at about 700°C (except for the $U_B = -65$ and -75 V samples, which oxidised at $\sim 400^\circ\text{C}$). This can be compared to TiN coatings which oxidise at about 600°C. This indicates that the C/Cr coating exhibits better oxidation resistance than a TiN coating. As seen in Figure 4.44, the increase in weight in the initial stage (from room temperature, RT to $\sim 50^\circ\text{C}$) of the oxidation curve could be attributed to the formation of a very thin oxide film on the coating surface when the coating is exposed to air. This is not surprising as all metals (except gold) tend to form oxides at low temperature and even at room temperature [181]. For all the applied bias voltages, no obvious weight gain was observed between 50 - 400°C. This shows that the C/Cr coating can withstand temperatures up to at least 400°C without severe oxidation. However, just beyond 400°C to $\sim 420^\circ\text{C}$, an immediate weight loss was observed in coatings deposited at $U_B = -65$ V and $U_B = -75$ V. This could be due to oxidation of Cr to form Cr_2O_3 and the onset of carbon dissolution particularly from the carbon weak phase along the column boundaries (white contrast lines revealed by the TEM images shown in Figure 4.29(a) and Figure 4.31(a)). This can form CO_2 and escaped with the vent gas out of the crucible. This temperature is within the reported oxidation temperature range of 350 - 450°C for DLC films [182] when heated in air. However, the above phenomenon was not observed in a coating deposited at higher bias voltages from $U_b = -95$ to $U_b = -350$ V. Further increase in the temperature to 1000 °C resulted in greater weight gain on all the investigated samples. Figure 4.45 shows glancing angle XRD patterns after TG analysis for coatings deposited at various bias voltages. The XRD traces look very similar for all the bias voltages applied. The peaks correspond to chromium oxide (Cr_2O_3), iron oxides typically magnetite (Fe_3O_4), and very weak reflections of pure iron

from the stainless steel substrate. At temperatures as high as 1000 °C, the coating was lost and the XRD patterns obtained in Figure 4.45 possibly result from the oxidised substrate.

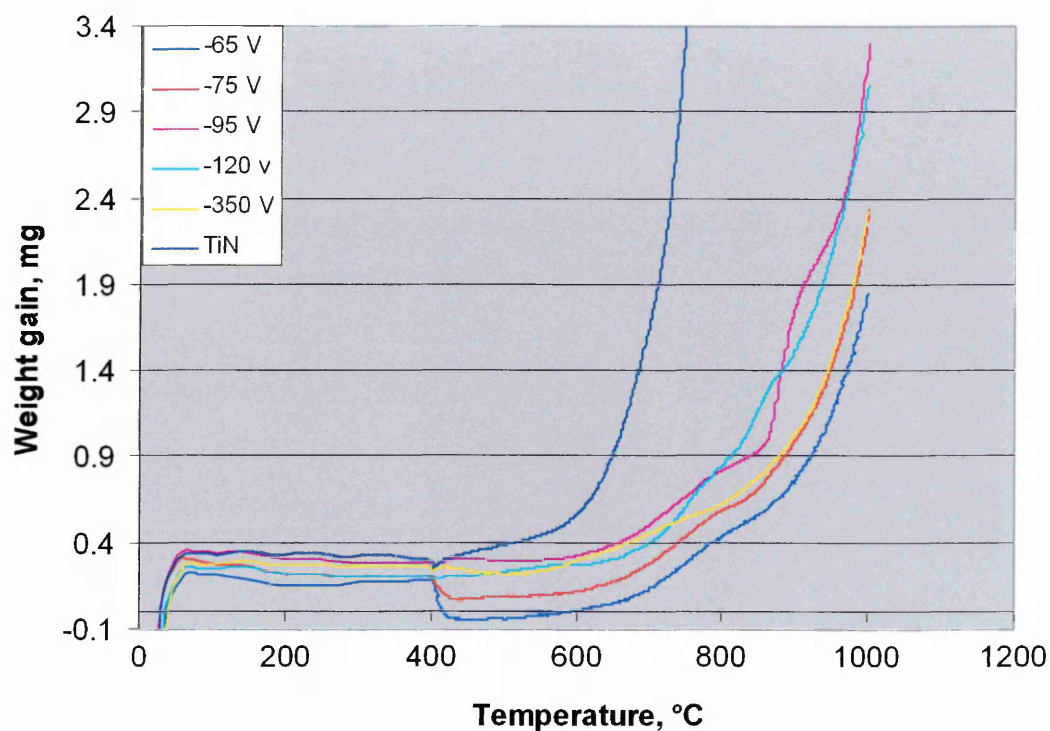


Figure 4.44 TGA results for C/Cr coating deposited at various bias voltages (TiN coating was taken for reference)

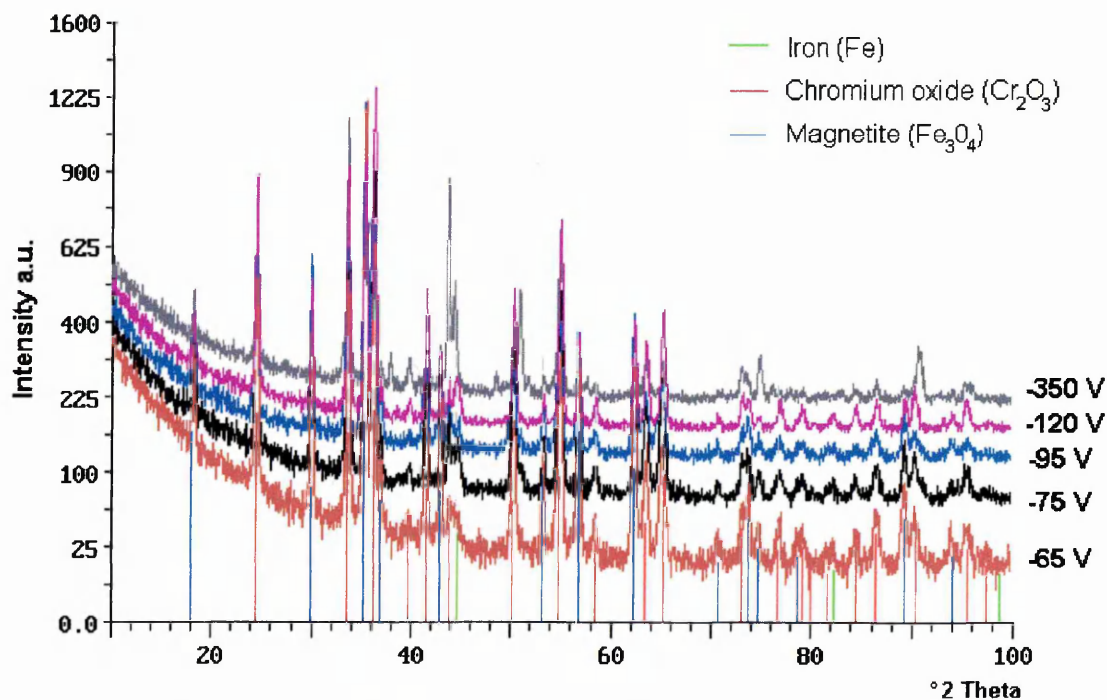


Figure 4.45 Glancing angle XRD patterns after TGA tests for C/Cr coatings deposited at various bias voltages

Figure 4.46(a) shows the SEM image of the as-deposited coating. The white contrast particles were coating growth defects. The background “scratches” (parallel to the black colour lines) were due to the substrate surface morphology. Figure 4.46(b)-(f) show the surface morphology of the samples after TGA tests. Figures 4.46(b)-(c) clearly show the preferential oxidation of the coating at growth defects (highlighted by white arrows), which are well understood as the weak region which produces direct paths between the coating surface and the substrate which allow transport of oxygen to the substrate and substrate elements to the surface during heat treatment [183]. Diffusion of oxygen to the substrate via coating growth defects and pinholes during the oxidation process may cause expansion of the volume below the defects, resulting in local oxide detachment when the deflection of the oxide is excessively large. Detachment of this oxide layer will expose the substrate and enhance localised oxidation of the substrate material. The coating deposited at $U_B = -350$ V (Figure 4.46(f)) was completely oxidised, leaving flake-like chromium oxide on the iron-oxide surface. The EDX analysis of the oxidised surfaces shown in Figure 4.47 suggests the presence of Cr oxide and Fe oxides on the surface after TG test, which is in agreement with the XRD analysis. The amount of iron oxide was estimated to increase with increasing bias voltage as evidenced by the increased Fe peak intensity which was particularly obvious for the coating deposited at $U_B = -350$ V. The EDX point analysis of the bright contrast islands marked with “X” (Figure 4.46) and shown in Figure 4.48 suggests that the bright islands contained a mixture of chromium oxide and iron oxide, but are more iron-rich as indicated by the higher intensity iron peak. Figure 4.49 gives the EDX/elemental mapping of the oxidised surface of the coatings deposited at $U_B = -65$ V and $U_B = -350$ V, showing the distribution of iron oxide and chromium oxide. Upon closer examination of the chromium oxide surfaces, an interesting feature was observed on the surface occupied by chromium oxide. This is shown in Figure 4.50. The surface morphology of the chromium oxide appeared very much like octahedral and dodecahedral diamond.

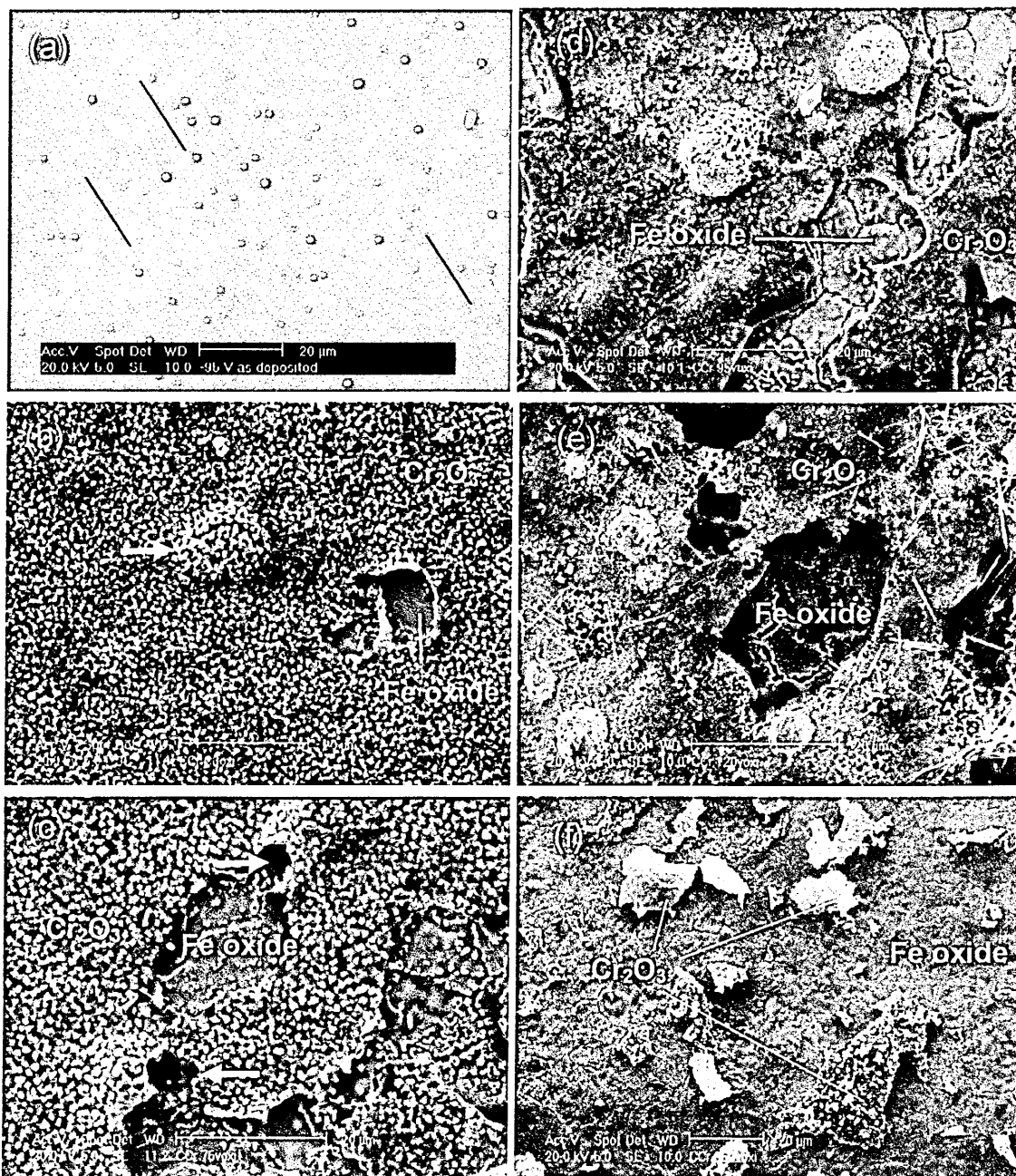


Figure 4.46 SEM surface morphology of the (a) as deposited coating, and oxidised surface after TG tests of coating deposited at (b) $U_B = -65$ V, (c) $U_B = -75$ V, (d) $U_B = -95$ V, (e) $U_B = -120$ V, (f) $U_B = -350$ V, after TGA tests. Arrows show initiation of diffusion processes at growth defects

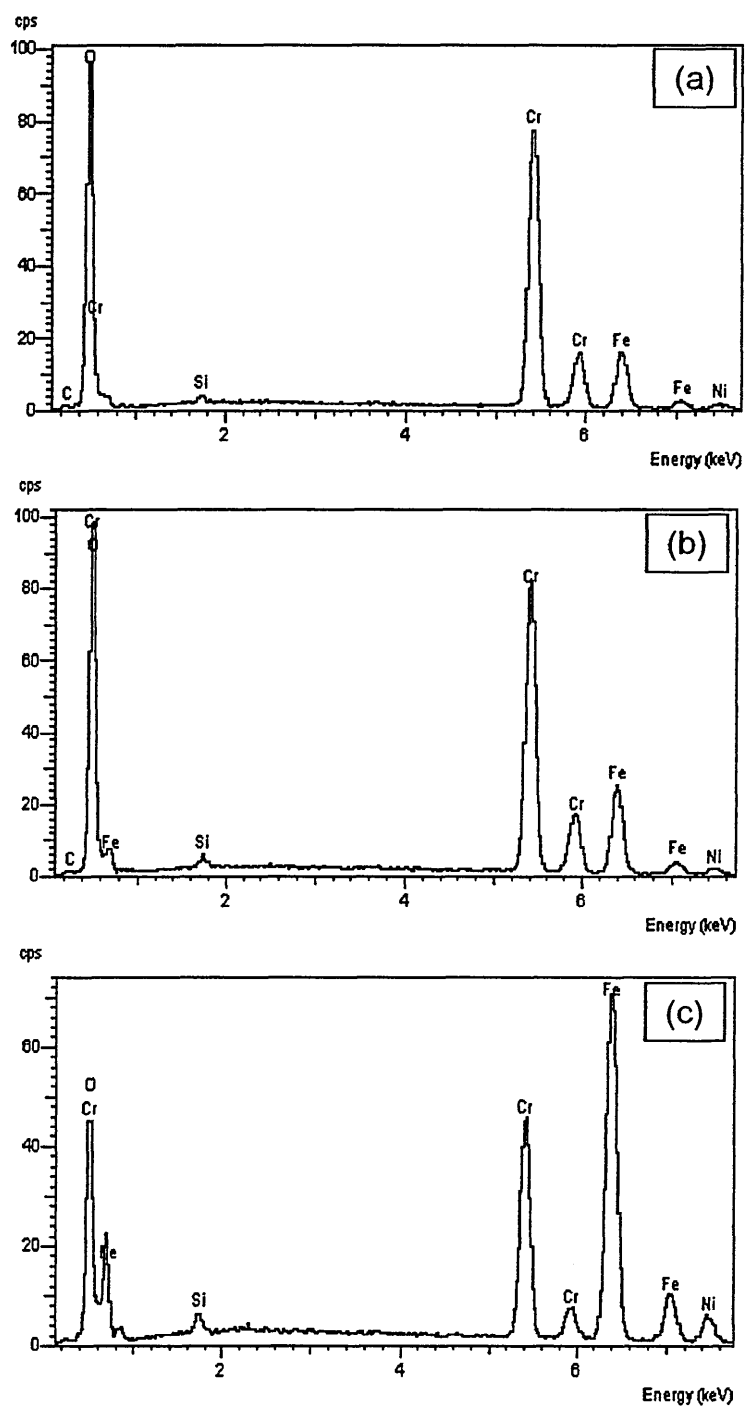


Figure 4.47 SEM/EDX analysis after TGA tests of coating deposited at (a) $U_B = -65$ V, (b) $U_B = -95$ V, (c) $U_B = -350$ V

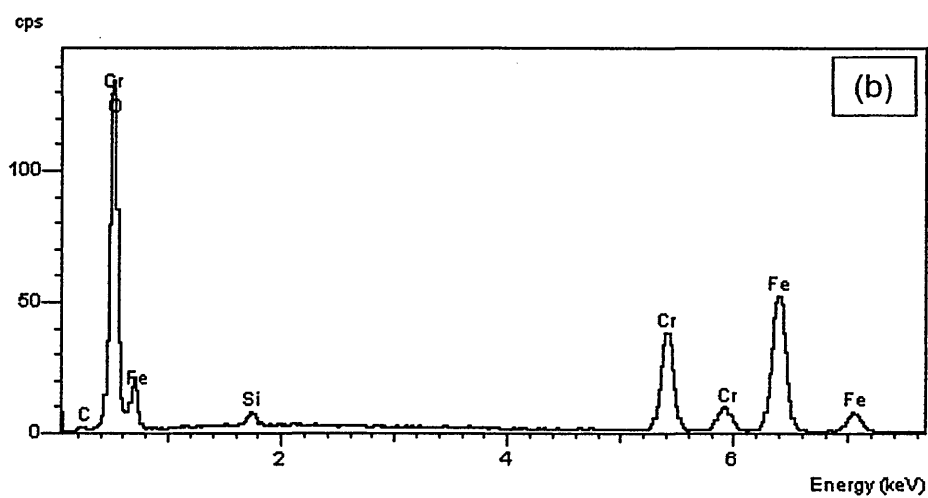
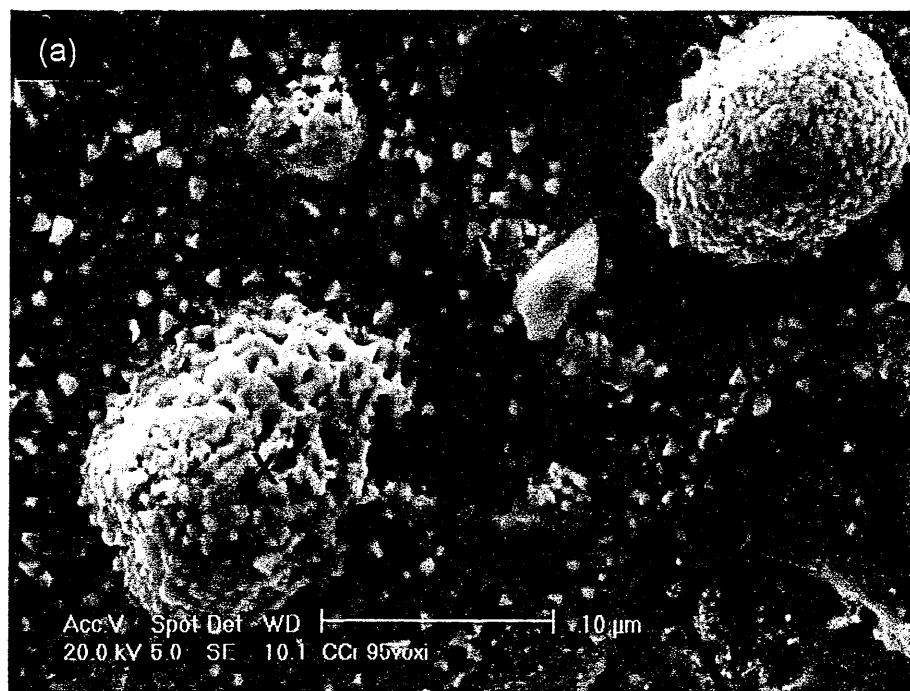


Figure 4.48 SEM image of the oxidised surface of coating deposited at $U_B = -95$ V,
(b) EDX analysis of the bright particles marked with “X”

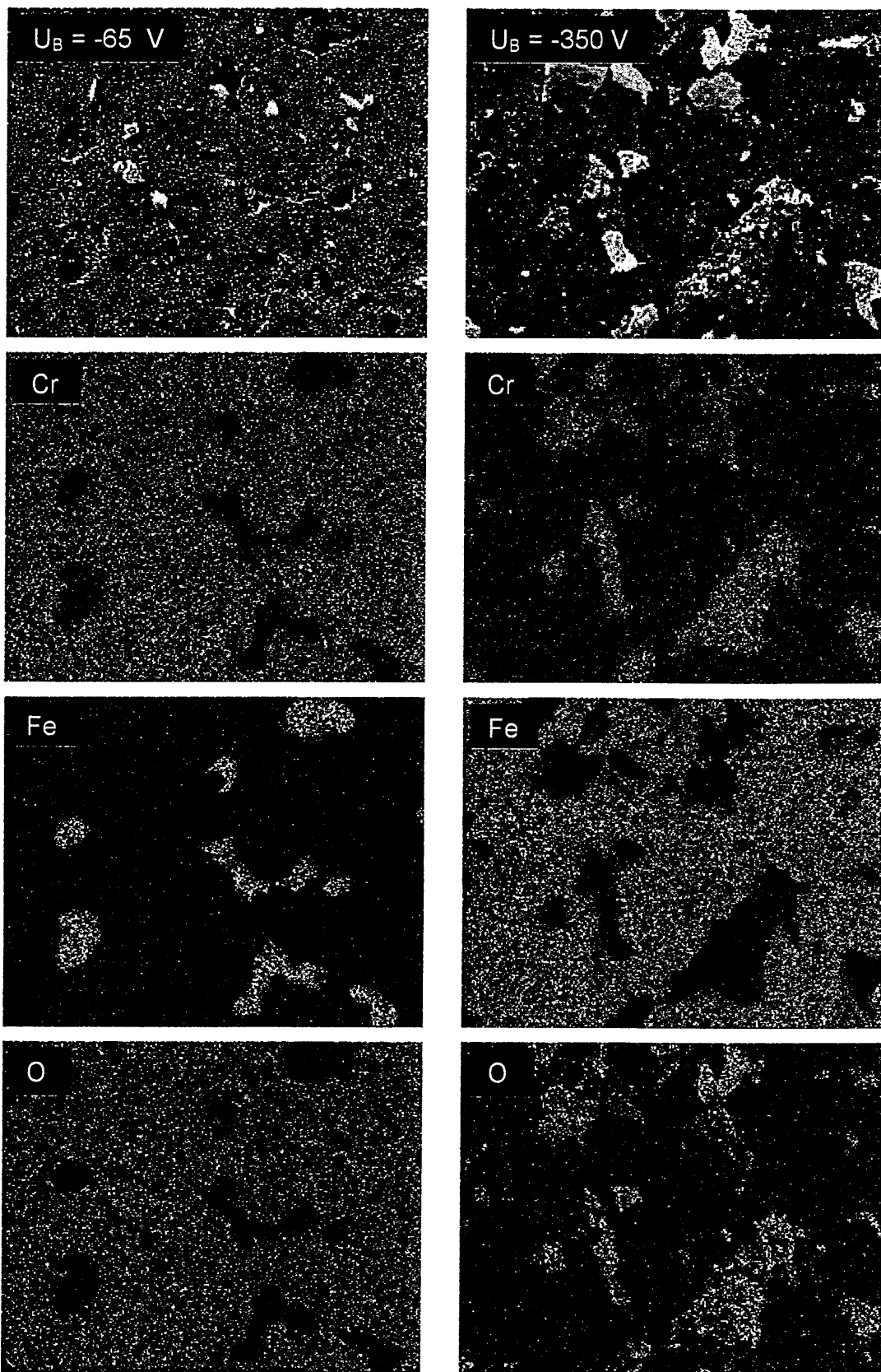


Figure 4.49 SEM images (top) and EDX/elemental mapping of oxidised surfaces of $U_B = -65 \text{ V}$ and $U_B = -350 \text{ V}$ samples

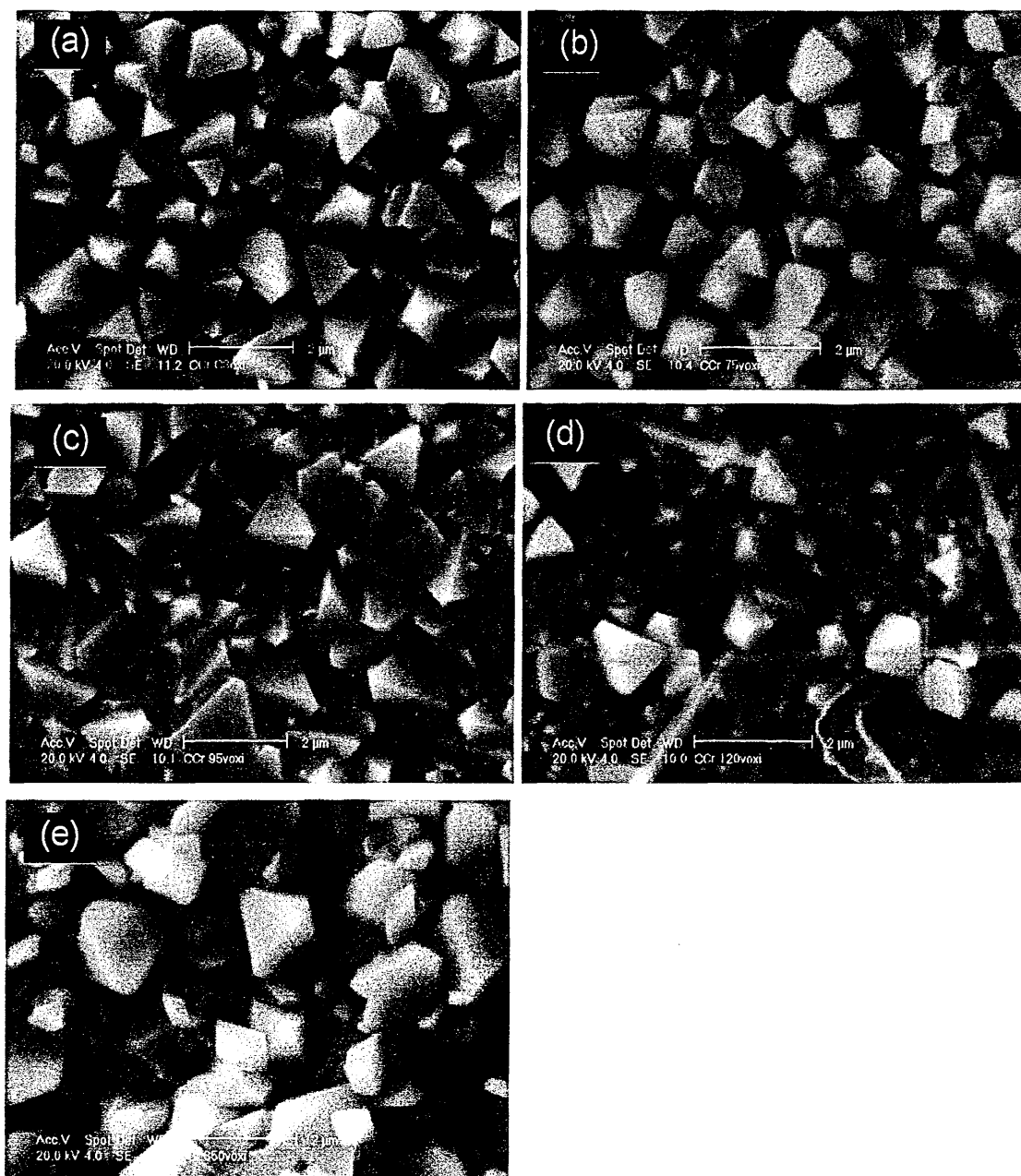


Figure 4.50 High magnification SEM surface morphology of chromium oxide formed on the oxidised surface after TGA tests: (a) $U_B = -65$ V, (b) $U_B = -75$ V, (c) $U_B = -95$ V, (d) $U_B = -120$ V, (e) $U_B = -350$ V

4.6.2 Isothermal heat-treatment

Figure 4.51 shows the glancing angle XRD results of the as deposited coating and the coatings after isothermal heat-treatment in air for 1 hour at 350 °C, 410 °C, 450 °C and 700 °C, respectively. As mentioned previously, the absence of the crystalline reflections in the as-deposited coating and the broad diffuse peaks indicates that the film microstructure is essentially amorphous, and for a bias voltage between $U_B = -65$ and -

120 V, the diffuse peaks appearing at 2θ values of $\sim 40^\circ$ and $\sim 80^\circ$ are corresponding to the positions of (110) and (211) reflections, respectively, from metallic chromium (see Figure 4.51(a)). The XRD pattern of an as-deposited $U_B = -350$ V sample shows the presence of (011) and (152) Cr_3C_2 at about 32° and 82° , respectively.

The XRD patterns of coatings annealed at various temperature show that the coating deposited at $U_B = -75$ V (Figure 4.51(b)) was fully oxidised to chromium oxide at a temperature 410°C and above, whereas for $U_B = -95$ V and $U_B = -120$ V samples (Figure 4.51(c) and (d) respectively), the coating can withstand temperatures up to 450°C (as the traces from the as deposited coating can still be observed) before being fully oxidised to chromium oxide (Cr_2O_3). For $U_B = -350$ V (Figure 4.51(e)), on top of the Cr_2O_3 peaks, (011) and (152) Cr_3C_2 reflections from the as deposited coating can still be observed up to 450°C , but it was fully oxidised to Cr_2O_3 at 700°C as revealed by a small shift in the peak at about 32° (Cr_3C_2) to 34° (Cr_2O_3). The coatings show preferential oxidation of the (110) Cr plane for bias voltage between $U_B = -75$ and -120 V, and of the (011) Cr_3C_2 plane for $U_B = -350$ V.

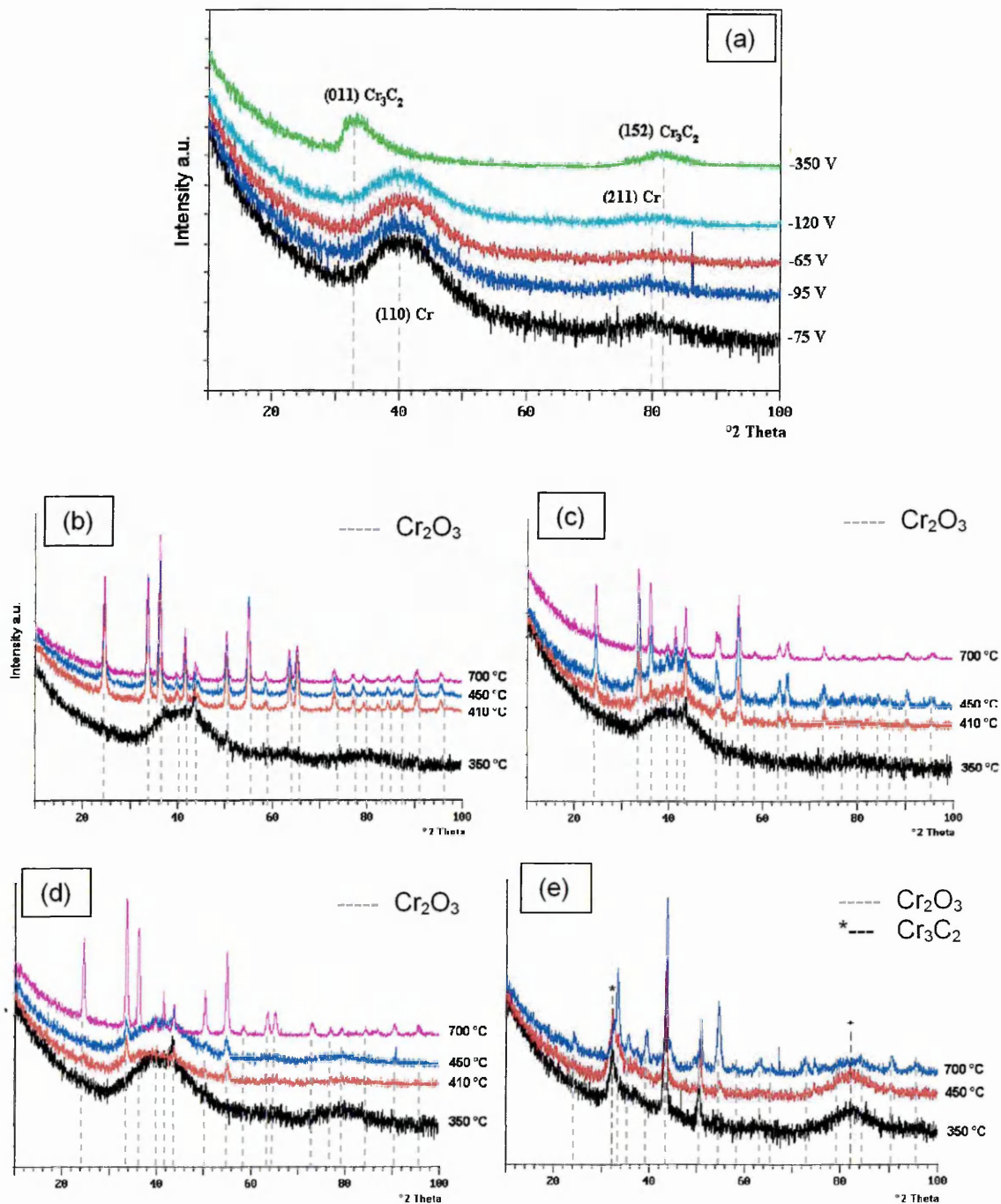


Figure 4.51 XRD patterns of (a) as deposited C/Cr coatings, and coating grown at (b) $U_B = -75$ V, (c) $U_B = -95$ V, (d) $U_B = -120$ V, and (e) $U_B = -350$ V, after being heat treated at the indicated temperature

Figure 4.52 to Figure 4.55 show the SEM surface morphology and the EDX analysis of the surface after heat treatment at 350 °C, 410 °C, 450 °C and 700 °C, for coatings deposited at various bias voltages. For all the applied bias voltages, no obvious changes occur in the microstructure of the coatings after being heat treated at 350 °C, 410 °C, 450 °C and 700 °C, except the surface was more porous as compared to the as-deposited coatings. This could be due to vaporisation of carbon oxide [184] during heat treatment. At 450 °C (Figure 4.54), EDX analysis detected a substantial increase in the oxygen level for coatings deposited at $U_B = -65$ and $U_B = -75$ V, only a slight increased for the $U_B = -95$ V sample, and remain nearly unaffected for coatings deposited at $U_B = -120$ and $U_B = -350$ V. At 700 °C (Figure 4.55), the intensity of the oxygen signal in the coatings exceeded that of chromium for bias voltages between $U_B = -65$ and -120 V, suggesting the formation of chromium oxide on the surface. Although the surface morphology and the EDX analysis of oxidised $U_B = -350$ V sample looks almost similar to the as-deposited coating, oxidation of the substrate has already begun around the edge of the sample (see Figure 4.55, -350 V-edge).

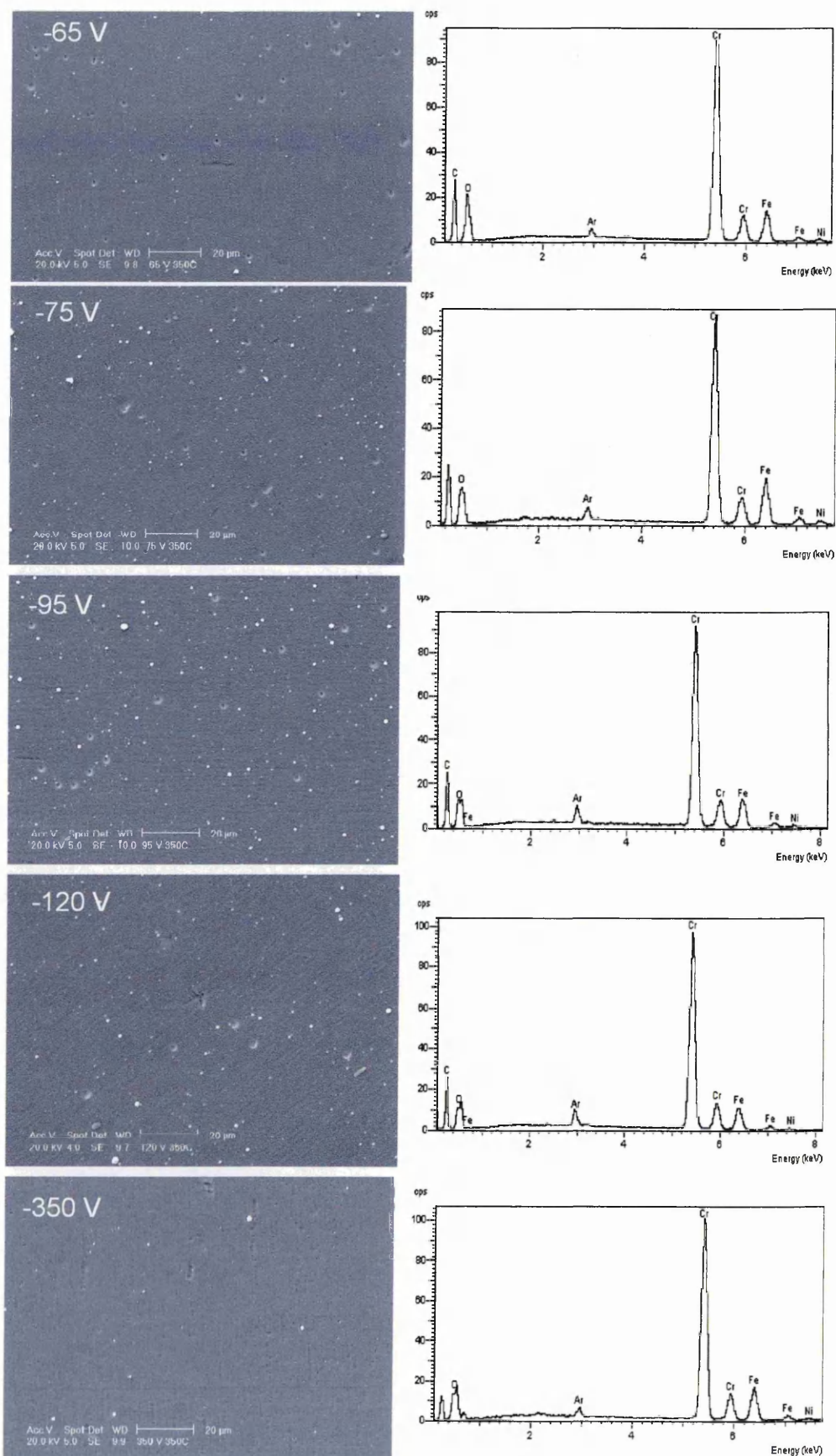


Figure 4.52 Surface morphology for coating deposited between $U_B = -65 \text{ V}$ and $U_B = -350 \text{ V}$ after heat treatment at 350 °C for 1 hour

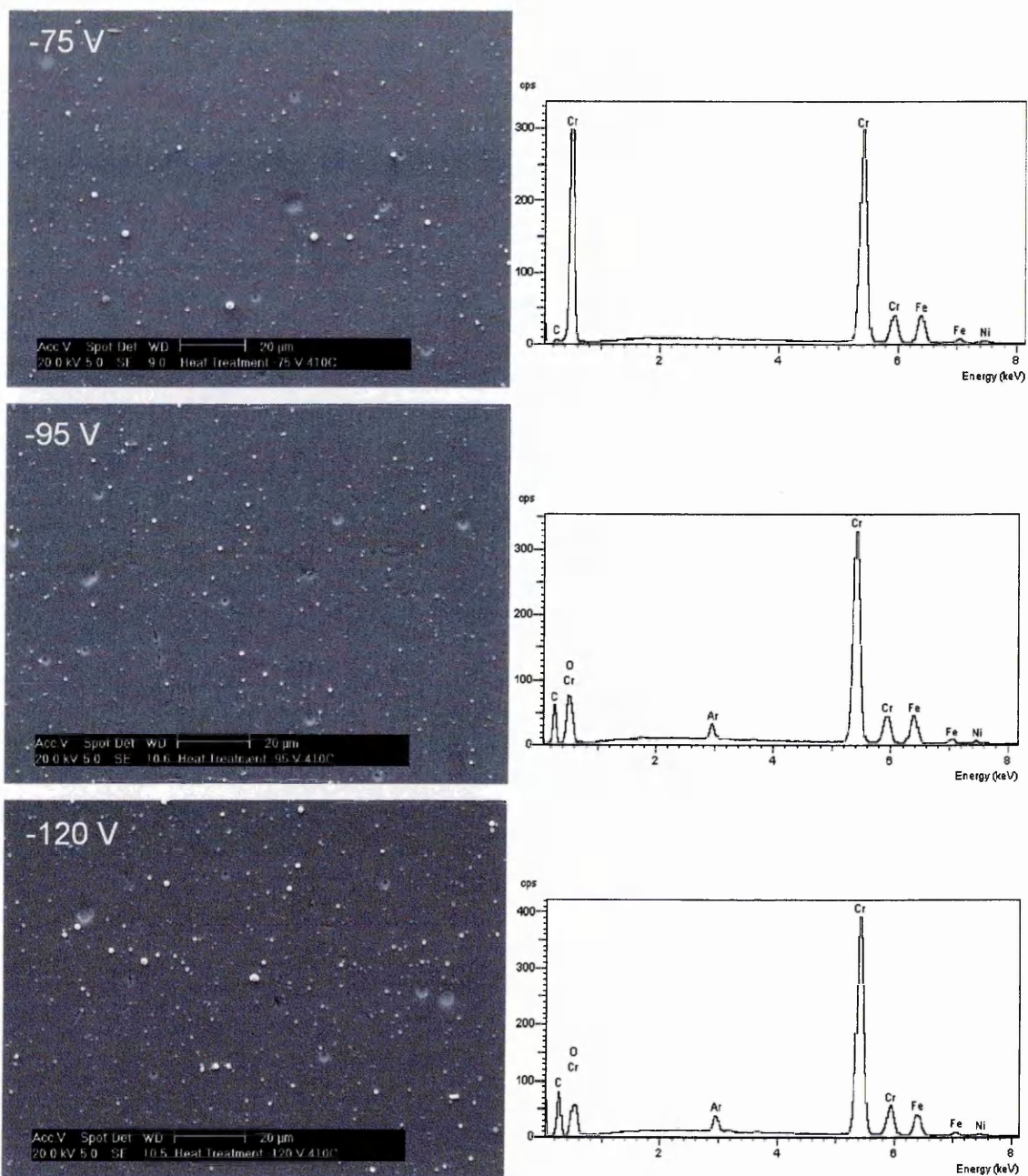


Figure 4.53 Surface morphology for coating deposited between $U_B = -75$ V and $U_B = -120$ V after heat treatment at 410 °C for 1 hour

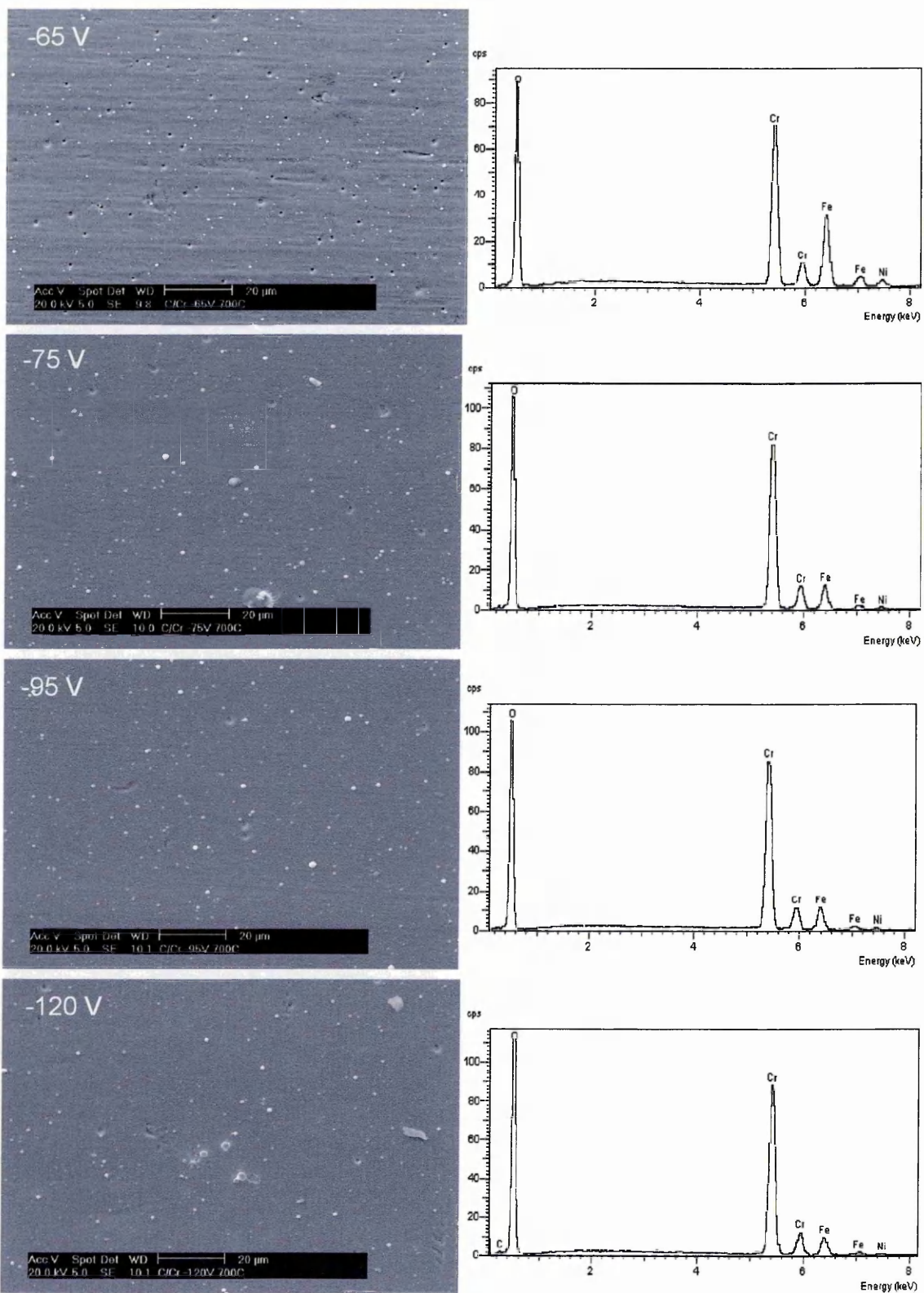


Figure 4.55 continues on next page

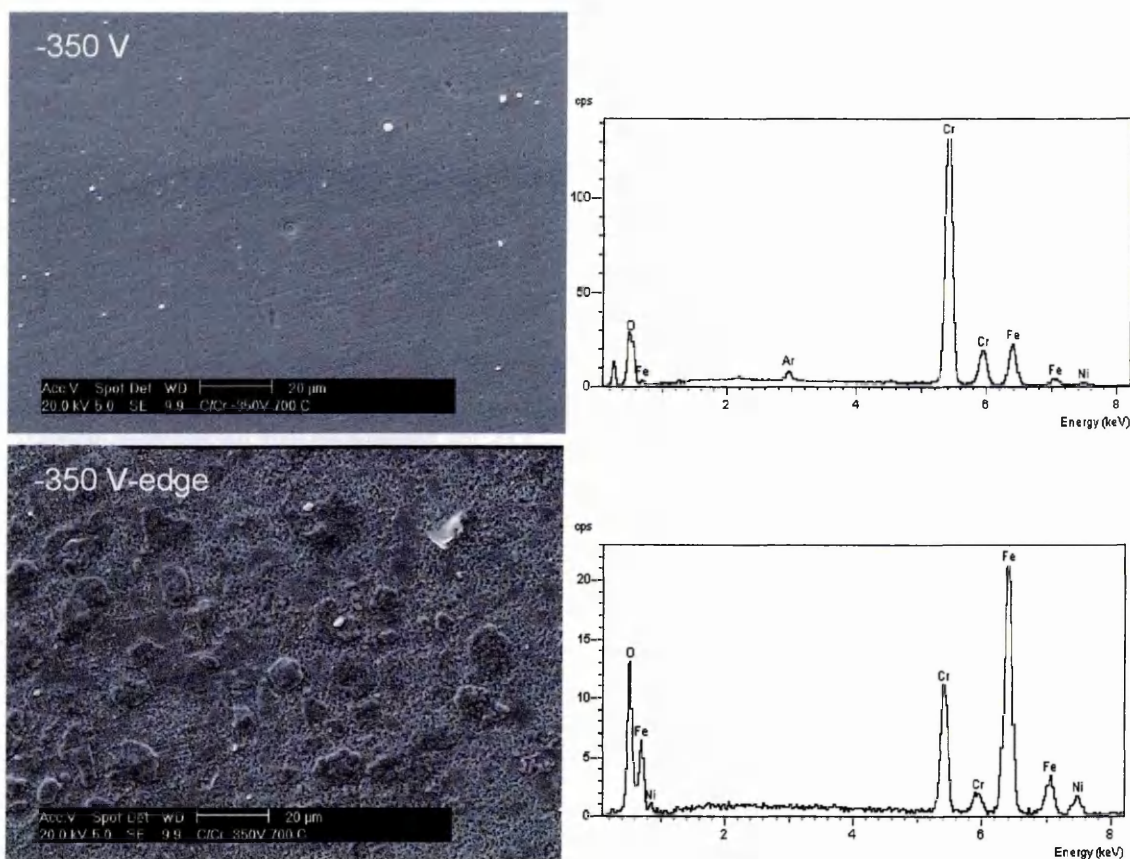
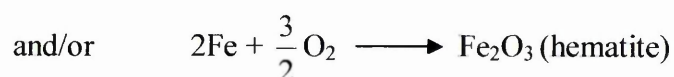


Figure 4.55 Surface morphology for coating deposited between $U_B = -65$ V and $U_B = -350$ V after heat treatment at 700 °C for 1 hour; the -350 V-edge shows the surface around the edge of coating deposited at $U_B = -350$ V after heat treatment

Figure 4.56 shows the initiation and growth of spiky globules at coating growth defects after heat treatment at 700 °C, regardless of the applied bias voltage. The EDX point analysis and elemental mapping of the spiky globule (Figure 4.56(d) and (e)) suggested that the globules were iron oxide, which could be grown from the substrate through the inward diffusion of O_2 and outward diffusion of iron via coating growth defects, surface cavities or grain boundaries. The mechanism of the onset of the oxidation process at localised coating growth defects that led to the formation of the spiky globule could be explained as follows:

- (a) Oxygen travels via growth defects (< 5 µm) to the substrate, reacts with the substrate through reactions



and forms iron oxide underneath the coating.

- (b) The oxide gradually increases in size ($> 5 \mu\text{m}$) and expands, resulting in coating detachment in order to 'release' itself (brighter contrast spike).
- (c) The oxide continues to grow in size ($> 10 \mu\text{m}$), forming the 'spiky' globule (which has been shown to be iron oxide by EDX analysis and EDX elemental mapping), and finally occupy the growth defect position.

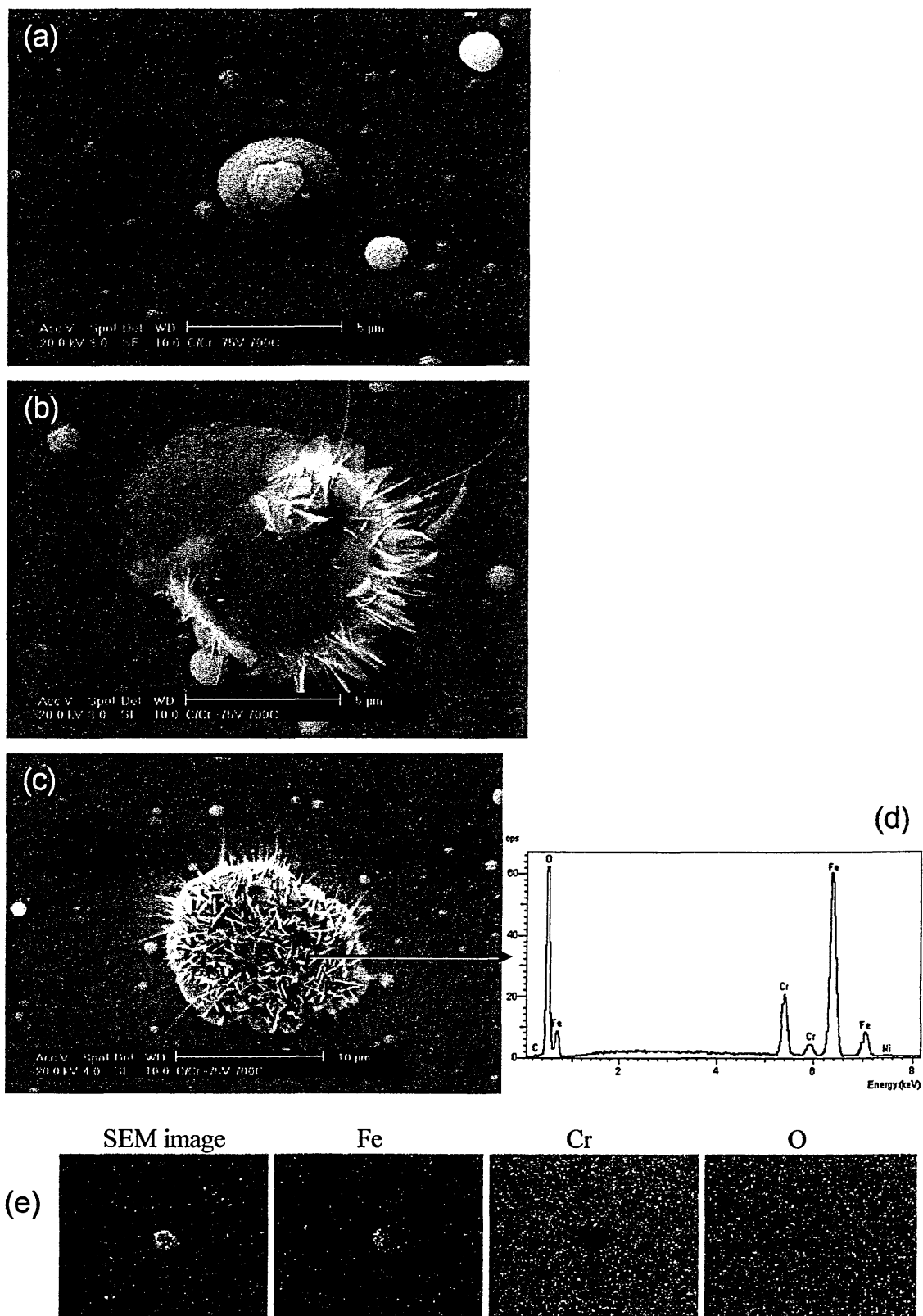


Figure 4.56 (a-c) Initiation and growth of spiky iron oxide globule; (d) EDX analysis, and (e) elemental mapping analysis of the spiky globule

Figure 4.57 shows the Raman spectra of samples annealed at 350 °C, 410 °C, 450 °C and 700 °C. For all the applied bias voltages, the Raman spectra of the coating annealed at 350 °C were similar to the as-deposited coating (see Figure 4.18 which showed the characteristic D and G-bands at about 1380 cm⁻¹ and 1580 cm⁻¹, respectively) and indicated no structural change at this temperature. At 410 °C, the coating deposited at $U_B = -75$ V (Figure 4.57(a)) clearly shows an upward shift of D and G bands from 1380 to 1400 cm⁻¹ and 1580 to 1596 cm⁻¹, respectively and a significant rise of D-band intensity with the G-band gradually disappearing with increased heating temperatures to 700 °C. Similar behaviour was also observed at 700 °C for coatings deposited at $U_B = -95$ and -120 V (Figure 4.57(b) and 4.57(c) respectively), both spectra showing an upward shift of D and G bands from 1380 to 1400 cm⁻¹ and 1590 to 1618 cm⁻¹, respectively, but no obvious change in the Raman spectra of both coatings between 350 °C and 450 °C, indicating the films are structurally stable up to 450 °C. The Raman spectrum of a $U_B = -350$ V sample heated at 350 °C shown in Figure 4.57(d) was similar to the as-deposited film (see Figure 4.18), which was featureless and detected no free carbon bonds (no D and G bands) suggesting no change in the Me-carbide character of the coating. However, at 450 °C the D and G bands begin to develop in magnitude. This may indicate conversion from Me-carbide to an amorphous carbon structure. The Raman spectra of the film heated at the higher temperature of 700 °C suggested complete conversion to highly disordered nano-crystalline graphite (D-band at 1338 cm⁻¹ and G-band at 1590 cm⁻¹ with shoulder at 1618 cm⁻¹) [171], and looks very much like the Raman spectrum of the bulk graphite target (see Figure 4.19) used in the deposition process (see chapter 5 for further discussion).

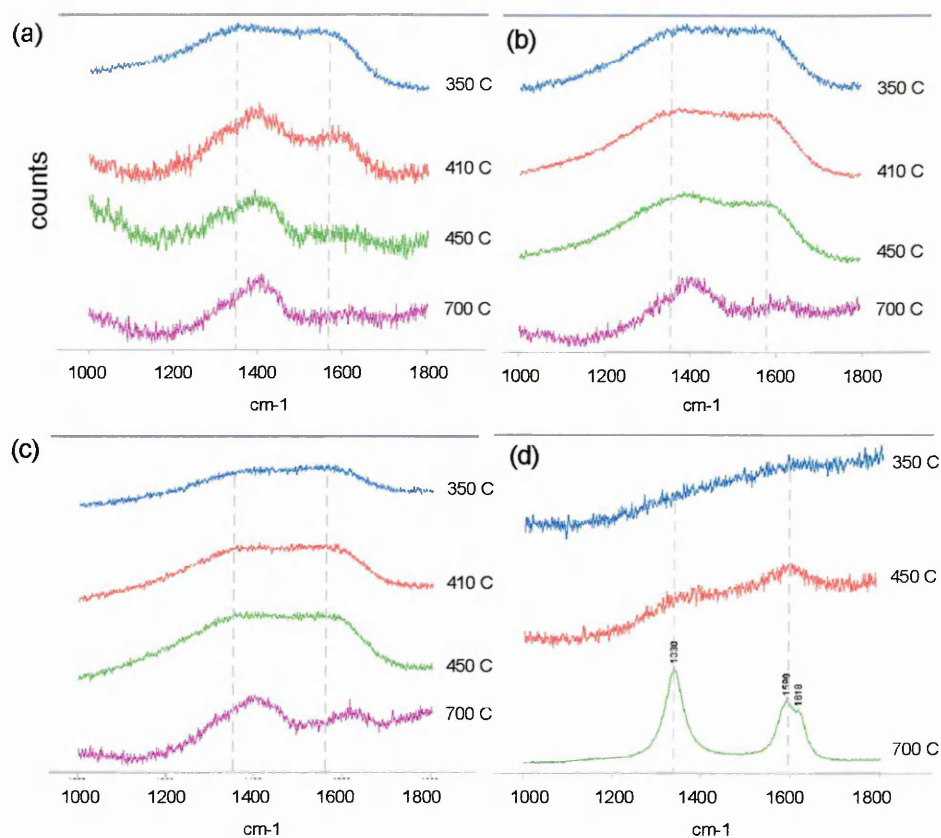


Figure 4.57 Raman spectra of coating deposited at (a) $U_B = -75$ V, (b) $U_B = -95$ V, (c) $U_B = -120$ V, (d) $U_B = -350$ V, heat-treated at the indicated temperature

4.7 Corrosion tests

The corrosion and corrosion-wear behaviour of C/Cr coatings in a 0.01% NaCl solution were investigated using a potentiodynamic polarisation test and a tribocorrosion test (modified SRET) respectively. The corroded surfaces of samples prepared between $U_B = -75$ and $U_B = -350$ V were examined using a SEM and an optical microscopy. This work has been published [185]. The pitting mechanism of the coating and the substrate will be discussed in Chapter 5.

4.7.1 Potentiodynamic polarisation test

The corrosion behaviour of C/Cr coated 316 stainless steel (SS) steels deposited at various bias voltages is shown in Figure 4.58. The polarisation curve of uncoated

stainless steel is included as a reference. The results show that the free corrosion potential, E_{corr} of the coated samples ($E_{\text{corr}} \sim -50$ mV) are more positive than those of the 316 stainless steel substrates ($E_{\text{corr}} \sim -122$ mV), which suggests [186] that C/Cr coatings improve the ability to resist pitting corrosion of the steel substrate in 0.01% NaCl solution. In addition, the reduced corrosion current density, by about one order of magnitude in the coated samples ($\sim 2\text{-}3 \times 10^{-9}$ A/cm²), further suggests better corrosion resistance of C/Cr coated samples than the uncoated sample ($\sim 2\text{-}3 \times 10^{-8}$ A/cm²). For potentials below +450 mV, the corrosion resistance of C/Cr coatings improved with increasing bias voltage except for the $U_B = -350$ V sample which shows a slightly increased current density when compared to the $U_B = -95$ V and $U_B = -120$ V samples. For example, for the potential of +300 mV (see Figure 4.59), a strong correlation was found between bias voltage and the anodic current density in the polarisation tests, where the current density decreases from $\sim 4.7 \times 10^{-7}$ to 1×10^{-7} A/cm² with increasing bias voltage from $U_B = -65$ to -95 V and then increases slightly to $\sim 1.4 \times 10^{-7}$ A/cm² with further increase in the bias voltage to $U_B = -350$ V. However, above +450 mV, the current density of the coatings accelerating towards higher values being particular noticeable for $U_B = -65$ V, -95 V and -350 V samples. Except for the $U_B = -120$ V sample, the corrosion rate increased (substantial increased in the current density with a slight increase in the potential) between the potential range of ~ 460 and 490 mV for the $U_B = -65$ V sample, ~ 470 and 560 mV for the $U_B = -95$ V sample, and ~ 490 and 590 mV for the $U_B = -350$ V sample.

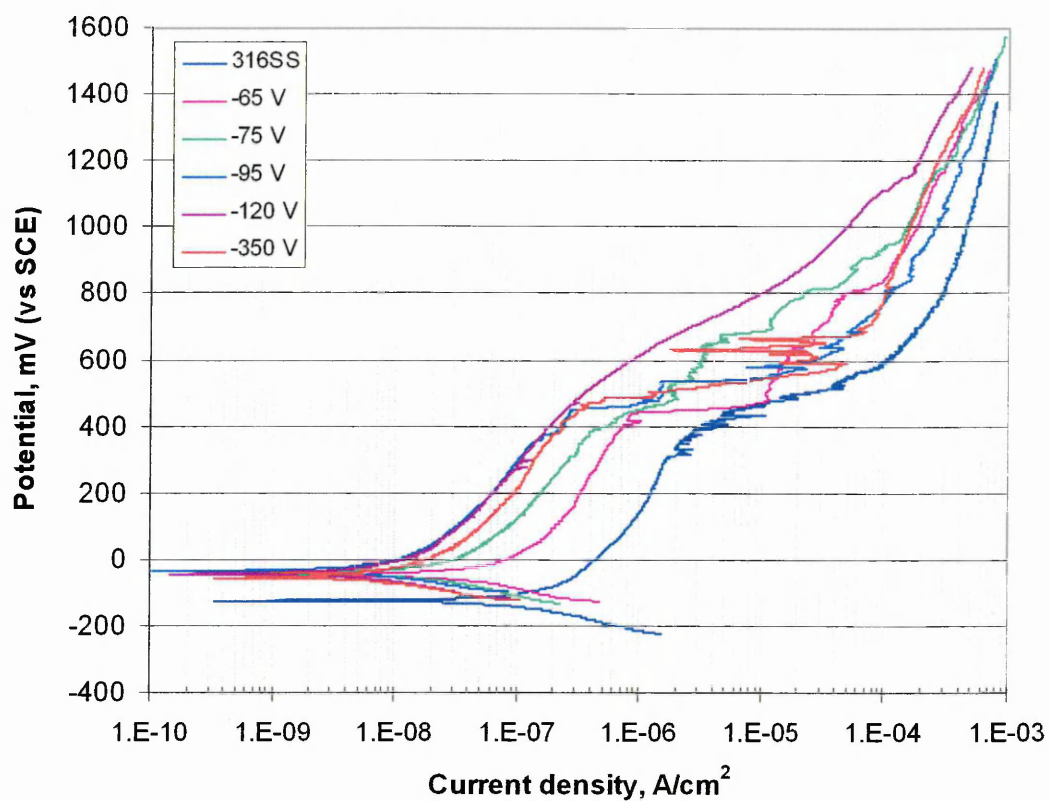


Figure 4.58 Potentiodynamic polarisation curves for uncoated (316SS) and C/Cr coated samples

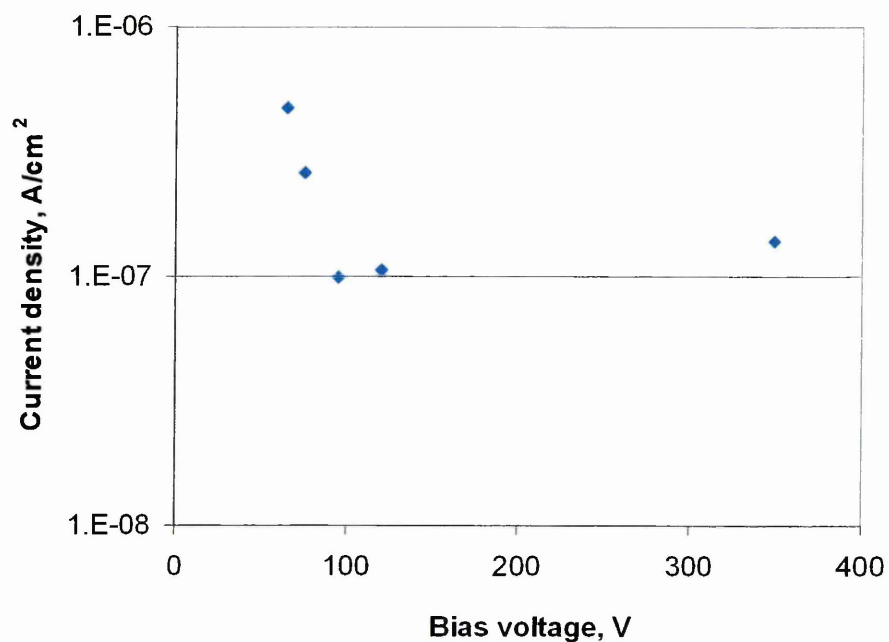


Figure 4.59 Comparison of anodic current density at a working electrode potential of +300 mV against the substrate bias voltage for C/Cr coated samples

The SEM surface morphologies after polarisation tests of coatings deposited at various substrate bias voltages are presented in Figure 4.60 (low magnification) and Figure 4.61 (higher magnification) (see Figure 4.24 for the surface morphology of as-deposited coatings). The white contrast droplets on the coating surface in Figure 4.61 are coating growth defects (macroparticles). Pitting and detachment of coatings were observed on all samples after polarisation tests. It was noted from Figure 4.60 to 4.61 that coatings deposited at $U_B = -120$ V exhibited only localised coating delamination without pitting through the substrate, whereas samples prepared between $U_B = -65$ and -95 V, and $U_B = -350$ V show both localised delamination and pitting. This may explain the smoother and better polarisation curve of the $U_B = -120$ V sample (see Figure 4.58). Evidence of localised pitting (Figure 4.62(a) and (d)) initiating from local growth defects such as pinholes and macroparticles is presented in Figure 4.62. Arrows show the possible penetration paths of the solution into the substrate defects, such as dissolved macroparticles (Figure 4.62(b)-(c)) and through under-dense structure around growth defects (Figure 4.62(e)), leading to pitting and dissolution of the coating and the substrate. The cross-sectional SEM image of the film deposited at $U_B = -350$ V (Figure 4.62(f)) has a very dense structure that would be expected to slow down oxygen diffusion.

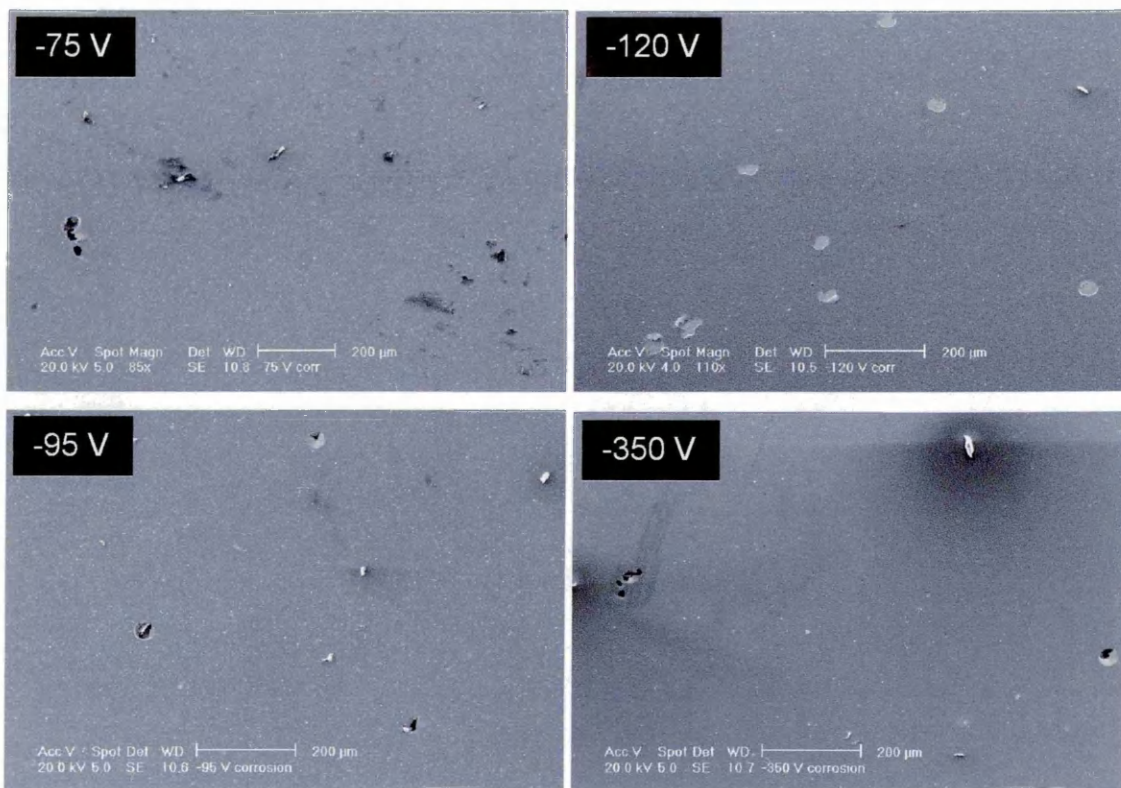


Figure 4.60 SEM images after potentiodynamic polarisation tests of C/Cr films deposited at the indicated bias voltage

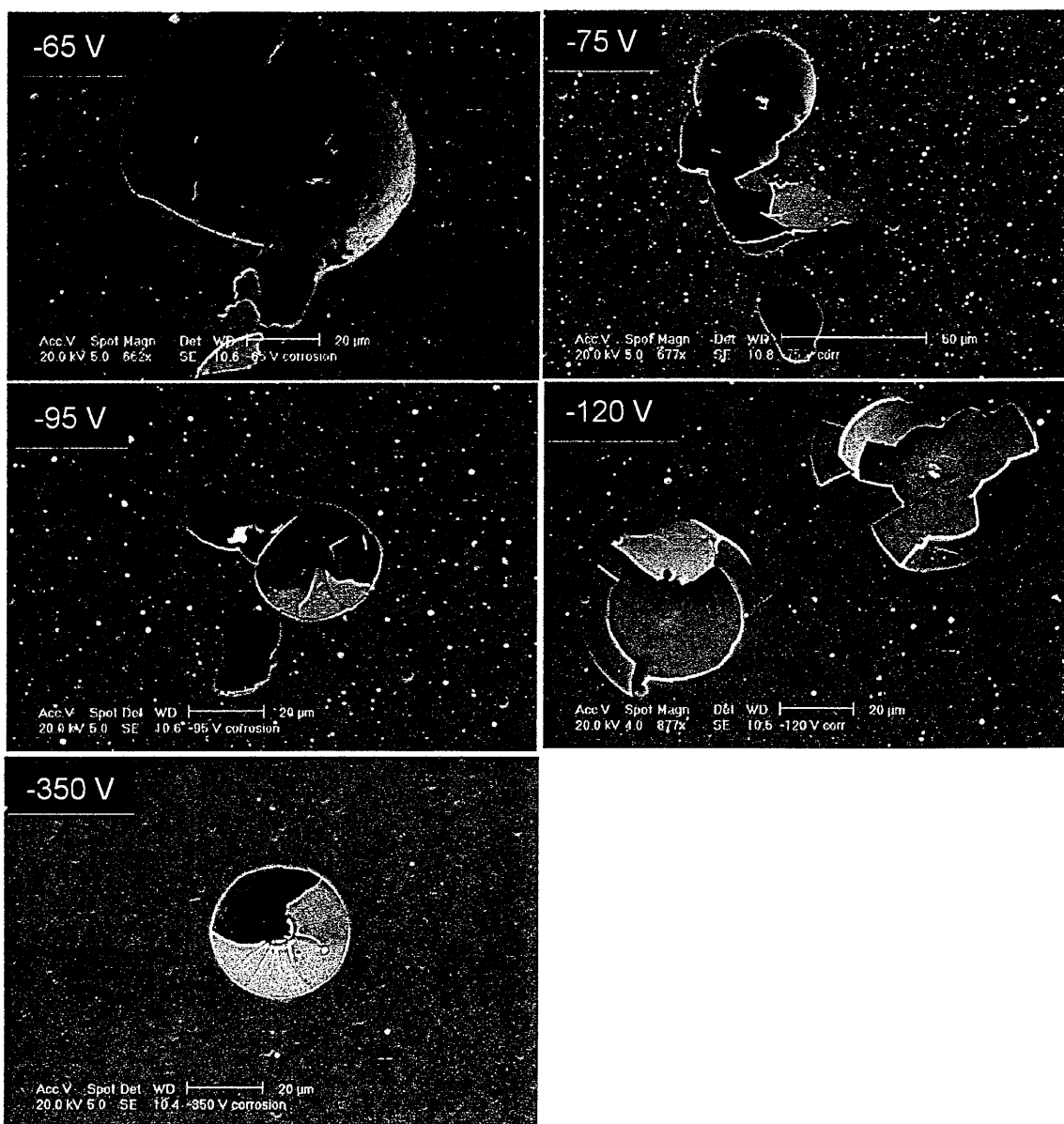


Figure 4.61 SEM surface morphology after potentiodynamic polarisation tests for C/Cr coated samples prepared at the indicated bias voltage

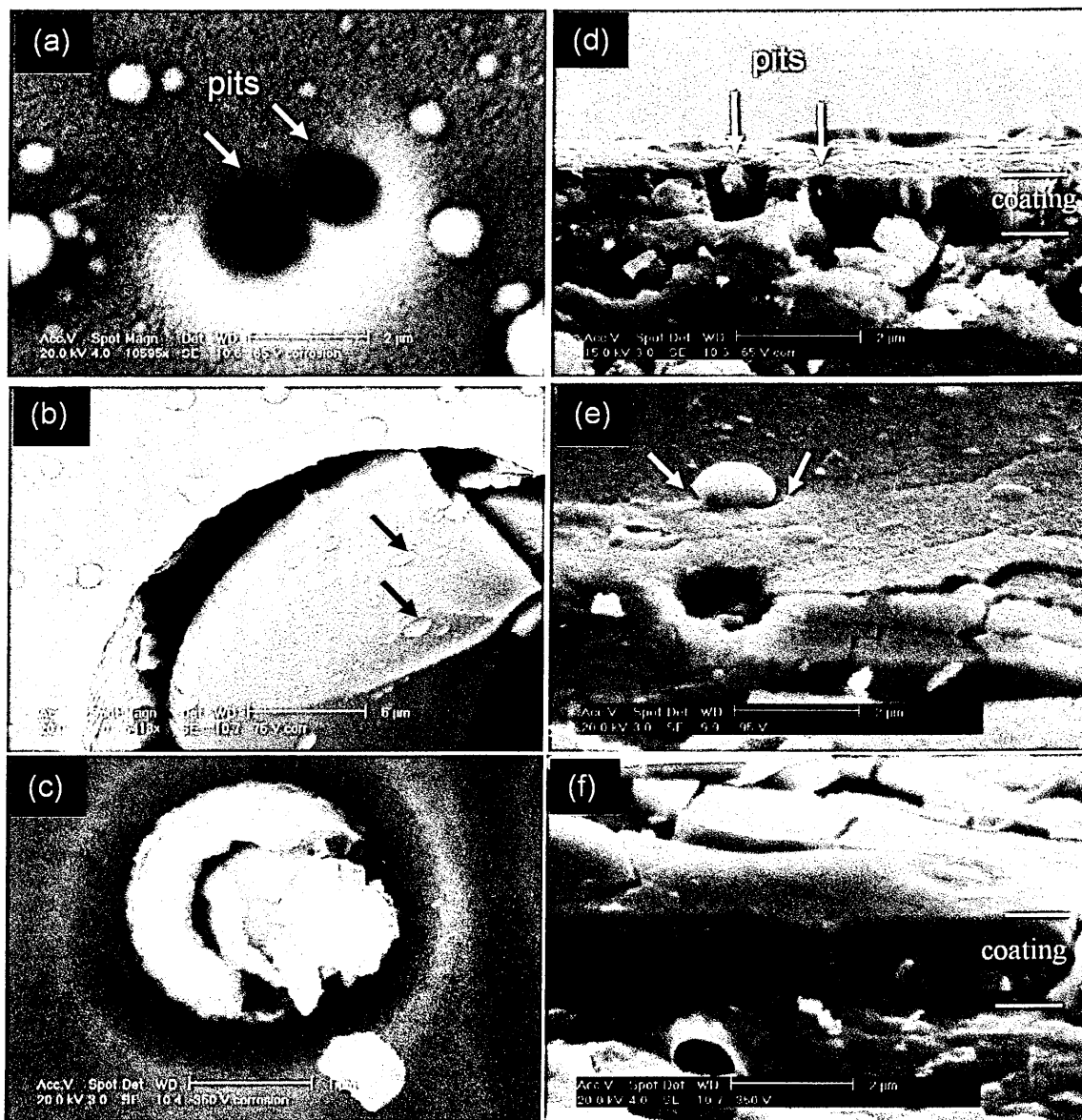


Figure 4.62 Pitting mechanisms: surface morphology of (a) $U_B = -65$ V, (b) $U_B = -75$ V, (c) $U_B = -350$ V, and cross-section of the polarised samples (d) $U_B = -65$ V, (e) $U_B = -95$ V, (f) $U_B = -350$ V (note: cracking of the coating was the consequence of poor cross-section sample preparation)

4.7.2 Tribocorrosion test

Test 1: Calibration of the system

The results of the tribocorrosion calibration test carried out in air and tap water are presented in Figure 4.63. For both calibration environments, the output signal was very consistent and linear, with output signal increasing linearly with increasing applied load. A linear response was also obtained regardless of whether the sample was coated

or uncoated, as shown in Figure 4.64. Thus, it was concluded that the load applied on the arm (via the pan) is proportional to the load applied on the sample. Note that the calibration curves shown in Figure 4.63 and 4.64 are based upon the SS substrate. Different substrate materials may, subject to their deformation behaviour, produce different calibration curves.

It was noted that the eccentricity due to the centrifugal force of sample rotation can not be fully eliminated using the ball bearing support at the end of the sample (see Figure 3.3). Thus, the sample moved laterally during rotation which led to a simultaneous horizontal displacement of the sample of about 50–100 μm . This can contribute to a scatter of the results recorded. In addition, when the tribocorrosion test was carried out at a load $\geq 4\text{ N}$ for a longer period of time (e.g. greater than 30 min), the corrosion cell moved, leading to a misalignment of the sample from its centre of rotation, causing the sample to stop rotating. Therefore, careful set-up of the sample, tank, and sliding probe is essential for tribocorrosion testing.

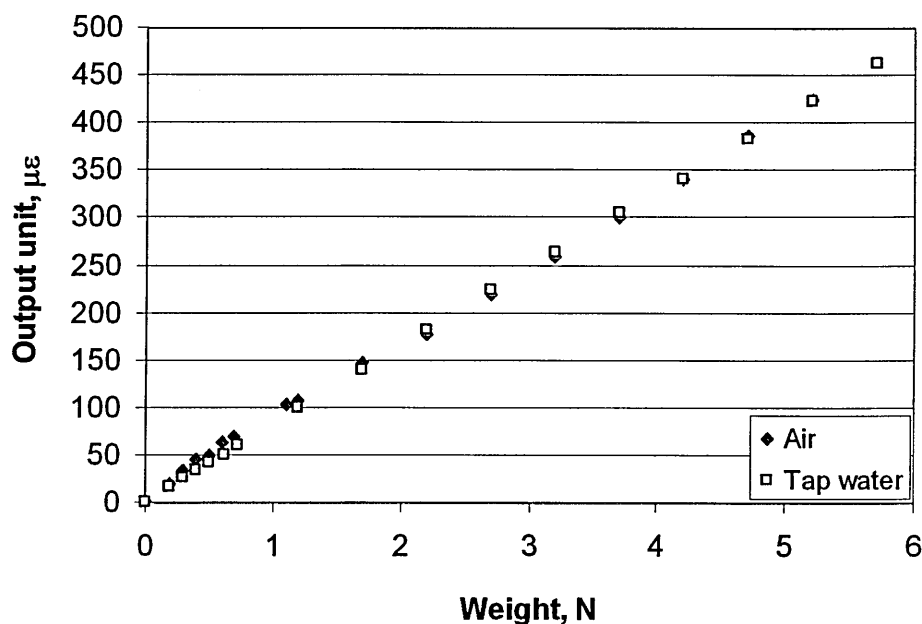


Figure 4.63 Tribocorrosion calibration results in air and tap water for SS sample

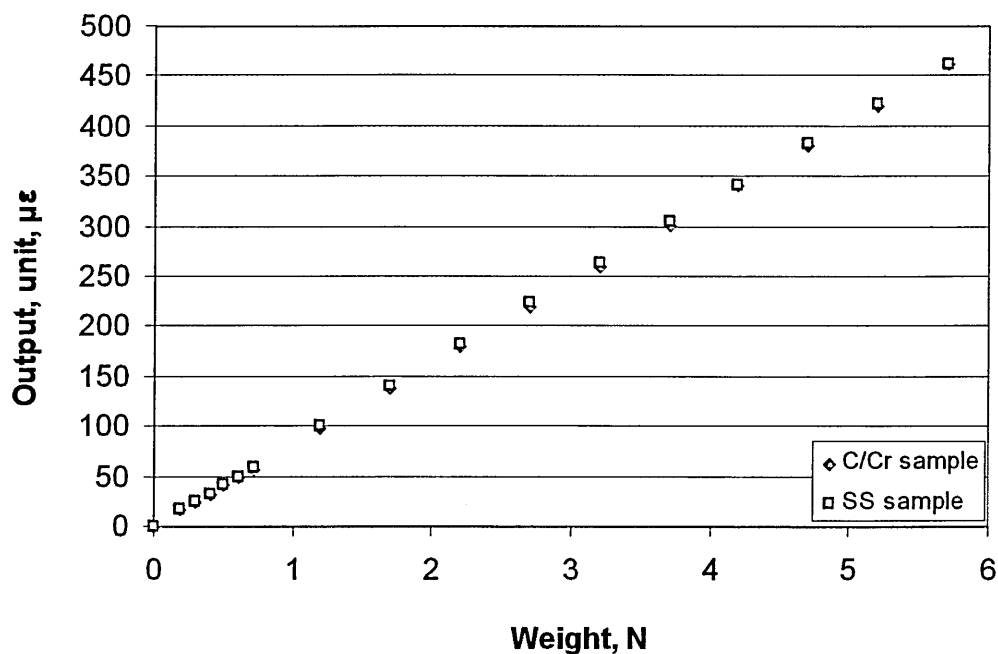


Figure 4.64 Tribocorrosion calibration results in tap water for SS and C/Cr coated samples

Test 2: Effects of applied load on E_{corr}

Figure 4.65 shows the variation of the open circuit potential (OCP or E_{corr}) measured under unloaded and mechanically loaded conditions. The E_{corr} recorded during the tests is a mixed potential reflecting the activity of the unworn material and the activity of the material in the wear track. Thus, a galvanic coupling between damaged and undamaged sites on the sample surface takes place. An applied normal force was found to cause a change in the free corrosion potential of the samples. The initial part of the graph, from 0 to 5 min, shows the E_{corr} of the freshly ground 316 SS sample at zero load (non-contact). After 5 min, a 1 N load was applied to the rotating sample, where an instantaneous decrease of the E_{corr} was observed (note: similar behaviour was observed when a 3 N load was applied). A similar potential trend has been observed by Ponthiaux et. al. [187]. When the sliding counterface is applied to the surface, the corrosion potential suddenly decreases, this potential shift is associated with passive film damage. Here, three possible processes occur: (i) the surface changes from a passive to active state induced by wear [188], followed by (ii) local dissolution of the base material as a consequence of the galvanic coupling between the passive surface layer and the bare base material, and (iii) a larger area of active material in the wear track (i.e. larger wear track) due to increased load [187], this is shown and discussed in

Experiment 3 later. During tribocorrosion, material removal takes place simultaneously by mechanical wear and corrosion. Most corrosion-resistant metallic materials such as stainless steels are protected by a thin 1–2 nm thick oxide passive film, which forms on the surface by spontaneous reaction with oxygen in the environment [189]. Abrasion leads to local removal of the passive film resulting in exposure of bare metal to the aggressive environment, which subsequently, may or may not, repair itself by oxidation. Passive film breakdown therefore leads to a substantial increase in the anodic partial current [190], and to an increase in local corrosion rate. On unloading, E_{corr} increases (anodic shift), and approaches the initial E_{corr} value (prior to loading) as a result of sample repassivation.

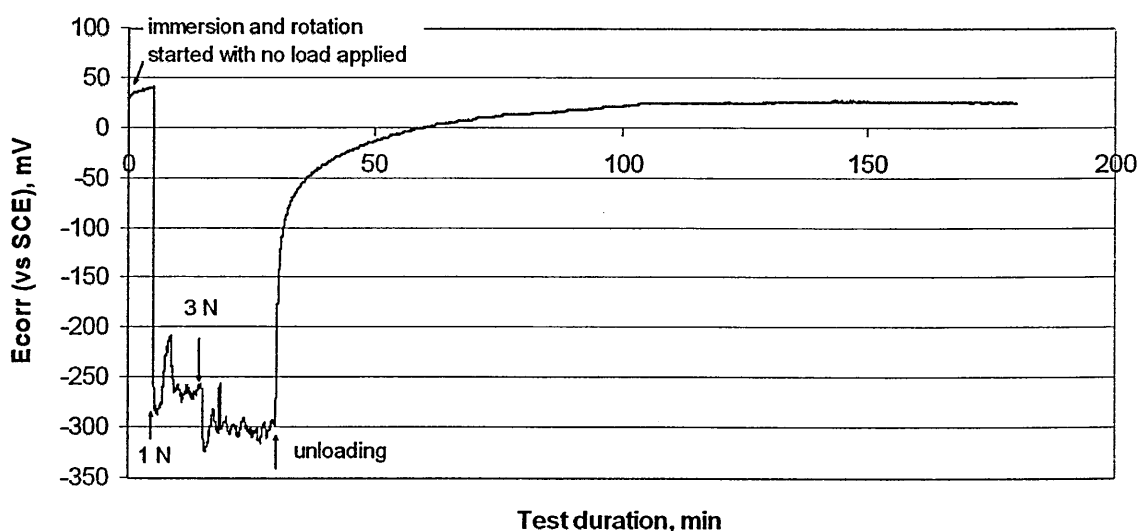


Figure 4.65 Influence of loading and unloading on the open circuit potential of SS in 0.01% NaCl

Figure 4.66 shows the variation in the free corrosion potential of a C/Cr coated sample under tribocorrosion conducted in 0.01% NaCl at 1 N load. E_{corr} , at the onset of the test, decreases from -23 mV to -170 mV after ~20 min of sliding contact. Some recovery/stabilisation of the surface occurs during loading as E_{corr} increases gradually to -140 mV. The sudden change in the potential to above 0 mV occurred when the sliding contact was removed. This negative shift in the corrosion potential, which occurs on loading is similar to that for the stainless steel sample discussed above, and could be the result of (i) removal of the coating passive film due to mechanical interaction between the counterbody, the sample and corrosion of the exposed area, and (ii) subsequent

reformation (contact with the electrolyte) of the chromium passive oxide layer on the sample surface [188, 191]. The time taken for the regeneration (i.e. recovery) of the passive film depends on the repassivation tendency of the material and the nature of the electrolyte.

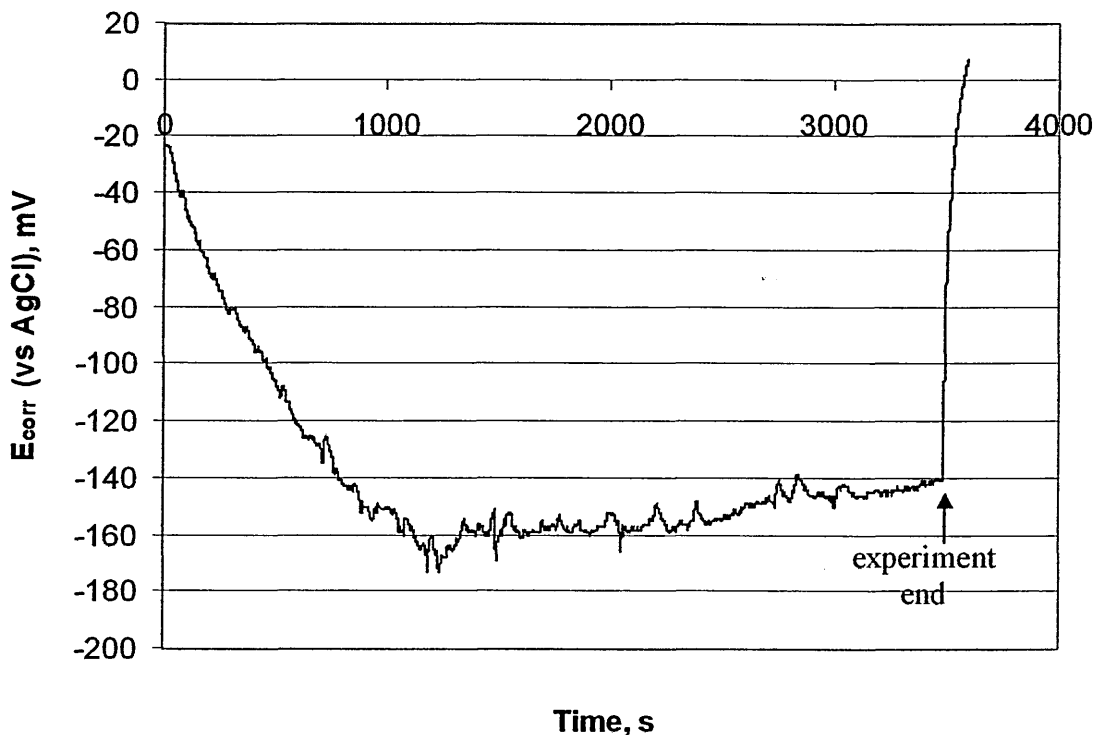


Figure 4.66 E_{corr} versus time for C/Cr coated SS at a load of 1 N in 0.01% NaCl

Test 3: Effects of applied load on localised corrosion activity

The initial tribocorrosion test was conducted under open circuit conditions. Figure 4.67 shows the SRET line scan under various applied loads for uncoated and C/Cr coated stainless steel. Note that the displacement on the x-axis corresponds to the position along the circumference of the sample (position 0 \equiv position 47123 μm). Abrasion between the alumina ball and the rotating sample led to an increase in anodic and cathodic activities (see Figure 4.67) indicating an increase in corrosion activity (negative direction) due to the activation of the anodic reaction. Note that the SS sample (Figure 4.67(a)) experiences about one order of magnitude higher anodic activity than the C/Cr coated sample (Figure 4.67(b)). In-situ monitoring of the sample using the line scan mode revealed the active sites as ‘movable anodes’, where the anodic areas varied in magnitude and location with applied load and exposure time. Increasing the load

from 1 N to 6 N caused an increase in the number and magnitude of the local active sites and increased removal of material from the wear track.

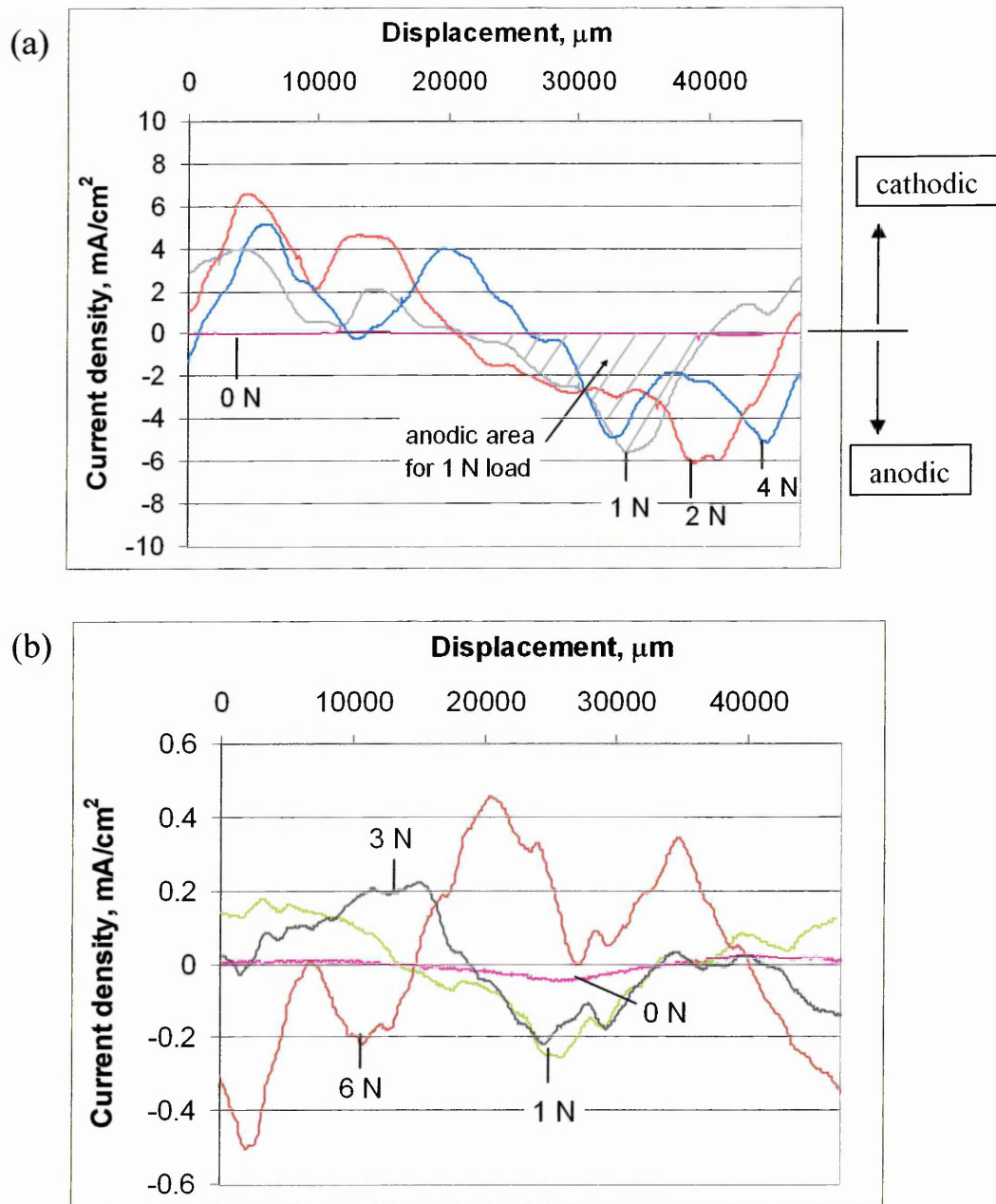


Figure 4.67 SRET line scan under various applied loads for identical contact times (30 s per load) for (a) SS and (b) C/Cr coated samples (note that portion negative values relate to anodic activity and positive values to cathodic activity)

Figure 4.68 presents the damage, mC/cm^2 , after loading for uncoated (SS) and C/Cr coated samples. The damage, being equivalent to the total volume of metal loss

(mC/cm^2), was calculated based on the area under the anodic portion of the SRET line scan curve in Figure 4.67 by using Simpson's rule (see shaded area). This value was observed to increase with increasing load, being particularly obvious for the SS sample. Furthermore, this analysis clearly shows that the C/Cr coating reduces the substrate damage at various applied loads as can be seen by the large reduction in the damage parameter determined for the C/Cr coated sample compared to that for the uncoated sample. This may be attributed to the chemical inertness and self-lubricating characteristics of the graphite present in the coating, resulting in a reduction in the overall friction between the two rubbing surfaces. To identify the trend of the effect of applied load on the damage generated, two tests were carried out on (1) uncoated stainless steel for a contact time of 5 min per load at various loads between 1 N and 4 N, with each load applied at a new position on the sample, and (2) C/Cr coated sample for a contact time of 5 min per load at the same contact point. The results of the SRET line scans and the equivalent total volume of metal loss in terms of mC/cm^2 (based on the calculation described above) for (1) and (2) are shown in Figure 4.69 and Figure 4.70 respectively. Similar behaviour, as observed in Figure 4.67 and 4.68, was noted i.e. increased anodic current density, and area under the anodic portion of the SRET line scan for an increase in load. However, when comparing Figure 4.69 and Figure 4.70 with Figure 4.68, a slight decrease in the damage was observed at 3-4 N for the uncoated sample, and 4-5 N for C/Cr coated samples. The wear tracks generated at the corresponding load (from 1 to 4 N) are shown in Figure 4.69(b) and the area under the wear tracks obtained using a stylus profilometer was plotted as the secondary Y-axis in Figure 4.69(c). The results show that there is a correlation between the damage generated under the anodic portion of the SRET line scan and the material loss in the wear track, resulting from the interaction between corrosion and mechanical wear. Permanent wear scars for different loads was generated on the sample after tribocorrosion testing are shown in Figure 4.69(b). The wave peaks on the outer edge of the wear track are possibly due to plastic flow of the indented metal around the sliding ball [192].

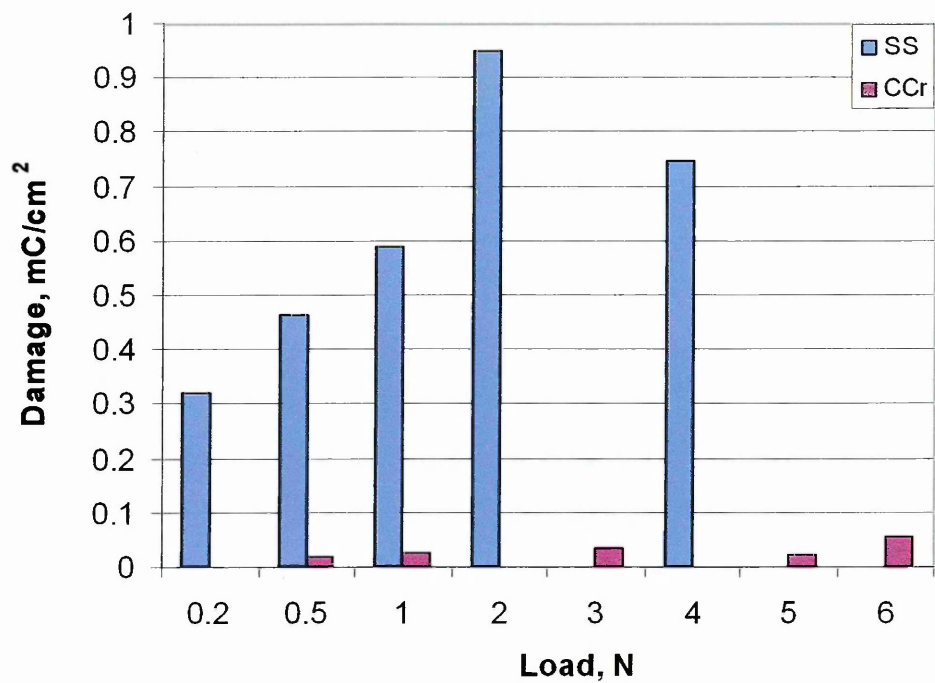


Figure 4.68 Equivalent total volume of metal loss (mC/cm^2) calculated from SRET line scans shown in Figure 4.67

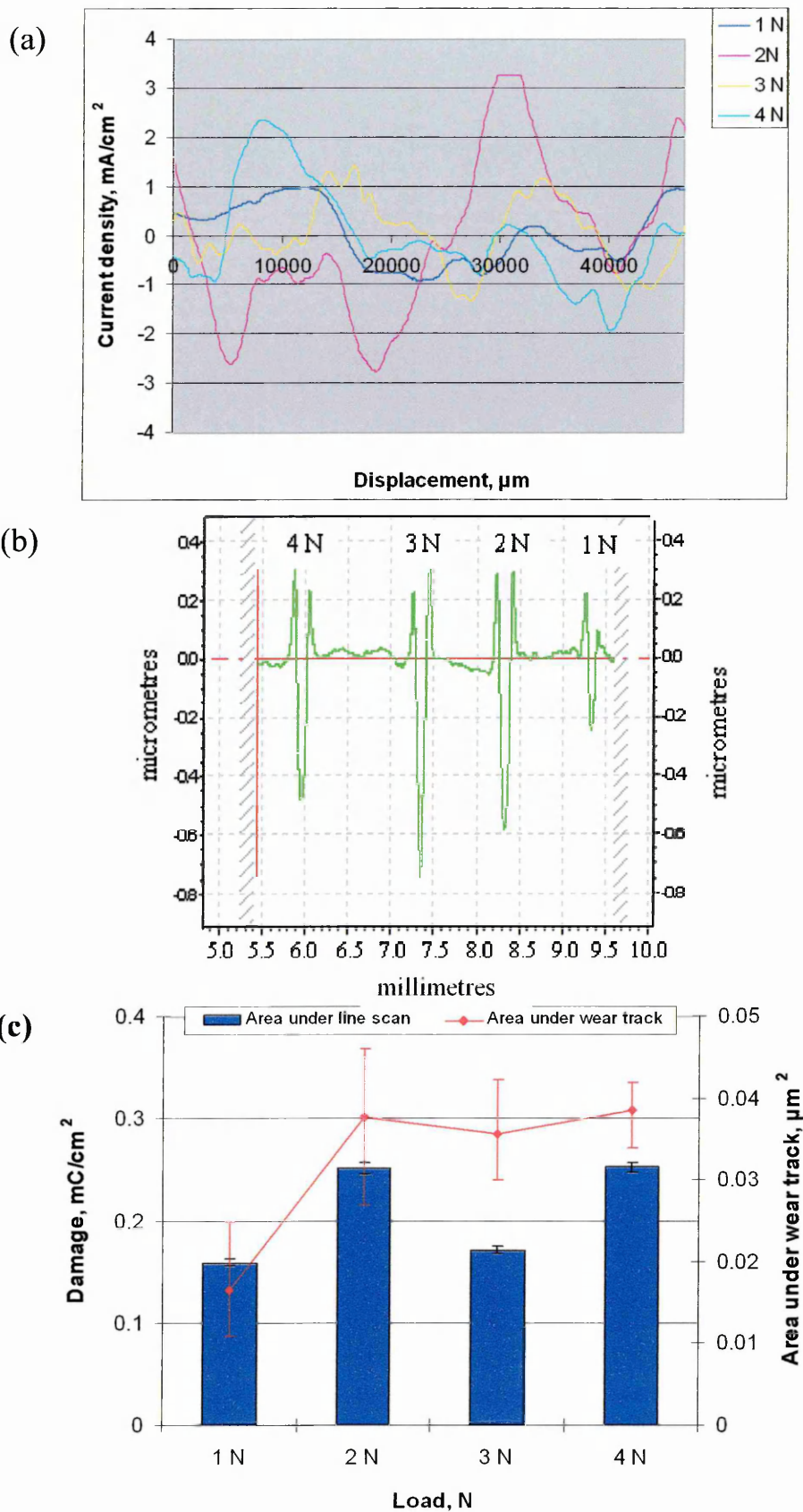


Figure 4.69 Uncoated SS sample (a) SRET line scan under various applied loads for 5 min contact time per load at new position for each load, (b) the corresponding wear track generated at the load indicated, (c) Area under the wear tracks and equivalent total volume of metal loss (mC/cm²) calculated from SRET line scan shown in (a) as a function of load

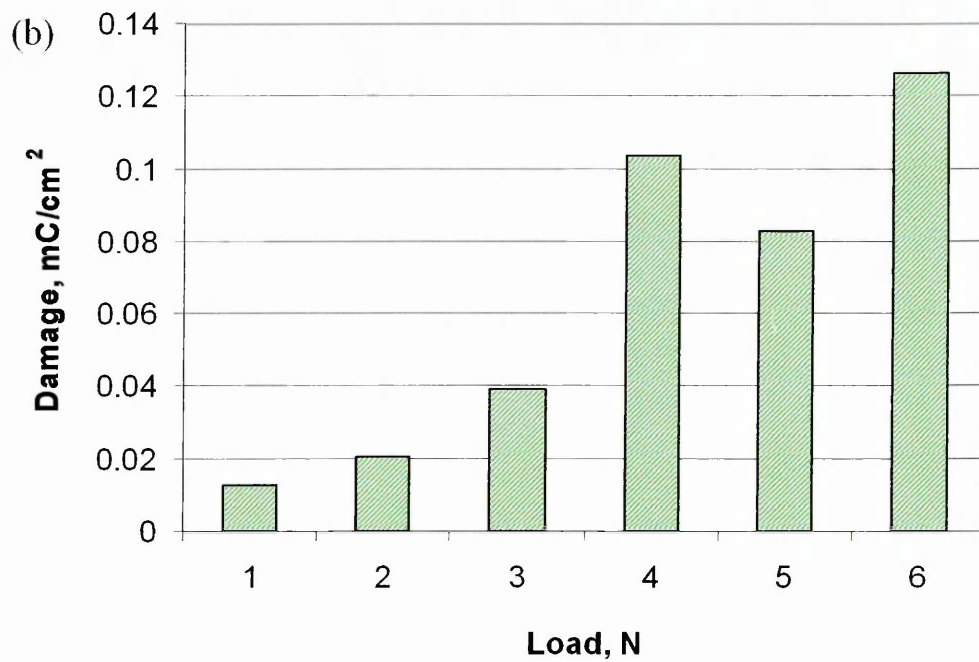
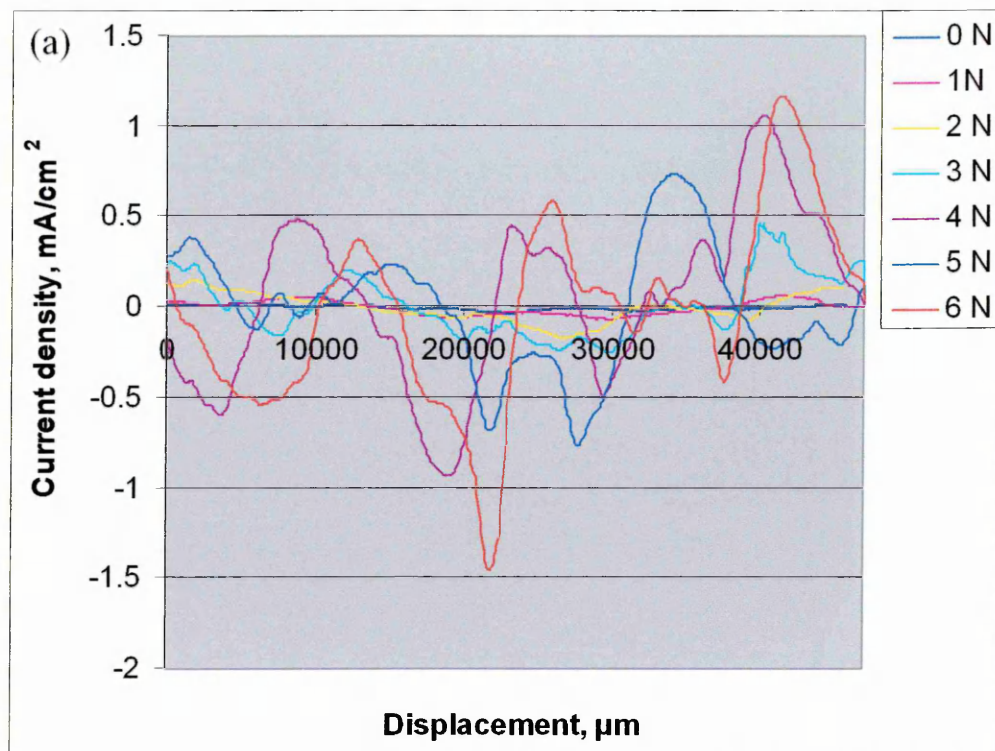


Figure 4.70 C/Cr coated sample (a) SRET line scan under various applied loads for 5 min contact time per load on same contact point, (b) Equivalent total volume of metal loss (mC/cm^2) calculated from SRET line scan shown in (a)

Figure 4.71 shows the damage (area under the SRET line scans) generated at various loads from 0.5 N to 5 N as a result of testing for durations from 5 s to 60 min. The damage generated after 5 s, i.e. almost instantaneously after a load was applied is large, which then decreases significantly after about 30 s (except at 1 N in Figure 4.71(a) and at 0.5 N of Figure 4.71(b)) and increases again with further increase in the contact time. This trend may be correlated to the graph plotted in Figure 4.65 showing the effect of load on open circuit potential (E_{corr}) of the sample, where E_{corr} decreases significantly upon immediate loading, followed by gradual increase to a maximum after about 3-4 min and a further decrease until finally remaining almost constant at their stable state. The fluctuation of E_{corr} is due to fluctuations in the normal force related to the mechanical stiffness [190] of the SRET-tribometer used in the experiment, and the result demonstrates the sensitivity of the measured potentials to the prevailing mechanical conditions.

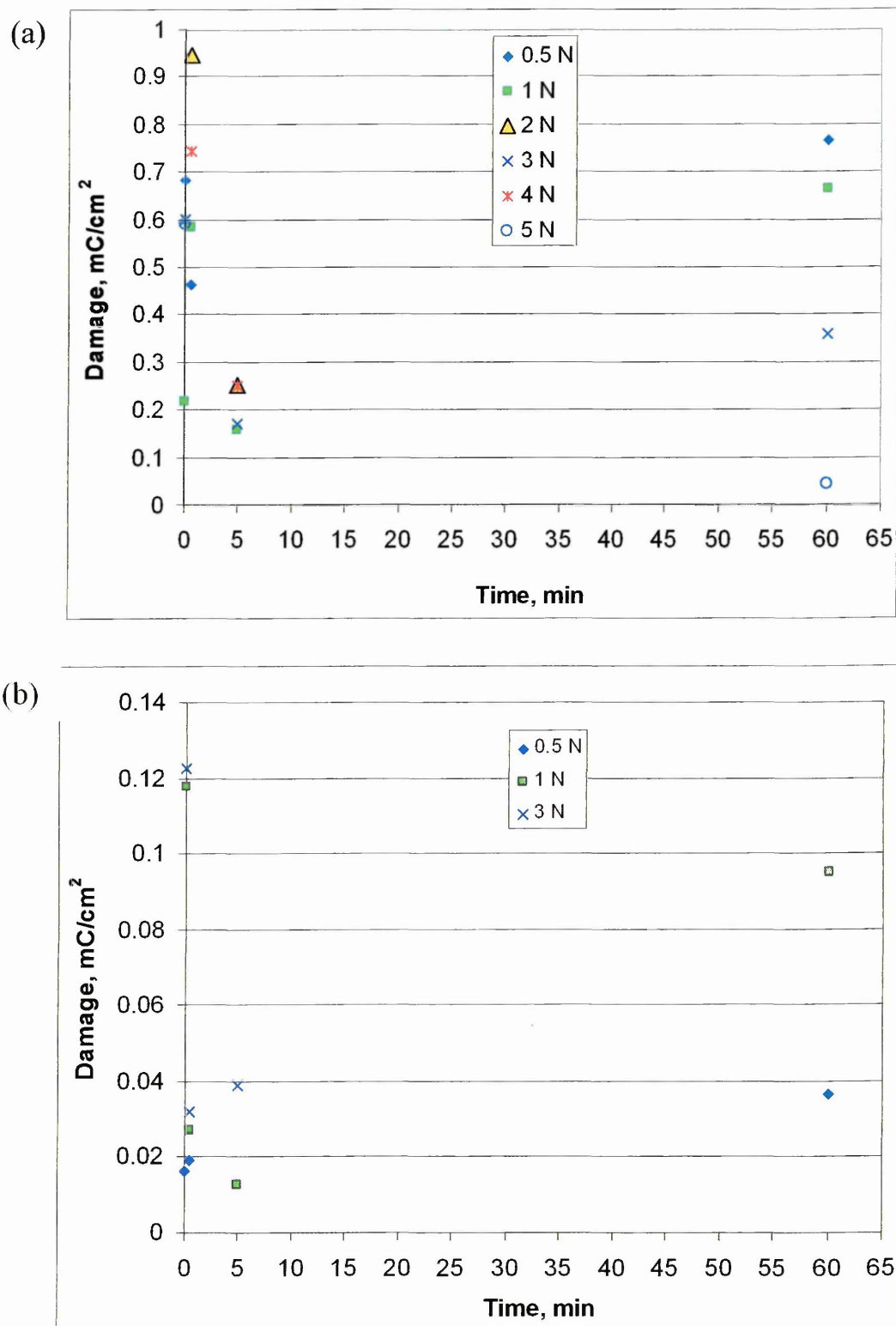


Figure 4.71 Damage (area under SRET line scan) generated at various loads as a function of loading time for (a) stainless steel, and (b) C/Cr coated samples

Test 4: Effects of loading and unloading on sample recovery

Figure 4.72 is the line displacement map scan at a fixed location (versus time) of the tribo-corrosion activity of the C/Cr coated sample showing the effect of abrasion by the alumina ball obtained by monitoring the SRET activity during contact and non-contact conditions. The real-time local tribocorrosion activity can be detected under contact mode (when load is applied), and is observed to decrease upon unloading (note the darkest region), which then reduces due to surface repassivation, immediately upon removal of the contact component (e.g. zero load). However, upon immediate contact of a load (5 N), the sample experienced increased damage. Sample recovery time depends on the repassivation rate of the bulk substrate or coating and the nature of the environment.

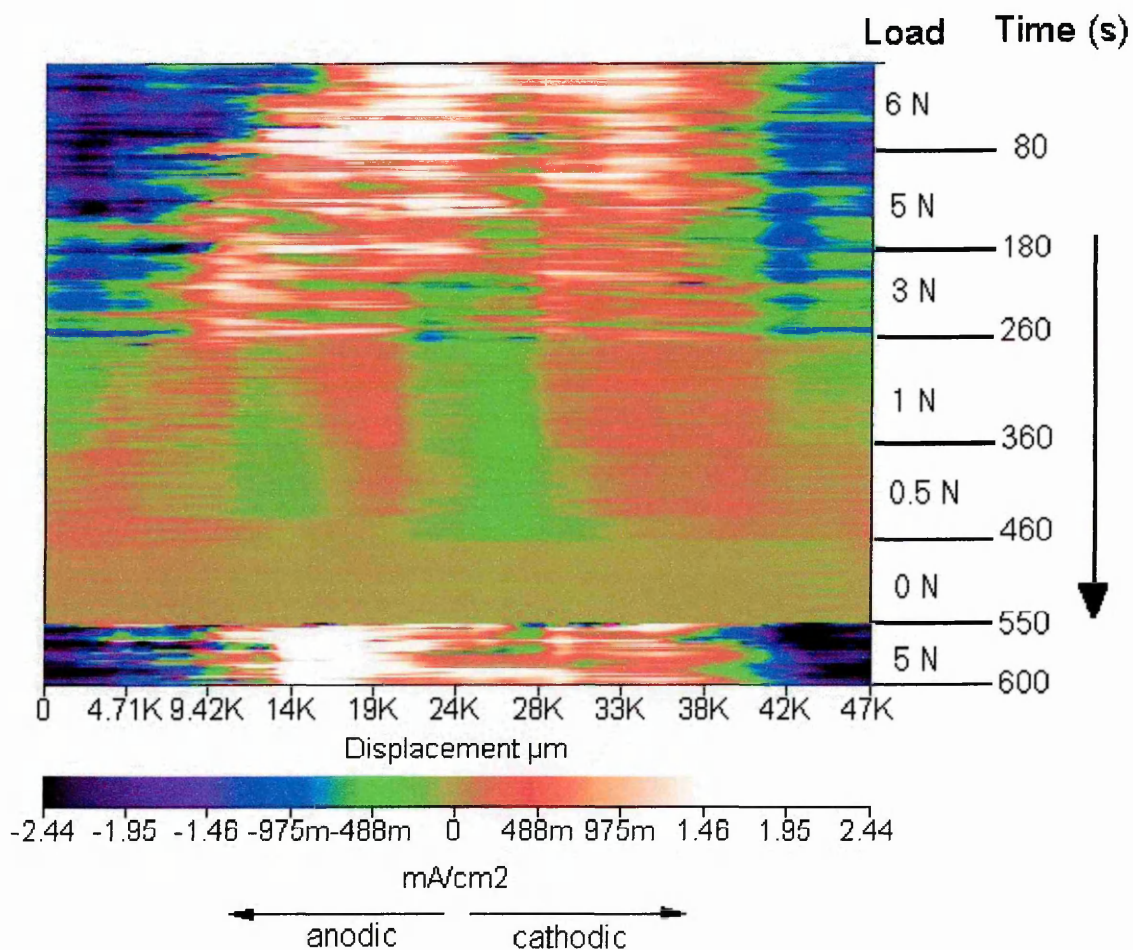


Figure 4.72 Line displacement versus time scan upon unloading and loading

Figure 4.73 shows the results of the effect of different loads, namely 0.5, 1, 3, and 5 N on the changes in local corrosion activity of C/Cr coated samples. Loads were applied at the same position on the sample. The sample was unloaded after each applied

load to see whether or not the sample recovers after 1 hr sliding. Here, 5 s represents the curve immediately after 5 s a load was applied, while the curve labelled 1 hr represents activity after sliding contact for 1 hr. At each load, after testing for 1 hr, the sample was unloaded and the signal was monitored. Figure 4.74 shows the recovery (repassivation) curves after 1 hr loading at 3 N. As shown in Figure 4.73, the current density during loading increased due to damage of the passive film [193]. As abrasion ceases, the current density decreases dramatically to a negligible value. The unloading line scan, after 1 hr sliding contact at 3 N presented in Figure 4.74 shows recovery after 90 s (note: lines were obtained at 15 s intervals and fluctuated with time). Unfortunately, it is extremely difficult to determine the exact recovery time of the sample, because the sample recovered (significant reduction in current density) almost immediately after the load is removed due to repair of the passive film. Although no exact recovery time could be obtained upon unloading from various loads, it was believed that the applied load may affect the recovery time, where the higher the load, the longer the time it takes to recover upon unloading. This may be due to the increase in damage area generated at higher loads, as found in Test 3.

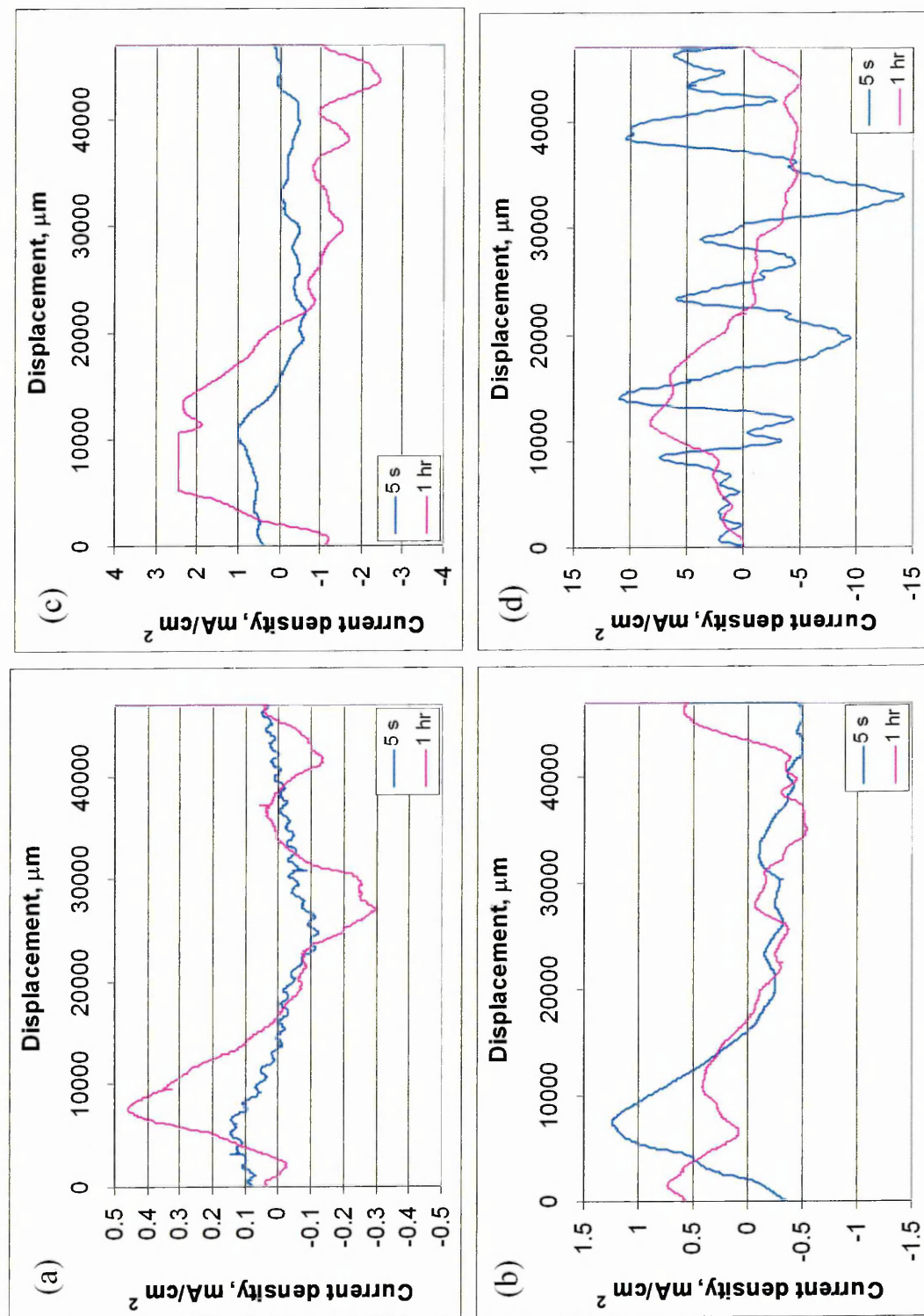


Figure 4.73 SRET line scan for C/Cr coated sample subjected to repeated loading and unloading sequence at (a) 0.5 N, (b) 1 N, (c) 3 N, (d) 5 N

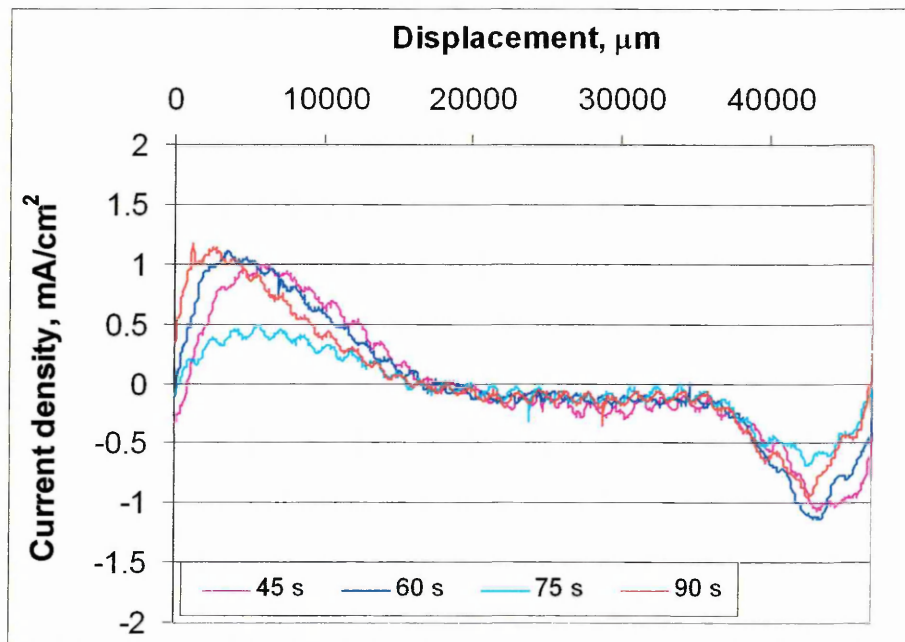


Figure 4.74 Unloading line scan after 1 hr sliding showing the corrosion activity after 45, 60, 75, and 90 s following unloading at 3 N (C/Cr sample). No corrosion activity was observed after approximately 2 min of unloading.

Test 5: Effects of coating on tribocorrosion damage in different environments

These tests were carried out by applying a 1 N load for duration of 1 hr in three different test environments (see Table 3.4 in Chapter 3 for details), namely:

- Air (i.e. sliding wear test)
- 0.01% NaCl solution at E_{corr} (i.e. tribocorrosion)
- 0.01% NaCl solution under cathodic protection

From these experiments, it was found that the testing environment affects:

- amount of wear
- wear coefficient
- wear morphology

Table 4.5 summarises the average values of the parameters extracted from the wear track and the worn surface on the ball. The wear volumes on the samples were determined by measuring the area under the wear tracks using a laser profilometer, and multiplying it by the circumference (length) of the wear track [192, 194]. At least four positions along the length of the wear track were measured to obtain the average area. Even though there was material loss in the wear track during mechanical interaction

between the ball and the sample, for ease of calculating the sliding distance, the circumference of the sample has been used instead of the circumference of the wear track. Therefore, by using the radius of 7.5 mm, the circumference of the sample was calculated to be 47.12 mm, and the total sliding distance for 1 hr at 100 rpm sliding speed was 282.72 m. The wear coefficient was calculated based on Archard's law [192, 194], but takes no account of the hardness of the sample in this study:

Wear coefficient, K = wear volume/(applied force \times sliding distance) $\text{m}^3\text{N}^{-1}\text{m}^{-1}$

	(a) In air		(b) In 0.01% NaCl at Ecorr		(c) In 0.01% NaCl under cathodic protection	
	316 SS	C/Cr	316 SS	C/Cr	316 SS	C/Cr
Diameter of worn area on ball, μm	686 - 764	234 - 415	240 - 309	~179	205 - 275	200 - 218
Worn track width, μm	670 - 744	95 - 400	312	~164	237	221-240
Worn area, mm^2	6.4E-3	5.0E-5*	2.5E-4	1.1E-4	1.8E-4	1.1E-4
Wear volume, m^3	3.04E-11	2.39E-13	1.21E-12	5.25E-13	8.59E-13	5.25E-13
Wear coefficient, $\text{m}^3\text{N}^{-1}\text{m}^{-1}$	1.08E-13	8.44E-16	4.26E-15	1.86E-15	3.04E-15	1.86E-15

* estimated value due to very shallow wear track that falls outside the measurement capability of the profilometer

Table 4.5 Summary of the parameters extracted from the wear track and the worn surface on the ball

Figure 4.75(a) presents the wear track profiles of the SS and C/Cr coated samples developed in 0.01% NaCl, compared with the SS sample wear track generated in air. Here, it can be seen that the C/Cr coated sample exhibits a shallower and more reduced wear track than that of the bare substrate. Figure 4.75(b) presents the wear coefficient of uncoated and C/Cr coated samples tested under various test environments. Uncoated SS samples show the highest wear coefficient of $1.08 \times 10^{-13} \text{ m}^3\text{N}^{-1}\text{m}^{-1}$ while the C/Cr coated sample exhibited the lowest wear coefficient of $8.44 \times 10^{-16} \text{ m}^3\text{N}^{-1}\text{m}^{-1}$ when tested in air. The reduced wear coefficient of C/Cr coated sample in air may be attributed to the C-rich transfer layer, the self-lubricating effect of graphite [3] and the adsorbed gases (e.g. hydrogen or oxygen) which reduce the adhesion between the surfaces in contact namely the substrate and counterpart, by passivating dangling bonds of the graphite crystallites [195]. Under test environments (b) and (c), the uncoated sample shows a substantial reduction in the wear coefficient by nearly two orders of magnitude; but the C/Cr coated sample showed a slight increase in the wear coefficient to $1.86 \times 10^{-15} \text{ m}^3\text{N}^{-1}\text{m}^{-1}$ as compared to the sample tested in air. This trend was in good agreement with the one observed for a DLC coated Ti6Al4V substrate under dry sliding (at temperature of 310 K) and in 0.9 % NaCl solution [196], where the wear rate of the coating tested in 0.9 % NaCl was reported to increase slightly as compared to the one tested under dry sliding. This could be due to the removal of a C-rich transfer layer into the NaCl solution boundary layer during sliding. Alternatively it may be attributed to an additional galvanic effect between the damaged wear track and undamaged surrounding area. Figure 4.76 shows that the coating was substantially worn off in the wear tracks since, after testing in 0.01% NaCl at E_{corr} and under cathodic protection, the substrate was severely exposed as compared to the one tested in air. In the case of the SS sample, the reduction in wear is attributed primarily to the lubricating effect of the electrolyte between rubbing surfaces.

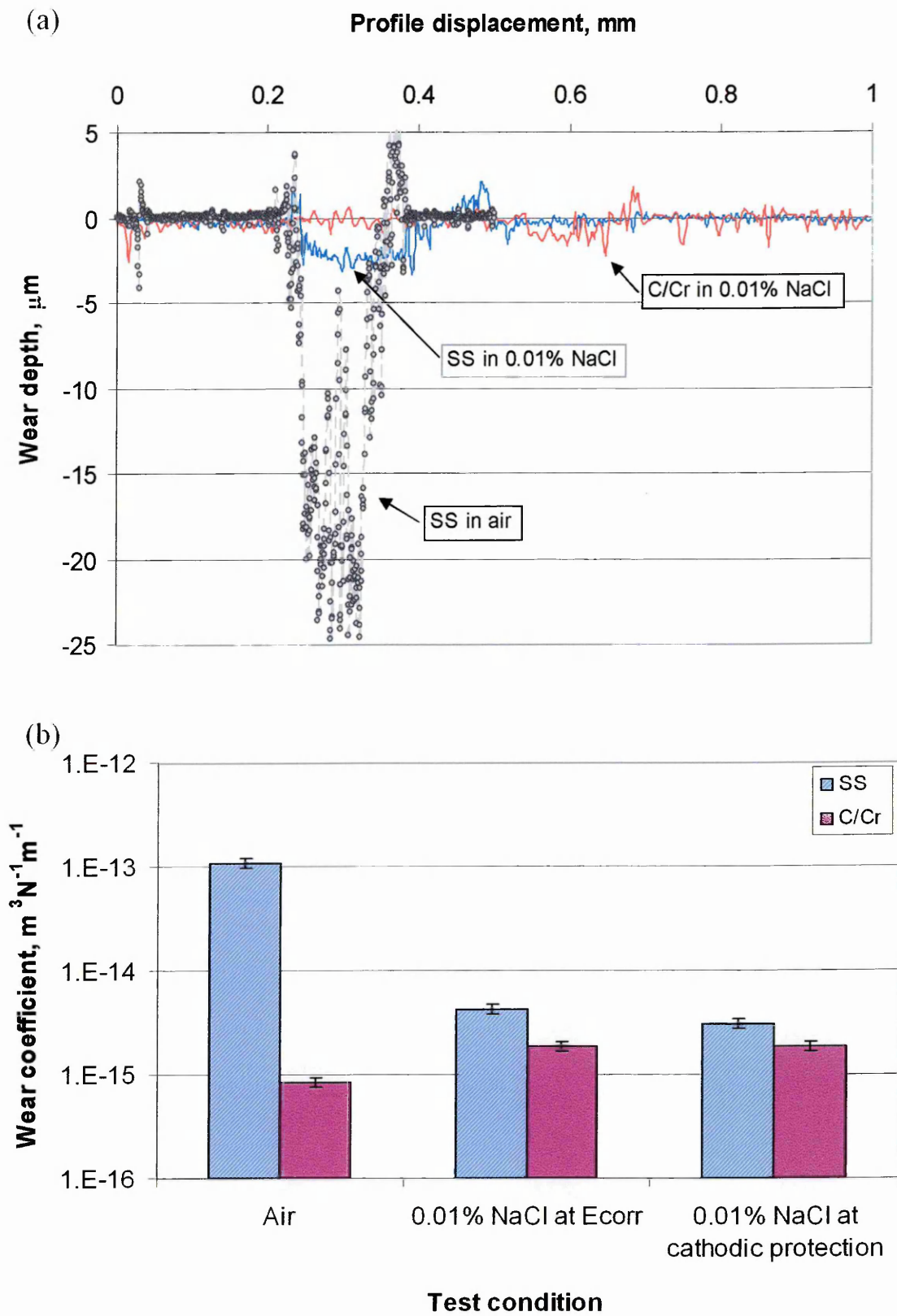


Figure 4.75 (a) Typical wear track profiles and (b) wear coefficients determined for various test environments after 1 hr testing

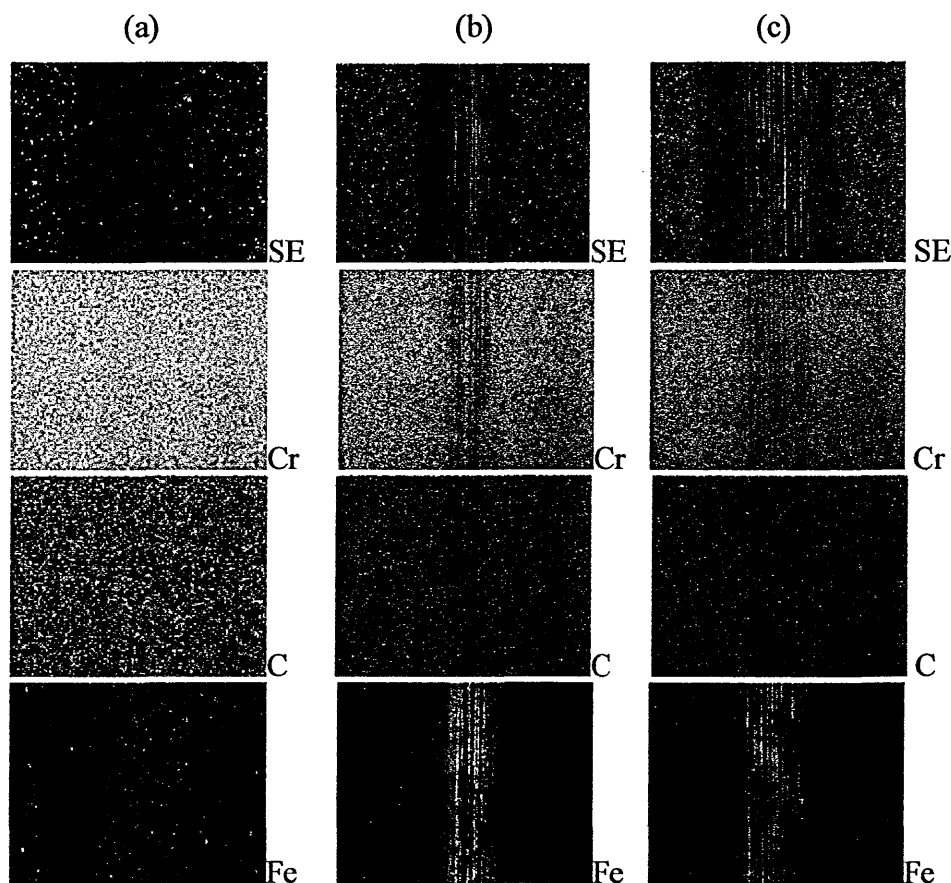


Figure 4.76 SEM/EDX elemental mapping of the wear track generated on C/Cr coated samples after 1 hr testing in (a) air, and 0.01% NaCl at (b) E_{corr} , and (c) cathodic protection

Figure 4.77 presents the optical images of the alumina ball and the wear track on an uncoated SS sample. Severe damage was observed on both the sample and the ball after testing in air (Figure 4.77 (a) and (b), respectively). The formation of wear debris which accumulates in the wear track and promotes third-body sliding, resulted in the highest observed material loss and wear coefficient. When tested at E_{corr} and under cathodic polarisation, both the ball and the sample experienced less material loss (see Figure 4.77 (c) to (f)) and brown debris (possibly iron oxide) was observed around the wear track and the ball. García and co-workers [197] reported that the corrosive-wear of AISI 316 tested in aggressive environments consists of two processes; (i) mechanical delamination of the passive layer in the wear track, followed by (ii) a progressive electrochemical re-passivation of that active wear track area (representing that part of the wear track that temporarily loses its passive character due to the mechanical

interaction during sliding). Passive materials such as stainless steel generally resist corrosion by the formation of a thin, dense, passive oxide film. However, mechanical loading interaction by sliding contact between two rubbing surfaces can deteriorate and remove part of the passive film. The extent of combined corrosion/wear depends on the type of materials in contact, the composition of the environment, the applied load, and the electrode potential of the substrate [197].

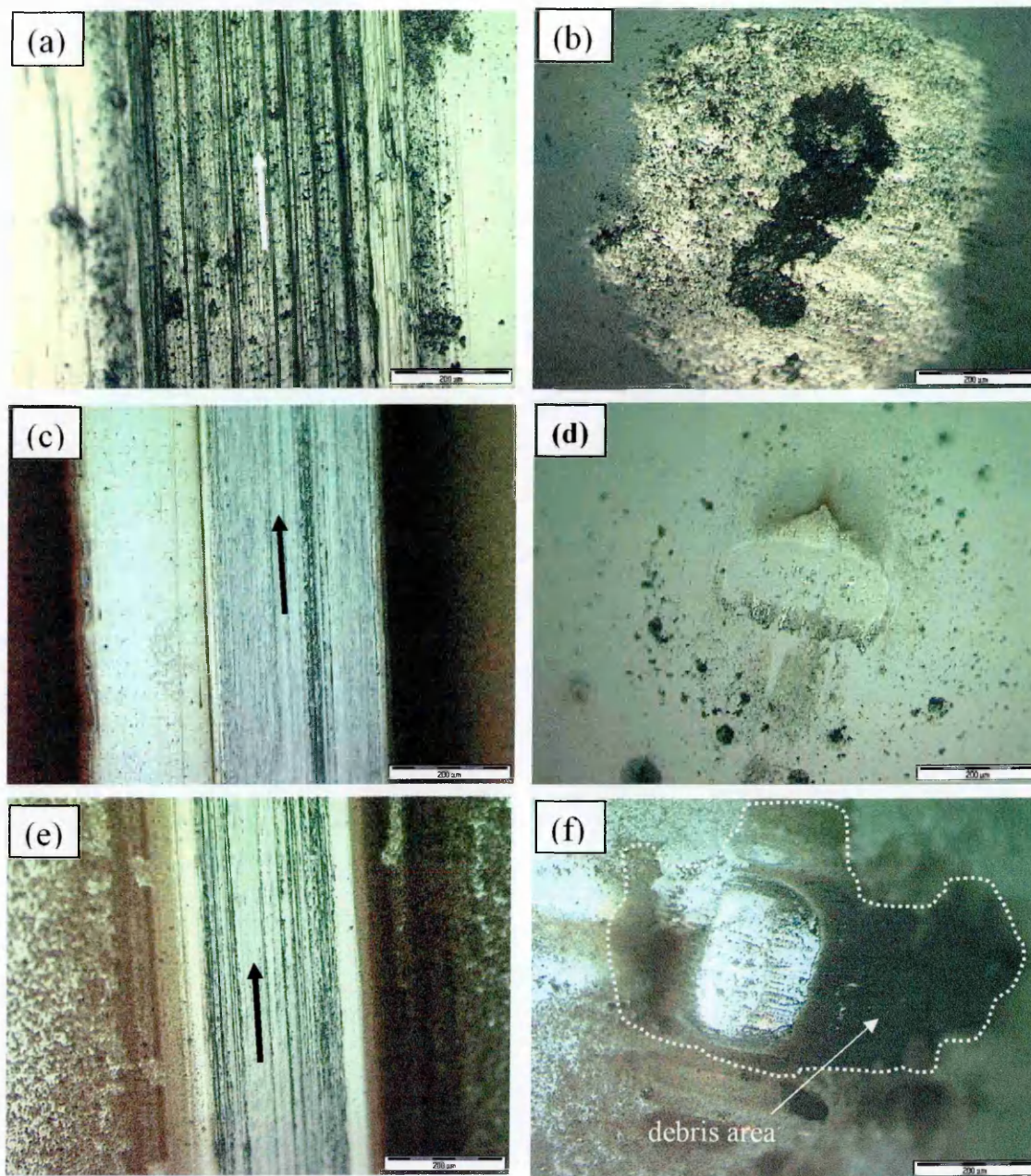


Figure 4.77 Optical images of the wear scar (arrow shows the sliding direction) of uncoated SS sample and alumina ball counter part tested (a-b) in air, (c-d) at E_{corr} , and (e-f) under cathodic polarisation. All markers: 200 microns.

C/Cr coated samples appear to exhibit different wear behaviour under different test environments. The SEM surface morphology of the wear scars and the optical images of the counter part under various test environments are shown in Figure 4.78 and Figure 4.79 respectively. C/Cr coating performed best in air (Figure 4.78a), which shows a small and smooth wear track compared to the sample tested at both E_{corr} and under a cathodic potential, which in both cases showed larger and rougher wear tracks

with a sign of plastic deformation on the substrate (Figure 4.78 (b) – (c)). A transfer layer was present around the wear track for the coating tested in air and under cathodic protection (but not observed for the coating tested at E_{corr}). This was also seen on their corresponding ball surfaces (see Figure 4.79). For DLC and carbon-based coatings, a transfer layer was normally observed during tribological test in air [21, 94, 195] where the transfer layer formed during tribo-contact produced a lubricating effect which reduced friction between the sample and the counter part.

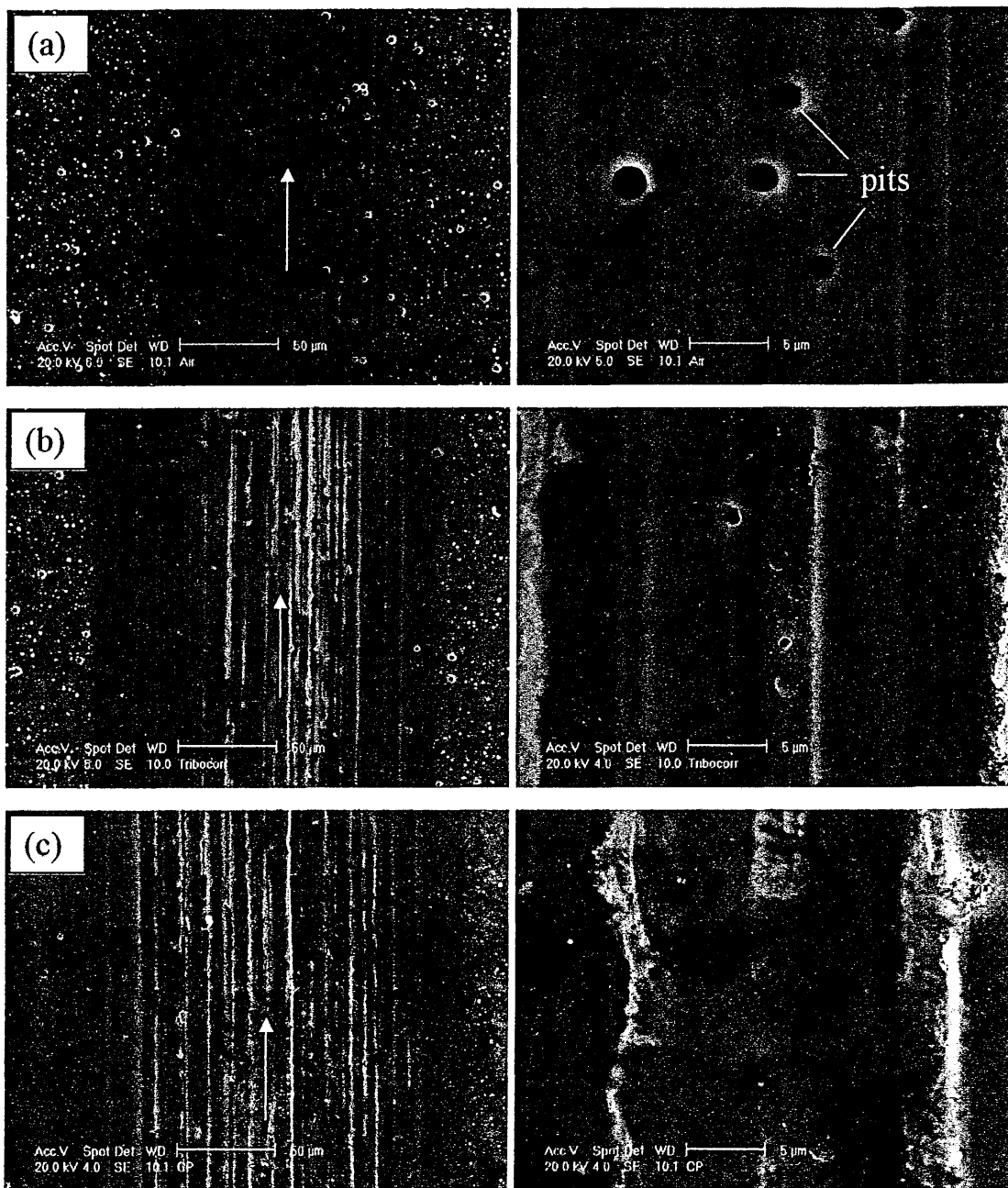


Figure 4.78 SEM images of the wear scar of C/Cr coated sample tested (a) in air, (b) at E_{corr} , and (c) under cathodic protection (images on the right represent the magnified picture of the centre of the wear tracks in (a) to (c))

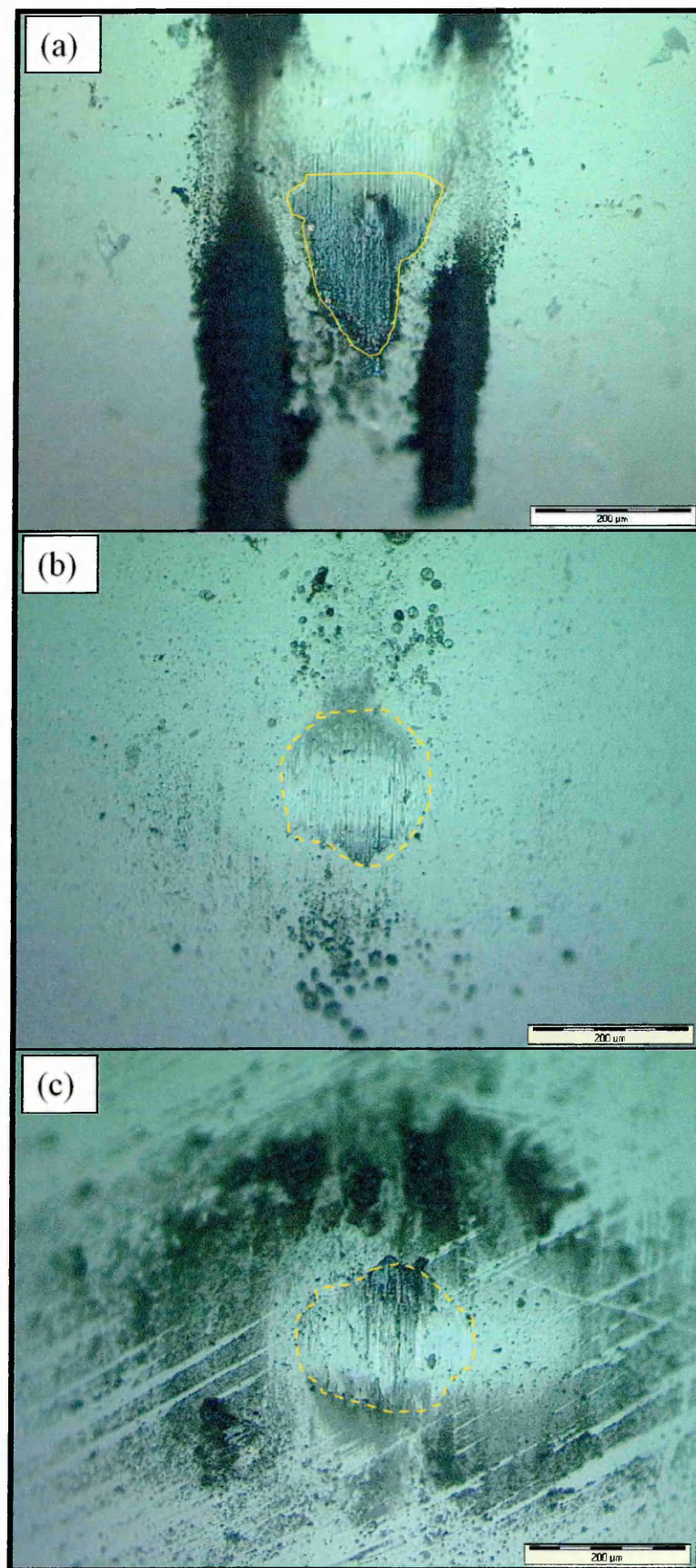


Figure 4.79 Optical images of the counter part of C/Cr coated samples tested (a) in air, (b) at E_{corr} , and (c) under cathodic polarisation

4.8 Performance in dry high-speed milling test

The cutting performance of uncoated and C/Cr coated end mills were tested using a Mazak FJV-25 high-speed machine available in the School of Engineering at Sheffield Hallam University, using automotive aluminium alloy (Al-Si8Cu3Fe) as the work piece material. Two experiments as previously described in Chapter 3 were carried out. The cutting performance of C/Cr coated tools were further discussed in the next chapter.

Test 1

The relationship between flank wear and the amount of material removed after milling tests, for coatings deposited at $U_B = -65, -75, -95$ and -120 is presented in Figure 4.80 (the curve with higher volume removed and the lower flank wear indicates best tool life-time). Most of the tested tools exhibited a 3-period curve, which comprise fast initial wear, steady wear and accelerated wear. This is particularly obvious for the uncoated end mill and an end mill coated with C/Cr at $U_B = -65$ V. Both these tools show discernible accelerated flank wear after removing approximately $2.8 \times 10^5 \text{ mm}^3$ of material. A similar 3-period curve has also been reported for TiAlN/VN coatings [198]. An end mill coated with C/Cr at $U_B = -95$ V initially exhibited fast wear until 0.075 mm flank wear, then the flank wears off in a much steadier manner until it reaches 0.23 mm. This could be attributed to its low friction, high wear resistance and good coating-substrate adhesion. In comparison, because of poorer adhesion and higher stress in coatings grown at $U_B = -120$ V, the end mill coated at this bias voltage shows a fast initial flank wear up to 0.16 mm, a short steady wear period, and then an accelerated wear after removing $3.5 \times 10^5 \text{ mm}^3$ of material. Figure 4.81 shows the volume of material removed after 1.5 passes, as a function of the bias voltage. The cutting tests in dry high-speed machining conditions clearly demonstrated that C/Cr coatings enhanced the tool performance and the tool life compared to the uncoated end mill. The $U_B = -95$ V sample out-performed uncoated and samples coated at $U_B = -65, -75$ and -120 V, achieving a factor of two higher for the material removed volume i.e. $6.4 \times 10^5 \text{ mm}^3$ (with low flank wear of 0.23 mm) compared to that of the uncoated tool ($3.4 \times 10^5 \text{ mm}^3$, and flank wear of 0.27 mm).

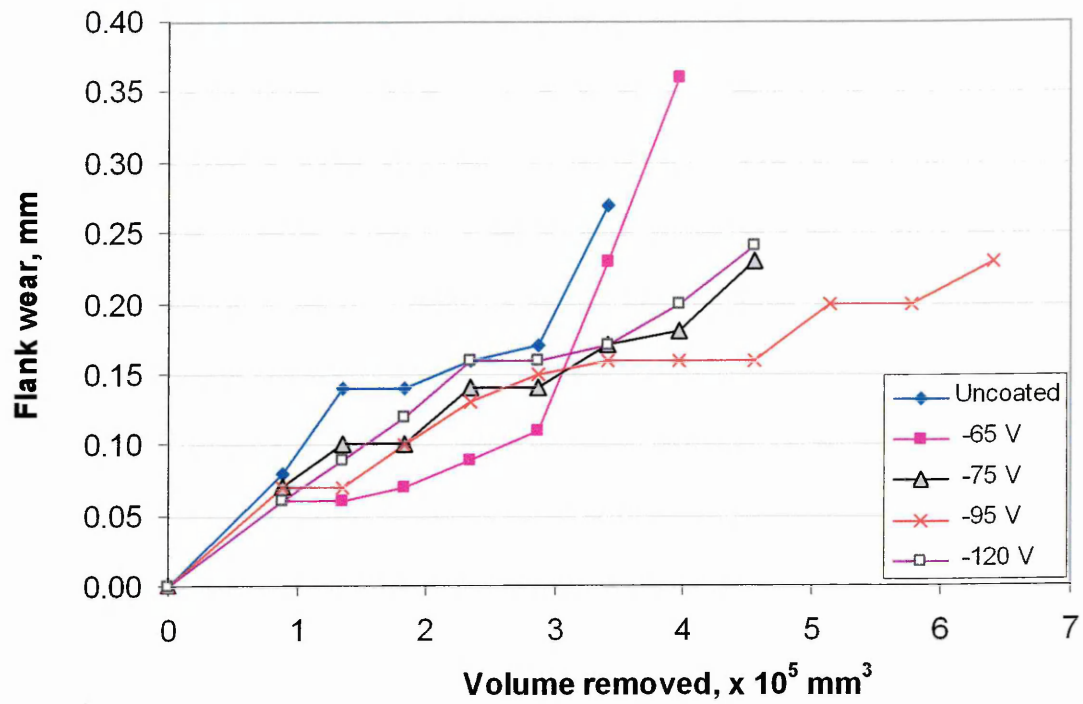


Figure 4.80 Flank wear versus volume removed for uncoated and C/Cr coated samples prepared at various bias voltages

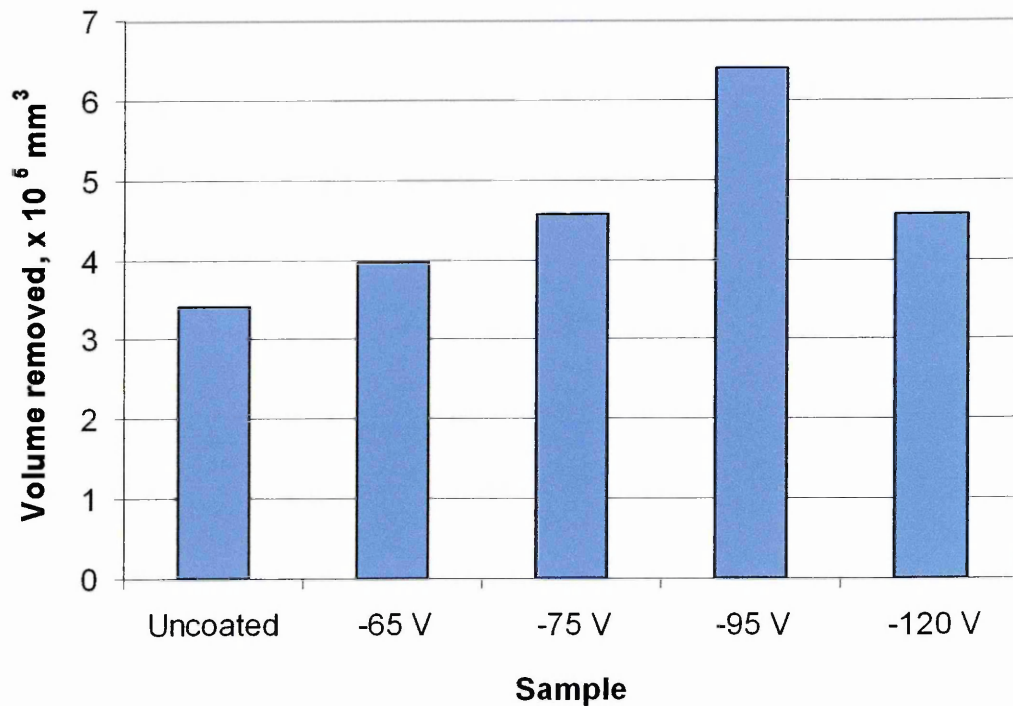


Figure 4.81 Amount of volume removed for uncoated and C/Cr coated end mills deposited at various bias voltages

Test 2

SEM analysis

Figure 4.82 shows the SEM images of uncoated and C/Cr coated end mills after milling a constant volume (135720 mm^3) of Al-Si8Cu3Fe alloy. A large amount of material was observed sticking (material transfer) to the flank of the uncoated and sample coated at $U_B = -65 \text{ V}$. In contrast, the flank of the end mills coated with C/Cr at $U_B = -95 \text{ V}$ and $U_B = -120 \text{ V}$ experienced little material transfer without excessive build up. Figure 4.83 to Figure 4.86 present the close-up investigation of the flank and the built-up edge (BUE) showing the SEM surface morphologies and the EDX analysis of uncoated and C/Cr coated end mills prepared at $U_B = -65$, -95 , and -120 V . As can be seen in Figure 4.83 and Figure 4.84, for uncoated and $U_B = -65 \text{ V}$ samples, an excessive amount of aluminium (intense Al peak as revealed by EDX analysis) from the work piece material was transferred and built up on the flank. Therefore, in test 1, both of these samples experienced the highest flank wear and removed the lowest amount of material during tests. The built up material could have been picked up during milling tests due to softening of the work piece material as a result of high local temperature at the cutting edge, which may reach the melting point ($T_m < 600^\circ\text{C}$) of the aluminium (work piece material). In contrast, the cutting edges of end mills coated with C/Cr at $U_B = -95$ and $U_B = -120 \text{ V}$ (see Figure 4.85 and Figure 4.86, respectively) were much smoother, and only a small amount of material build up on the flank was observed. EDX analysis was carried out on the flank of both of these samples, which were labelled with A (away from the cutting edge) and B (at the cutting edge) in Figure 4.85 and Figure 4.86. From both figures, spectrum A shows an intense peak of W and weak Co peaks corresponding to the substrate and intense Cr and weaker N peaks corresponding to the coating, and Al (plus Si and Cu peaks as also seen in spectrum B) are similar to those expected in the composition of the work-piece material. A weak O peak was observed in regions A and B, and this was more intense in region A. This may suggest that oxygen resulted from contamination of the specimen surface when exposed to ambient atmosphere, and the intensity weakened at the cutting edges as a result of the coating being worn away during milling tests and during build up of Al. This oxygen peak may also result from the oxidation process during milling tests because of the high local temperature at the cutting edge. Figure 4.87 is the EDX elemental mapping showing the distribution of Cr, W, O, and Al around the cutting edge of a $U_B = -120 \text{ V}$ sample. This result further

confirmed that the built-up material on the flank was aluminium which was transferred from the work-piece material during the dry milling test.

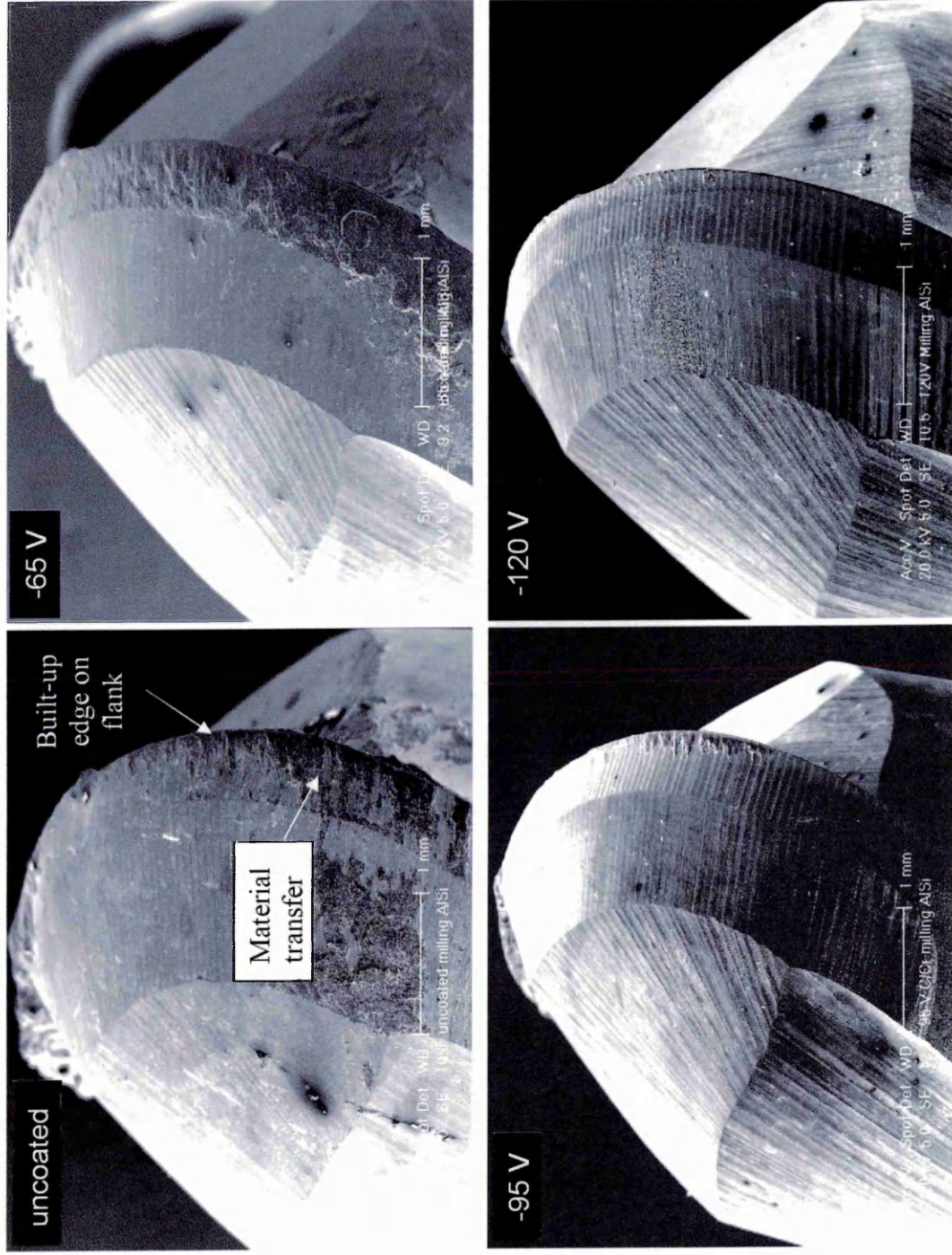


Figure 4.82 SEM images of uncoated and C/Cr coated ($U_B = -65, -95, -120$ V) end mills after milling 135720 mm³ AlSi alloy

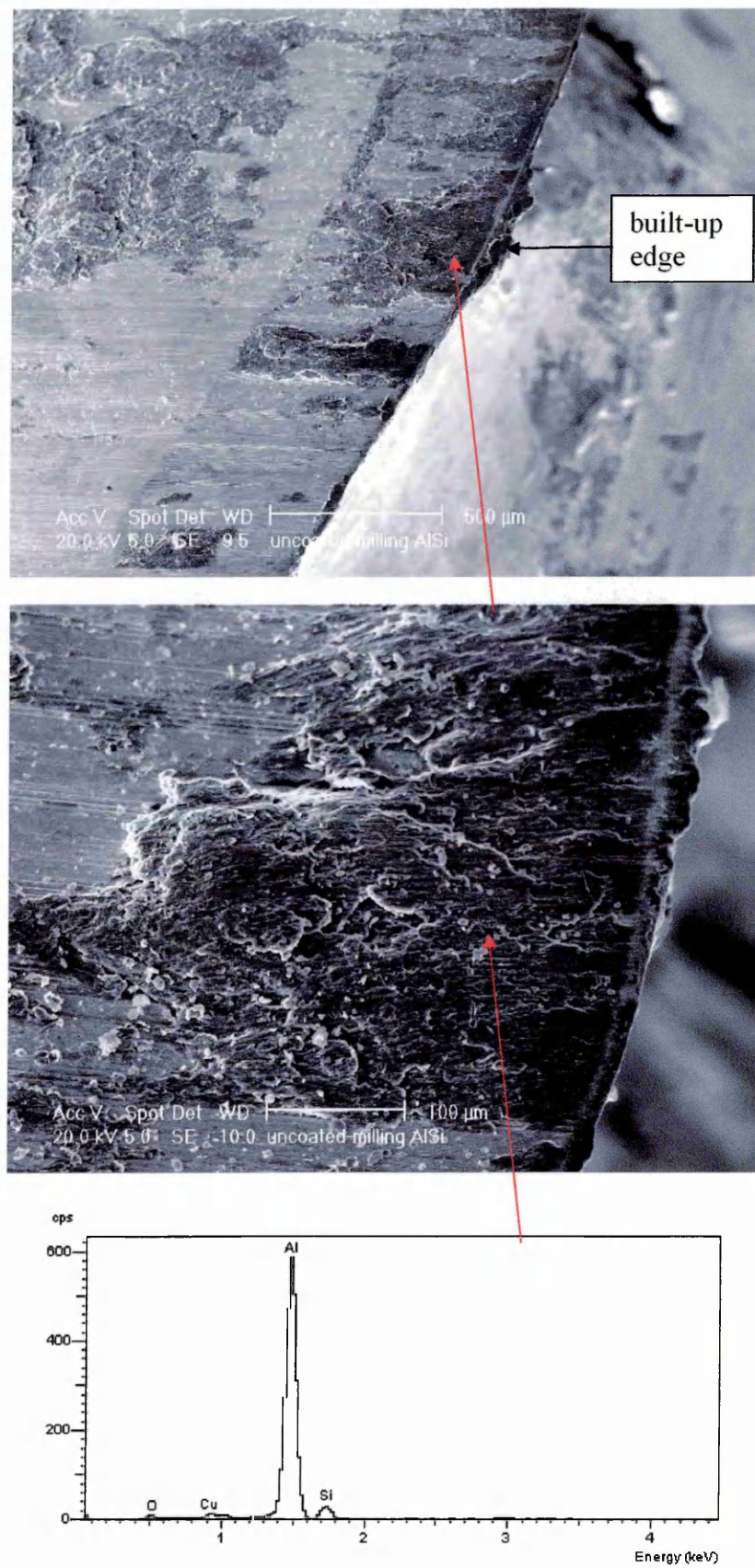


Figure 4.83 SEM surface morphology of the flank and the EDX analysis of the built-up material of uncoated sample

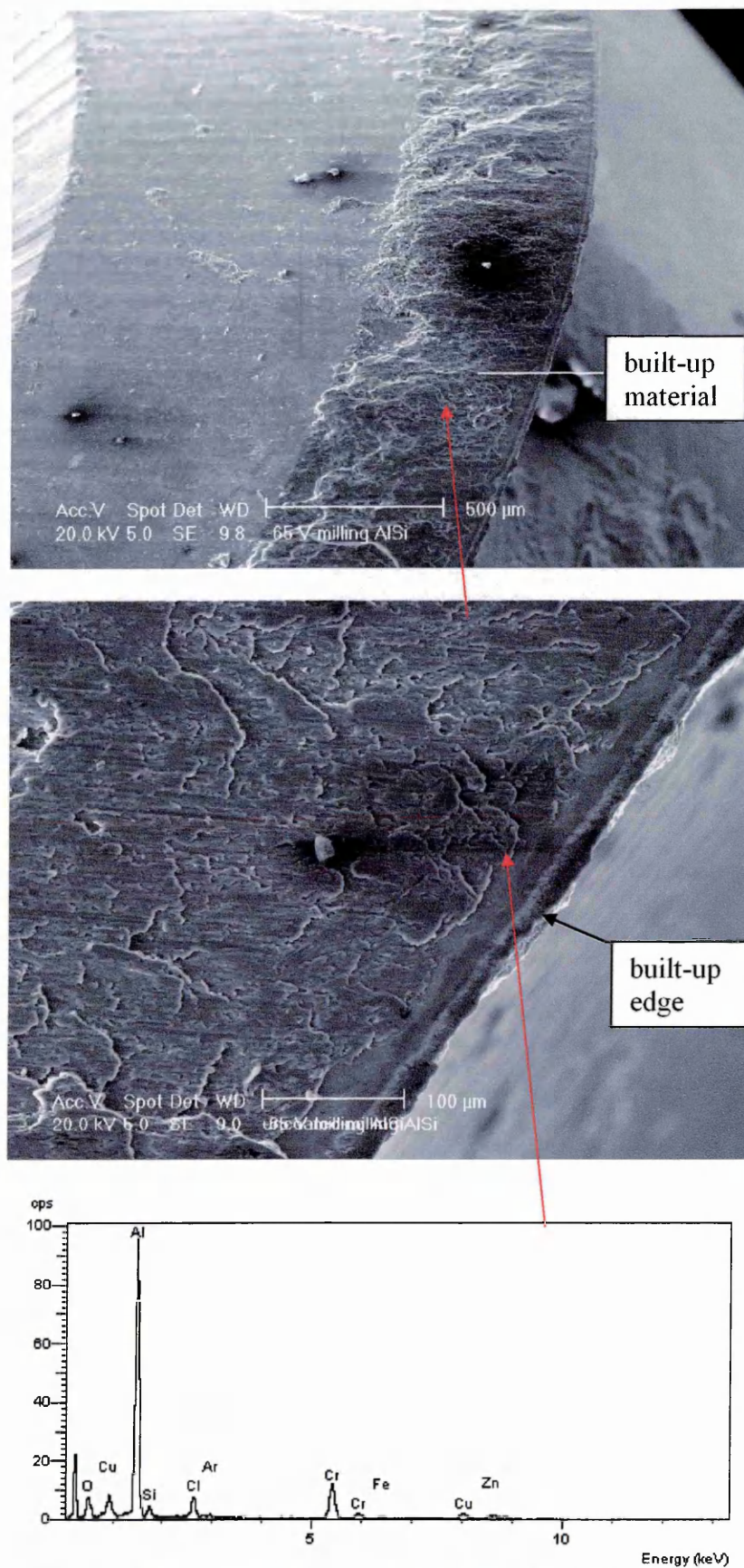


Figure 4.84 SEM surface morphology of the flank and the EDX analysis of the built-up material of $U_B = -65$ V sample

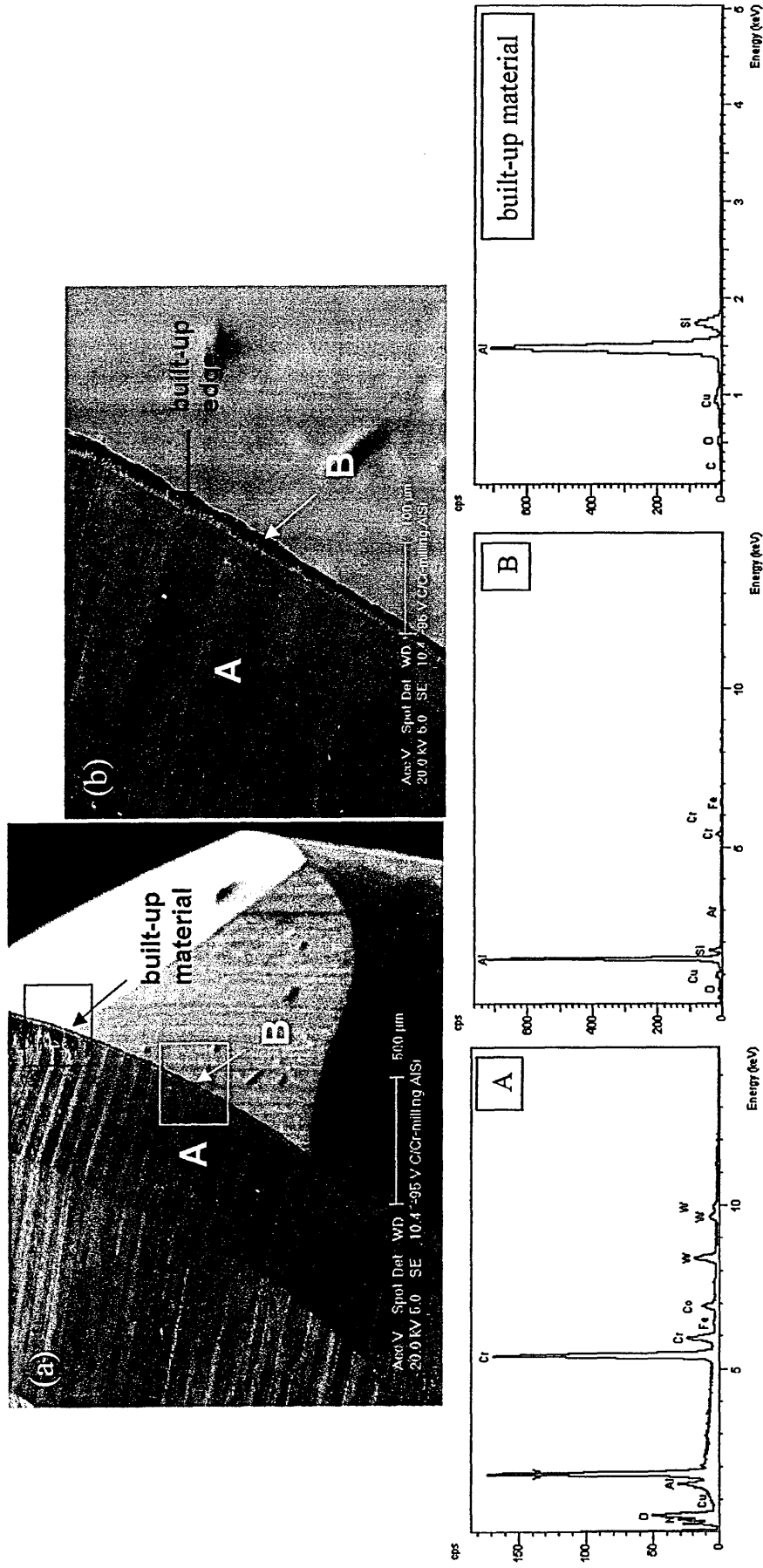


Figure 4.85 $U_B = -95$ V sample (a) SEM surface morphology of the flank, (b) magnified image of built-up edge highlighted with yellow, (c) backscattered electron image (BSE) of built-up material highlighted with red, (bottom) EDX analysis of the area indicated with A, B and built-up material

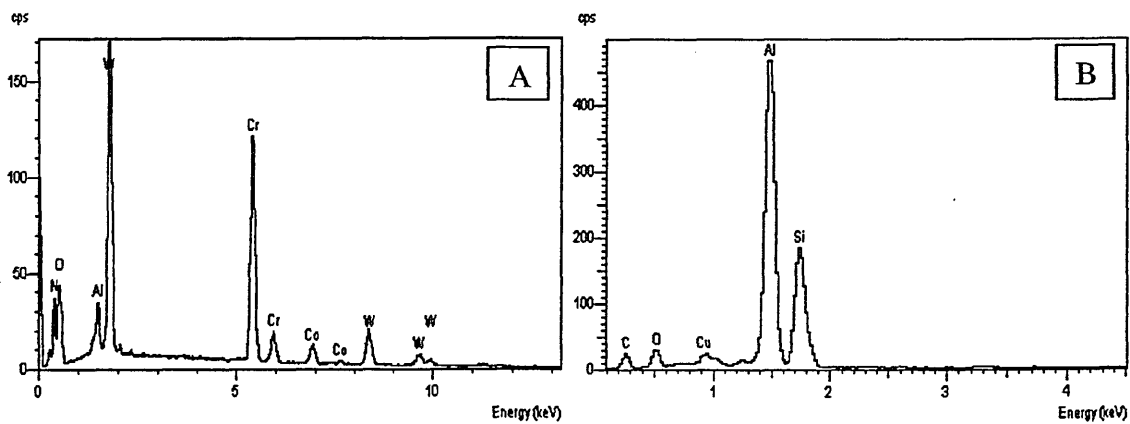
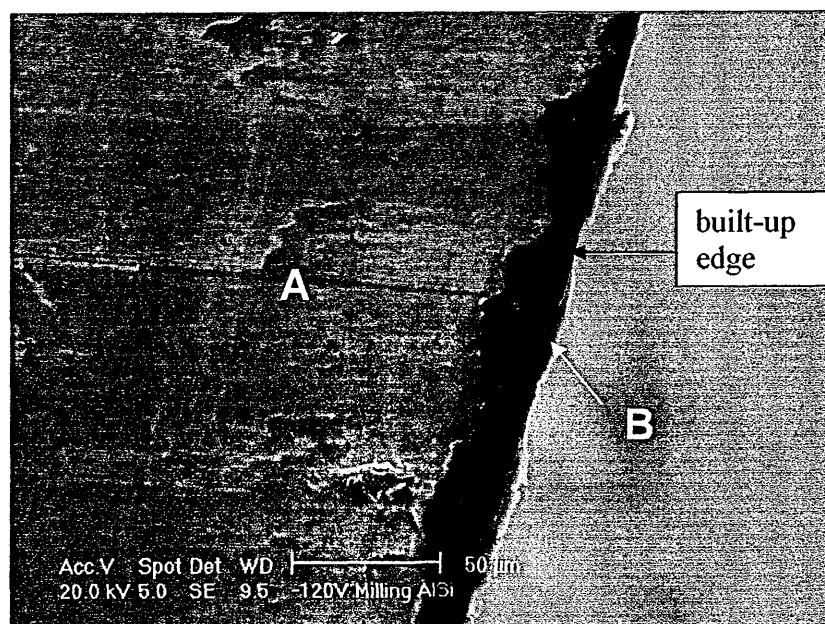
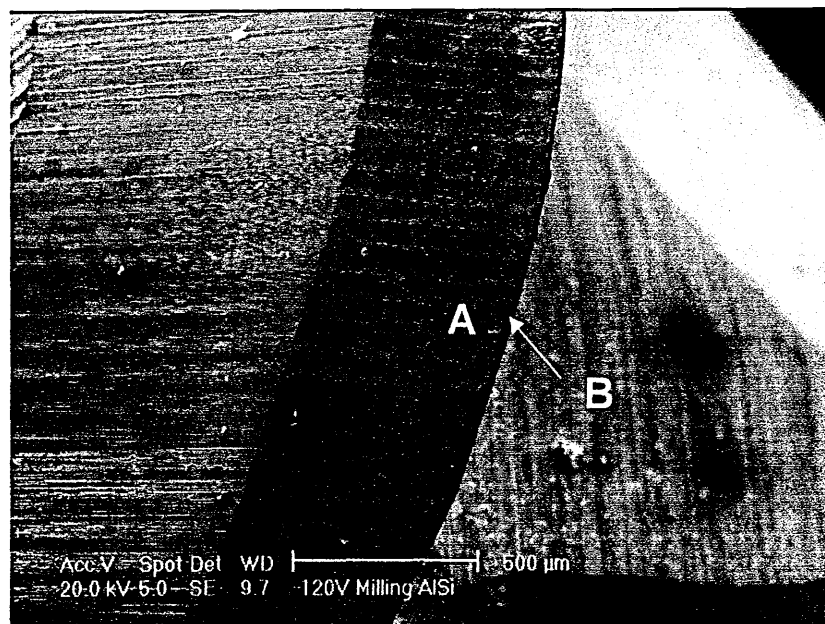


Figure 4.86 $U_B = -120$ V sample: SEM surface morphology of the flank and the EDX analysis of the area indicated with A and B shown in (a)

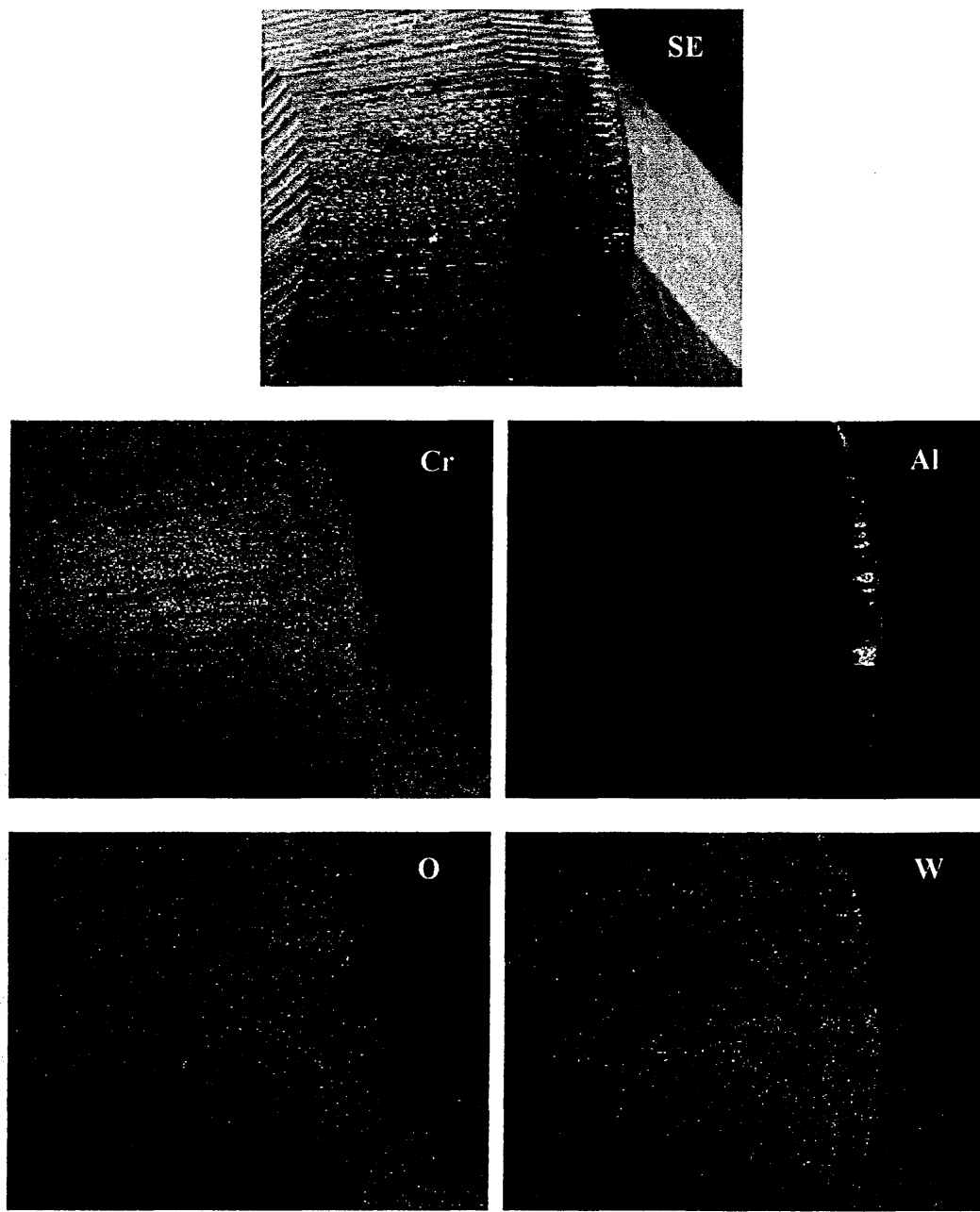


Figure 4.87 SEM-EDX Elemental mapping of endmill coated with C/Cr at $U_B = -120$ V

Raman spectroscopy analysis

Raman analysis of swarf/chip produced during milling tests will give information of the surface oxide formed. Figure 4.88, Figure 4.89, and Figure 4.90 show the optical images and the Raman spectra acquired from the flank of end mill, flat end and sharp end of a chip, respectively, after removing 135720 mm^3 of Al-Si8Cu3Fe alloy. The sharp peak at $\sim 520 \text{ cm}^{-1}$ is assigned to bulk AlSi, see Figure 4.89 and Figure 4.90 for the spectrum of bulk AlSi taken for reference. The broad band appeared at about $855\text{-}950 \text{ cm}^{-1}$ and

the sharp peaks appeared at about 1366, 1400, and between 1613-1681 cm^{-1} correspond to $\alpha\text{-Al}_2\text{O}_3$ [177, 199]. Raman analysis on the flank further revealed the low Al adherence tendency on the end mill coated with C/Cr at $U_B = -95$ V and $U_B = -120$ V (see Figure 4.82 for SEM images) as no bulk AlSi peak was observed at ~ 520 cm^{-1} (see Figure 4.88). Only a very weak or negligible peak of Al_2O_3 appeared at ~ 1650 cm^{-1} , this indicated little material transfer on these samples, which is in good agreement with the SEM observations. In contrast, the Raman spectra obtained at the flank of uncoated and C/Cr coated ($U_B = -65$ V) samples, shown in Figure 4.88, revealed the presence of bulk AlSi and Al_2O_3 peaks, particularly pronounced on the uncoated end mill. This observation agrees well with the SEM analysis shown in the preceding section. The Raman spectra for both the flat and sharp ends of the chip shown in Figure 4.89 and 4.90 were identical to the spectrum taken from bulk AlSi alloy, except an additional broad band of $\alpha\text{-Al}_2\text{O}_3$ was detected at the flat end (Figure 4.89) of the chip produced by uncoated, $U_B = -95$ and -120 V C/Cr coated samples, which could be due to higher temperature (promoting oxidation) at the flat end compared to the cooler sharp end of a chip [200].

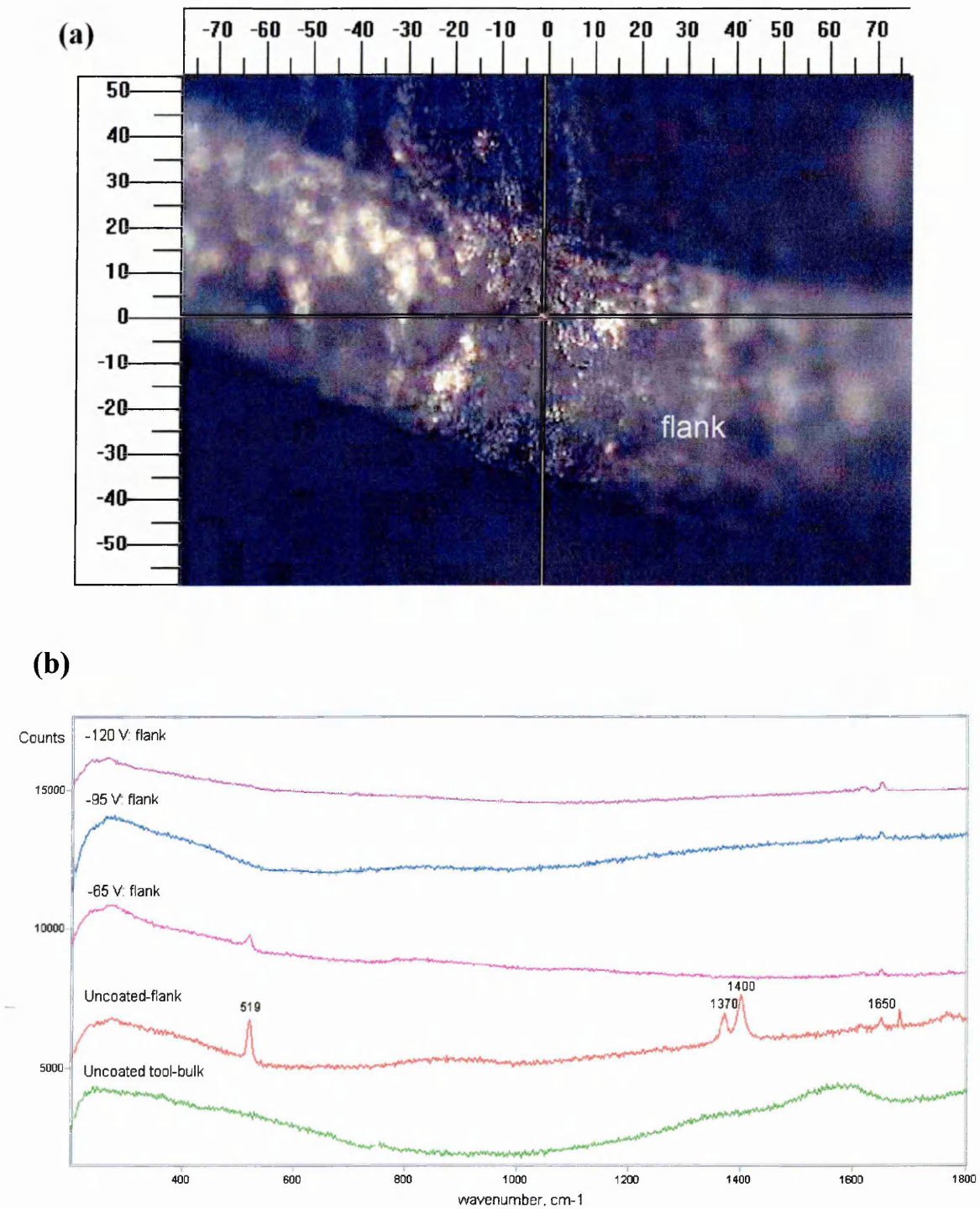


Figure 4.88 (a) Optical image showing the flank of end mill where a Raman spectrum was taken, (b) Raman spectra of the flank for uncoated and C/Cr coated ($U_B = -65, -95, -120$ V) end mills. Note that the green spectrum is for reference which was taken from uncoated end mill before the milling test

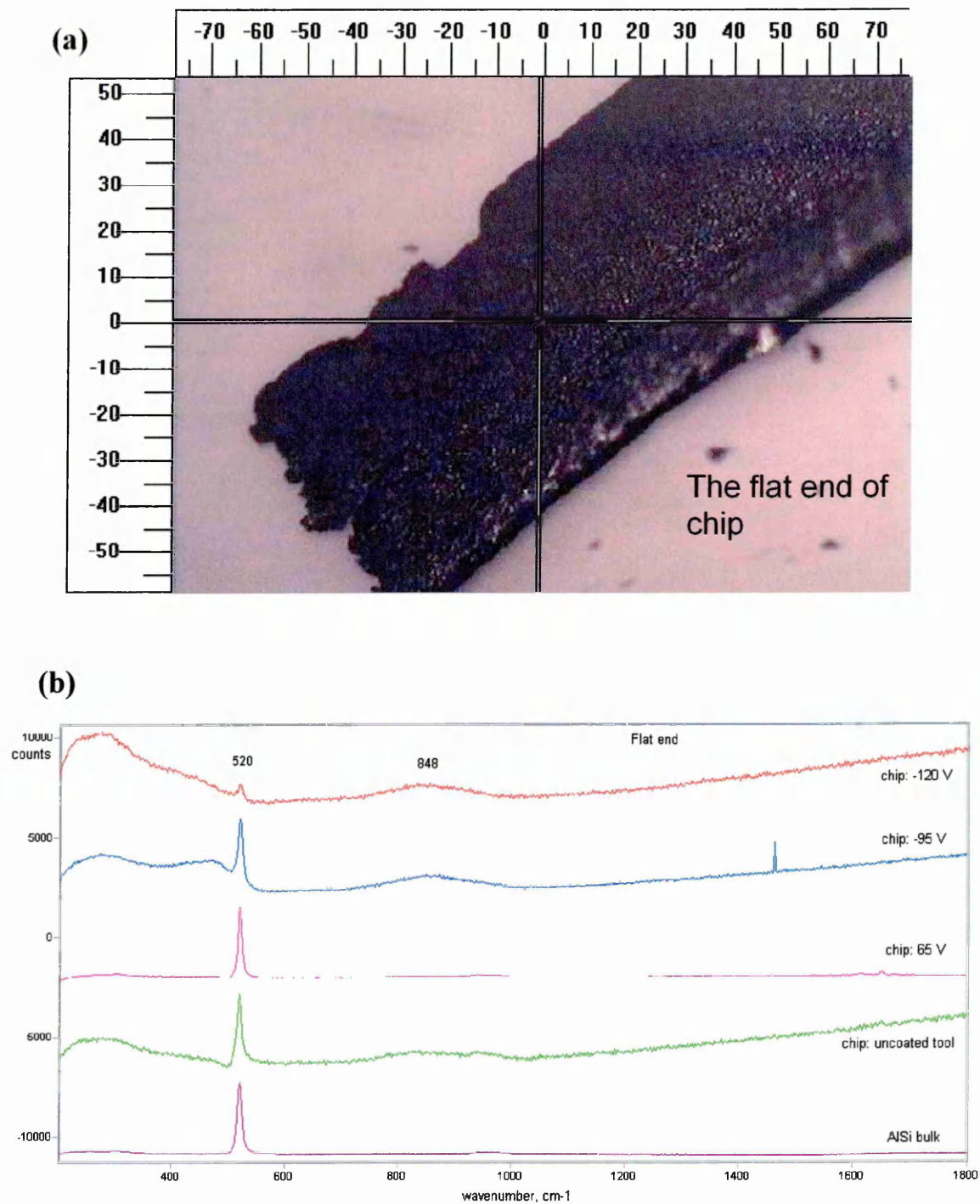


Figure 4.89 (a) Optical image of the flat end swarf/chip of removed workpiece material, (b) Raman spectra of the flat end of the chip removed after milling tests using uncoated and C/Cr coated ($U_B = -65, -95, -120$ V) end mills. The spectrum of bulk AlSi workpiece material shown in purple is taken for reference

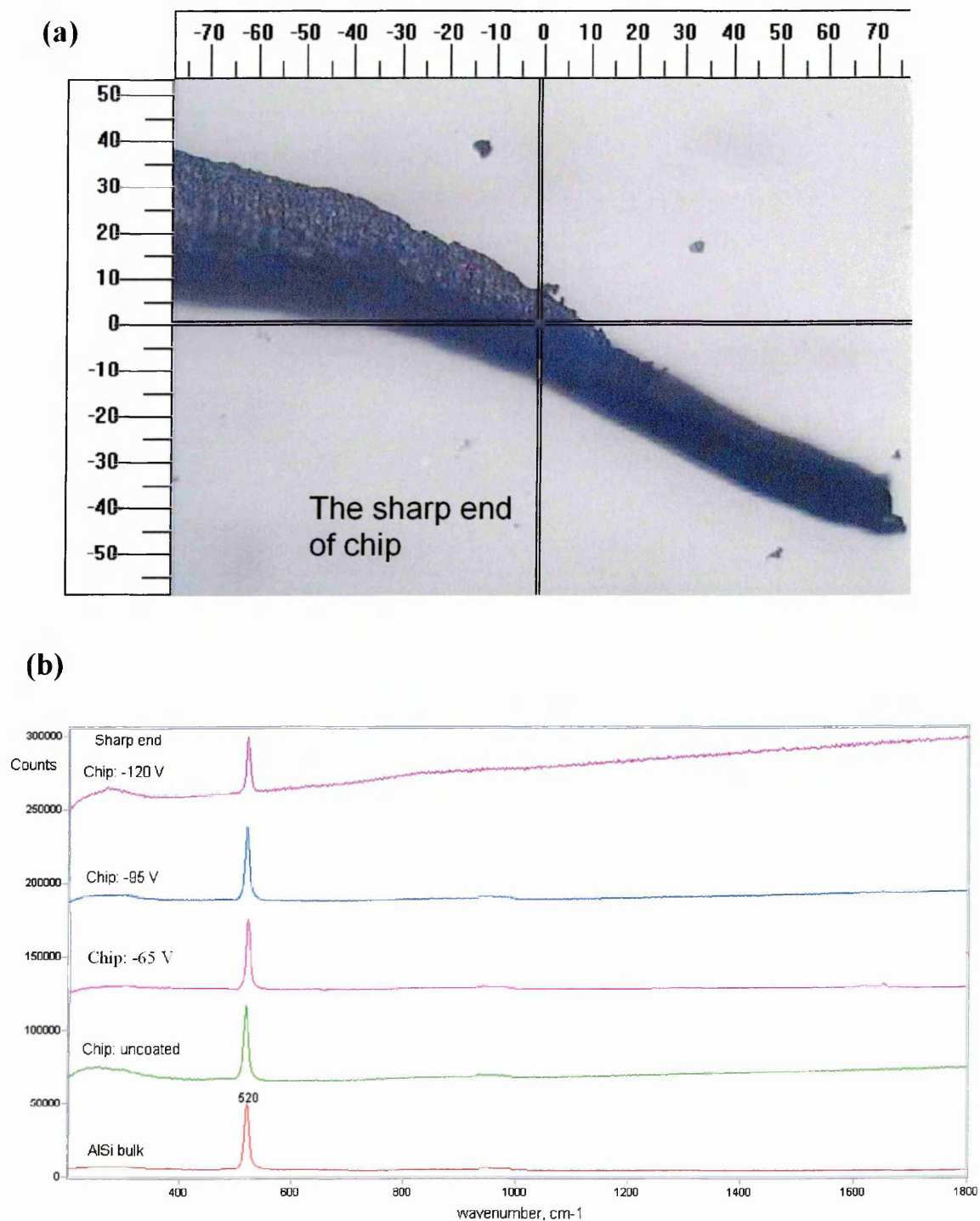


Figure 4.90 (a) Optical image of the sharp end swarf/chip of removed workpiece material, (b) Raman spectra of the sharp end of the chip removed after milling tests using uncoated and C/Cr coated ($U_B = -65, -95, -120$ V) end mills. The spectrum of bulk AlSi workpiece material shown in red is taken for reference

CHAPTER 5

Discussion

5.1 Ion bombardment induced microstructure evolution and the proposed coating growth model

C/Cr coatings prepared by the combined steered cathodic arc/unbalanced magnetron sputtering technique are amorphous and contain a high amount of sp^2 -bonded graphitic carbon phase, as revealed by XRD, XPS, Raman, TEM and selected area diffraction (SAD) patterns. Amorphous materials are expected to have novel properties in many aspects owing to their non-crystalline structure which contain no vulnerable grain boundaries. It is known that energetic particle bombardment can play a role analogous to higher temperature and stabilise film structures not normally obtained at the same substrate temperature by vapour deposition. In this research, for the investigated bias voltage range between $U_B = -65$ and -350 V, ion bombardment during film growth has demonstrated additional control of the film structure of the C/Cr coatings that has led to the formation of a new type microstructure. The microstructure evolution in C/Cr coatings was classified into three distinct bias voltage ranges, these are low energy range ($U_B = -65$ V to $U_B = -95$ V), middle energy ($U_B = -120$ V) and high energy ($U_B > -120$ V). In the low energy range, as the bias voltage increases from $U_B = -65$ V to $U_B = -95$ V, the coating structure changes from columnar with carbon accumulated at the grain boundaries to a dense structure which comprises of randomly distributed onion-like carbon clusters. At higher bias voltages ($U_B = -120$ V), the column boundaries disappeared completely, the onion-like carbon clusters increased in both their size and number, and became partially aligned in the direction parallel to the growth direction. Further increase in the bias voltage to $U_B = -350$ V (high energy) led to migration, segregation and self-organisation of the carbon atoms as a result of strong bombardment with Ar^+ ions, and, finally, to the formation of a new type of self-organised multilayer structure. Each of the above mentioned bias voltage ranges is

discussed in the following paragraphs and a structure model for the growth of self-organised multilayer C/Cr coatings under intense ion bombardment is introduced.

At the low energy range, i.e. bias voltage between $U_B = -65$ and -95 V (see Figure 4.31), XTEM Z-contrast imaging (Figure 4.32) investigations revealed a novel nanostructure in which the basic nano-lamellae obtained as a result of substrate rotation in front of the C and Cr targets were modified by an ion-irradiation induced nanocolumnar structure. The intense ion-irradiation of the immiscible film components caused local enrichment of Cr and C that propagated in the growth direction resulting in Cr-rich nanocolumns separated by C-rich boundaries in an overall amorphous structure. The formation of a nanocolumnar structure under high-flux ion irradiation is similar to the one observed [201] during reactive sputter-deposition of metastable $Ti_{1-x}Ce_xN$ alloys with $x > 0.1$. Under conditions of very high flux low-energy ion-irradiation, with $J_i/J_n \sim 10$, $E_i = 45$ eV, and energy per neutral atom $W = J_i/J_n * E_i = 450$ eV/atom, intense ion mixing in the near surface takes place resulting in the formation of local TiN- and CeN-rich areas that propagate along the growth direction. The conditions of ion irradiation used in this experiment, for the low energy range, are very similar in terms of the energy input, W , to the film due to ion bombardment, J_i/J_n of ~ 5.2 , $E_i = 65-95$ eV, and $W = 338-494$ eV/atom. With these energies a near-surface region with a thickness comparable to the period of artificial modulation is subjected to intense mixing. The nanolayered configuration, expected for multi-target deposition, is thus severely modified by a network of self-organized nanocolumns, resulting in the observed novel nanostructure. In addition to the nanocolumnar structure, more careful observation of the lattice resolution image shown in Figure 4.33 reveals that the onion-like clusters seem to be directionally oriented (highlighted by arrows) and tend to form a layered structure. The initial stages of the process of self-organisation and alignment of the clusters can be observed already at $U_B = -95$ V (see Figure 4.33, arrowed).

During medium energy ($U_B = -120$ V, see Figure 4.34) film growth, the coating becomes denser, more crystalline, and more aligned in the growth direction. The width of the column boundaries is markedly reduced with increasing bias voltage from $U_B = -65$ to -120 V. This effect is attributed to both an increase in the kinetic energy of the ions and an increase in the deposition temperature from 260°C to about 310°C as a consequence of the increased ion energy, which increases the surface diffusivity of the adatoms. In agreement with the general observations in the literature [8], densification of the coatings may result from the effects of bombardment of the growing films by

energetic particles. This enhances surface mobility of condensed species, promotes the displacement of surface atoms towards more stable positions in terms of surface energy, and results in the elimination of voids, cavities, and vacancies in the coatings.

At $U_B = -350$ V (high energy), see Figure 4.37, a well-defined multilayer structure was observed, consisting of white contrast (C-rich) onion like clusters aligned to form layers, surrounded by a darker contrast matrix of a more ordered chromium carbide-rich phase. The average periodicity (bilayer thickness) of this distinct structure is ~ 20 nm, which is almost one order of magnitude larger than that calculated on the basis of the total deposition thickness and sample rotation frequency. This leads to the conclusion that the formation of this new type multilayer structure, with abnormally large periodicity, occurs via a segregation and self-organisation mechanism triggered by the high- energy ion irradiation of the growing film.

To test this hypothesis, four experiments were performed [159]. In the first experiment, coatings were deposited using higher bias voltages of $U_B = -450$ V and -550 V. The layered structure was reproduced at $U_B = -450$ V, however, a larger bilayer thickness of 25 nm was measured, see Figure 5.1(a). Thus, confirming that the process of self- assembling is influenced by the ion bombardment. Further increase of the energy up to 550 eV led to complete disappearance of the multilayer structure, Figure 5.1(b), which indicated that this peculiar coating growth mechanism only operates in a specific bombardment energy range.

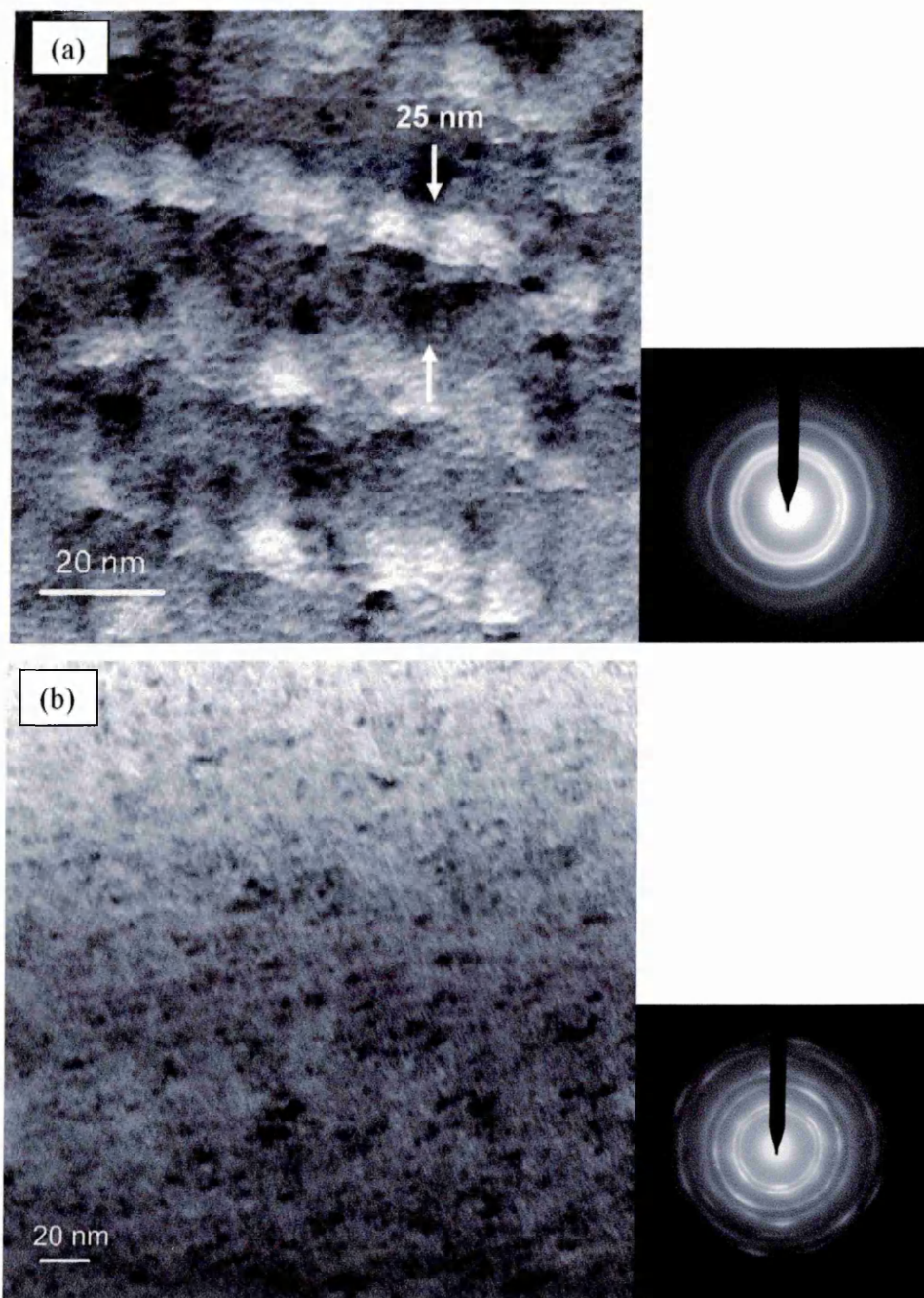


Figure 5.1 XTEM micrograph and SAD pattern of film deposited at (a) $U_B = -450$ V, (b) $U_B = -550$ V

As a large portion of the kinetic energy of the ions transforms into heat during surface bombardment, the deposition temperature of the samples rises to as high as 450° C at $U_B = -350$ V. High deposition temperatures increase the probability of phase and structural transformation. Therefore, in a second experiment, the effect of high temperatures on the formation of a self-assembled multilayer has been studied. In this experiment, C/Cr coatings have been deposited at a high temperature of 450°C but at low bias voltage of $U_B = -75$ V, similar to the temperature achieved at $U_B = -350$ V. The

BF XTEM image of this coating presented in Figure 5.2 shows no layered but a columnar structure with carbon accumulated at the grain boundaries, which is typical for the case of low energy ion bombardment, see Figure 4.29(a). This experiment further confirmed that in C/Cr films, the ion bombardment plays a dominant role in the phase separation and growth of self-organised layered structures.

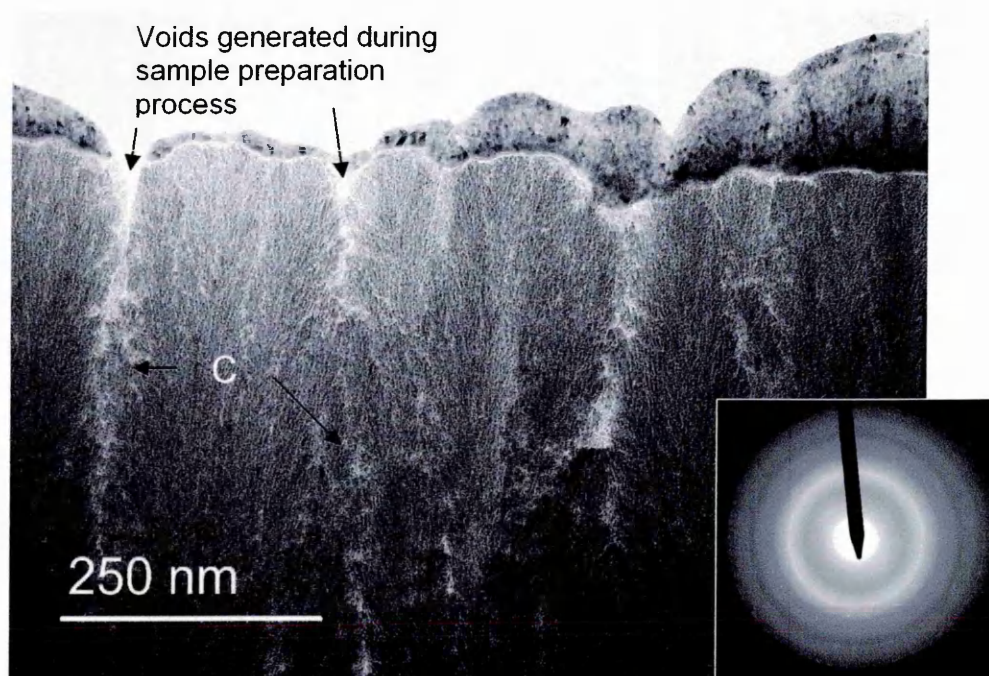


Figure 5.2 BF-XTEM image and SAD pattern of film grown at temperature of 450 °C at $U_B = -75$ V

In a third experiment, the reproducibility of these structures and the processes behind them have been investigated by depositing a coating in one deposition run by applying alternatively in four cycles, low ($U_B = -75$ V) and high ($U_B = -350$ V) bias voltages to the substrate, see Figure 4.39. In each cycle, one low energy followed by one high energy layer has been alternatively deposited for a constant deposition time of 30 min for each individual layer. On top of the 0.25 μm thick CrN base layer one can clearly see four pairs of layers containing both representative structures in their finest detail. The typical structures for both low and high-energy bombardment conditions have been repeatedly reproduced with high precision. In each pair, the high-energy layer ($U_B = -350$ V) is thinner and smoother compared to that deposited at $U_B = -75$ V, due to the intensive re-sputtering. In each cycle the low-energy irradiation has produced a

columnar structure with column boundaries enriched in C with a rough top surface of the coating. In contrast high-energy irradiation has resulted in a precise layered structure, in which carbon rich clusters (showing white contrast areas) are aligned in layers surrounded by a more metal rich (darker contrast areas) matrix. ADF STEM imaging and quantitative EELS analysis (see Figure 4.41) showed that the clusters are almost pure C (Point 3: 91.34 at.% C, 4.72 at.% Cr, 3.94 at.% O), while the matrix are Cr-rich (Point 4: 48.16 at.% C, 41.88 at.% Cr, 9.96 at.% C). This result complements XRD, TEM selected area diffraction pattern observations, Raman and XPS results, which suggest the possible formation of Cr_{23}C_6 , Cr_7C_3 or Cr_3C_2 phases. It can be speculated that the high ion energy (≥ 350 eV) increased the probability of C and Cr reacting because, during film condensation. The C and Cr adatoms may or may not be completely thermally equilibrated. They have a finite stay or residence time on the surface [202] during which they may move over the surface due to their increased kinetic energy, interact with each other to form a stable chromium carbide cluster and be chemically adsorbed on the surface.

Finally in the fourth experiment, the effect of the average composition on the layer separation process has been studied. C/Cr coatings with carbon to chromium ratio of $\sim 1:1$, a concentration, which is similar to that produced at $U_B = -350$ V have been deposited at low bias voltage of $U_B = -75$ V and using higher power (3 kW) on the Cr target. BF-XTEM analysis (Figure 5.3) shows the columnar structure with carbon segregated at the column boundaries typical micrograph for the low bias voltage range. Thus, all four experimental routes explored, demonstrated unambiguously that the process of segregation and self-assembling in the non-reactively sputtered C/Cr coatings to form a new type of multilayer structure with abnormally large spacing is at least partially the result of the intensive ion irradiation during growth. Figure 5.4 is the schematic representation of the microstructures formed between the investigated bias voltage range ($U_B = -65$ and -350 V), and this has been discussed previously.

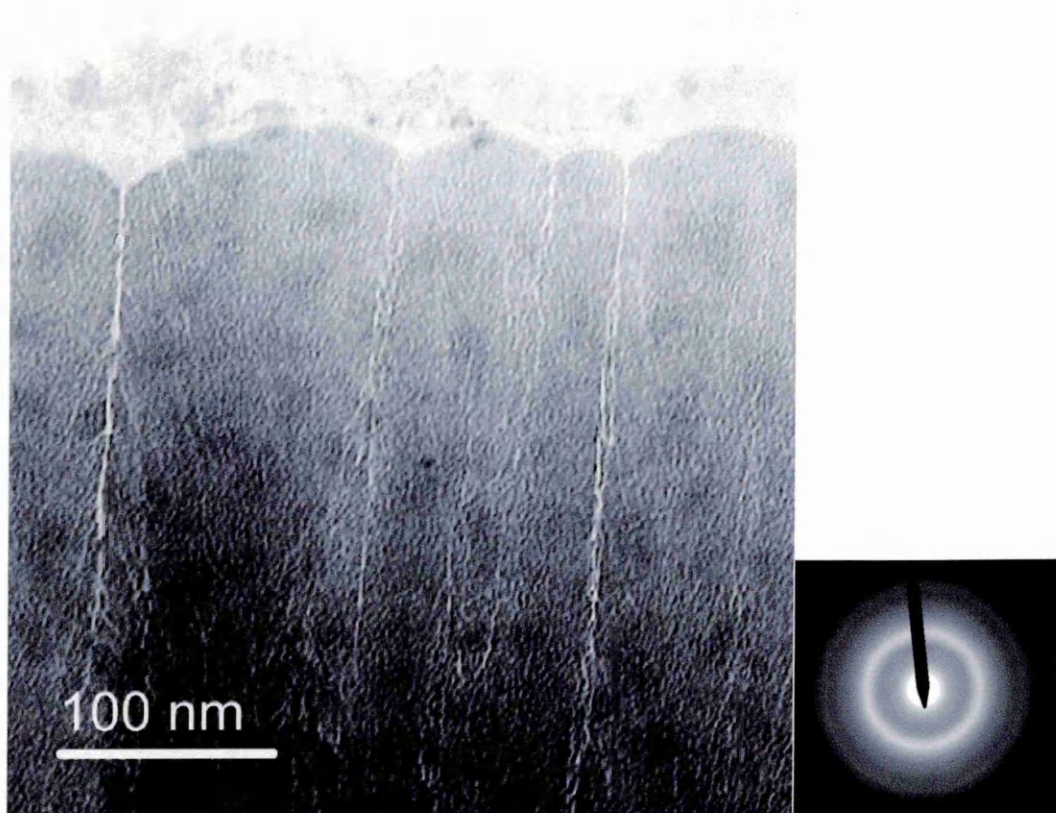


Figure 5.3 BF-XTEM image and SAD pattern of film grown at temperature of 260 °C, at $U_B = -75$ V, and Cr target power of 3 kW

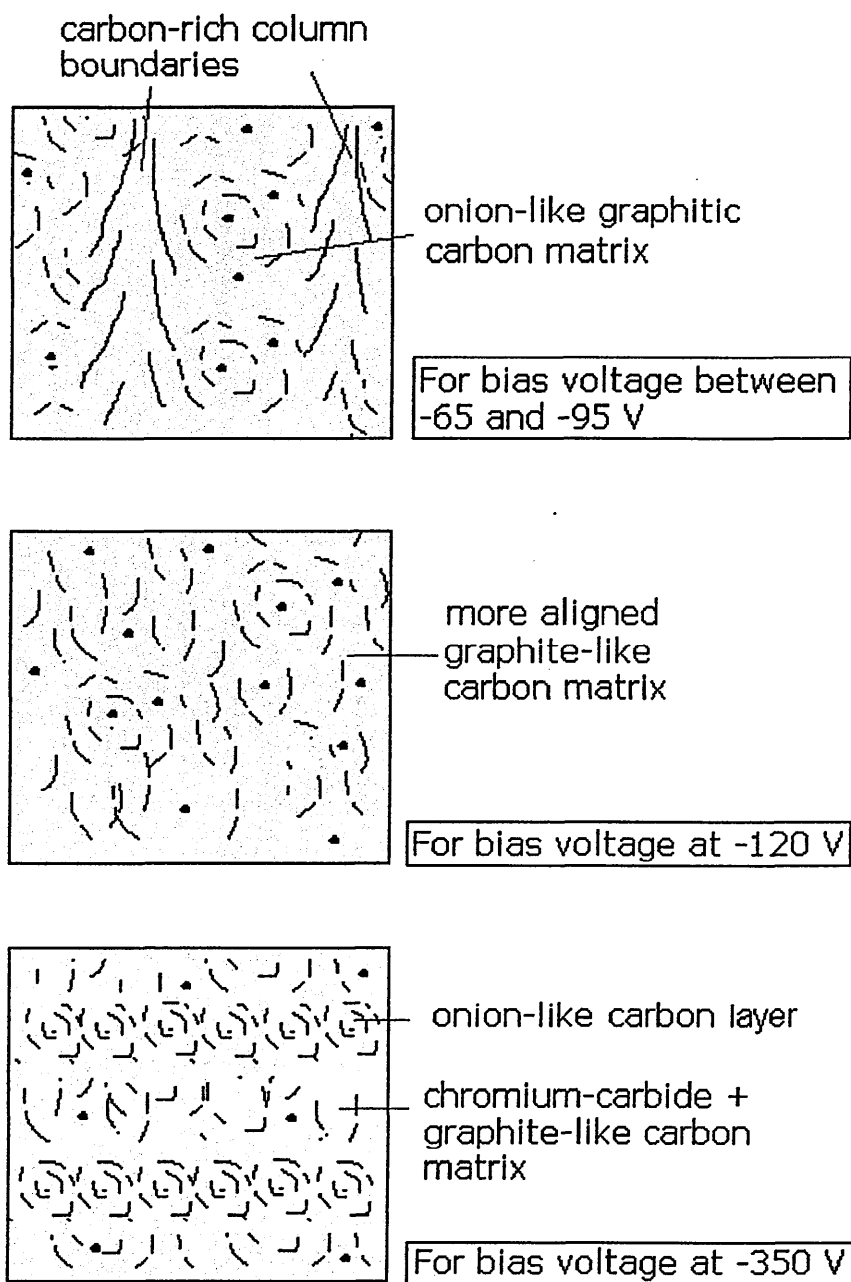


Figure 5.4 Schematic of the microstructures formed between $U_B = -65$ and -350 V

Figure 5.5 gives an overview of the microstructures developed in C/Cr coatings deposited between $U_B = -75$ V and $U_B = -550$ V, and the corresponding temperature induced by ion bombardment (y-axis). In the following paragraphs, a coating growth model is proposed accounting for the irradiation-induced ion mixing, re-sputtering, condensation surface temperature effects, nucleation and kinetic segregation process, as well as the diffusivity of the coating elements to explain the phase separation and formation of the self-organised layered nanostructure observed in C/Cr coatings.

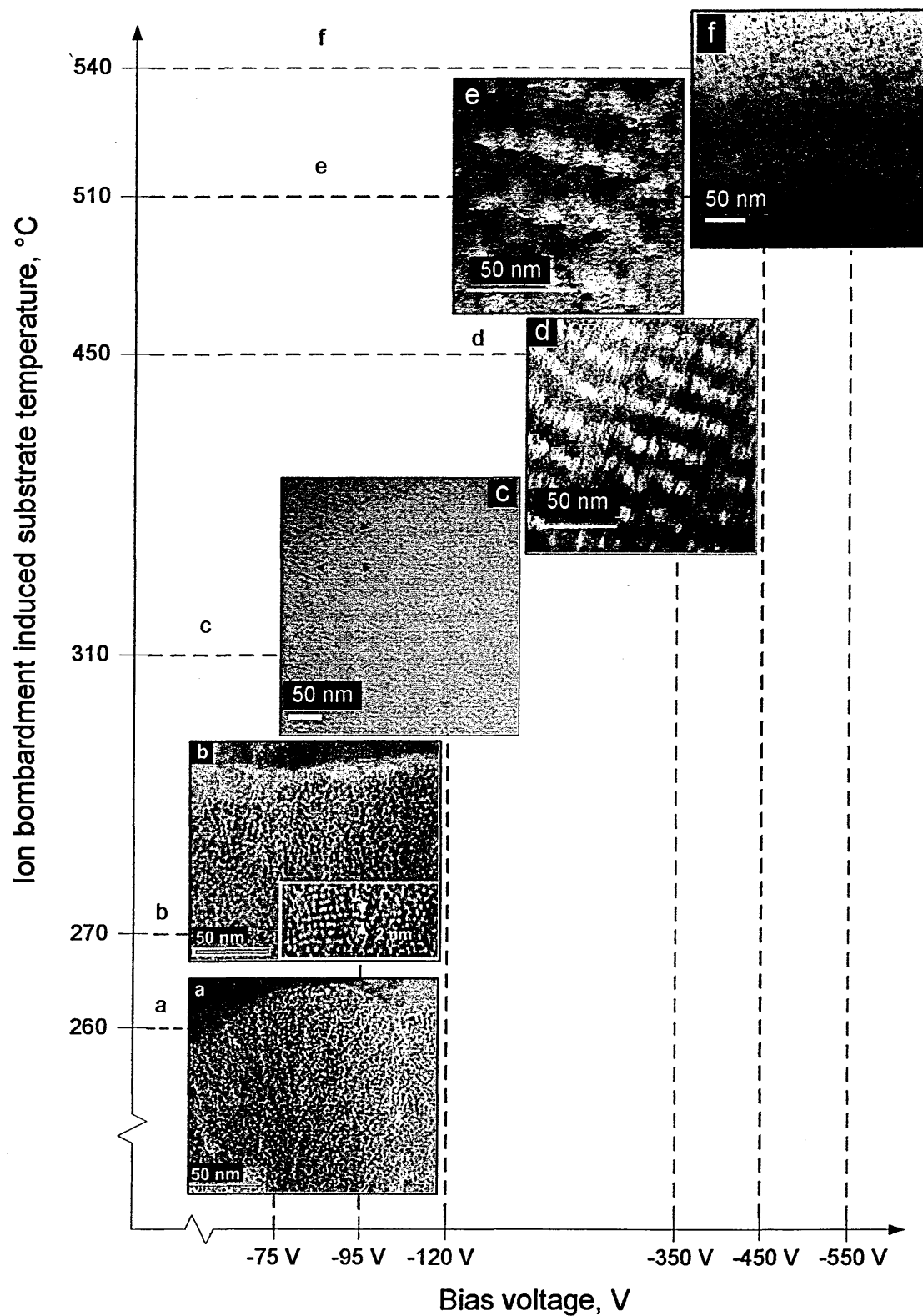


Figure 5.5 BF-XTEM views of the various types of structures developed in the C/Cr coatings deposited at bias voltages between $U_B = -75$ V and $U_B = -550$ V with their corresponding temperature induced by ion bombardment

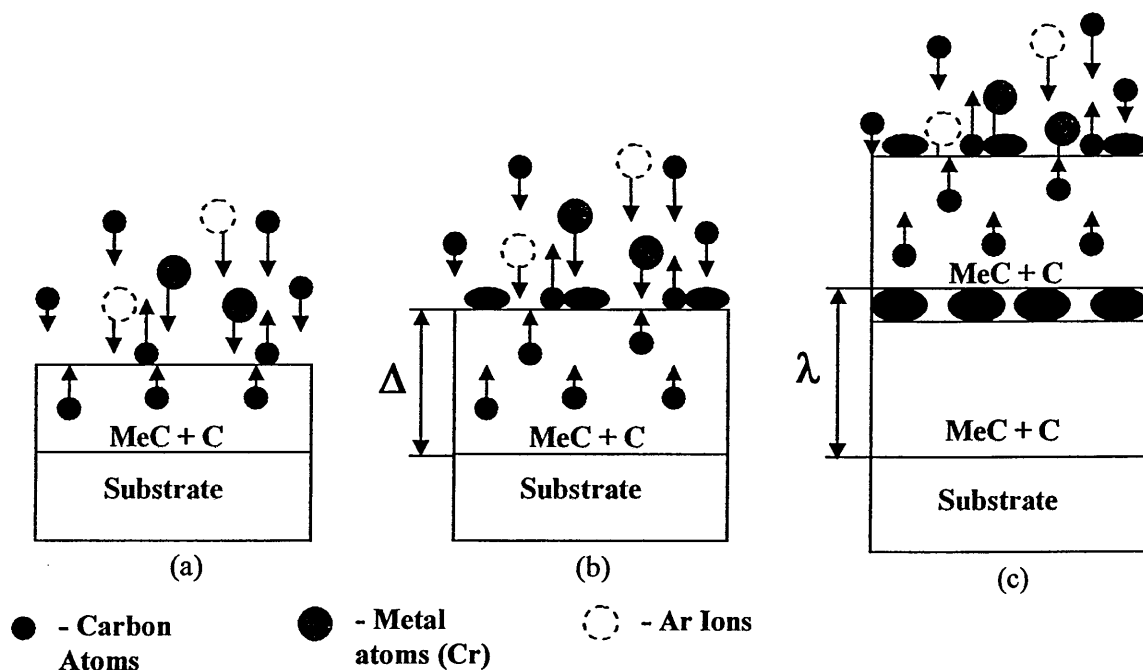


Figure 5.6 Schematic diagram of formation of nanoscale multilayer structure in the C-Me system due to irradiation induced self-organisation mechanism.
 Δ -critical thickness (volume) of the Me-C layer, λ - bi-layer thickness

Figure 5.6 schematically summarises the main steps in multilayer evolution: formation of a MeC + C layer (Figure 5.6(a)), formation of C clusters (Figure 5.6(b)) and repetition of the process (Figure 5.6(c)). The proposed coating growth model has been published in [159].

I) Formation of the (MeC + C) layer, Figure 5.6(a)

It has been realised that the layer adjacent to the CrN base layer which grows first, is a uniform (MeC + C) layer, which appears as a dark ribbon in the BF XTEM image in Figure 5.5(d)-(e), and is better seen in the dark-field image (Figure 4.35) as a white contrast layer. Formation of a mixture of Me-carbide plus free carbon (MeC + C) phases is anticipated based on the composition of the film as determined by EELS, (point 4, Figure 4.41(a)) and confirmed by the results obtained by the Raman, XPS and TEM-SAD analysis for the sample prepared at $U_B = -350$ V as discussed in Chapter 4 (section 4.5). In this initial phase of the condensation process under the present parameters, three main processes operate in parallel: (I) formation of Me-carbide phases (Cr_3C_2 and/or Cr_7C_3), (II) segregation of the excess amount of carbon not incorporated

in the carbides and (III) re-sputtering of a large portion of the free carbon. Although the sputtering yield of solid carbon is one of the smallest compared to other materials (0.12 at 500eV, Ar^+ , Table 2.2 [38]), it is very likely that the light carbon adatoms (not strongly bonded yet with each other or incorporated in other phases) will be subjected to preferential re-sputtering for the duration of their life-time on the condensation surface by the bombarding Ar^+ ions. The sputter yield of C is amplified as the Cr content in the film increases resulting in enhanced backscattering of primary Ar and secondary collision partners and hence a larger probability of sputtering surface carbon atoms [203]. In parallel, due to the higher temperature at the condensation surface (and more importantly due to the temperature difference created by the condensation and ion bombardment processes) the highly mobile segregated carbon atoms will start diffusing outwards from the bulk of the coating to the surface. Direct evidence for the existence of a significant, ~ 100 K temperature difference between simultaneously measured surface and substrate temperatures has been provided by *in situ* spectroscopic ellipsometry measurements for two systems, silicon [204] and MWCVD, (Micro Wave CVD) deposited diamond films [205]. It is expected that in conditions of ion bombardment an even steeper temperature gradient will form, further accelerating the carbon diffusion processes.

II) Formation of C clusters and repetition of the process Figure 5.6 (b) and (c)

When the MeC + C layer reaches a certain thickness, almost pure carbon clusters form spontaneously all over the condensation surface to form a layer, which follows the surface topography. As the film grows the concentration of segregated carbon increases and carbon rich regions will stochastically form. The sputter-yield amplification effect will be suppressed in such areas because the solid carbon phase has a very small sputtering yield and it will act as a sink of carbon atoms. Once nucleated, the carbon-rich clusters will grow further in a 3-D mode by collecting atoms, mainly mobile surface carbon atoms as well as excess bulk atoms from the Me-carbide matrix. Once the excess carbon is depleted the growth of the clusters is interrupted and they will be surrounded (overgrown) by the Me-Carbide phase, initiating a new process of C segregation layer formation. The C nucleation process will be repeated again after a certain film thickness, Δ (Figure 5.6(b)) when the surface concentration of the segregated and excess mobile bulk carbon reaches the necessary critical value. This explains the observed increase of the bilayer period, λ , (Figure 5.6(c)) of the self-

organised multilayers with the increase of the bias voltage as discussed previously (see Figure 5.1(a)). Due to the more intensive re-sputtering at higher bias voltages the overall carbon concentration in the MeC + C layer is expected to be lower, therefore a larger volume, (thicker layer) of MeC + C is required to provide the critical number of carbon atoms for nucleation of carbon clusters on the surface. In addition, the local curvature of the surface may influence the re-sputtering rate of carbon due to the angular dependence of the sputtering yield. In several places in the 75 eV/ 350 eV sample we observe suppression of the carbon cluster formation, and this is correlated with large local curvature of the underlying 75 eV layer (region marked with arrows in Figure 4.39).

The operation of the above described self-organised layer formation mechanism becomes possible due to the presence of elements with long-range diffusion such as carbon, the ion-induced phase formation of a Me-carbide phase and segregation of excess carbon, and the particular conditions of ion mixing achieved on the condensation surface due to the intensive ion irradiation in a defined energy window.

5.2 Mechanical and tribological behaviour

The excellent adhesion of C/Cr coatings deposited by the combined steered cathodic arc/unbalanced magnetron sputtering technique resulted from the effective Cr^+ ion etching prior to the coating deposition step. The bombardment by highly charged metal ions generated by a steered cathodic arc discharge provided an intensive sputter cleaning of the substrate surface and a tailored interface formation [141]. The interface between the substrate and the CrN base layer was dense and sharp, as can be seen in the XTEM image shown in Figure 5.7. This finding is consistent with the literature [141] which reported that metal ion (Cr^+) substrate pre-treatment and introduction of a stress reducing base layer can be used to control adhesion problems arising from the inherent high internal stresses. Although the adhesion of C/Cr films is excellent, it was found to be strongly affected by the energy of ion bombardment during film growth, because of the increased film residual stress with increasing bias voltage.

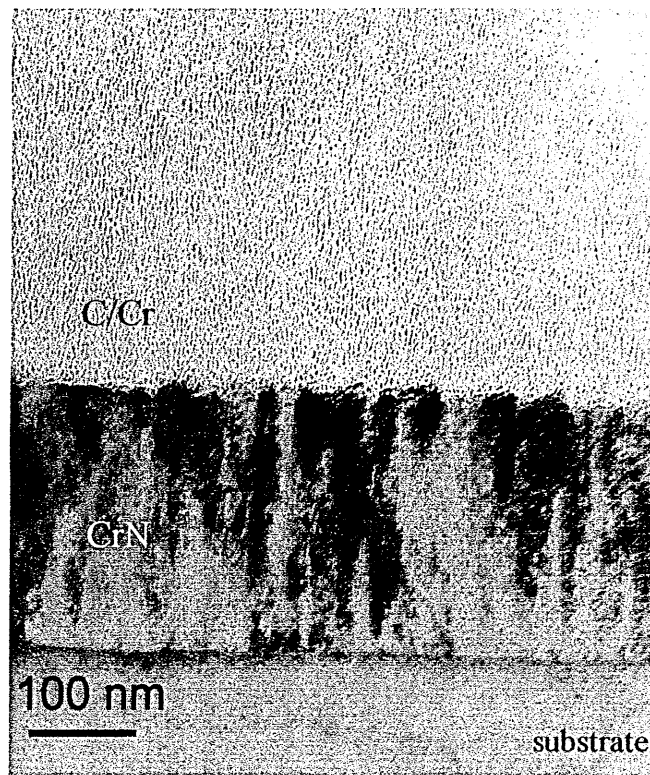


Figure 5.7 XTEM image showing the substrate-CrN base layer interface, and C/Cr coatings

As previously described in Section 4.4.5, the compressive stress in C/Cr coatings was observed to rise to a maximum as the bias voltage increases to $U_B = -120$ V. Thereafter as the bias voltage is increased further to $U_B = -350$ V, the intrinsic compressive stress was found to decrease. A similar observation was reported recently, which suggests that stress was generated as a direct result of atomic implantation due to energetic ion bombardment [206-207]. They reported that increases in the energies of the incident species may cause the stress in the growing film to go through a maximum, thereafter, the stress starts to be relieved or reduced [208]. This is because, as the energy of implanting ions increases, the size of the thermal spike (the volume of the heated region caused by ion impact) increases, thus allowing more atomic movement, meaning that the heated atoms can substantially rearrange their bonding and undergo stress relaxation to reduce the local density (high local density means high stress).

From the results obtained by Raman spectroscopy (see section 4.5.3), the D-band position was found to have a close dependence on the stress in the C/Cr coatings, in which the D-band shifts to higher wave-numbers as the compressive stress in the

coatings increases (see Figure 5.8). This observation is in agreement with a recent report that peak shifting provides a direct relationship between processing conditions and the residual stresses where tensile stress in the coating causes the D and G bands to shift towards lower wave-numbers, whereas the compressive stress causes peak shifting towards higher wave-numbers [174].

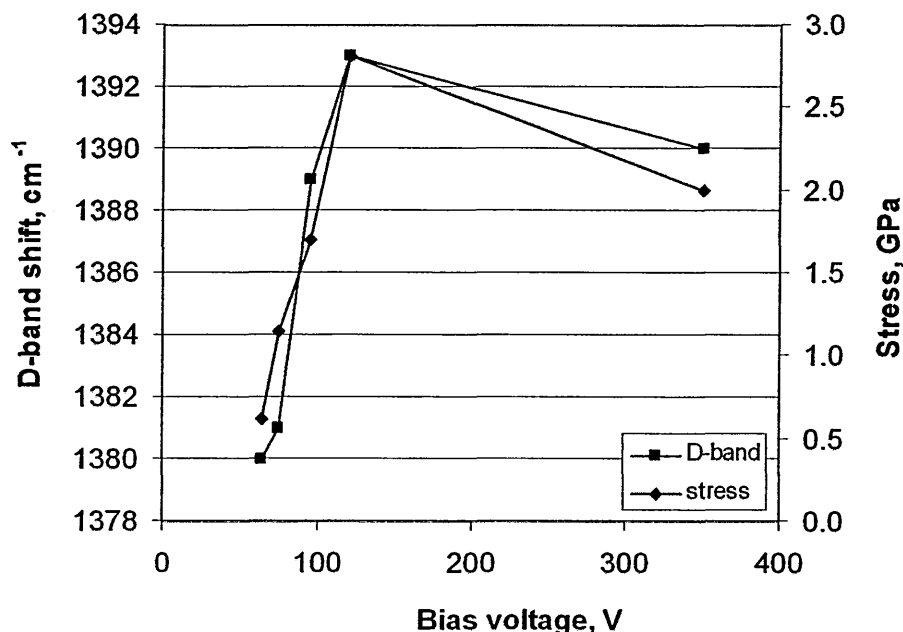


Figure 5.8 D-band shift and stress as a function of bias voltage for C/Cr coatings

The effect of the bias voltage on the friction behaviour of the C/Cr coatings has been studied. A strong correlation between the microstructure, the residual stress, the I_D/I_G ratio in the films and their friction behaviour were found. As shown in Figure 4.9, the coefficient of friction of C/Cr coatings was found to decrease from 0.22 to 0.16 with increasing substrate bias voltage from $U_B = -65$ to -95 V, then increases to 0.31 as the bias voltage was increased further to $U_B = -350$ V. This finding agrees well with that for the recently reported amorphous pure carbon thin films grown by magnetron sputtering [164]. This result can be well correlated with the findings of XTEM, which show decreasing surface roughness and significant densification of the coating as the bias voltage is increased from $U_B = -65$ to -350 V due to the ion-irradiation effect. The coating deposited at $U_B = -65$ V is rougher and shows under-dense columnar structure with a weak carbon phase present accumulated at the grain boundaries. During sliding, the rough surface experiences greater asperity contact which increases the tendency for plastic deformation and mechanical inter-locking resulting in the formation of wear debris which could be trapped in the wear track. As shown previously for a columnar

structure [209], the tangential friction force exerted on the coating surface during sliding can bend, plastically deform and break the columns, releasing large particles, which act as a third body in the tribo-contact, thus increasing both the friction and the wear. This process becomes even more accelerated if a weaker (pure carbon) phase is responsible for providing the bonding between the individual columns. The friction force in this case can easily open tensile cracks and detach the individual columns due to the lower tensile strength of the carbon phase. In contrast, at a higher bias voltage of $U_B = -95$ V, as a result of surface smoothening (less asperity contact) and densification of the coating, sliding wear occurs layer-by-layer resulting in a lower friction coefficient and a smoother friction curve. This is well correlated with the smooth and narrow wear track as seen in Figure 4.28. Another reason for the reduced friction coefficient at $U_B = -95$ V is seen in the formation of the much denser and more uniform structures based on randomly distributed onion-like features as well as the increase of the I_D/I_G ratio and therefore the amount of the sp^2 bonded carbon in the coating, which reaches its maximum at $U_B = -95$ V (see Figure 5.9). However as the bias voltage increased further to $U_B = -350$ V, the I_D/I_G ratio decreased slightly (reduced sp^2), but the friction coefficient ($\mu = 0.31$) increased significantly. This can be expected as the enhanced ion bombardment at higher bias voltages leads to increased residual stress and formation of Me-carbides, which reduces the amount of the free and highly lubricious graphite phase in the coating.

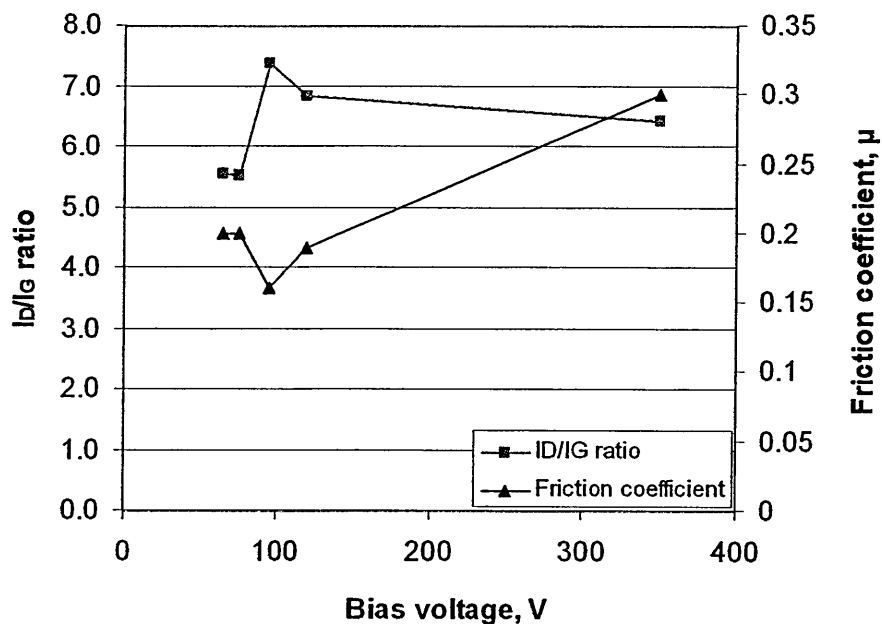
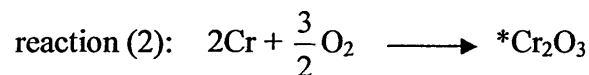
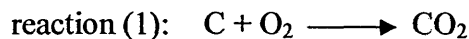


Figure 5.9 I_D/I_G ratio and friction coefficient as a function of bias voltage for C/Cr coatings

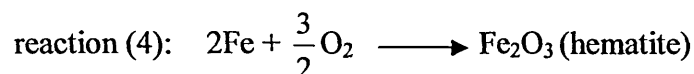
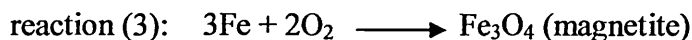
The wear resistance of the coatings correlates well with their friction performance, specifically, films with higher friction coefficient suffer higher wear rates. The excellent wear behaviour of the C/Cr film, especially the low wear coefficient ($6 \times 10^{-17} \text{ m}^3 \text{ N}^{-1} \text{ m}^{-1}$) can be attributed to the observed curved onion-like structure of the coating. It has been reported [15] that, this type of structure tends to show high material integrity and toughness due to the unique slip hindering mechanism resulting from the cross-linking and the geometrical interlocking of the graphite planes.

5.3 Oxidation behaviour

For all the applied bias voltages, the oxidation of the coating and the substrate may occur through the following reactions:



(* the only stable chromium oxide formed on heating in oxygen at various temperature)



The oxidation behaviour of C/Cr coatings was found to strongly depend on the microstructure, which is strongly influenced by the bias voltage. To aid the explanation, the oxidation mechanism of C/Cr coatings was discussed by dividing the bias voltages into three ranges, these are (i) between $U_B = -65$ and -75 V, (ii) between $U_B = -95$ and -120 V, and (iii) $U_B = -350$ V. These are the bias voltage ranges where significant microstructure evolution and phase transition (as revealed by XRD, XPS and Raman after heat treatment) in the coatings were observed.

The TG data (see Figure 4.44) showed a two stage (stage I and stage II) oxidation of the coating deposited at low bias voltage between $U_B = -65$ and -75 V, but this effect was not seen for films prepared at higher bias voltage. This finding was in good agreement with the one observed during the oxidation of DLC films [182] and Cr-doped DLC films [210], which reported that the weight loss (stage I oxidation) at $290 - 342^\circ\text{C}$ [210] and 350°C [182] was due to evaporation of oxidised carbon according to reaction (1), and the weight gain (stage II oxidation) at 400°C [210] and 450°C [182] resulted from the oxidation of the film underlayer. In this study, weight loss (stage I

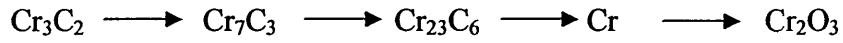
oxidation) of C/Cr films was found at about 400 - 420°C, which was attributed to the onset of carbon dissolution as CO₂ gas which escaped with the vent gas. This process was even more accelerated for the carbon weak phase along the column boundaries within the pronounced columnar structure produced at low bias voltage. The stage II oxidation of C/Cr coating began at about 660 - 670°C, and a weight gain resulted from the formation of chromium oxide. Further increase in the temperature to 1000°C produced a greater weight gain due to an increase in the amount of iron oxide and chromium oxide. Coating deposited at $U_B = -75$ V can survive up to 350°C, and up to 450°C for films grown between $U_B = -95$ and -120 V. It can be speculated that the coating surface was fully oxidised and covered with a layer of protective chromium oxide (Cr₂O₃) at 410°C for $U_B = -75$ V, and 700°C for $U_B = -95$ and -120 V. This is because the broad diffuse peak from the as deposited coating was no longer present at these temperatures, see Figure 4.51. Coatings deposited at higher bias voltage between $U_B = -95$ and -120 V exhibit better oxidation resistance than films grown at $U_B = -75$ V due to the smoother, denser and smaller column boundaries or almost columnar free structure, which contained uniformly distributed onion-like clusters, that reduce the oxygen penetration process. For all the applied bias voltages, peaks from the original coating disappeared at 700 °C (see Figure 4.51), this is either due to an oxide thickness that exceeded the X-ray penetration depth, or spallation of the coating [211]. The latter was unlikely, since a strong substrate signal was not found and the surface observed under SEM remain undamaged except for the more porous surface (see Figure 4.55). Hence, this may indicate some structural changes in the films during oxidation at the above mentioned temperature range. This interpretation was in good agreement with the structure transition observed by Raman spectra of the heat-treated samples (Figure 4.57).

The Raman spectra of the heat-treated surface showed a sharper D-band, a distinct increase in the intensity of the D-band concurrently with gradual disappearance of the G-band, and detected an upward shift of D and G bands frequency from 1380 to 1400 cm⁻¹ and 1580 to 1596 cm⁻¹, respectively, with increasing heating temperature. This observation is in good agreement with the results reported on oxidation of DLC films [182, 184, 210, 212-213] and carbons [214] by other researchers. Tallant et. al [213] found that the conversion of DLC to nano-crystalline graphite (“glassy” carbon) began at 300°C and was completed after heating to 450 – 600°C in ambient air, as evidenced by small changes in the D (1350-1380 cm⁻¹) and G (1532-1598 cm⁻¹) band

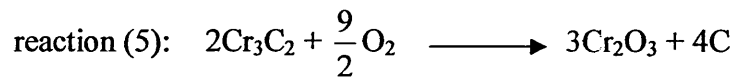
frequencies and a progressive increase in the intensity of the D-band of the DLC Raman spectra with increasing heating from 300 to 450°C. Wang et. al. [182] showed the increase in the D-band intensity and upward shift of the G-band (from about 1550 to 1580 cm^{-1}) as the heating temperature increased from 25 to 300°C. Zhang and Koka [212] also reported similar results, but their DLC film was found to convert from amorphous to nanocrystalline graphite above 600°C. Kulikovskiy et. al. [184] reported that the temperature at which the D-band starts to develop is depended on the hardness of the film, where the onset of this effect is observed at higher annealing temperature (at 300°C and above) for a harder film. They also found separation and narrowing of the D and G bands, and shifting of the G-band from 1540 to 1600 cm^{-1} , with increasing annealing temperature. They explained this effect as a result of occupancy of oxygen between the principal layers which gradually shift the G-band position with increasing oxygen penetration depth. Therefore, from the results obtained in this research, it can be concluded that the increase in the intensity and narrowing of the D-band, and shifting of D and G bands to higher frequency could be attributed to the conversion of amorphous carbon to nanocrystalline graphite and an increase in the sp^2 bonding, as the heating temperature increases. The increase in the degree of crystallisation (removal of disorder in the graphitic structure) on the other hand, was associated with an increase in bond angle disorder (disorder in the graphite lattice) as evidenced by the increase in D-band intensity due to the variation or breaking of symmetry and bonding at the edges of the graphite planes [213, 215]. According to Schwan et. al. [216], D band should not be detected in a completely sp^3 network and hence the I_D/I_G ratio will tend to zero. In other words, the sp^2 content increases as the I_D/I_G ratio increases. As mentioned previously for this experiment, the relative intensity of the D- to G-band increases (G band tends to zero at 700°C) with increasing heating temperature, therefore an increase in temperature will increase the sp^2 bonding in the C/Cr coatings. This agrees well with [216]. However, for films deposited between $U_B = -95$ and -120 V, the above effects were not observed until 700°C where the D-band shifted from 1380 to 1400 cm^{-1} , and the G-band shifted from 1590 cm^{-1} to a higher frequency of 1618 cm^{-1} . A recent paper [210] also reported an upward shift of the G-band position from 1570 to 1620 cm^{-1} with increasing annealing temperature, and attributed this to the increased graphitic composition in the films.

The oxidation mechanism of coatings deposited at $U_B = -350$ V was more complicated than for the films produced at lower bias voltage. It can be speculated that

this is due to the presence of a metal-carbide phase in the carbon matrix. This metal-carbide phase was suggested as type Cr_3C_2 by XRD analysis presented in Figure 4.16. As seen in Figure 4.51, the C/Cr coatings deposited at $U_B = -350$ V began to oxidise at 350°C and were fully oxidised to chromium oxide at 700°C . It is noteworthy to mention that the (011) Cr_3C_2 peak became narrower and sharper, and the (152) peak became more pronounced as compared to the as-deposited coating when the temperature increased from 350 to 450°C , which could result from pronounced crystallisation of the carbide [217] and stress relaxation as a result of annealing. However, at 700°C , these peaks were not observed and the only reflections were from Cr_2O_3 . The conversion from Cr_3C_2 to Cr_2O_3 could begin between the temperature range of 450 to 700°C , possibly about 550°C as revealed by TG analysis, which showed rapid oxidation (weight gain) of the coating at about 550°C . This temperature range is in good agreement with the reported oxidation temperature of Cr_3C_2 powders i.e. between 370 and 700°C [217]. It has been reported that when Cr_3C_2 is exposed to air or oxygen, carbon is predominantly oxidised, and there is possibility of formation of lower carbides such as Cr_7C_3 and Cr_{23}C_6 , and metallic chromium at the interface between the oxide layer and the remaining carbide via the following process [218]:



However, in this experiment, the XRD patterns only showed the presence of Cr_3C_2 and Cr_2O_3 between 350 and 450°C , and only Cr_2O_3 was observed at 700°C . A similar observation was also reported by Loubière et. al. [217] and they suggested that the Cr_7C_3 , Cr_{23}C_6 , and Cr phases formed during oxidation were thermodynamically unstable and oxidised quickly. Apart from this, it can be speculated that the carbide may also react with oxygen straight away, forming Cr_2O_3 and releasing previously ‘bound’ carbon. The reaction could be possibly written as follows:



The carbon atoms released from the carbide lattice during oxidation led to an increase in the carbon composition within the films. This may explain why the Raman spectra from the coating became more graphite-like with increasing heating temperature, and converted to highly disordered graphite at 700°C , as revealed by the presence of the D-band at 1338 cm^{-1} , the G-band at 1590 cm^{-1} , and a weak disordered band near 1618 cm^{-1} (an example of the Raman spectrum of highly disordered graphite is shown in [171]). A similar phenomenon was also observed in a DLC-coated Al_2O_3 -TiC recording head,

where the diffused carbon from the TiC lattices contributes to the onset of a more graphite-like Raman spectrum [212].

5.4 Corrosion behaviour

C/Cr coated stainless steel (SS) substrates showed an improved corrosion resistance compared to the uncoated SS substrate. The improved corrosion resistance of the C/Cr coated sample was attributed to the C/Cr coatings that provided a barrier between the substrate and the corrosive medium, by inhibiting the diffusion of oxygen and water to the substrate, and possibly the formation of a protective Cr_2O_3 layer. Carbon and chromium are more noble than Fe in the galvanic series, thus if the substrate is perfectly covered by the coating, the coating should protect the substrate from corrosion. Unfortunately, it is very difficult or nearly impossible to produce a perfect coating without defects with the current deposition technologies, and it is of no surprise that coating growth defects such as macroparticles, droplets or pinholes, are also present in coatings prepared by the combined steered cathodic/unbalanced magnetron sputtering technique [54-55]. SEM images clearly showed the onset of pitting at coating growth defects (see Figure 4.62). The growth defects may provide paths that allow the solution to reach the substrate material and lead to galvanic corrosion at the coating to substrate interface. This has been demonstrated by Wang et. al [55], as schematically illustrated in Figure 5.10. It has been proven [55, 219] that through-coating thick macroparticle inclusions are dangerous in terms of coating performance as most corrosion is initiated by galvanic or crevice corrosion between the defect and the coating matrix. Pathways allowing solution access to those defects can eventually lead to substrate pitting and corrosion at the coating/substrate interface. In this experiment, the sources of corrosion of C/Cr coatings can be explained with Figure 5.10 [55] and are summarised as follows:

- (1) Galvanic corrosion (reaction 1) due to dissimilar metal contact (Cr from the coating and Fe from the substrate) in the presence of 0.01% NaCl solution at pinhole defects or pores in the coating (see Figure 4.62(a) and (d)). In this case, the Fe substrate is anodic to the C/Cr coating (cathode) and therefore corrodes. The primary anodic reaction is Fe dissolution:



with the cathodic reaction being the reduction of dissolved oxygen in the solution,



(2) Macroparticles present in conjunction with pinholes within the coating (can be seen in Figure 4.62(e)). Two possible corrosion mechanisms are:

- Galvanic corrosion between macroparticle and coating (reaction 2 and 3)
- Galvanic corrosion between coating and substrate* (reaction 4)

*Note: There appears to be an inconsistency in the schematic as this shows both dissolution of droplet and substrate.

The small local anodic area initiated from the growth defects can result in accelerated corrosive attack at the bottom of the remaining pinhole, leading to much bigger holes, which uncover the substrate. Hereby, the corrosion products at the interface between coating and substrate contribute to force ongoing coating delamination [220], see Figure 4.61. A recent publication on the corrosion of DLC coatings reported that the mechanisms for improving the corrosion resistance are attributed to the low electron conductivity of the DLC film, which reduces the electron transport and the exchange of electrical charges at the sample surface necessary for the electrochemical corrosion [220].

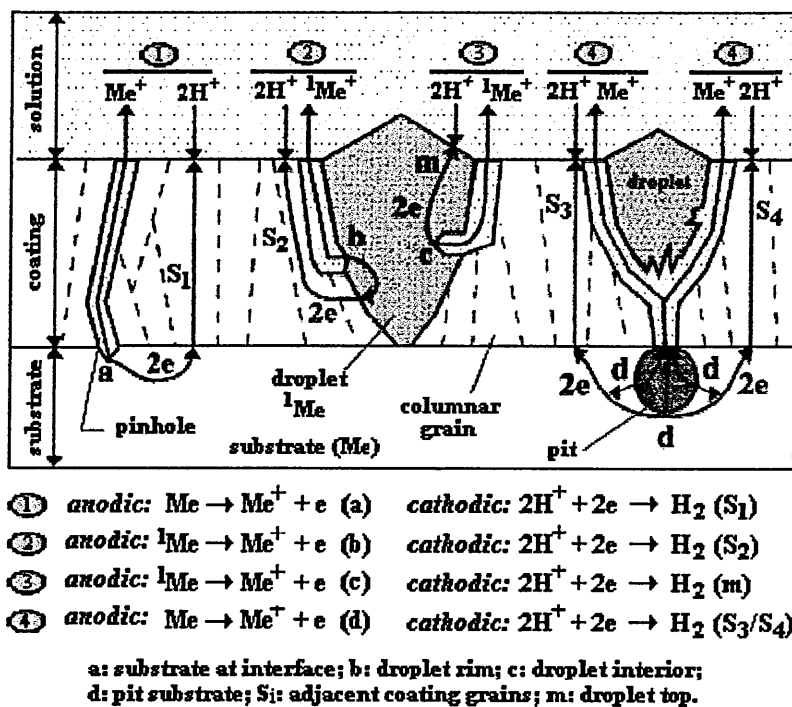


Figure 5.10 Corrosion mechanisms of coatings in the presence of solution [after [55]]

The corrosion resistance of C/Cr coatings depends on the nature of the microstructure of the films, i.e. columnar, amorphous or multilayer structure that form at different applied bias voltages. Films deposited between $U_B = -65$ V showed the least resistance to corrosion as compared to films deposited at higher bias voltages. This is due to the predominant sub-dense columnar structure of $U_B = -65$ V films, which provide a direct path for the transport of the solution towards the substrate. The corrosion resistance of C/Cr coating improved with increasing bias voltage to $U_B = -120$ V (see Figure 4.58), as can be seen by the smoother, denser and more uniformly distributed onion-like structure (see Figure 5.5), which slow down solution penetration.

5.5 Dry high speed machining

Cutting tools are made of high-speed steel or cemented carbide. In this research, only cemented carbide ball nose end mills are used as substrate material for milling tests. The objective of conducting this test is to find out if the tribological behaviour of C/Cr coatings determined in the laboratory tests correlates with the actual application determined by dry high speed milling tests. The results showed that they are well correlated. During machining, cutting or drilling, cutting tools are subjected to degradation by abrasive wear as well as by adhesive wear, and most importantly the generation of heat. It was reported that about 70% of the heat originates from the plastic deformation of the workpiece material, and the other 30% arises from friction between the tool and the workpiece material [221]. A large amount of heat is taken away by chippings, whereas another part is conducted into the deeper areas of the workpiece and the tool by mechanical contact. The high temperatures and forces at the tool tip could promote adhesive wear and microwelding between the chip from the workpiece and the cobalt binder phase in the cemented carbide [222]. By applying a layer of friction reducing or solid lubricant coating, as in this study C/Cr coating, the cutting edge geometry has been better preserved with little material transfer and the life-time of the end mills was enhanced by a factor of two as compared to the uncoated tools. This is particular noticeable for coatings deposited at $U_B = -95$ V, which have the ability to remove the highest amount of material, experience the smallest wear on the flank, and have little material pick-up, as shown in Figures 4.80 to 4.82. This indicates the potential use of C/Cr coatings for dry high-speed machining of “sticky” alloys. The

outstanding performance of the C/Cr coating deposited at $U_B = -95$ V correlates well with its excellent adhesion strength (critical load of 75 N), low friction ($\mu = 0.16$) and low wear coefficients ($\sim 6 \times 10^{-17} \text{ m}^3\text{N}^{-1}\text{m}^{-1}$), and good oxidation resistance (up to 700 °C where the coating does not spall but forms a protective chromium oxide, see Figure 4.55). Owing to their chemical inertness and low coefficient of friction, C/Cr coatings prevented adhesive effects between the tool and the work material. Cutting edges almost free of built up material have been observed by SEM (see Section 4.8) after machining automotive Al alloy (Al-Si8Cu3Fe) with C/Cr deposited at the optimised bias voltage of $U_B = -95$ V. The excellent performance of the C/Cr coating demonstrated with this study is expected to be improved even further when tools with optimised cutting edge geometry, (specific to Al cutting) are employed.

The cutting test results obtained during this research are in good agreement with those published by other researchers [221, 223-226]. They reported that carbon-based coatings are suitable candidates for dry milling applications of aluminium alloy due to their combined low coefficient of friction and high wear resistance, leading to the low tendency of adhesive effects between tool and a work material. Thus, a reduction in the formation of a built-up edge, which is essential in maintaining the sharpness of the edge, and therefore improved machinability and the quality of the work materials is achieved [223]. On top of that, the good thermal conductivity of graphite also plays an important role in dissipating frictional heat generated at the contact points between the tool and the workpiece material, thus reduce the adhesive tendency.

Aluminium and its alloys are widely used in the fields of die/mold, construction, automotive, electrical and communications industries, packaging, and appliances. However, because of the low melting temperature of aluminium, it softens during dry machining which shortens the tool life and has an adverse effect on the surface quality and edge quality, for example built-up edges and burrs [227]

CHAPTER 6

Conclusions

This research opens up a new field of applications of the ABSTM technique to deposit Me-Graphite i.e. C/Cr coatings. The systematic investigation of the effect of ion bombardment on the composition, microstructure, and functional properties of C/Cr coatings has led to an important contribution to the understanding of the growth processes taking place in the C/Cr system. A coating growth model accounting for the influence of ion bombardment on the growing C/Cr film was introduced to explain the phase separation and the formation of the self-organised layered nanostructure. The results show strong correlation between the microstructure, functional properties and performance of C/Cr coatings.

This thesis is concluded as follows:

1. Nano-scale multilayer C/Cr coatings with excellent adhesion ($L_c > 70\text{N}$) were successfully deposited by the combined steered cathodic arc/unbalanced magnetron sputtering (also known as Arc-Bond Sputtering or ABSTM) technique using three graphite targets and one Cr target. The ABSTM technique has been demonstrated as a promising process to grow high quality, excellent adhesion C/Cr coatings.
2. Under conditions of intensive ion irradiation, J_i/J_n from 5.2 to 6.9, and high energy per neutral atom from $W = 338 \text{ eVatom}^{-1}$ to 3150 eVatom^{-1} , for $E_i = 65$ to 450 eV respectively, the following structural effects in the coating have been observed:
 - Accumulation of carbon at the grain boundaries ($U_B = -65 \text{ V}, -75 \text{ V}$)
 - Pronounced densification and smoothening of the coating
 - Severe distortion of the artificial nanolayer structure resulting from the intense ion mixing ($U_B = -65 \text{ V}, -75 \text{ V}, -95 \text{ V}$)
 - Formation of a novel amorphous nanostructure, in which Cr-rich clusters are surrounded by a carbon-rich matrix. This new structure is formed as a result

of superposition of self-organised nanocolumns and the artificial nanolayers ($U_B = -65$ V, -75 V, -95 V)

- Cross-linking and geometrical interlocking of the graphite planes, formation of onion-like features
 - Formation of distinct nanoscale multilayered structure between $E_i = 350$ and 450 eV
3. The phase composition of C/Cr coatings transformed from more graphite like (sp^2 C-C bonded) to more Me-carbon (Cr-C bonded), where the content of the carbide phase increased with increasing bias voltage.
 4. Between $U_B = -350$ and -450 V, a new type of nanoscale multilayered structure was formed via an ion irradiation-induced self-organisation mechanism. A model has been proposed to explain the evolution of this new type multilayer structure comprising sequentially formed layers of nanocrystalline Me-carbide + C and layers of almost pure carbon clusters, with abnormally large bi-layer spacing of 20-25 nm observed in C/Cr coatings deposited by non-reactive magnetron sputtering in conditions of intense ion irradiation. More specifically, the new type multilayer structure has been observed to develop in conditions of high-flux ion irradiation ($J_i/J_n \sim 6.5-6.9$) and using ion bombarding energies in the range between 350-450 eV, where extremely intensive ion mixing occurs in the surface/subsurface region. This model accounts for the irradiation-induced ion mixing and crystallographic phase formation, re-sputtering, condensation surface temperature effects, nucleation and kinetic segregation process, as well as the enhanced near-surface diffusivity and pronounced smoothening of the growth front. The model proposes that the layered structure evolves in three steps; formation of a MeC + C layer, formation of C clusters, and overgrowing of the C clusters with a MeC + C tissue phase, which leads to the repetition of the process.
 5. The best tribological and cutting performance have been achieved with coatings deposited at $U_B = -95$ V ($\mu = 0.16$, $K_c \sim 6 \times 10^{-17} \text{ m}^3\text{N}^{-1}\text{m}^{-1}$). This result can be explained by the dense structure based on formation of onion-like carbon clusters as well as the increased sp^2 content in the film indicated by the increased I_D/I_G ratio determined from the Raman spectra of the C/Cr coatings.
 6. The oxidation resistance of C/Cr coatings outperformed that of the state-of-the-art TiN coating, and improved with increasing bias voltage from $U_B = -65$ to -350 V. Two stages of oxidation were observed. Stage I, which was only observed in films

deposited between -65 V and -75 V, began at about 400°C - 420°C due to rapid evaporation of carbon possibly along the carbon-rich column boundaries. Stage II oxidation, which was observed for all the applied bias voltages began at about 660 - 670°C due to oxidation of C/Cr coatings which led to the formation of chromium oxide.

7. In dry machining of automotive grade Aluminium alloy (Al-Si8Cu3Fe), C/Cr coatings have doubled the life-time of 8 mm ball nose end mills, demonstrating their big potential for application in cutting of “sticky alloys”, for example aluminium.
8. A conventional Scanning Reference Electrode Technique (SRET) has been successfully modified to provide a novel method for characterising the real-time localised tribocorrosion behaviour of uncoated and C/Cr coated samples. This test method may contribute significantly to the understanding of wear-corrosion synergism. The influence of various test conditions involving contact load and test environments have been demonstrated, and have been found to affect the following parameters:
 - local anodic current activity
 - the number of active anodic areas
 - sample (repassivation) recovery time
 - free corrosion potential
 - amount of wear
 - wear coefficient
 - wear morphology
9. For tribocorrosion tests conducted in dry air, C/Cr coated stainless steel exhibited 2-3 orders of magnitude improved wear resistance compared to the uncoated stainless steel. In both 0.01% NaCl at E_{corr} and under-cathodic protection at -500 mV (vs. Ag/AgCl), the C/Cr coated sample also out-performed the uncoated stainless steel by 2-3 times.

Further research

During the course of this research, the following further researches were identified:

- C/Cr coatings deposited at a wide range of bias voltage ($U_B = -65, -75, -95, -120, \text{ and } -350 \text{ V}$) have been investigated. New types microstructure induced by ion bombardment was found. It would be interesting to define the onset of self-organised multilayer structure in more detail.
- The oxidation behaviour of C/Cr coatings can be further explored using TEM, EDX/TEM to investigate the diffusion of Cr, C, and O across the coating cross-section.
- It would be interesting to incorporate other metals, for example Nb, V, Mo, and W into the carbon-based system. It was found that C/Nb coatings grown by the ABSTM gives an interestingly low friction coefficient of 0.12. Intensive investigation of C/Nb coatings would be advantageous to exploit their potential for biomedical applications due to their low friction coefficient ($\mu = 0.12$) and the reported biocompatibility.
- Nitrogen gas incorporation during coating deposition has been known to increase hardness of thin films. However, during the course of this research, a pilot run of C/Cr coatings with nitrogen gas incorporation did not have an advantageous effect on the properties of C/Cr coating. It would be interesting to investigate the effects of carbon containing gas incorporation, for example methane (CH_4), during C/Cr coating deposition on the friction coefficient and the hardness of C/Cr coating.
- The modified SRET has few drawbacks, which need further improvement. These are:
 - (i) Driving mechanism of sliding probe: It would be useful to introduce a pneumatic system on the sliding probe to give better control to its movement on loading and unloading. This could also reduce the possible friction exerted during tribocorrosion test with the current design.
 - (ii) As mention in section 4.7.2, the eccentric effect due to the centrifugal force of sample rotation cannot be fully eliminated using the ball bearing support at the end of the sample. Therefore the tank was forced to move forward when a

load of ≥ 4 N was applied and this resulted in displacement of rotation centre of the sample, which could halt the sample from rotating. It is necessary to improved the design to fix the tank onto the stage or to introduce a support to secure the position of the tank to prevent this problem, and possibly reduce the degree of scatter in the results obtained.

References

1. P.S. Sreejith, B.K.A. Ngoi, "Dry Machining: Machining of the Future", J. Materials Processing Technology 101 (2000) 287.
2. H.E. Sliney, "Solid lubricants", in ASM Handbook of Friction, Lubrication, and Wear Technology, Vol. 18, 1992, ASM International, The Materials Information Society, p. 113-122.
3. R. H. Savage, 1948, "Graphite Lubrication", J. Appl. Phys., Vol. 19, p. 1-10.
4. C.P. Chang, D.L. Flamm, D.E. Ibbotson, J.A. Mucha, "Diamond crystal growth by plasma chemical vapor deposition", J. Appl. Phys. 63 (1988) 1744.
5. T. Hurkmans, J. Kubinski, T. Trinh, W. Fleischer, G.J. Van der Kolk, "Perspective for Replacement of Hard Chrome by PVD", Society of Vacuum Coaters 505/856-7188, 42nd Annual Technical Conference Proceedings, 1999, p. 364.
6. J. Robertson, "Diamond-like amorphous carbon", Mat. Sci. Eng. R37 (2002) 129.
7. H. Dimigen and H. Hübsch, "Applying low-friction wear-resistant thin solid films by physical vapour deposition", Philips Tech. Rev. 41 (1983-84) 186-197.
8. J.A. Thornton, "The microstructure of sputter-deposited coatings", J. Vac. Sci. Technol. A 4 (6) (1986) 3059.
9. R. Messier, A.P. Giri, R.A. Roy, "Revised structure zone model for thin film physical structure", J. Vac. Sci. Technol. A 2(2) (1984) 500.
10. I. Petrov, P.B. Barna, L. Hultman, J.E. Greene, "Microstructural evolution during film growth", J. Vac. Sci. Technol. A 21(5) (2003).
11. G. Håkansson, "Growth of compound and superlattice thin films: effects of energetic particle bombardment, PhD Thesis, 1991, Linköping University.
12. K. Järrendahl, I. Ivanov, J.-E. Sundgren, G. Radnóczy, Zs. Czigany, J.E. Greene, "Microstructure evolution in amorphous Ge/Si multilayers grown by magnetron sputter deposition", J. Mater. Res. 12 (7) (1997) 1806.
13. H. Ljungcrantz, "Growth, microstructure and mechanical properties of Ti and TiN thin films, and TiN-based superlattices", PhD Thesis, 1995, Linköping University.

14. T.-Y. Lee, S. Kodambaka, J. G. Wen, R. D. Twisten, J. E. Greene, I. Petrov, "Directed nanostructural evolution in $\text{Ti}_{0.8}\text{Ce}_{0.2}\text{N}$ layers grown as a function of low-energy, high-flux ion irradiation", *Appl. Phys. Lett.* 84 (15) (2004) 2796.
15. J. Neidhardt, Zs. Czigány, I.F. Brunell and L. Hultman, "Growth of fullerene-like carbon nitride thin solid films by reactive magnetron sputtering; role of low-energy ion irradiation in determining microstructure and mechanical properties", *J. Appl. Phys.* 93 (5) (2003) 3002-3015.
16. J. Neidhardt, L. Hultman, E. Broitman, T. W. Scharf and I. L. Singer, "Structural, mechanical and tribological behavior of fullerene-like and amorphous carbon nitride coatings", *Dia. Relat. Mater.* 13 (10) (2004) 1882-1888.
17. C. Strondl, G.J. Van der Kolk, T. Hurkmans, W. Fleischer, "Mechanical and tribological properties of metal containing diamond-like carbon coatings (Me-DLC) deposited under different plasma confinement conditions", *Society of Vacuum Coaters* 505/856-7188, 44th Annual Technical Conference Proceedings, 2001, p. 67.
18. S. Yang, D.G. Teer, "Investigation of sputtered carbon and carbon/chromium multi-layered coating", *Surf. Coat. Technol.* 131 (2000) 412-416.
19. S. Yang, A.H.S. Jones, D.G. Teer, "The new development of sputtered carbon based coatings incorporated with Cr, Ti, B and Nitrogen", *Surf. Coat. Technol.* 133-134 (2000) 369-375.
20. S.K. Field, M. Jarratt, D.G. Teer, "Tribological properties of graphite-like and diamond-like carbon coatings", *Tribology International* 37 (2004) 949-956.
21. J. Stallard, D. Mercks, M. Jarratt, D.G. Teer, P.H. Shipway, "A study of the tribological behaviour of three carbon-based coatings, tested in air, water and oil environments at high loads", *Surf. Coat. Technol.* 177-178 (2004) 545-551
22. M. Diesselberg, H.-R. Stock, P. Mayr, "Friction and wear behaviour of PVD chromium nitride supported carbon coatings", *Surf. Coat. Technol.* 188-189 (2004) 612-616.
23. K. Bewilogua, C.V. Cooper, C. Specht, J. Schröder, R. Wittorf, M. Grischke, "Effect of target material on deposition and properties of metal-containing DLC (Me-DLC) coatings", *Surf. Coat. Technol.* 127 (2-3) (2000) 223.
24. I. Ahmad, S.S. Roy, P.D. Maguire, P. Papakonstantinou, J.A. McLaughlin, "Effect of substrate bias voltage and substrate on the structural properties of

- amorphous carbon films deposited by unbalanced magnetron sputtering”, *Thin Solid Films* 482 (1-2) (2005) 45-49.
25. C. Strondl, N.M. Carvalho, J.Th.M. De Hosson and T.G. Krug, “Influence of energetic ion bombardment on W-C:H coatings deposited with W and WC targets”, *Surf. Coat. Technol.* 2005 Article in Press.
 26. Hyun S. Myung, Yong S. Park, Jae W. Lee, B. Hong and Jeon G. Han, “Structures and mechanical properties of diamond like carbon films prepared by closed-field unbalanced magnetron sputtering”, *Thin Solid Films* 475 (1-2) (2005) 303-307
 27. N. Savvides, B. Window, “Diamondlike amorphous carbon films prepared by magnetron sputtering of graphite”, *J. Vac. Sci. Technol. A3* (6) (1985) 2386-2390
 28. N. Maréchal, E. Quesnel, Y. Pauleau, “Deposition process and characterization of chromium-carbon coatings produced by direct sputtering of a magnetron chromium carbide target”, *J. Mater. Res.* 9 (1994) 1820-1828.
 29. J.L. Derep, “A new microstructure in chromium-carbon coatings”, *Philosophical Magazine Letters*, 65 (3) (1992) 167-172
 30. S. Yang, D. Camino, A.H.S. Jones, D.G. Teer, “Deposition and tribological behaviour of sputtered carbon hard coatings”, *Surf. Coat. Technol.* 124 (2000) 110-116.
 31. B. Navinšek, P. Panjan, “Oxidation resistance of PVD Cr, Cr-N and Cr-N-O hard coatings”, *Surf. Coat. Technol.* 59 (1993) 244.
 32. T. Hurkmans, “The microstructure and properties of unbalanced magnetron sputtered CrN_x coatings”, PhD thesis, 2002, Sheffield Hallam University
 33. W.G. Moffatt, *Handbook of binary phase diagrams*, Volume 2, Genium, p. 2/92.
 34. P.Eh. Hovsepian, W.-D. Münz, “Advanced application tailored PVD coatings utilizing nanoscale multilayer/superlattice structures”, 45th Annual Technical Conference Proceedings (2002) p. 1.
 35. M. Ohring, “The materials Science of Thin Films, Academic Press Inc., 1992, ISBN 0-12-524990-X, p.79.
 36. S.M. Rossnagel, “Use of plasmas in deposition technologies”, in *Advanced Surface Coatings: a Handbook of Surface Engineering*, Chapman & Hall New York, 1991, p. 14-40.

37. S.L. Rohde and W.-D. Münz, "Sputter Deposition" in *Advance Surface Coatings, A Handbook of Surface Engineering*, eds. D.S. Rickerby and A. Matthews, 1991, Chapman and Hall New York, p. 103.
38. J.L. Vossen and J.J. Cuomo, "Glow discharge sputter deposition", *Thin Film Processes* (eds J.L. Vossen and W. Kern), Academic Press, New York (1978).
39. J.L. Cecchi, in *Handbook of Plasma Based Processing Technology*, eds. S.M. Rossnagel, J.J. Cuomo and W.D. Westwood, 1989, Noyes Publications, Park Ridge, NJ.
40. B. Chapman, "Glow Discharge Processes", Wiley, New York (1980), p.104.
41. D.M. Mattox, "Recent Advances in Ion Plating", *Polymer Preprints, Division of Polymer Chemistry, American Chemical Society*, 1974, p 443-450.
42. D. M. Mattox, "Ion plating — past, present and future", *Surf. Coat. Technol.* 133-134 (2000) 517-521.
43. D.M. Mattox, "Physical vapour deposition processes", *Product Finishing (Cincinnati)*, 65 (12) (2001) 72.
44. C. Weissmantel, "Deposition of Metastable Films by Ion Beam and Plasma Techniques", *Proceedings of the Ninth International Vacuum Congress and Fifth International Conference on Solid Surfaces*, Madrid, 1983, p. 299-308.
45. J. A. Thornton, "Magnetron sputtering: basic physics and application to cylindrical magnetrons", *J. Vac. Sci. Technol.* 15 (2) (1978) 171-176.
46. B. Window and N. Savvides, "Charged particle fluxes from planar magnetron sputtering sources", *J. Vac. Sci. Technol. A* 4 (2) (1986) 196.
47. R. L. Boxman, D.M. Sanders, P.J. Martin, *Handbook of Vacuum Arc Science and Technology*, 1995, Park Ridge, Noyes Publications.
48. A. Anders, S. Anders, B. Jüttner, H. Lück, *IEEE Trans Plas Sci*, 24 (1) (1996) 69.
49. P.J. Martin, "Coatings from the vacuum Arc", in *Handbook of Vacuum Arc Science and Technology*, eds. R.L. Boxman, P.J. Martin, D.M. Sanders, Noyes Publications, 1995, p. 393.
50. J. Musil, J. Vyskočil, S. Kadlec, "Hard coatings prepared by sputtering and arc evaporation", *Phys. of Thin Films* 17 (1993) 79-144.
51. I. G. Brown, A. Anders, S. Anders, M. R. Dickinson, R. A. MacGill, E. M. Oks, "Recent advances in vacuum arc ion source", *Surf. Coat. Technol.* 84 (1-3) (1996) 550.

52. W.-D. Münz, D.B. Lewis, S. Creasey, T. Hurkmans, T. Trinh, W. Vonijzendorf, "Defects in TiN and TiAlN coatings grown by combined cathodic arc/unbalanced magnetron technology", *Vacuum*, 46 (1995) 323-330.
53. W.-D. Münz, I.J. Smith, D.B. Lewis, S. Creasey, "Droplet formation on steel substrates during cathodic steered arc metal ion etching", *Vacuum* 48 (5) (1997) 473-481.
54. I. Petrov, P. Losbichler, D. Bergstrom, "Ion-assisted growth of $Ti_{1-x}Al_xN/Ti_{1-y}Nb_yN$ multilayers by combined cathodic-arc/magnetron sputter deposition", *Thin Solid Films* 302 (1997) 179.
55. H. W. Wang, M. M. Stack, S. B. Lyon, P. Hovsepian and W. -D. Münz, "The corrosion behaviour of macroparticle defects in arc bond-sputtered CrN/NbN superlattice coatings", *Surf. Coat. Technol.* 126 (2-3) (2000) 279-287.
56. A. Anders, "Approaches to rid cathodic arc plasmas of macro- and nanoparticles: a review", *Surf. Coat. Technol.* 120-121 (1999) 319.
57. R. L. Boxman, S. Goldsmith, "Macroparticle contamination in cathodic arc coatings: generation, transport and control", *Surf. Coat. Technol.* 52 (1) (1992) 39-50.
58. C. Schönjahn, "Surface treatment in a cathodic arc plasma – key step for interface engineering", PhD thesis, 2001, Sheffield Hallam University.
59. W. -D. Münz, "The unbalanced magnetron current status of development", *Surf. Coat. Technol.* 48 (1) (1991) 81.
60. W. -D. Münz, F.J.M. Hauzer, D. Schulze, B. Buil, "A new concept for physical vapor deposition coating combining the methods of arc evaporation and unbalanced-magnetron sputtering ", *Surf. Coat. Technol.* 49 (1991) 161-167.
61. W. -D. Münz, D. Schulze, F.J.M. Hauzer, "A new method for hard coatings: ABSTM (arc bond sputtering)", *Surf. Coat. Technol.* 50 (1992) 169-178.
62. P. Barna, M. Adamik, "Fundamental structure forming phenomena of polycrystalline films and the structure zone models", *Thin Solid Films* 317 (1998) 27.
63. C.V. Thompson, "Structure evolution during processing of polycrystalline films", *Annu. Rev. Mater. Sci.* 30 (2000) 159.
64. L.J. Meng, M. Andritschky, MP dos Santos, "Zinc oxide films prepared by dc reactive magnetron sputtering at different substrate temperatures", *Vacuum* 45 (1) (1994) 19-22.

65. L. Hultman, W.-D. Münz, J. Musil, S. Kadlec, I. Petrov, J.E. Greene, "Low-energy ($\sim 100\text{eV}$) ion irradiation during growth of TiN deposited by reactive magnetron sputtering: Effects of ion flux on film microstructure", *J. Vac. Sci. Technol. A* 9(3) (1991) 434.
66. J. Musil, "Hard and superhard nanocomposite coatings", *Surf. Coat. Technol.* 125 (2000) 322-330.
67. I. Petrov, A. Myers, J. E. Greene, J. R. Abelson, "Mass and energy resolved detection of ions and neutral sputtered species incident at the substrate during reactive magnetron sputtering of Ti in mixed Ar+N₂ mixtures", *J. Vac. Sci. Technol. A* 12 (5) (1994) 2846.
68. I. Petrov, L. Hultman, U. Helmersson, J.E. Sundgren, J.E. Greene, "Microstructure modification of TiN by ion bombardment during reactive sputter deposition", *Thin Solid Films* 169 (1989) 299-314.
69. D.M. Mattox, "Particle bombardment effects on thin-film deposition: A review", *J. Vac. Sci. Technol. A* 7 (3) (1989) 1105-1114.
70. K.H. Müller, "Ion-beam-induced epitaxial vapor-phase growth: A molecular-dynamics study", *Phys. Rev. B* 35 (15) (1987) 7906-7913.
71. P.J. Kelly, R.D. Arnell, "Development of a novel structure zone model relating to the closed-field unbalanced magnetron sputtering system", *J. Vac. Sci. Technol. A* 16(5) (1998) 2858.
72. G.M. Demyashev, A.L. Taube, E. Siores, "Superhard Nanocomposite Coatings", in "Handbook of Organic-Inorganic Hybrid Materials and Nanocomposites, Volume 1: Hybrid Materials" ed. H.S Nalwa, 2003, American Scientific Publishers, p.1.
73. P.B. Barna, M. Admik, J. Lábár, L. Kövér, J. Tóth, A. Dévényi, R. Manaila, "Formation of polycrystalline and microcrystalline composite thin films by codeposition and surface chemical reaction", *Surf. Coat. Technol.* 125 (2000) 147.
74. D. Bíró, A. Kovács, F. Misják, T. Szüts, P.B. Barna, "Self organised formation of layered structure in co-deposited Al-C thin films ", *Surf. Coat. Technol.* 180-181 (2004) 425.
75. S. A. Barnett, A. Madan, "Superhard superlattices", *Phys. World*, 11 (1) (1998) 45.

76. S. Hogmark, S. Jacobson, M. Larsson, "Design and evaluation of tribological coatings", *Wear* 246 (2000) 20.
77. X. Chu, S.A. Barnett, "Model of superlattice yield stress and hardness enhancements", *J. Appl. Phys.* 77 (9) (1995) 4403-4411.
78. W.-D. Münz, D.B. Lewis, P.Eh. Hovsepian, C. Schönjahn, A. Ehasarian, I.J. Smith, "Industrial scale manufactured superlattice hard PVD coatings", *Surf. Eng.* 17 (1) (2001) 15.
79. P. Eh. Hovsepian, D.B. Lewis, W.-D. Münz, "Recent progress in large scale manufacturing of multilayer/superlattice hard coatings", *Surf. Coat. Technol.* 133-134 (2000) 166.
80. L.A. Donohue, W.-D. Münz, D. B. Lewis, J. Cawley, T. Hurkmans, T. Trinh, I. Petrov, J. E. Greene, "Large scale fabrication of hard superlattice thin films by combined steered arc evaporation and unbalanced magnetron sputtering", *Surf. Coat. Technol.* 93 (1997) 69.
81. J.S. Koehler, "Attempt to design a strong solid", *Phys. Rev. B* 2 (1970) 547.
82. E.O. Hall, *Proceedings of the Physical Society B*, 64 (1951) 747.
83. N.J. Petch, "The cleavage strength of polycrystals," *J. Iron Steel Inst.*, 174 (1953) 25.
84. A. Niederhofer, P. Nesládek, H.-D. Maennling, K. Moto, S. Vepřek, M. Jílek, "Structural properties, internal stress and thermal stability of nc-TiN/a-Si₃N₄, nc-TiN/TiSi_x and nc-(Ti_{1-y}Al_ySi_x)N superhard nanocomposite coatings reaching the hardness of diamond", *Surf. Coat. Technol.* 120-121 (1999) 173.
85. S. Vepřek, "The search for novel, superhard materials", *J. Vac. Sci. Technol. A* 17 (5) (1999) 2401.
86. J. Patscheider, T. Zehnder, M. Diserens, "Structure-performance relations in nanocomposite coatings", *Surf. Coat. Technol.* 146-147 (2001) 201-208.
87. S. Vepřek, P. Nesládek, A. Niederhofer, F. Glatz, M. Jílek, M. Šíma, "Recent progress in the superhard nanocrystalline composites: towards their industrialization and understanding of the origin of the superhardness", *Surf. Coat. Technol.* 108-109 (1-3) (1998) 138.
88. J. Schiøtz, "Simulation of nanocrystalline metals at the atomic scale, what can we do? what can we trust?", *Proceeding of the 22nd Riso International Symposium of Materials Science, Roskilde, Denmark* (2001) 127-139.

89. P. B. Barna, G Radnóczy, F. M. Reicha, "Surface growth topography of grain boundaries in Al thin films", *Vacuum* 38 (7) (1988) 527-532.
90. S. J. Talasman, M. Ignat, "Negative resistance and self-organization in plasma", *Phys. Lett. A* 301 (2002) 83.
91. J. Ullmann, K. Baba, H. Martin, G. K. Wolf, "Effect of deposition conditions on the growth and behaviour of thin carbon films prepared by ion-assisted evaporation", *Surf. Coat. Technol.* 74-75 (1995) 746-753.
92. R. G. Lacerda, P. Hammer, F. L. Freire Jr., F. Alvarez, F. C. Marques, "On the structure of argon assisted amorphous carbon films", *Dia. Relat. Mater.* 9 (3-6) (2000) 796-800.
93. V. V. Uglova, V. M. Anishchik, Y. Pauleau, A. K. Kuleshov, F. Thiéry, J. Pelletier, S. N. Dub, D. P. Rusalsky, "Relations between deposition conditions, microstructure and mechanical properties of amorphous carbon-metal films", *Vacuum* 70 (2003) 181-185.
94. S. Yang, X. Li, N.M. Renevier, D.G. Teer, "Tribological properties and wear mechanism of sputtered C/Cr coating", *Surf. Coat. Technol.* 142-144 (2001) 85-93.
95. P. Eh. Hovsepien, W.-D. Münz, "Recent Progress in Large Scale Production of Nanoscale Multilayer/superlattice Hard Coatings", *Vacuum* 69 (1-3) (2002) 27-36.
96. P. Eh. Hovsepien, D.B. Lewis, C. Constable, Q. Luo, Y.N. Kok, W.-D. Münz, "Combined Steered Cathodic Arc/Unbalanced Magnetron Grown C/Cr Nanoscale Multilayer Coatings for Tribological Applications", *Surf. Coat. Technol.* 174-175 (2003) 762-769.
97. M. Grischke, R. Herb, O. Massler, J. Karner, H. Eberle, "High vacuum based deposition of carbon-based films for industrial applications", 44th Annual Technical Conference Proceedings-Philadelphia, Society of Vacuum Coaters 505/856-7188, 2001, p. 407-410.
98. A. Bloyce, "Carbon PVD coatings wear it well", *Materials World*, March 2000, p. 13.
99. V.M. Tiainen, "Amorphous carbon as a bio-mechanical coating — mechanical properties and biological applications", *Dia. Relat. Mater.* 10 (2001) 153.
100. A. Grill, "Diamond-like carbon coatings as biocompatible materials—an overview", *Dia. Relat. Mater.* 12 (2003) 166.

101. H. O. Pierson, "Handbook of Carbon, Graphite, Diamond and Fullerenes", 1993, Noyes Publications, ISBN 0-8155-1339-9, p. 40, 245, 337.
102. "Scientists create fifth form of carbon", news@nature.com, 22 March 2004.
103. S.R.P. Silva, "Microstructure of a-C" in properties of amorphous carbon, ed. S.R.P. Silva, 2003, ISBN 0852969619, INSPEC publication, p.3.
104. F.P. Bowden, D. Tabor, The friction and lubrication of solids, 1950, Oxford at the Clarendon Press, p. 187.
105. B. Bhushan, and B. K. Gupta, "Handbook of Tribology, Materials, Coatings, and Surface Treatments", 1991, McGraw-Hill Inc., pp. 2.36, 3.1, 5.1-5.25, 9.51-9.73, 14.106.
106. H. P. Boehm, "Chemical Identification of Surface Groups", Advances in Catalysis, 1966, Academic Press, New York, 179-272.
107. P. J. Bryant, P.L. Gutshall, L.H. Taylor, "A Study of Mechanisms of Graphite Friction and Wear", Wear 7 (1964) 118-126.
108. M.S. Dresselhaus, M.A. Pimenta, P.C. Eklund, and G. Dresselhaus, "Raman Scattering in Fullerenes and Related Carbon-Based Materials", in W.H. Weber and R. Merlin (eds), Raman Scattering in Materials Science, 2000, Springer London, p.315.
109. A. Erdemir and C. Donnet, "Tribology of Diamond, Diamond-Like Carbon, and Related Films", in Modern Tribology Handbook Vol. Two, Bhushan, B. (ed), 2001, CRC Press.
110. A.C. Ferrari, "Raman Spectroscopy of Amorphous Carbon Films: State of the Art", New Diamond and Frontier Carbon Technology 14 (2) (2004) 87.
111. P. Eh. Hovsepian, Y. N. Kok , A. P. Ehiasarian , A. Erdemir , J. -G. Wen, I. Petrov, "Structure and tribological behaviour of nanoscale multilayer C/Cr coatings deposited by the combined steered cathodic arc/unbalanced magnetron sputtering technique", Thin Solid Films 447-448 (2004) 7-13.
112. Y.N. Kok, P.Eh. Hovsepian, Q. Luo, D.B. Lewis, J.G. Wen, I. Petrov, "Influence of the bias voltage on the structure and the tribological performance of nanoscale multilayer C/Cr PVD coatings", Thin Solid Films 475 (1-2) (2005) 219-226.
113. Y.Y. Chang, D.Y. Wang, C.H. Chang, W.T. Wu, "Tribological analysis of nano-composite diamond-like carbon films deposited by unbalanced magnetron sputtering", Surf. Coat. Technol. 184 (2-3) (2004) 349-355.

114. A.H.S. Jones, D. Camino, D.G. Teer, J. Jiang, "Novel high wear resistant diamond-like carbon coatings deposited by magnetron sputtering of carbon targets", *J. Eng. Tribol.* 212 (4) (1998) 301-306.
115. K. Bewilogua, R. Wittorf, H. Thomsen, M. Weber, "DLC based coatings prepared by reactive d.c. magnetron sputtering", *Thin Solid Films* 447-448 (2004) 142.
116. J.H. Ouyang and S. Sasaki, "Friction and wear characteristics of a Ti-containing diamond-like carbon coating with an SRV tester at high contact load and elevated temperature", *Surf. Coat. Technol.* 195 (2-3) (2005) 234-244.
117. H. Dimigen, C.-P. Klages, "Microstructure and wear behavior of metal-containing diamond-like coatings", *Surf. Coat. Technol.* 49 (1991) 543-547.
118. A.A. Voevodin, M.S. Donley, J.S. Zabinski and J.E. Bultman, "Mechanical and tribological properties of diamond-like carbon coatings prepared by pulsed laser deposition", *Surf. Coat. Technol.* 76-77 (1995) 534-539.
119. Y. N. Kok and P.Eh. Hovsepian, "Resistance of Nanoscale C/Cr PVD Coatings against Environmental Attack", to be submitted for publication.
120. S. Aisenberg and R. Chabot, "Ion-Beam Deposition of Thin Films of Diamondlike Carbon", *J. Appl. Phys.* 42 (1971) 2953.
121. X.T. Zheng, S. Zhang, X.Z. Ding, D.G. Teer, "Comparison of three of carbon composite coatings with exceptional load-bearing capacity and high wear resistance", *Thin Solid Films* 420-421 (2002) 366-370.
122. A. Grill, V. Patel, "Tribological properties of diamond-like carbon and related materials", *Dia. Relat. Mater.* 2 (1993) 597.
123. A. Erdemir, "Molecular Engineering of Diamond-Like Carbon Films for Super-Low Friction and Wear Properties", 44th Annual Technical Conference Proceedings-Philadelphia, April 21-26, 2001, Society of Vacuum Coaters, p. 397-402.
124. Y. Pauleau and F. Thiéry, "Deposition and characterization of nanostructured metal/carbon composite films", *Surf. Coat. Technol.* 180-181 (2004) 313-322.
125. A. S. Loir, F. Garrelie, C. Donnet, M. Belin, B. Forest, F. Rogemond and P. Laporte, "Deposition of tetrahedral diamond-like carbon thin films by femtosecond laser ablation for applications of hip joints", *Thin Solid Films* 453-454 (2004) 531.

126. D. Sheeja, B. K. Tay and L. N. Nung, "Feasibility of diamond-like carbon coatings for orthopaedic applications", *Dia. Relat. Mater.* 13 (1) (2004) 184-190.
127. S. Aisenberg, "Properties and applications of diamondlike carbon films", *J. Vac. Sci. Technol. A* 2 (2) (1984) 369-371.
128. S.R. Kasi, H. Kang, J.W. Rabalais, "Chemically bonded diamondlike films from ion-beam deposition", *J. Vac. Sci. Technol. A* 6 (3) (1988) 1788.
129. D.P. Monaghan, D.G. Teer, P.A. Logan, I. Efeoglu, R.D. Arnell, "Deposition of wear resistant coatings based on diamond-like carbon by unbalanced magnetron sputtering", *Surf. Coat. Technol.* 60 (1993) 525.
130. Y. Lifshitz, "Diamond-like carbon-present status", *Diamond Relat. Mat.*, 8 (1999) 1659-1676.
131. A.A. Voevodin, M.S. Donley, J.S. Zabinski, "Pulsed laser deposition of diamond-like carbon wear protective coatings: a review", *Surf. Coat. Technol.* 92 (1-2) (1997) 42-49.
132. A. Erdemir, O. L. Eryilmaz, I. B. Nilufer, G. R. Fenske, "Synthesis of superlow-friction carbon films from highly hydrogenated methane plasmas", *Surf. Coat. Technol.*, 133-134 (2000) 448-454.
133. A.K. Gangopadhyay, P.A. Willermet, M. A. Tamor, W. C. Wassell, "Amorphous hydrogenated carbon films for tribological applications I. Development of moisture insensitive films having reduced compressive stress", *Trib. Int.* 30 (1997) 9.
134. E. Bergmann, J. Vogel, "Influence of composition and process parameters on the internal stress of the carbides of tungsten, chromium, and titanium", *J. Vac. Sci. Technol. A* 5 (1987) 70.
135. U. Wiklund, M. Larsson, "Low friction PVD titanium-carbon coatings", *Wear* 241 (2000) 234-238.
136. J.P. Sullivan, T.A. Friedmann, A.G. Baca, "Stress relaxation and thermal evolution of film properties in amorphous carbon", *J. Electron. Mater.* 26 (9) (1997) 1021.
137. J. Brand, R. Gadow and A. Killinger, "Application of diamond-like carbon coatings on steel tools in the production of precision glass components", *Surf. Coat. Technol.* 180-181 (2004) 213-217.

138. E. Harry, A. Rouzaud, P. Juliet, Y. Pauleau, "General properties and scratch adhesion characterization of carbon-containing tungsten films", *Surf. Coat. Technol.* 116-119 (1999) 81-85.
139. A.A. Voevodin, S.V. Prasad, J.S. Zabinski, "Nanocrystalline carbide/amorphous carbon composites", *J. Appl. Phys.* 82 (1997) 855.
140. Q. Wei, R.J. Narayan, A.K. Sharma, J. Sankar, J. Narayan, "Preparation and mechanical properties of composite diamond-like carbon thin films", *J. Vac. Sci. Technol. A* 17 (1999) 3406.
141. C. Schönjahn, A. P. Eghasarian, D.B. Lewis, R. New, W.-D. Münz, R.D. Twisten, I. Petrov, "Optimization of *in situ* substrate surface treatment in a cathodic arc plasma: A study by TEM and plasma diagnostics", *J. Vac. Sci. Technol. A* 19(4) (2001) 1415.
142. H. N. McMurray, D.A. Worsley, "Scanning Electrochemical Techniques for the Study of Localised Metallic Corrosion", *Research In Chemical Kinetics*, Vol. 4, 1997, Blackwell Science Ltd., p. 149-202.
143. R. Akid, "Localised Corrosion: a new evaluation approach", *Materials World* 1995 p. 522-525.
144. H. S. Isaacs, V. Brijesh, "Scanning Reference Electrode Techniques in Localised Corrosion", *Electrochemical Corrosion Testing* (eds. F. Mansfeld and U. Bertocci), ASTM STP 727, 1981, American Society for Testing and Materials, pp. 3-33.
145. K. R. Trethewey, D.A. Sargeant, D.J. Marsh, A.A. Tamimi, "Applications of the scanning reference electrode technique to localized corrosion", *Corrosion Science* 35 (1-4) (1993) 127.
146. H. N. McMurray, S.R. Magill, B.D. Jeffs, "Scanning reference electrode technique as tool for investigating localised corrosion phenomena in galvanised steels", *Ironmaking and Steelmaking*, 23 (2) (1996) 183.
147. R. Akid, D. J. Mills, "A comparison between conventional macroscopic and novel microscopic scanning electrochemical methods to evaluate galvanic corrosion", *Corrosion Science* 43 (2001) 1203.
148. H. N. McMurray, *Corrosion*, "Localised corrosion behaviour in aluminium-zinc alloy coatings investigated using the scanning reference electrode technique", 57 (4) (2001) 313.

149. R. Akid, G.M. Treacy, D.J. Mills & M.Toff "Application of the rotational Scanning Reference Electrode Technique to assess the anticorrosion performance of organic and metallic coatings", EuroCorr 2000, 10-14th Sept. 2000, Queen Mary & Westfield College, University of London, UK.
150. CSM instrument presentation slides-Nanoindentation, 2004.
151. J. Albert Sue, "Stress Determination for Coatings", in ASM Handbook Vol.5 Surface Engineering, 1994, The Materials Information Society, p. 647-653.
152. A.P. Ehasarian, "Development of PVD coating processes informed by plasma diagnostics", PhD thesis, 2002, Sheffield Hallam University.
153. W. Zhu, H. Kong, J. T. Glass, "Characterization of Diamond Films", in Diamond Films and Coatings, eds. R. F. Davis, 1993, Noyes Publications, p. 322.
154. M. Mayer, SIMNRA, a Simulation Program for the Analysis of NRA, RBS and ERDA, Proceedings of the 15th International Conference on the Application of Accelerators in Research and Industry, J. L. Duggan and I.L. Morgan (eds.), American Institute of Physics Conference Proceedings 475 (1999) p. 541 (and <http://www.rzg.mpg.de/~mam/>).
155. P.R. Chalker, "Characterisation of coatings and interfaces", in Advanced Surface Coatings: a Handbook of Surface Engineering, Eds. D.S. Rickerby and A. Matthew, 1991, Chapman and Hall, New York, p. 279.
156. R.F. Davies, Diamond films and coatings, Development, properties, and applications, 1993, Noyes publications, p. 249.
157. K. R. Trethewey, D.A. Sargeant, D.J. Marsh, S. Haines, "New methods of quantitative analysis of localised corrosion using scanning electrochemical probes", in Modelling Aqueous Corrosion, (eds) K.R. Trethewey and P. R., Roberge, 1994, British Crown, Printed in the Netherlands, pp. 417-442.
158. H.A. Horner, Ordinary national certificate mathematics, Vol. 1, 1966, p. 193.
159. P. Eh. Hovsepian, Y. N. Kok, A.P. Ehasarian, R. Haasch, J.-G. Wen, I. Petrov, "Phase separation and formation of the self-organised layered nanostructure in C/Cr coatings in conditions of high ion irradiation", paper presented at ICMCTF 2005, to be published in Surf. Coat. Technol.
160. V.V. Uglov, A.K. Kuleshov, D.P. Rusalsky, M.P. Samzov, A.N. Dementshenok, "Friction coefficient, microstructure and thermal stability of amorphous a-C coatings", Surf. Coat. Technol. 158-159 (2002) 699-703.

161. J.-E. Sundgren, B.-O. Johansson, S.-E. Karlsson, "Influence of substrate bias on composition and structure of reactively R.F. sputtered TiC films", *Thin Solid Films* 80 (1981) 77-83.
162. M. Li, F. Wang, "Effects of nitrogen partial pressure and pulse bias voltage on (Ti,Al)N coatings by arc ion plating", *Surf. Coat. Technol.* 167 (2-3) (2003) 197-202.
163. D.J. Kester, R. Messier, "Macro-effects of resputtering due to negative ion bombardment of growing thin films", *J. Mater. Res.* 8 (8) (1996) 1928.
164. Y.S. Park, H.S. Myung, J.G. Han, B. Hong, "Tribological properties of amorphous carbon thin films grown by magnetron sputtering method", *Surf. Coat. Technol.* 180-181 (2004) 218.
165. X.L. Peng, T.W. Clyne, "Mechanical stability of DLC films on metallic substrates: Part I—Film structure and residual stress levels", *Thin Solid Films* 312 (1998) 207-218.
166. B. K. Gupta, Bharat Bhushan, "Micromechanical properties of amorphous carbon coatings deposited by different deposition techniques", *Thin Solid Films* 270 (1995) 391-398.
167. J.M. Lackner, C. Stotter, W. Waldhauser, R. Ebner, W. Lenz, M. Beutl, "Pulsed laser deposition of diamond-like carbon coatings for industrial tribological applications", *Surf. Coat. Technol.* 174-175 (2003) 402
168. M. Čekada, M. Maček, D.K. Merl, P. Panjan, "Properties of Cr(C,N) hard coatings deposited in Ar-C₂H₂-N₂ plasma", *Thin Solid Film* 433 (2003) 174.
169. X. Han, F. Yan, A. Zhang, P. Yan, B. Wang, W. Liu, Z. Mu, "Structure and tribological behavior of amorphous carbon films implanted with Cr⁺ ions", *Mater. Sci. Eng. A* 348 (2003) 319.
170. Y.N. Kok, P.Eh. Hovsepian, R. Haasch, I. Petrov, "Raman spectroscopy study of C/Cr coatings deposited by the combined steered cathodic arc/unbalanced magnetron sputtering technique", *Surf. Coat. Technol.* 200 (1-4) (2005) 1117-1122.
171. R. Merlin, A. Pinczuk, W.H. Weber, "Overview of Phonon Raman Scattering in Solids", in (eds) W.H. Weber and R. Merlin "Raman Scattering in Materials Science", Springer, 2000, ISBN 3-540-67223-0, p. 21.

172. R.D. Dillon, J.A. Woollam, V. Katkanant, "Use of Raman scattering to investigate disorder and crystallite formation in as-deposited and annealed carbon films", *Phys. Rev. B* 29 (6) (1984) 3482.
173. E.D. Obraztsova, M. Fujii, S. Hayashi, V.L. Kuznetsov, Yu.V. Butenko, A.L. Chuvilin, "Raman identification of onion-like carbon", *Carbon* 36(5-6) (1998) 821.
174. C.A. Taylor, M.F. Wayne and W.K.S. Chiu, "Residual stress measurement in thin carbon films by Raman spectroscopy and nanoindentation", *Thin Solid Films* 429 (2003) 190.
175. B.K. Tay, X. Shi, H.S. Tan, H.S. Yang, Z. Sun, "Raman studies of tetrahedral amorphous carbon films deposited by filtered cathodic vacuum arc", *Surf. Coat. Technol.* 105 (1998) 155.
176. S. Chowdhury, M.T. Laugier, I.Z. Rahman, "Effects of substrate temperature on bonding structure and mechanical properties of amorphous carbon films", *Thin Solid Films* 447-448 (2004) 174.
177. C.P. Constable, J. Yarwood, P. Hovsepian, L.A. Donohue D.B. Lewis and W.-D. Munz, "Structural determination of wear debris generated from sliding wear tests on ceramic coatings using Raman microscopy", *J. Vac. Sci. Technol. A* 18(4) (2000) 1681.
178. I. Petrov, P. Losbichler, D. Bergstrom, J.E. Greene, W.-D. Münz, T. Hurkmans, T. Trinh, "Ion-assisted growth of $Ti_{1-x}Al_xN/Ti_{1-y}Nb_yN$ multilayers by combined cathodic-arc/magnetron-sputter deposition", *Thin Solid Films* 302 (1997) 179-192.
179. D. H. Hwang, D. E. Kim and S. J. Lee, "Influence of wear particle interaction in the sliding interface on friction of metals", *Wear* 225-229 (1999) 427.
180. R.F. Egerton, M.J. Whelan, "Electron energy loss spectra of diamond, graphite and amorphous carbon, *J. Electron Spectroscopy and Related Phenomena* 3 (1974) 232-236.
181. O. Hubaschewski and B.E. Hopkins, "Oxidation of Metals and Alloys", 1967, Butterworth & CO., p. 1.
182. D.Y. Wang, C.L. Chang, W.Y. Ho, "Oxidation behavior of diamond-like carbon films", *Surf. Coat. Technol.* 120-121 (1999) 138.

183. I. Milosev, J.M. Abels, H.-H. Strehblow, B. Navinsek, M. Metikos-Hukovic, "High temperature oxidation of thin CrN coatings deposited on steel", *J. Vac. Sci. Technol. A* 14 (4) (1996) 2527.
184. V. Kulikovskiy, P. Boháč, V. Vorlíček, A. Deineka, D. Chvostová, A. Kurdyumov, L. Jastrabík, "Oxidation of graphite-like carbon films with different microhardness and density", *Surf. Coat. Technol.* 174-175 (2003) 290.
185. Y.N. Kok, R. Akid, P.Eh. Hovsepian, "Tribocorrosion testing of stainless steel (SS) and PVD coated SS using a modified scanning reference electrode technique", *Wear*, 259 (7-12) (2005) 1472-1481.
186. G. F. Huang, Zhou Lingping, Huang Weiqing, Zhao Lihua, Li Shaolu and Li Deyi, "The mechanical performance and anti-corrosion behavior of diamond-like carbon film", *Dia. Relat. Mater.* 12 (8) (2003) 1406-1410.
187. P. Ponthiaux, F. Wenger, D. Drees, J.P. Celis, "Electrochemical techniques for studying tribocorrosion processes ", *Wear* 256 (5) (2004) 459.
188. L. Fedrizzi, S. Rossi, F. Bellei, F. Deflorian, "Wear–corrosion mechanism of hard chromium coatings", *Wear* 253 (2002) 1173-1181.
189. S. Mischler, A. Spiegel and D. Landolt, "The role of passive oxide films on the degradation of steel in tribocorrosion systems", *Wear* 225-229 (1999) 1078.
190. D. Landolt, S. Mischler, M. Stemp, "Electrochemical methods in tribocorrosion: a critical appraisal", *Electrochimica Acta* 46 (24-25) (2001) 3913.
191. P. A. Dearnley, G.A. Smith, "Corrosion–wear mechanisms of hard coated austenitic 316L stainless steels", *Wear* 256 (5) (2004) 491.
192. S. Mischler, P. Ponthiaux and Commission Tribocorrosion du CEFRACOR Centre Français de l'Anticorrosion, F - 75007 Paris, France, "A round robin on combined electrochemical and friction tests on alumina/stainless steel contacts in sulphuric acid", *Wear* 248 (2001) 211.
193. M. Stemp. S. Mischler, D. Landolt, "The effect of contact configuration on the tribocorrosion of stainless steel in reciprocating sliding under potentiostatic control", *Corr. Sci.* 45 (2003) 625.
194. S. Mischler, A. Spiegel, M. Stemp, D. Landolt, "Influence of passivity on the tribocorrosion of carbon steel in aqueous solutions", *Wear* 251 (2001) 1295.
195. A. Grill, "Tribology of diamondlike carbon and related materials: An updated review", *Surf. Coat. Technol.* 94-95 (1997) 507-513.

196. S.W. Jiang, B. Jiang, Y. Li, Y.R. Li, G.F. Yin, C.Q. Zheng, "Friction and wear study of diamond-like carbon gradient coatings on Ti6Al4V substrate prepared by plasma source ion implant-ion beam enhanced deposition", *Appl. Surf. Sci.* 236 (1-4) (2004) 285.
197. I. García, D. Drees, J.P. Celis, "Corrosion-wear of passivating materials in sliding contacts based on a concept of active wear track area", *Wear* 249 (2001) 452.
198. Q. Luo, G. Robinson, M. Pittman et. al. "Performance of nano-structured multilayer PVD coating TiAlN/VN in dry high speed milling of aerospace aluminium 7010-T7651", *Surf. Coat. Technol.* 200 (1-4) (2005) 123-127.
199. C.P. Constable, "Raman microscopic studies of PVD deposited hard ceramic coatings", PhD Thesis, 2000, Sheffield Hallam University.
200. C. P. Constable, J. Yarwood, G. Robinson, Q. Luo, D. B. Lewis, W.-D. Munz, "Investigation of wear processes on worn tools using Raman microscopy", *Surface Engineering* 18 (2) (2002) 127.
201. T. Y. Lee, S. Kodambaka, J.G. Wen, R.D. Twisten, J.E. Greene, I. Petrov, "Directed nanostructural evolution in $\text{Ti}_{0.8}\text{Ce}_{0.2}\text{N}$ layers grown as a function of low-energy, high-flux ion irradiation", *Appl. Phys. Lett.* 84 (15) (2004) 2796.
202. Kasturi L. Chopra, "Nucleation, growth, and structure of films", in *Thin Film Phenomena*, 1979, McGraw-Hill Inc., p. 137.
203. S. Berg, A. M. Barklund, B. Gelin, C. Nender, I. Katardjiev, "Atom assisted sputtering yield amplification", *J. Vac. Sci. Technol. A* 10(4) (1992) 1592.
204. D. Dineka, V. Suendo, P. Roca I Cabarrocas, "Temperature dependence of the optical functions of amorphous silicon-based materials: application to in situ temperature measurements by spectroscopic ellipsometry", *Thin Solid Films* 468 (2004) 298.
205. M. Wakagi, B.G.Hong, H.V. Nguen, R.W. Collins, W.Drawl, R.Messier, "Characterization of substrate temperature and damage in diamond growth plasmas by multichannel spectroellipsometry", *J.Vac.Sci. Tecnol. A* 13(4) (1995) 1917.
206. M.M.M. Bilek, D.R. McKenzie, "A comprehensive model of stress generation and relief processes in thin films deposited with energetic ions", *Surf. Coat. Technol.* 2005, article in press.

207. M.M.M. Bilek, M. Verdon, L. Ryves, T.W.H. Oates, C.T. Ha and D.R. McKenzie, "A model for stress generation and stress relief mechanisms applied to as-deposited filtered cathodic vacuum arc amorphous carbon films", *Thin Solid Films* 482 (1-2) (2005) 69-73.
208. C.A. Davis, "A simple model for the formation of compressive stress in thin films by ion bombardment", *Thin Solid Films* 226 (1993) 30-34.
209. Q. Luo, W.M. Rainforth, W.-D. Münz, "TEM observations of wear mechanisms of TiAlCrN and TiAlN/CrN coatings grown by combined steered-arc/unbalanced magnetron deposition", *Wear* 225-229 (1999) 74.
210. M.C. Chiu, W.P. Hsieh, W.Y. Ho, D.Y. Wang, F.S. Shieu, "Thermal stability of Cr-doped diamond-like carbon films synthesized by cathodic arc evaporation", *Thin Solid Films* 476 (2) (2005) 258-263.
211. Z. Zhou, W.M. Rainforth, D.B. Lewis, S. Creasy, J.J. Forsyth, F. Clegg, A.P. Ehiasarian, P.Eh. Hovsepian, W.-D. Munz, "Oxidation behaviour of nanoscale TiAlN/VN multilayer coatings", *Surf. Coat. Technol.* 177-178 (2004) 198.
212. L. Zhang, R.V. Koka, *Mater. Chem. Phys.* "A study on the oxidation and carbon diffusion of TiC in alumina–titanium carbide ceramics using XPS and Raman spectroscopy", 57 (1998) 23.
213. D.R. Tallant, J.E. Parmeter, M.P. Siegal, R.L. Simpson, "The thermal stability of diamond-like carbon", *Dia. Relat. Mater.* 4 (1995) 191.
214. M. Nakamizo, R. Kammereck, P.L. Walker, JR., "Laser Raman studies on carbons", *Carbon* 12 (1974) 259.
215. Y. Wang, D.C. Alsmeyer, R.L. McCreery, "Raman spectroscopy of carbon materials: structural basis of observed spectra", *Chem. Mater.* 2 (1990) 557.
216. J. Schwan, S. Ulrich, V. Batori, H. Ehrhardt, S.R.P. Silva, "Raman spectroscopy on amorphous carbon films", *J. Appl. Phys.* 80 (1) (1996) 440.
217. S. Loubière, Ch. Laurent, J.P. Bonino, A. Rousset, "Elaboration, microstructure and reactivity of Cr₃C₂ powders of different morphology", *Mater. Res. Bulletin* 30 (12) (1995) 1535.
218. S.F. Korablev, A.V. Lysenko, S.I. Filipchenko, "Chemical and kinetic peculiarities of the oxidation of powdery chromium carbide", *Soviet Powder Metallurgy and Metal Ceramics* 27 (1988) 584.

219. S. H. Ahn, J. H. Lee, J. G. Kim, J. G. Han, "Localized corrosion mechanisms of the multilayered coatings related to growth defects", *Surf. Coat. Technol.* 177-178 (2004) 638-644.
220. A.D. Reisel, C. Schürer, G. Irmer, E. Müller, "Electrochemical corrosion behaviour of uncoated and DLC coated medical grade Co28Cr6Mo", *Surf. Coat. Technol.* 177-178 (2004) 830-837.
221. K. Enke, "Dry machining and increase of endurance of machine parts with improved doped DLC coatings on steel, ceramics and aluminium", *Surf. Coat. Technol.* 116-119 (1999) 488.
222. R. F. Bunshah, "Deposition technologies: An overview", in *Handbook of Deposition Technologies for Films and Coatings, Science, Technology and Application*, ed. R. F. Bunshah, second edition, 1994, p. 17.
223. Haruyo Fukui, Junya Okida, Naoya Omori, Hideki Moriguchi and Keiichi Tsuda, "Cutting performance of DLC coated tools in dry machining aluminum alloys", *Surf. Coat. Technol.* 187 (1) (2004) 70.
224. M. Lahres, P. Muller-Hummel, O. Doerfel, "Applicability of different hard coatings in dry milling aluminium alloy", *Surf. Coat. Technol.* 91 (1997) 116.
225. T. C. S. Vandevelde, K. Vandierendonck, M. Van Stappen, W. Du Mong, P. Perremans, "Cutting applications of DLC, hard carbon and diamond films", *Surf. Coat. Technol.* 113 (1-2) (1999) 80.
226. H. L. Coldwell, R. C. Dewes, D. K. Aspinwall, N. M. Renevier and D. G. Teer, "The use of soft/lubricating coatings when dry drilling BS L168 aluminium", *Surf. Coat. Technol.* 177-178 (2004) 716-726.
227. J-D. Kim, Y-H Kang, "High-speed machining of aluminium using diamond endmills", *Int J Mach Tools Manuf.* 37 (1997) 1155-1165.

Appendix

Papers Published in Refereed Journals

Y.N. Kok, P.Eh. Hovsepian, Q. Luo, D.B. Lewis, J.G. Wen, I. Petrov, "Influence of the bias voltage on the structure and the tribological performance of nanoscale multilayer C/Cr PVD coatings", *Thin Solid Films* 475 (1-2) (2005) 219-226.

Y.N. Kok, P.Eh. Hovsepian, R. Haasch, I. Petrov, "Raman Spectroscopy study of C/Cr coatings deposited by the combined steered cathodic arc/unbalanced magnetron sputtering technique", *Surface and Coatings Technology* 200 (1-4) (2005) 1117-1122.

Y.N. Kok, R. Akid, P.Eh. Hovsepian, "Tribocorrosion testing of stainless steel (SS) and PVD coated SS using a modified scanning reference electrode technique", *Wear* 259 (7-12) (2005) 1472-1481.

Influence of the bias voltage on the structure and the tribological performance of nanoscale multilayer C/Cr PVD coatings

Y.N. Kok^{a,*}, P.Eh. Hovsepien^a, Q. Luo^a, D.B. Lewis^a, J.G. Wen^b, I. Petrov^b

^aMaterials Research Institute, Sheffield Hallam University, Howard Street, Sheffield S1 1WB, UK

^bMaterials Science Department and Frederick Seitz Materials Research Laboratory, University of Illinois, 1101 West Springfield Avenue, Urbana, IL 61801, USA

Available online 26 October 2004

Abstract

Nanoscale multilayer C/Cr coatings have been deposited by utilising the combined steered cathodic arc/unbalanced magnetron sputtering technique. The coating microstructure and tribological performance have been investigated as a function of the bias voltage, ranging from $U_b = -65$ to -350 V. The XRD results revealed that C/Cr coatings are amorphous at low U_b , but became more crystalline when the U_b increased to -350 V. High-resolution XTEM analysis indicated coating densification and smoothening as well as formation of novel amorphous nanostructure, in which carbon-rich clusters are surrounded by a Cr-rich matrix, leading to the formation of self-organised multilayer structure as the bias voltage was increased from -65 to -350 V. An increase of the bias voltage from -65 to -350 V resulted in an increase in the hardness from 8 to 25 GPa and Young's modulus, E from 186 to 319 GPa. A pin-on-disc test showed that the friction coefficient was reduced from 0.22 to 0.16 when the bias voltage was increased from -65 to -95 V. However, a further increase in the bias voltage to -350 V led to an increase in the friction coefficient to 0.31. The lowest wear coefficient $K_c \sim 6.25 \times 10^{-17} \text{ m}^3 \text{ N}^{-1} \text{ m}^{-1}$ was achieved at $U_b = -120$ V. Standard HSS drills, 8 mm in diameter, coated with C/Cr have been tested using solution annealed AISI 304 stainless steel as the work piece material. An improvement of the lifetime by a factor of ~ 9 has been achieved as compared to the uncoated tools. In this test, the C/Cr coating outperformed a number of commercially available PVD coatings, such as TiCN, TiAlCrN and showed similar performance to TiAlCrYN.

© 2004 Elsevier B.V. All rights reserved.

Keywords: Sputtering; C/Cr coating; Bias voltage; Tribology; Microstructure

1. Introduction

The extensive research in solid lubricant carbon-based coatings arises from the low friction coefficient and low shear strength of the graphite which confers excellent tribological performance in various industrial applications, such as cutting tools, automotive components, precision parts, and bearings [1–4]. It has been suggested that the excellent tribological performance of carbon-based coatings during sliding in ambient atmosphere results from the following factors:

(a) the nature of the sp^2 bonding with weak van der Waals bond between the hexagonal crystallographic structure of graphite,

- (b) low surface energy of the sliding surface and low interlamellar binding energy due to the adsorbed gases (e.g., hydrogen, oxygen, hydroxyl) or water vapour [5–7],
- (c) ability of graphite to form a transfer layer through atomic linkages between the metal and graphite because of the presence of oxides or condensable gases [8],
- (d) wear-induced graphitisation process [9–11], and
- (e) reorientation of the graphite nanocrystallised clusters of the outmost surface (~ 2.5 nm) of the coating which results in planes parallel to the rubbing surface [12].

The tribological performance of carbon-based coatings depends very much on the testing atmosphere and conditions [10,13], the deposition techniques, and the deposition parameters. Of particular importance in this respect is the substrate bias voltage which controls the ion bombardment

* Corresponding author Tel.: +44 114 221 3043; fax: +44 114 221 3053.
E-mail address: y.n.kok@shu.ac.uk (Y.N. Kok).

energy on the growing film and plays a crucial role in determining the properties of the coating. Low energy (~25–5000 eV) ion irradiation [14] during film growth is known to enhance adatom mobility, control the nucleation and growth kinetics, induce additional stresses, and thus modify the properties, composition, and the structure of the growing thin film [15,16]. It has been speculated that the structure of the sputtered carbon coatings that consists of very fine grains of graphite-like carbon with cross bonding between the graphite-like layers is due to the ion bombardment conditions during sputtering [4]. A recent publication [17] on the metal-doped (i.e., chromium) carbon film has reported that the low friction coefficient of the film was due to the densification and the smoothening caused by ion irradiation effects. However, the effect of ion bombardment on the evolution of the microstructure and on the tribological behaviour of C/Cr coatings has not yet been understood fully.

The aim of this paper is to explain the effects of ion bombardment on microstructural evolution and tribological performance of C/Cr coatings. To achieve this, coatings grown under a wide range of bias voltages, U_b , between –65 and –350 V, have been investigated.

2. Experimental procedure and characterisation techniques

C/Cr coatings were deposited by the combined steered cathodic arc/unbalanced magnetron sputtering (ABS™: Arc-Bond Sputtering) technique [18,19] using Hauzer HTC 1000-4 PVD coater. The details of the coating process have been reported previously elsewhere [11,17]. C/Cr coatings were deposited in three major steps: (i) Cr^+ ion etching using a steered cathodic arc discharge at a substrate bias voltage of –1200 V. It has been demonstrated that the metal ion bombardment favours local epitaxial film growth, which enhances adhesion between coating and substrate [20,21]. Additionally, the Cr^+ etching minimises the surface roughness of the subsequent coatings [22]; (ii) deposition of CrN base layer by unbalanced magnetron sputtering to further enhance the adhesion; and (iii) deposition of C/Cr coatings by unbalanced magnetron sputtering from three graphite targets and one chromium target at 260 °C. The coatings were deposited at different bias voltages of –65, –75, –95, –120, and –350 V in nonreactive Ar atmosphere.

The adhesion of the films was evaluated by CSEM REVETEST scratch tester by measuring the critical load of coating failure, L_c . The tribological studies were conducted using a pin-on-disc (CSEM tribometer) apparatus. The tests have been carried out in ambient atmosphere (RH: 13–34%, temperature: 25–28 °C) under the testing conditions of 5 N normal load, 0.1 ms^{-1} sliding speed, sliding distance of 1.3 km, using a 6-mm 100Cr6 steel ball. The cross-sectional area of the wear track was measured using a laser profilometer, four measurements were taken on each sample at 90° apart. The coating thickness was measured by ball

cratering techniques (CSEM Calotest). The hardness and the Young's modulus, E , of the coating were determined by nanoindentation test (Nano-Instrument XP), by setting the maximum penetration depth to 250 nm; 25 measurements were taken in order to obtain statistical average results. The stress of the coatings was determined by the deflection method using Stoney's equation [23]:

$$\sigma = (E_s d^2) / [6(1 - \nu_s) R d_c]$$

where E , d , ν , and R are the Young's modulus, thickness, Poisson ratio (0.3 was used in the calculation), and the radius of curvature of the coated substrate, respectively; subscripts s and c denote the substrate and the coating, respectively. The coatings for the stress measurement have been deposited on a rectangular steel substrates ($E_s=260 \text{ GPa}$) with a dimensions $0.1 \times 10 \times (50 \pm 0.5) \text{ mm}^3$. The maximum deflection of the coated substrate was measured by optical microscopy (Society Genevoise Optical Measuring Machine). Secondary Neutral Mass Spectrometry [SNMS, quantitative-using certified reference materials (CRM)], VG SIMSLAB was used for the compositional depth profiling of the films.

The structure of C/Cr was investigated by X-ray diffraction (XRD) analysis utilising Philips PW 1710 automated diffractometer, using glancing angle (fix at 1° incidence angle) and $\theta/2\theta$ geometries, scanning from 10° to 100° with a step size of 0.04°. Cross-sectional transmission electron microscopy (XTEM; Philips CM20 operated at 200 kV) and high-resolution TEM (HRTEM; JEOL 2010F operated at 200 kV) were used to study the microstructure of the coatings.

3. Results and discussion

3.1. Compositional analysis

The SNMS depth profiling results showed that for the applied bias voltages in the range of –65 to –120 V, the concentration of carbon and chromium in the films remained constant at ~68 and ~32 at.%, respectively. However, at $U_b=-350 \text{ V}$, the carbon content decreased by ~15 at.%, which gave a film concentration of 53 at.% C and 47 at.% Cr (i.e., C to Cr ratio of nearly 1:1). The decrease in carbon content could be due to the following reasons resulting from high-energy ion bombardment: (1) the continuous and simultaneous dilation process resulting in removal of the less tightly bonded carbon atoms and background gas [24]; (2) resputtering of the weakly bonded carbon adatoms during the coating growth stage [25] due to its small single bond radius of 0.077 nm as compared to 0.125 nm for Cr atom.

3.2. XRD analysis

Fig. 1(a) and (b) shows the glancing angle and $\theta/2\theta$ X-ray diffraction, respectively, of the films deposited at various bias

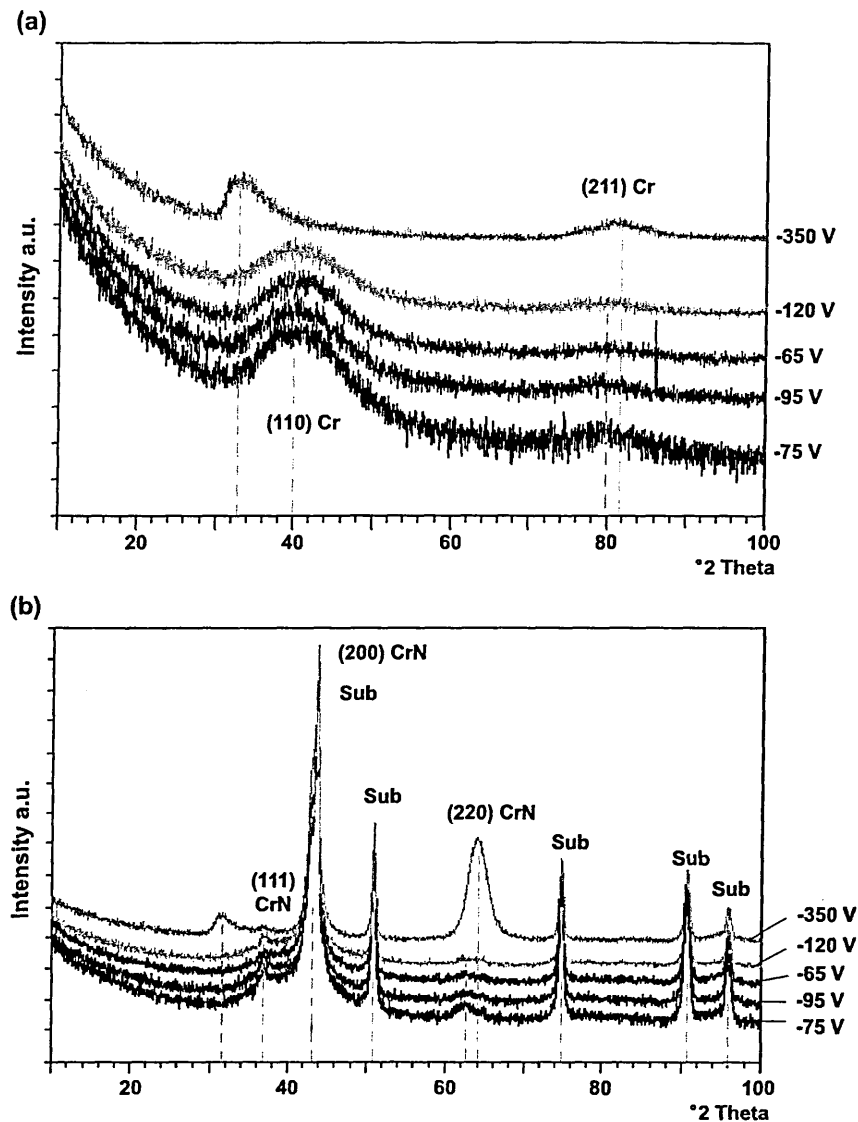


Fig. 1. (a) Glancing angle and (b) $\theta/2\theta$ X-ray diffraction of the films deposited at different bias voltage.

voltages. It was observed that the X-ray diffraction patterns of coatings deposited at U_b between -65 and -120 V were identical. In Fig. 1(a), the absence of the crystalline reflections and the broad diffuse peaks indicates that the film microstructure is essentially amorphous. For U_b between -65 and -120 V, the diffuse peaks appear at 2θ values of $\sim 40^\circ$ and $\sim 80^\circ$ corresponding to the positions of (110) and (211) reflections, respectively, from metallic chromium. At -350 V, the (110) Cr is not present whereas the (211) peak is shifted towards higher angular position. However, a diffuse peak at $\sim 2\theta = 32^\circ$ is present which is close to the (011) Cr_3C_2 reflection. As no other peak corresponding to Cr_3C_2 is present, it is not possible to unambiguously state that the carbide phase has been formed. Fig. 1(b) shows the presence of (111), (200), and (220) peaks from the CrN base layer, which is in agreement with our previous observation [11].

3.3. Microstructure analysis by XTEM and HRTEM

Fig. 2(a) is a bright-field (BF) XTEM image, showing the microstructure of films deposited at $U_b = -350$ V, including the substrate, CrN base layer and the novel multilayer C/Cr coating. Fig. 2(b) and (c) show the near surface region of the films deposited at U_b of -65 and -120 V, respectively, with their corresponding selected area diffraction (SAD) patterns. On all micrographs, carbon appears as the bright region and Cr as the darker region [17,26]. The coating deposited at $U_b = -65$ V is considerably rougher but it becomes smoother and denser as the bias voltage is increased from -65 to -350 V. This is due to the effects of bombardment of the growing films by energetic particles, which enhances the surface mobility of the condensed species, promotes the displacement of surface atoms towards more stable positions in terms

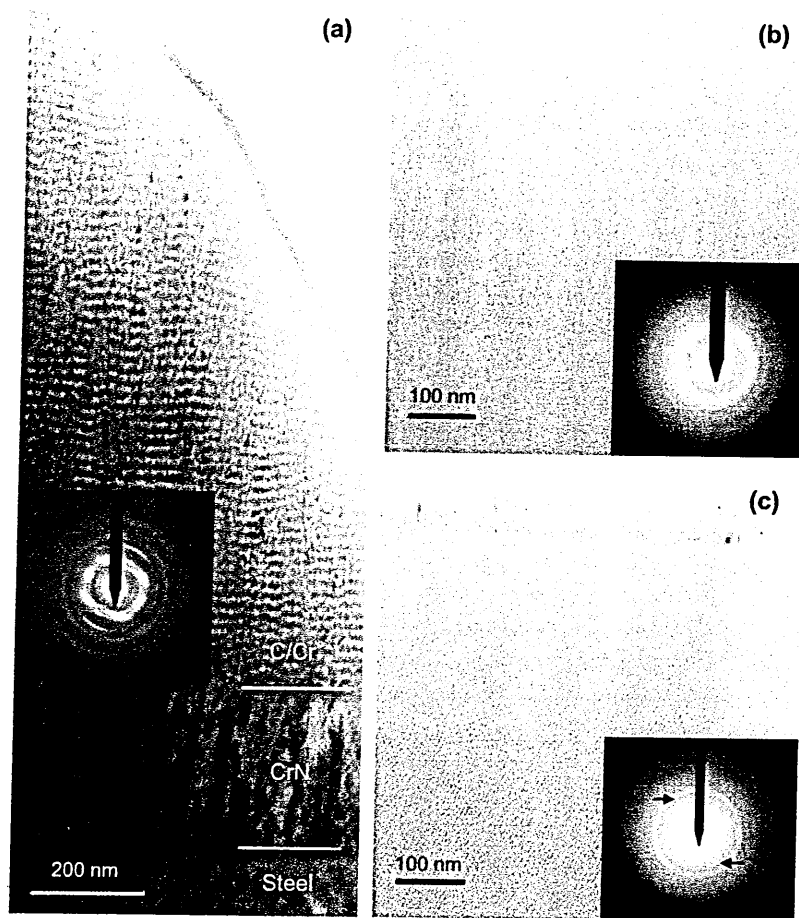


Fig. 2. Bright-field XTEM images showing (a) the architectures of coating deposited at $U_b = -350$ V, and near surface region for (b) $U_b = -65$ V, (c) $U_b = -120$ V, with the corresponding SAD patterns.

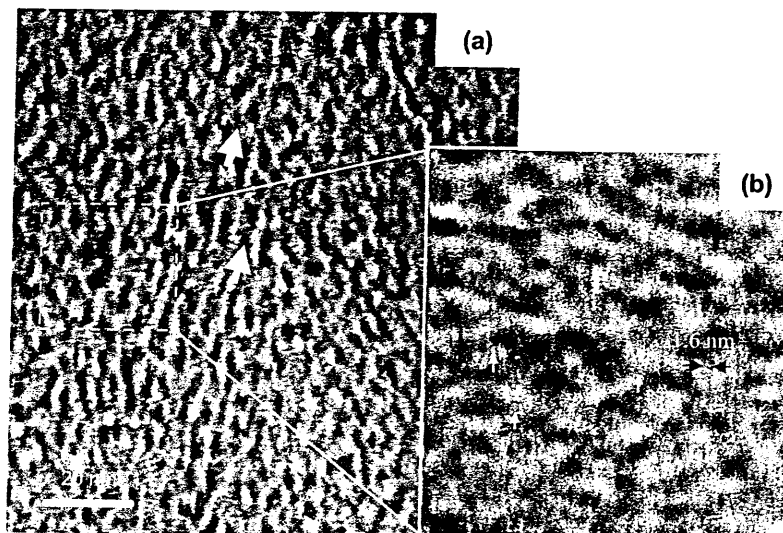


Fig. 3. (a) Higher magnification bright-field images of coatings deposited at $U_b = -120$ V; (b) magnified image of dotted box region (rotated 90° clockwise) showing the artificial multilayer structure (shown by arrows).

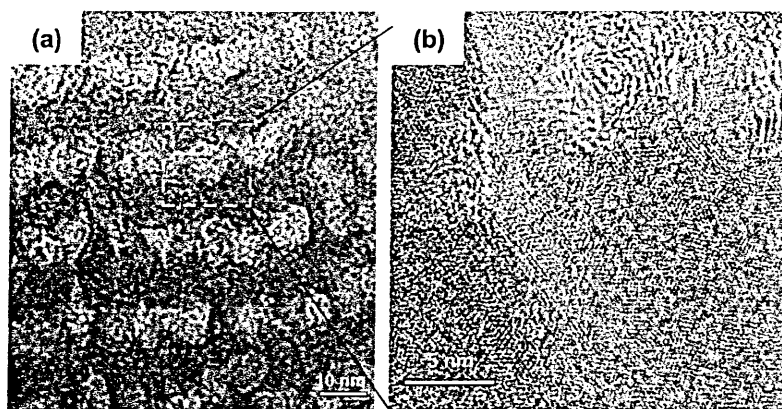


Fig. 4. HRTEM image of the (a) multilayer structure formed at $U_b = -350$ V; (b) magnified image of the nano-onion-like carbon.

of surface energy, and results in the elimination of voids, cavities, and vacancies in the coatings [27]. The coatings deposited between -65 and -95 V show columnar structures with carbon accumulated at the grain boundaries (the white phase between the columns) [17], as shown in Fig. 2(b). However, the width of the column boundaries is markedly reduced as the bias voltage increased from -65 to -95 V (not shown in the figure). This effect is attributed to an increased nucleation probability, accelerating growth and coalescence of the nuclei as the ion energy is increased [16,28,29]. At $U_b = -120$ V [see Fig. 2(c)], the columnar structure transforms to a more uniformly distributed random structure where the number of the onion-like clusters increases both in size and number, the crystallites become slightly aligned in the growth direction [shown by arrows in Fig. 3(a)] as compared to that of U_b between -65 and -95 V. Fig. 3 shows the higher magnification images for $U_b = -120$ V. The artificial multilayer structure with an estimated periodicity of ~ 1.6 nm was highlighted in the dotted box region and included in Fig. 3(b) (the image has been rotated through 90° clockwise to give a better representation of the layer structure). The SAD patterns (Fig. 2 insets) of coating deposited between -65 and -120 V were identical, both showing halo-like diffuse ring patterns, which further revealed the short-range order or amorphous structure of C/Cr coatings. Nonetheless, the crystallinity of the coatings increased with increasing bias voltage, as can be seen by careful observation of the SAD pattern; crystalline diffraction arcs can be seen around the most intense diffuse ring as shown by arrows in Fig. 2(c) (inset). The increased crystallinity of the growing films could be attributed to both

an increase in the kinetic energy of the ions and an increase in the deposition temperature from ~ 260 to ~ 450 °C as a consequence of the increased bias voltage, which increases the surface diffusivity of the adatoms. At -350 V, a rather complex diffraction pattern [Fig. 2(a) inset] was observed, which showed pronounced crystalline reflections from graphitic carbon, chromium crystallites, and chromium carbides (Cr_{23}C_6 , Cr_7C_3 , Cr_3C_2) in the matrix of amorphous carbon. It is obvious that a higher bias voltage of -350 V substantially influences the structure of C/Cr films by affecting the nucleation kinetics, and the degree of preferred orientation of the growing films.

Fig. 4(a) shows the pronounced multilayer structure of the film deposited at $U_b = -350$ V, with an average periodicity of ~ 20 nm which is almost one order of magnitude larger than that for the coatings deposited between -65 and -95 V (bilayer thickness of ~ 2 nm) [17]. The structure comprises of carbon-rich layers (brighter layers segmented in clusters) and chromium-rich layers (darker layers with uniform structure), which are possibly carbides. The carbon layers are built up from the graphite-like carbon which is arranged in nano-onion-like manner, as shown in the magnified image in Fig. 4(b). It can be speculated that the formation of the multilayer structure with the abnormally large bilayer thickness is due to the segregation and self-organisation of the carbon atoms, and possibly the formation of Cr-based carbides, as a result of increased adatom mobility and increased temperature induced by higher-energy ion bombardment. In order to separate the effects of temperature only and increased Cr content, from ion bombardment effects, coatings were also prepared at a higher temperature (400 °C) and at a higher Cr

Table 1
Summarised property of C/Cr coatings

Bias voltage (V)	μ	L_c (N)	Thickness (μm)	Hardness (GPa)	E (GPa)	Stress (GPa)	K_c ($\text{m}^3 \text{N}^{-1} \text{m}^{-1}$)
-65	0.22	48	~ 1.96	8.23	186	0.62	$2.85\text{e}-16$
-75	0.21	75	~ 1.82	11.90	211	1.14	$1.22\text{e}-16$
-95	0.16	70	~ 1.78	17.30	283	1.70	$6.75\text{e}-17$
-120	0.19	50	~ 1.53	19.90	300	2.81	$6.25\text{e}-17$
-350	0.31	20	~ 1.48	25.00	319	2.00	$3.02\text{e}-16$

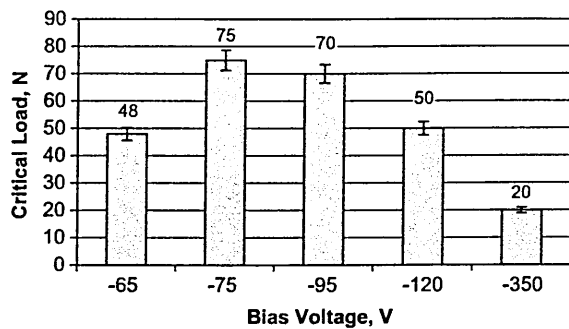


Fig. 5. Critical load as a function of bias voltage.

target power at a bias voltage of -75 V. The transformation from the typical columnar to the distinct multilayer structure could only be observed under conditions of high-energy ion bombardment ($U_b = -350$ V); therefore, the sole influence of high temperature and the high Cr content could be disregarded.

3.4. Mechanical and tribological properties

Table 1 summarises the mechanical and the tribological properties of C/Cr coatings deposited at various bias voltages. The thickness, hardness and the Young's modulus, E , of the

films showed a clear dependence on the substrate bias voltage. An increase in the U_b from -65 to -350 V resulted in decreases in thickness from ~ 1.96 to ~ 1.48 μm , hardness increases from 8.23 to 25 GPa, and an increase in the Young's modulus, E , from 186 to 319 GPa. The stress increased from 0.62 to 2.81 GPa with increasing bias voltage from -65 to -120 V. Further increases in the U_b to -350 V resulted in a reduction in the stress to 2 GPa. The stress values are in good agreement with the levels reported for other carbon-based coatings [30,31]. The decreases in the compressive stress at $U_b = -350$ V could be due to the formation of the layered structure, thermal relaxation of the structure, the enhancement of the adatom mobility which contributes to the relaxation of the compressive stress of the film [30].

Fig. 5 shows the critical load as a function of the bias voltage. The critical load, L_c increased from 48 to 75 N as the bias voltage was increased from -65 to -75 V. Further increase in the U_b to -350 V led to a reduction in the L_c to 20 N. For all the applied bias voltages, no formation of microflakes and spalling of the coatings could be observed inside and at the rim of the scratch, respectively. This demonstrates excellent adhesion between coating and substrate. The pin-on-disc test results shown in Fig. 6(a) demonstrate a clear dependence between the friction coefficient and the bias voltage. The friction coefficient, μ , decreased from 0.22 to 0.16 when the U_b was increased from -65 to -95 V. However, further increases in the U_b to -350 V led to an increase in the friction coefficient to 0.31. The friction curves as shown in Fig. 6(b) become smoother as the bias voltage was increased from -65 to -95 V. It has been reported in our previous work [17] that the coating deposited at -65 V has a rougher surface, larger column diameter which open along column boundaries and crack, thus generating large wear particles during sliding. In addition, the rough surface experiences greater asperity contact, increases tendency to plastic deformation and mechanical interlocking during sliding, resulting in the formation of wear debris, which accumulate in the wear track and promote third-body sliding leading to higher friction and wear coefficients.

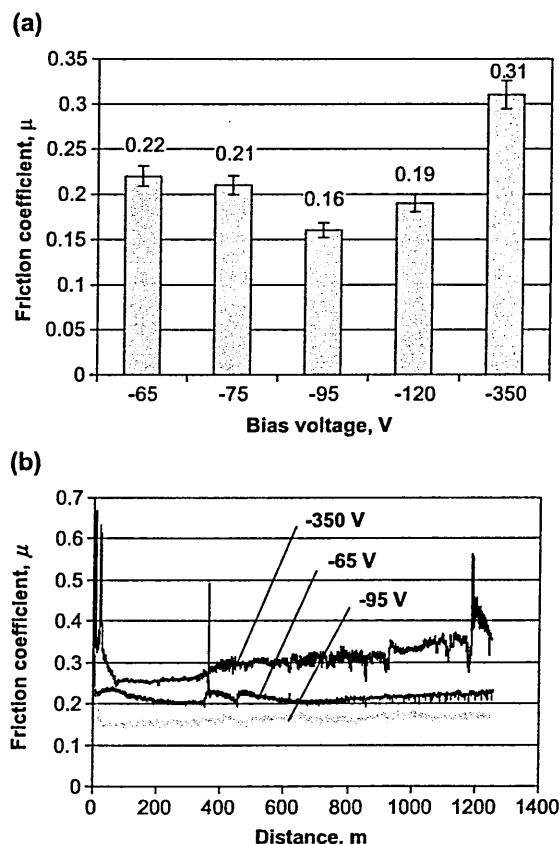


Fig. 6. (a) Friction coefficient and (b) friction curves of C/Cr coatings as a function of bias voltage.

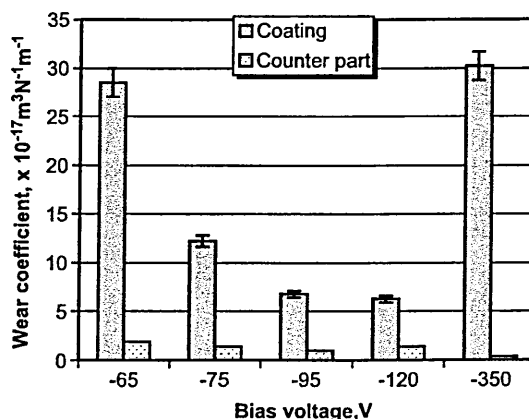


Fig. 7. Wear coefficient as a function of bias voltage.

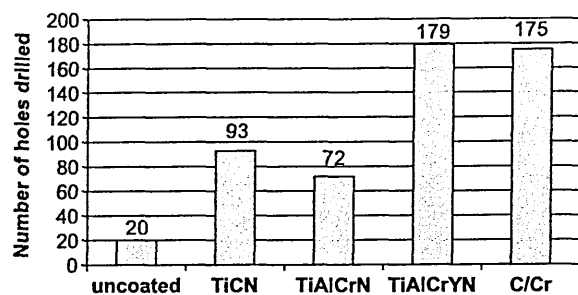


Fig. 8. Number of holes drilled as a function of different coatings.

In contrast, at the higher bias voltage of -95 V, as a result of surface smoothening (less asperity contact) and densification of the coating, sliding wear occurs layer by layer resulting in a lower friction coefficient and a smoother curve. At -350 V, the friction curve becomes rougher and the friction coefficient increases gradually after a sliding distance of ~ 320 m. This could be attributed to the lower carbon content which reduces the lubrication effect, and the high compressive stress in the coating. Fig. 7 shows the sliding wear coefficient of the coatings after pin-on-disc tests. The wear resistant of the coatings correlates well with their friction performance, specifically, films with higher friction coefficient suffer higher wear rates. With increased bias voltage from -65 to -120 V, the wear coefficient of the coatings, K_c , decreased from $\sim 2.8 \times 10^{-16}$ to $\sim 6 \times 10^{-17} \text{ m}^3 \text{ N}^{-1} \text{ m}^{-1}$. However, further increases in the bias voltage to -350 V increased the sliding wear coefficient K_c to $\sim 3 \times 10^{-16} \text{ m}^3 \text{ N}^{-1} \text{ m}^{-1}$.

3.5. Drilling test

Fig. 8 shows the number of holes drilled as a function of different types of coatings. The drilling tests were conducted at a velocity of 38 m/min , with a feed rate of 0.14 mm/rev to a hole depth of 15 mm , using standard HSS drills, 8 mm in diameter coated with C/Cr, using solution treated AISI 304 stainless steel as the work piece material. An improvement of the lifetime by a factor of ~ 9 has been achieved by C/Cr-coated tools as compared to the uncoated tools. In this test, the C/Cr coating outperformed a number of commercially available PVD coatings such as TiCN, TiAlCrN and showed similar performance to TiAlCrYN, a dedicated high-temperature oxidation-resistant coating.

4. Conclusions

The results presented in this paper clearly demonstrate the significant influence of the ion bombardment on the microstructures and the properties of C/Cr coatings:

- High-energy ion bombardment increases adatom mobility and therefore induces surface smoothening, film densification, and nuclei coalescence and enhances the crystallinity of C/Cr coatings.

- The intensive ion radiation in the bias voltage range between -65 and -350 V has promoted segregation and self-organisation of the carbon atoms in the coating.
- C/Cr coatings transformed from the typical columnar structure to a novel multilayer structure with abnormally large bilayer thickness of $\sim 20 \text{ nm}$, as the bias voltage increases from -65 to -350 V.
- The structural transformations were found to strongly influence the tribological and mechanical properties of C/Cr coatings.
- Best performance has been achieved with coatings deposited at $U_b = -95 \text{ V}$ ($\mu = 0.16$, $K_c \sim 6 \times 10^{-17} \text{ m}^3 \text{ N}^{-1} \text{ m}^{-1}$), which has a uniformly distributed amorphous structure.

Acknowledgements

Y.N.K. gratefully acknowledges the studentship from Sheffield Hallam University. The authors acknowledge the use of the facilities of the Center for Microanalysis of Materials, which is partially supported by DOE, at the University of Illinois. The authors would like to thank Dr. Stuart Read from Corus R&D, Sheffield UK, for the SNMS analysis, and Tuukka Savisalo from Sheffield Hallam University for hardness and Young's modulus measurements.

References

- [1] M. Grischke, R. Herb, O. Massler, J. Kamer, H. Eberle, Society of Vacuum Coaters, 44th Annual Technical Conference Proceedings, 2001, p. 407.
- [2] A. Bloyce, Mater. World (2000 (March)) 13.
- [3] S. Yang, D.G. Teer, Surf. Coat. Technol. 131 (2000) 412.
- [4] S. Yang, D. Camino, A.H.S. Jones, D.G. Teer, Surf. Coat. Technol. 124 (2000) 110.
- [5] A.D. Sarkar, Wear of Metals, Pergamon Press, 1976, p. 137.
- [6] R.H. Savage, J. Appl. Phys. 19 (1948) 1.
- [7] A. Grill, Surf. Coat. Technol. 94–95 (1997) 507.
- [8] F.J. Clauss, Solid Lubricants and Self-Lubricating Solids, Academic Press, 1972, p. 45.
- [9] Y. Liu, E.I. Meletis, J. Mater. Sci. 32 (1997) 3491.
- [10] Y. Liu, A. Erdemir, E.I. Meletis, Surf. Coat. Technol. 94/95 (1997) 463.
- [11] P.Eh. Hovsepian, D.B. Lewis, C. Constable, Q. Luo, Y.N. Kok, W.-D. Münz, Surf. Coat. Technol. 174–175 (2003) 762.
- [12] S. Yang, X. Li, N.M. Renevier, D.G. Teer, Surf. Coat. Technol. 142–144 (2001) 85.
- [13] Y. Liu, A. Erdemir, E.I. Meletis, Surf. Coat. Technol. 86–87 (1996) 564.
- [14] J.E. Greene, S.A. Barnett, J. Vac. Sci. Technol. 21 (2) (1982) 285.
- [15] L. Hultman, U. Helmersson, S.A. Barnett, J.E. Sundgren, J.E. Greene, J. Appl. Phys. 61 (2) (1987) 552.
- [16] Miko Marinov, Thin Solid Films 46 (1977) 267.
- [17] P.Eh. Hovsepian, Y.N. Kok, A.P. Ehasarian, A. Erdemir, J.-G. Wen, I. Petrov, W.-D. Münz, Thin Solid Films 447–448 (2004) 7.
- [18] W.-D. Münz, F.J.M. Hauzer, D. Schulze, B. Buil, Surf. Coat. Technol. 49 (1991) 161.
- [19] W.-D. Münz, D. Schulze, F.J.M. Hauzer, Surf. Coat. Technol. 50 (1992) 169.

- [20] I. Petrov, P. Losbichler, D. Bergstrom, J.E. Greene, W.-D. Münz, T. Hurkmans, T. Trinh, *Thin Solid Films* 302 (1997) 179.
- [21] C. Schönjahn, L.A. Donohue, D.B. Lewis, W.-D. Münz, I. Petrov, J. Vac. Sci. Technol., A, *Vac. Surf. Films* 18 (4) (2000) 1718.
- [22] W.-D. Münz, I.J. Smith, D.B. Lewis, S. Creasey, *Vacuum* 48 (5) (1997) 473.
- [23] J. Albert Sue, "Stress Determination for Coatings", in *ASM Handbook Vol. 5 Surface Engineering*, The Materials Information Society, 1994, p. 647.
- [24] S. Aisenberg, *J. Vac. Sci. Technol., A, Vac. Surf. Films* 2 (2) (1984) 369.
- [25] V.V. Uglov, A.K. Kuleshov, D.P. Rusalsky, M.P. Samzov, A.N. Dementshenok, *Surf. Coat. Technol.* 158–159 (2002) 699.
- [26] N.J.M. Carvalho, J.Th.M. Dehossan, *Thin Solid Films* 388 (2001) 150.
- [27] N. Maréchal, E. Quesnel, Y. Pauleau, *J. Mater. Res.* 9 (7) (1994) 1820.
- [28] M. Ohring, *The Materials Science of Thin Films*, Academic Press, Boston, 1992.
- [29] M. Odén, C. Ericsson, G. Håkansson, H. Ljungcrantz, *Surf. Coat. Technol.* 114 (1999) 39.
- [30] X.L. Peng, T.W. Clyne, *Thin Solid Films* 312 (1998) 207.
- [31] B.K. Gupta, Bharat Bhushan, *Thin Solid Films* 270 (1995) 391.

Raman spectroscopy study of C/Cr coatings deposited by the combined steered cathodic ARC/unbalanced magnetron sputtering technique

Y.N. Kok^{a,*}, P.Eh. Hovsepian^a, R. Haasch^b, I. Petrov^b

^aMaterials and Engineering Research Institute, Sheffield Hallam University, Howard Street, Sheffield S1 1WB, UK

^bMaterials Science Department and Frederick Seitz Materials Research Laboratory, University of Illinois, 1101 West Springfield Avenue, Urbana, IL 61801, USA

Available online 18 March 2005

Abstract

C/Cr coatings were prepared by the combined steered cathodic arc/unbalanced magnetron sputtering technique with a wide range of bias voltages, U_b from -65 to -350 V. The paper focuses on the microstructure evolution and phase transformations in the coatings and their influence on the tribological performance of C/Cr coatings as a function of the bias voltage. Raman spectroscopy on the surface of the as deposited coatings and in the wear track generated in pin-on-disc tests has been carried out in conjunction with TEM and SEM studies of coatings microstructure and XPS analysis of the chemical bonding in the films. The Raman spectra from the surface of the C/Cr coatings consists of two main Raman features on a strong photoluminescence background: broad bands around $\sim 1380\text{ cm}^{-1}$ and $\sim 1572\text{ cm}^{-1}$, which are designated to D (disorder) and G (graphitic) peaks, respectively. The broad D and G bands further confirm the TEM-selected area diffraction (SAD) analysis, which shows an amorphous character of the coating. The downshift of the G -band by $\sim 2\text{--}10\text{ cm}^{-1}$ from the planar graphite (1582 cm^{-1}) is ascribed as the shell curvature of the carbon plane, which could be due to the presence of Cr. We assume the D -band position has a close dependence on the stress in the coating, which results in shifting of the D -band to higher wave number as the stress in the coatings increases. The Raman spectra show better resolution of the D and G peaks for samples deposited at low bias voltage ($U_b = -65$ to $U_b = -75$ V). However, these peaks become more diffused and difficult to resolve, with a much lower intensity as the applied bias voltage increases and completely disappears at $U_b = -350$ V, which suggests formation of metal carbides in the coating. This interpretation was further confirmed by the XRD, TEM and SAD pattern observations. The I_D/I_G ratio correlates well with the friction behaviour of the films. The friction coefficient decreases and reaches its minimum of $\mu = 0.16$ at $U_b = -95$ V due to the increase in the sp^2 content in the film, which is accompanied by a maximum I_D/I_G ratio of 7.15.

© 2005 Elsevier B.V. All rights reserved.

Keywords: C/Cr coating; Magnetron sputtering; Raman spectroscopy; Structure; Bias voltage; Friction

1. Introduction

C/Cr coatings, produced by the combined steered cathodic arc/unbalanced magnetron sputtering (ABS) technique, has been reported to possess superior mechanical and tribological properties and act as solid lubricants [1–3]. A considerable interest in the research of thin carbon films arises from the possibility to change the film properties, by tailoring the microstructure i.e. from graphite-like to

diamond-like with an amorphous or crystalline structure, and to vary the sp^2/sp^3 ratio depending on the deposition techniques and conditions [4–6].

Raman spectroscopy has been widely used to characterise carbon-based materials [7–9], specifically DLC coatings. In this study, Raman spectroscopy in combination with X-ray Photoelectron Spectroscopy (XPS), Cross-sectional Transmission Electron Microscopy (XTEM) and Selected Area Diffraction (SAD) analyses have been employed to obtain structural information of the carbon fraction in the graphite-like C/Cr coatings. This information has been used to explain the tribological behaviour of the ABS (Arc-Bond sputtering) deposited carbon-chromium films.

* Corresponding author. Tel.: +44 114 221 3043; fax: +44 114 221 3053.
E-mail address: y.n.kok@shu.ac.uk (Y.N. Kok).

2. Experimental procedures

2.1. Coating deposition

C/Cr coatings were deposited by the combined steered cathodic arc/unbalanced magnetron sputtering (ABS™: Arc-Bond sputtering) technique [10] using a Hauzer HTC 1000-4 PVD coater. The coatings were deposited by unbalanced magnetron sputtering from three graphite and one chromium targets, at different bias voltages, (U_b) of -65 , -75 , -95 , -120 , and -350 V in a non-reactive Ar atmosphere. A low energy Cr^+ ion implantation during the metal ion etching step and a deposition of CrN base layer were employed to enhanced coating adhesion. The details of the coating process have been reported elsewhere [1–3].

2.2. Characterisation techniques

- The wear resistance of the coatings was investigated using a pin-on-disc test (CSEM tribometer), under the following test conditions: 5 N normal load, 1.3 km sliding distance, 0.1 m/s sliding speed, 100 Cr6 steel ball as counter part, at room temperature: 25–28 °C, relative humidity: 13–34%.
- The Raman measurements were performed using a Renishaw Raman System 1000 spectrometer. The excitation wavelength used was 632.8 nm from a HeNe red laser.
- Photoelectron spectroscopic analysis was performed using a Physical Electronics model PHI 5400 X-ray photoelectron spectrometer using a Mg K_α source (300 W, 15 kV, 20 mA).
- The microstructure of the coatings was investigated using a Transmission Electron Microscope (Philips CM20 and JEOL 2010F, at 200 keV) and the wear tracks were examined using a Scanning Electron Microscope (Philips XL40, at 20 kV).

3. Results and discussions

3.1. As deposited coating

3.1.1. Microstructure

Fig. 1a–c, show the microstructure evolution of C/Cr coatings as a function of the bias voltage. The bright field TEM image of the film deposited at $U_b = -65$ V (Fig. 1a) shows a pronounced columnar structure, in which the columns are separated by regions appearing in a bright contrast. Investigation by HAADF (high-angle annular dark field) and high-resolution XTEM analyses revealed that the bright lines are not voids but areas occupied by a weak carbon phase [2]. The coating deposited at $U_b = -95$ V sample (Fig. 1b) is denser, has smaller column boundaries with a main structure containing uniformly dis-

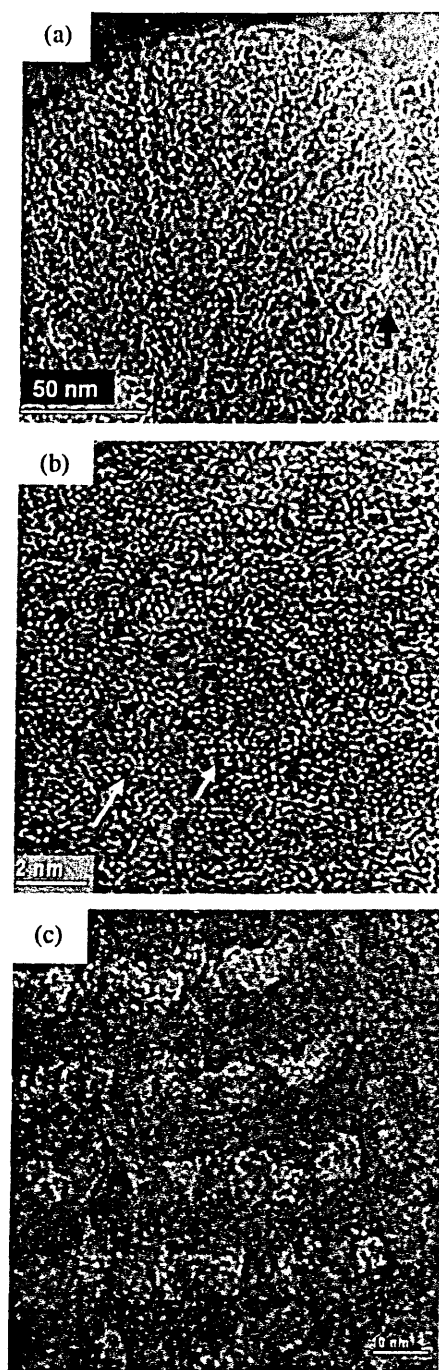


Fig. 1. Cross-sectional TEM images of coatings deposited at: a) $U_b = -65$ V, dark arrow shows the carbon-rich column, b) $U_b = -95$ V, dark arrow-heads highlight the onion-like carbon clusters) and c) $U_b = -350$ V, self-organised layered structure comprising aligned carbon onions in a Me-carbon matrix.

tributed onion-like clusters. More careful observation of the image reveals that the clusters seem to be directionally oriented (highlighted by white arrows) and tend to form layered structures. The initial stages of this process of self-

organisation and alignment of the clusters can be observed already at $U_b = -95$ V. At a bias voltage of $U_b = -350$ V a novel self-organised multilayer structure, consisting of a crystalline carbide phase and carbon-rich amorphous region, is formed as a consequence of migration, separation and self-organisation of carbon atoms, induced by the strong bombardment with Ar^+ ions [2,3].

3.1.2. X-ray Photoelectron Spectroscopy (XPS)

High resolution C1s XPS spectra of coatings deposited at $U_b = -75$ V and $U_b = -350$ V, after 2 min and 4 min Ar^+ etching revealed that the intensity of the Cr-C component increases with sputtering time for both samples. This behaviour can be attributed to the preferential sputtering of the light carbon atoms during the Ar^+ etching, which results in increase of the intensity of the Cr-C peak. This trend is preserved in the whole bias voltage range with a highest intensity of the Cr-C peak achieved at the highest bias voltage of $U_b = -350$ V. The trend clearly indicates more Cr-C bonding relative to free carbon and therefore, suggests formation of Me-carbide (Cr_7C_3 or Cr_3C_2) phases in the coating.

3.1.3. Raman spectra

The Raman spectra from the surface of the C/Cr coatings consist of two main Raman features: broad bands around ~ 1380 cm^{-1} and ~ 1572 cm^{-1} , which are designated to *D* (disorder) and *G* (graphitic) peaks respectively (Fig. 2a). The Raman spectra show better resolved *D* and *G* peaks for samples deposited at low bias voltage ($U_b = -65$ V to $U_b = -75$ V). However, the peaks become more diffused and difficult to resolve (featureless), and their intensity decreases with increasing applied bias voltage to $U_b = -350$ V, which suggests formations of chromium-carbides in the matrix. This interpretation was further confirmed by the XRD, TEM and SAD patterns observations [3], and complements the XPS results. The spectrum from the sample produced at $U_b = -350$ V looks very similar to the spectrum from cemented carbide used as a reference sample. The carbide spectrum is featureless and no free carbon bonds can be detected (no *D* and *G* bands). This observation brings further evidence for the Me-carbide character of the C/Cr coatings produced under the conditions of intensive ion bombardment.

The Raman spectra shown in Fig. 2a were decomposed into two bands with Gaussian line shapes to determine the *D* and *G* bands position, and to calculate the I_D/I_G ratio, which relates to the sp^2/sp^3 content of the films. It was noted that there is a shift in the *G* and *D* band positions, with *G* band shifted towards lower wave numbers (1572 – 1580 cm^{-1}) from the planar graphite (1582 cm^{-1}) and *D* band shifted towards higher wave numbers (1380 – 1390 cm^{-1}). The downshift of the *G* peak can be attributed to the change in the bond angle disorder [11] or to an increase in 4-fold coordination (diamond) [12]. Additionally, the downshift of *G*-peak from the position 1582 cm^{-1} can be attributed to the

influence of shell curvature [13]. For onion-like carbon a specific Raman band at 1572 cm^{-1} was reported. In our study, the *G*-band of the coatings was downshifted by ~ 2 – 10 cm^{-1} from the planar graphite (1582 cm^{-1}). It can be speculated that the downshift results from the occupancy of dangling bonds by Cr atoms that caused bond angle disorder and lead to shell curvature of the carbon plane.

The *D*-band position has a close dependence on the stress in the coating, where the *D*-band shifts to higher wave numbers as the compressive stress in the coatings increases. Fig. 2b shows the *D*-band shifts to a higher wave number from 1380 to 1393 cm^{-1} as the bias voltage increases from $U_b = -65$ V to $U_b = -120$ V, and downshifts by approximately 3 cm^{-1} when the bias voltage increases further to $U_b = -350$ V. It can be stated that the *D*-band shift follows the trend of the compressive stress in the coating as a function of the bias voltage. As the bias voltage increases from $U_b = -65$ V to $U_b = -120$ V the compressive stress increases from 0.62 to 2.81 GPa, respectively, and decreases to 2 GPa when the bias voltage further increases to $U_b = -350$ V. This observation is consistent with recent reports that Raman peak shifting provides a direct relationship between processing conditions and the residual stresses [14].

As previously reported, the friction coefficient (μ) of C/Cr films decreases from $\mu = 0.2$ to $\mu = 0.16$ when the bias voltage increases from $U_b = -65$ V to $U_b = -95$ V, and reaches a higher value of $\mu = 0.31$ when the bias voltage increases to $U_b = -350$ V [3]. A similar trend was also reported for amorphous pure carbon thin films grown by magnetron sputtering [15]. We found a strong relation between the friction behaviour of the films and their microstructure, residual stress and the I_D/I_G ratio (Fig. 2c). It has been reported that increased I_D/I_G ratio indicates an increase in the sp^2 bonding [16]. The reduction of the coefficient of friction from $\mu = 0.2$ to $\mu = 0.16$ when the bias voltage increases from $U_b = -65$ V to $U_b = -95$ V can be explained by the increase of the amount of the sp^2 bonded carbon in the coating, indicated by the increase of the I_D/I_G ratio which reaches its maximum at $U_b = -95$ V. Another reason for the reduced friction coefficient, which is indicative for improved wear resistance, is seen in the formation of much denser and more uniform structures based on randomly distributed onion-like features as well as in the smoother surface of the coatings deposited at $U_b = -95$ V [2]. In contrast, coatings deposited at lower bias voltages ($U_b = -65$ V and $U_b = -75$ V) are rougher and show sub-dense columnar structure with weak carbon phase accumulated at the grain boundaries (Fig. 1a). As shown previously for columnar structures the tangential friction force can bend, plastically deform and break the columns, releasing large particles, which act as a third body in the tribo-contact thus increasing both the friction and the wear during sliding [17]. This process is even more accelerated if a weaker (pure carbon) phase is responsible for providing the bonding between the individual columns. The friction force in this case can easily open tensile cracks

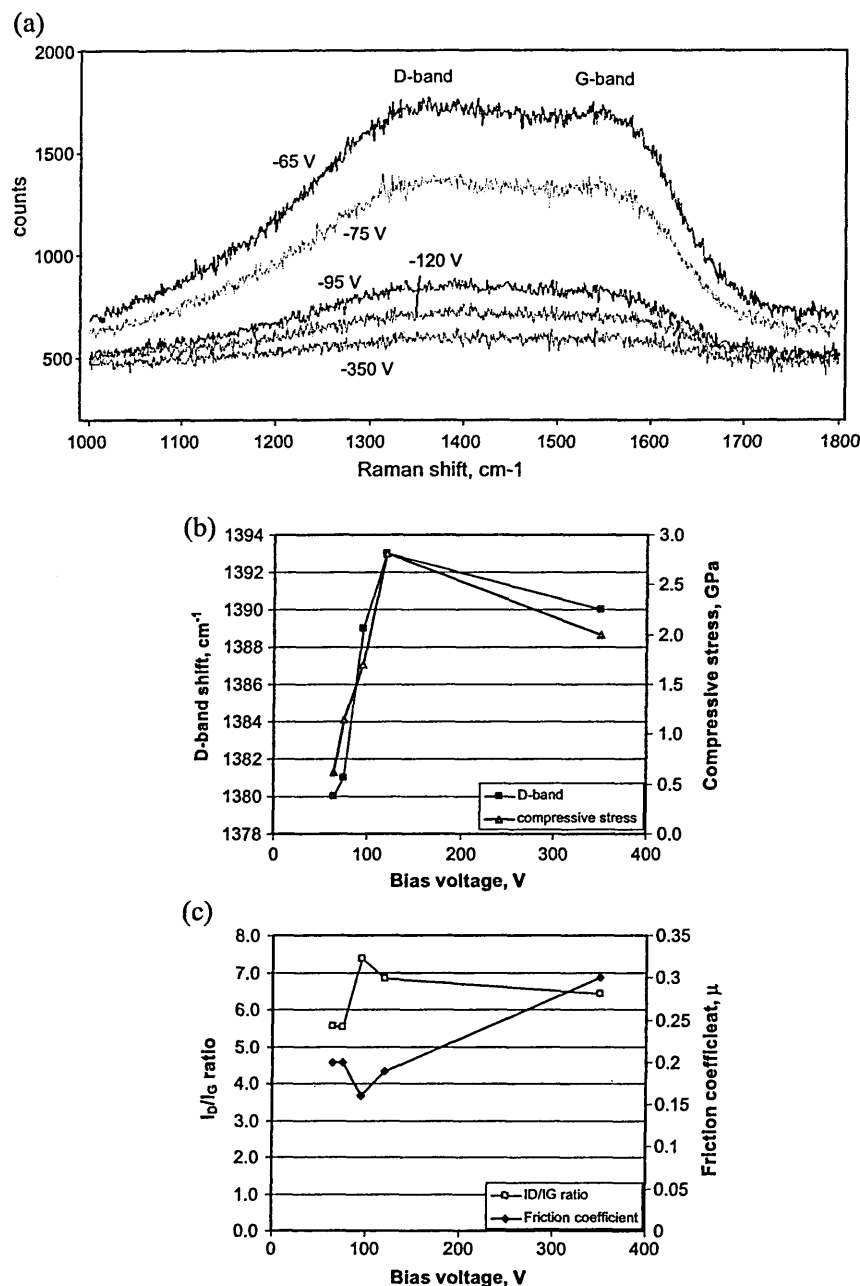


Fig. 2. (a) Raman spectra of C/Cr coatings deposited at various bias voltages, (b) D-band shift and stress as a function of bias voltage, (c) I_D/I_G ratio and friction coefficient as a function of bias voltage.

and detach the individual columns due to the lower tensile strength of the carbon phase. Further increase in the bias voltage to $U_b = -350$ V results in slight decrease of the I_D/I_G ratio, but significant increase of the friction coefficient ($\mu = 0.31$). This can be expected as the enhanced ion bombardment at higher bias voltages leads to increased residual stress and although the compressive stress decreases from 2.81 GPa to 2 GPa when the bias voltage increases from $U_b = -120$ V to $U_b = -350$ V, it still remain high as compared to the film deposited at $U_b = -65$ V, (0.62

GPa). Another reason for the increased coefficient of friction at high bias voltages is the formation of Me-carbides, which reduces the amount of the free and highly lubricious graphite phase in the coating.

3.2. In the wear track

The wear tracks formed in the pin-on-disc tests were investigated using Raman spectroscopy and SEM observations. The Raman spectra and the corresponding SEM

images of the wear tracks are shown in Fig. 3. For all bias voltages except $U_b = -350$ V, the I_D/I_G ratio of the wear tracks has been found to be lower than that of the coatings. As shown in Fig. 3a and b the intensity ratio changes mainly due to increase of the intensity of the G band of the material in the wear track, which indicates that during sliding the carbon transforms to a more ordered state.

The SEM pictures of the wear tracks clearly show the excellent wear behaviour of the coatings produced at $U_b = -95$ V compared to that at either lower ($U_b = -65$ V) or higher ($U_b = -350$ V) bias voltages. The wear track of the $U_b = -95$ V sample is very smooth and narrow (track

width = 280 μm). In contrast, the wear track of $U_b = -65$ V sample is wider (track width = 350 μm) and the coating is obviously worn out as the substrate has been exposed, imaged as a narrow band in the middle of the track. On the other hand, although the wear track of the $U_b = -350$ V sample appears smooth and is much wider (track width = 430 μm) suggesting high wear of the coating but also more wear on the counter part. This can be expected as the hardness of the coating produced at $U_b = -350$ V is higher due to the presence of Me-carbide phases. The results from the SEM observations complement the friction coefficient measurements and well correlate with the XPS and Raman findings.

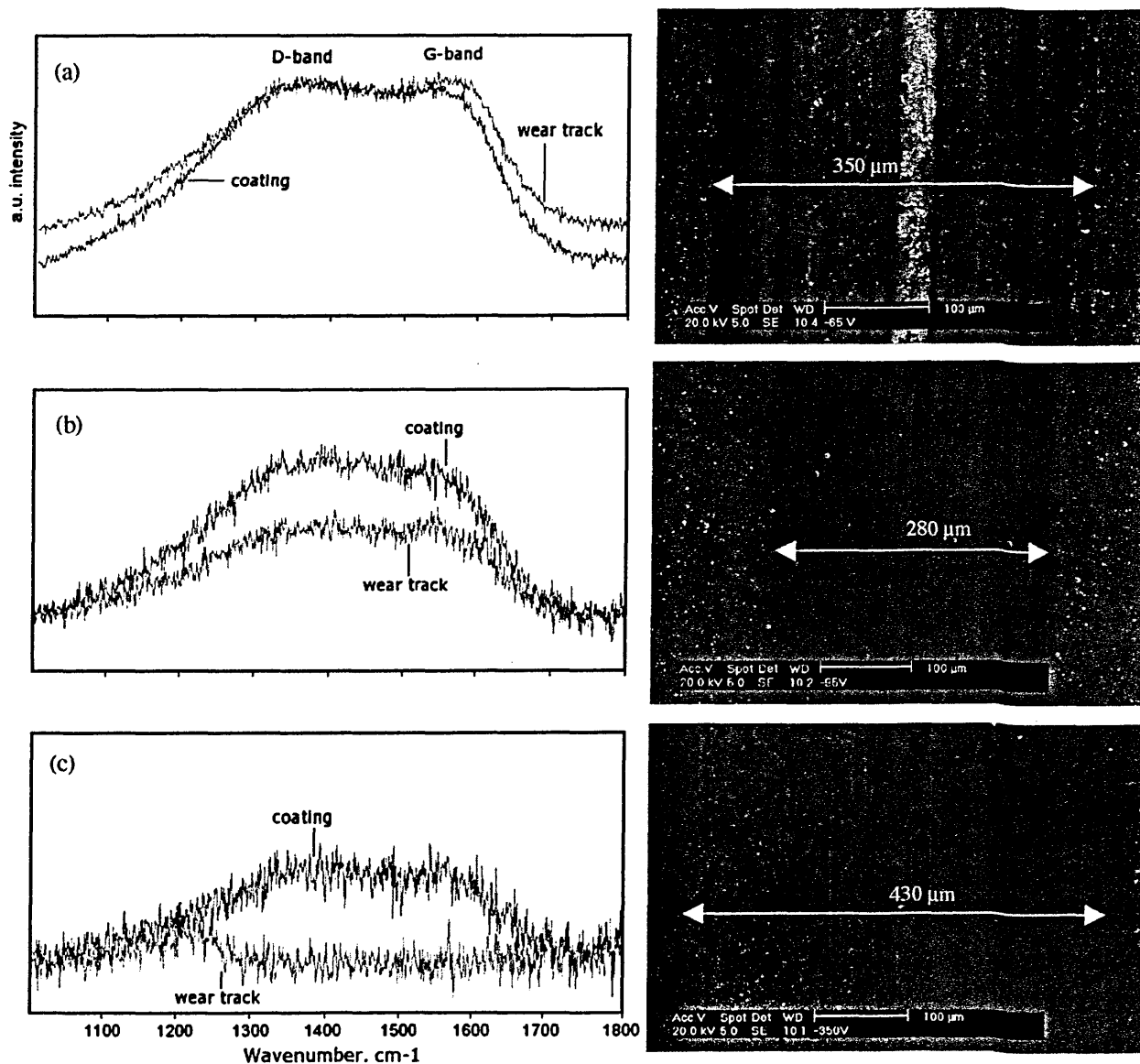


Fig. 3. Raman spectra of C/Cr coating and the wear track (left); SEM images of the wear track with the corresponding bias voltages (right): (a) $U_b = -65$ V, (b) $U_b = -95$ V, (c) $U_b = -350$ V.

4. Conclusions

- The microstructure and phase composition of C/Cr coatings are strongly influenced by the deposition conditions and more specifically by the bias voltage. As the bias voltage increases from $U_b = -65$ V to $U_b = -350$ V the structure changes from columnar to dense, based on onion-like carbon clusters to self-organised layered structures. The phase composition on the other hand transforms from more graphite-like (sp^2 C–C bonded) to more Me-carbon (Cr–C bonded), where the content of the carbide phase increases with increase of the bias voltage.
- The lowest friction coefficient of $\mu = 0.16$ was achieved with coatings deposited at $U_b = -95$ V. This result can be explained with the very dense structure based on formation of onion-like carbon clusters as well as the increased sp^2 content in the film indicated by the increased I_D/I_G ratio determined from the Raman spectra of the C/Cr coatings.

Acknowledgements

YNK would like to thank Dr. Ian Gee from SHU for the fruitful discussions of the XPS spectra. The authors appreciate the use of the facilities of the Center for Microanalysis of Materials, at the University of Illinois, which is partially supported by the U.S. Department of Energy under grant DEF G02-91-ER45439.

References

- [1] P.Eh. Hovsepian, D.B. Lewis, C. Constable, Q. Luo, Y.N. Kok, W.-D. Münz, *Surf. Coat. Technol.* 174–175 (2003) 762.
- [2] P.Eh. Hovsepian, Y.N. Kok, A.P. Eghasarian, A. Erdemir, J.-G. Wen, I. Petrov, *Thin Solid Films* 447–448 (2004) 7.
- [3] Y.N. Kok, P.Eh. Hovsepian, Q. Luo, D.B. Lewis, J.G. Wen, I. Petrov, *Thin Solid Films* 475 (1–2) (2005) 219.
- [4] J. Ullmann, K. Baba, H. Martin, G.K. Wolf, *Surf. Coat. Technol.* 74–75 (1995) 746.
- [5] R.G. Lacerda, P. Hammer, F.L. Freire Jr., F. Alvarez, F.C. Marques, *Dia. Relat. Mater.* 9 (2000) 796.
- [6] V.V. Uglova, V.M. Anishchik, Y. Pauleau, A.K. Kuleshov, F. Thiéry, J. Pelletier, S.N. Dub, D.P. Rusalsky, *Vacuum* 70 (2003) 181.
- [7] J. Schwan, S. Ulrich, V. Batori, H. Ehrhardt, S.R.P. Silva, *J. Appl. Phys.* 80 (1) (1996) 440.
- [8] A.C. Ferrari, J. Robertson, *Phys. Rev., B* 61 (20) (2000) 14095.
- [9] A. Cuesta, P. Dhamelincourt, J. Laureyns, A. Martinez-Alonso, J.M.D. Tascon, *Carbon (N. Y.)* 32 (8) (1994) 1523.
- [10] W.-D. Münz, D. Schulze, F.J.M. Hauzer, *Surf. Coat. Technol.* 50 (1992) 169.
- [11] R.D. Dillon, J.A. Woollam, V. Katkanant, *Phys. Rev.* 29 (6) (1984) 3482.
- [12] X. Han, F. Yan, A. Zhang, P. Yan, B. Wang, W. Liu, Z. Mu, *Mater. Sci. Eng., A* 348 (2003) 319.
- [13] E.D. Obratsova, M. Fujii, S. Hayashi, V.L. Kuznetsov, Yu.V. Butenko, A.L. Chuvilin, *Carbon (N. Y.)* 36 (5–6) (1998) 821.
- [14] C.A. Taylor, M.F. Wayne, W.K.S. Chiu, *Thin Solid Films* 429 (2003) 190.
- [15] Y.S. Park, H.S. Myung, J.G. Han, B. Hong, *Surf. Coat. Technol.* 180–181 (2004) 218.
- [16] R.G. Lacerda, P. Hammer, F.L. Freire Jr., F. Alvarez, F.C. Marques, *Dia. Relat. Mater.* 9 (2000) 796.
- [17] Q. Luo, W.M. Rainforth, W.-D. Münz, *Wear* 225–229 (1999) 74.

Tribocorrosion testing of stainless steel (SS) and PVD coated SS using a modified scanning reference electrode technique

Y.N. Kok *, R. Akid, P.Eh. Hovsepian

Materials Research Institute, Sheffield Hallam University, Sheffield, S11WB, UK

Received 27 August 2004; received in revised form 20 January 2005; accepted 1 February 2005

Available online 10 May 2005

Abstract

A conventional scanning reference electrode technique (SRET) has been modified to provide a novel method for characterising the real-time localised tribocorrosion behaviour of uncoated and physical vapour deposition (PVD) coated samples. The modification was carried out based upon the principle of a ball-on-cylinder contact. Here a sliding probe, in this case a changeable alumina ball, is positioned diametrically opposite a pseudo (Pt) reference electrode probe which is positioned 100 μm away from the surface of a cylindrical specimen which rotates at a set speed. The contact probe, specimen and reference probe are immersed within a chosen electrolyte, which for this study, is aqueous 0.01% NaCl. The dynamic corrosion activity is monitored via the Pt probe by recording variations in ionic flux emanating at the surface of the corroding sample. The SRET can operate in two modes, namely line scan, in which corrosion activity along the circumference of the specimen is measured, or map scan in which a 2D corrosion activity area map of the surface of the specimen is obtained. This paper presents the design, calibration procedures, and real-time tribocorrosion behaviour of uncoated and PVD (C/Cr) coated 316 stainless steel as a function of the contact load, and test conditions. Evidence of the effects of wear damage due to contact by the alumina ball was obtained by monitoring the SRET activity during loading (contact) and unloading conditions. The real-time local tribocorrosion activity can be detected immediately a load was applied. Such activity was found to stop, due to surface repassivation, upon removal of the load (alumina ball). The results show that the applied loads affect the free corrosion potential, local current density, active anodic areas and the sample recovery time of the tested samples. The wear tracks were investigated using optical and scanning electron microscopy and laser profilometer. Correlation of tribocorrosion damage and contact load has been investigated.

© 2005 Elsevier B.V. All rights reserved.

Keywords: Tribocorrosion; SRET; PVD; C/Cr coatings

1. Introduction

Tribocorrosion is the joint effects of corrosion and wear that degrade materials by both mechanical and electrochemical processes. As defined by Landolt et al. [1], tribocorrosion is an irreversible transformation of material in tribological contact caused by simultaneous physico-chemical and mechanical surface interactions. The combined effects of both can result in significant material losses that are greater than the simple sum of pure corrosion and pure erosion/wear, and cause accelerated damage in a number of industries such as slurry handling, crushing and grinding,

and power-generation. However, the actual understanding of the synergism between wear and corrosion processes in sliding contacts is rather limited. As an alternative novel method of studying the corrosion/wear synergy of coated samples, modification of a conventional scanning reference electrode technique (SRET) system has been carried out based upon the principle of a ball-on-cylinder contact, thereby providing a novel method for characterising the real-time localised tribocorrosion behaviour of uncoated and physical vapour deposition (PVD) coated samples.

SRET was chosen for this experiment because it has been demonstrated to be a useful tool for the investigation of localised corrosion [2–10] due to its ability to provide quantitative information regarding local anodic and cathodic processes [11]. Furthermore, it is a non-invasive, highly

* Corresponding author. Tel.: +44 114 225 4062; fax: +44 114 225 3501.
E-mail address: y.n.kok@shu.ac.uk (Y.N. Kok).

sensitive, and reliable electrochemical method which can be used to image and quantify real-time localised electrochemical activity. SRET measures microgalvanic potentials existing local to the surface of the materials under investigation, using a pseudo reference electrode probe which scans over the surface. This non-intrusive technique provides dynamic information on corrosion activity by recording variations in ionic flux in the electrolyte, on a microscopic scale [3]. In this paper we present the results of tribocorrosion experiments conducted on stainless steel (SS) and PVD coated stainless steel (PVDSS) using a modified SRET.

2. Experimental procedures

2.1. Sample preparation

C/Cr coatings were deposited on a SS substrate by the combined steered cathodic arc/unbalanced magnetron sputtering (also known as ABSTM: Arc-Bond Sputtering) technique using a Hauzer HTC 1000-4 PVD coater. C/Cr coatings were deposited in three major steps: (i) Cr⁺ ion etching using a steered cathodic arc discharge at a substrate bias voltage of -1200 V. It has been demonstrated that the metal ion bombardment favours local epitaxial film growth, which enhances adhesion between coating and substrate [12,13]. Additionally, the Cr⁺ etching minimises the surface roughness of the subsequent coatings [14]; (ii) deposition of CrN base layer by unbalanced magnetron sputtering to further enhance the adhesion; and (iii) deposition of C/Cr coatings at bias voltage of -75 V by unbalanced magnetron sputtering

Table 1

Properties of C/Cr coating

Composition (at.%)	70% C, 30% Cr
Thickness (μm)	1.8
Hardness (GPa)	11.9
Adhesion critical load, L_c (N)	75
Chemical bonding	sp^2 C–C

from three graphite targets and one chromium target at 260°C in a non-reactive Ar atmosphere. The details of the coating process have been reported elsewhere [15,16]. The properties of C/Cr coating is given in Table 1. The cylindrical substrate used for the SRET tests was a 316 grade SS (composition: 0.06% C, 17.0% Cr, 8.0% Ni, 2.0% Mn, 1.0% Si) having a dimension of 15 mm diameter \times 110 mm long. Prior to coating deposition, the substrates were ground with 240, 320, 400, 800 and 1200 grit paper and polished to a mirror finish with 6 and 1 μm diamond paste and subsequently cleaned in an industrial size automated ultrasonic cleaning line.

2.2. Design of tribocorrosion test rig

The modification of the SRET rig was carried out based upon the principle of a ball-on-cylinder contact. The aim of this modification was to provide a novel method for characterising the real-time localised tribocorrosion behaviour of uncoated and coated samples. Figs. 1 and 2 schematically present the design of the modified SRET for tribocorrosion testing. The load is applied based on a cantilever approach, where a load cell (SP02 Platform load cell available from Amber Instruments Ltd., max. load 50 N, gauge factor of 0.5) is

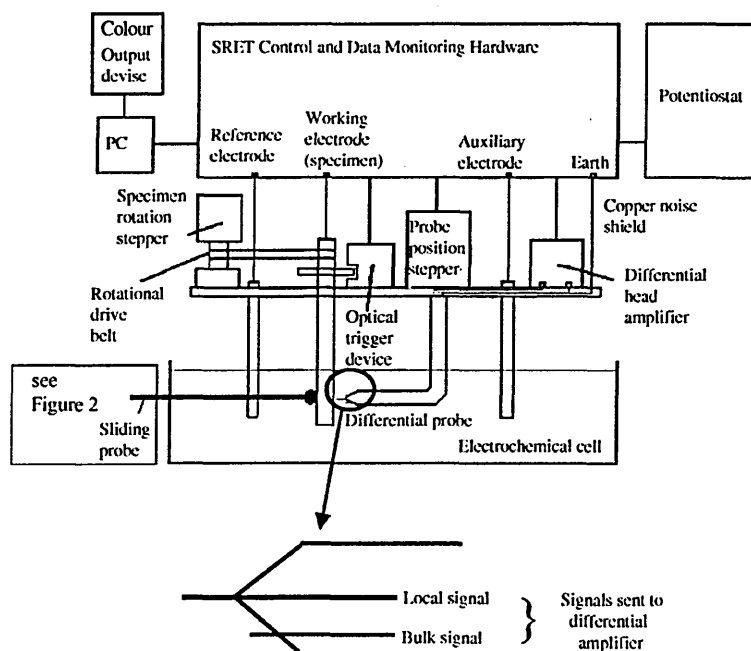


Fig. 1. Schematic of SRET experimental set up including probe geometry.

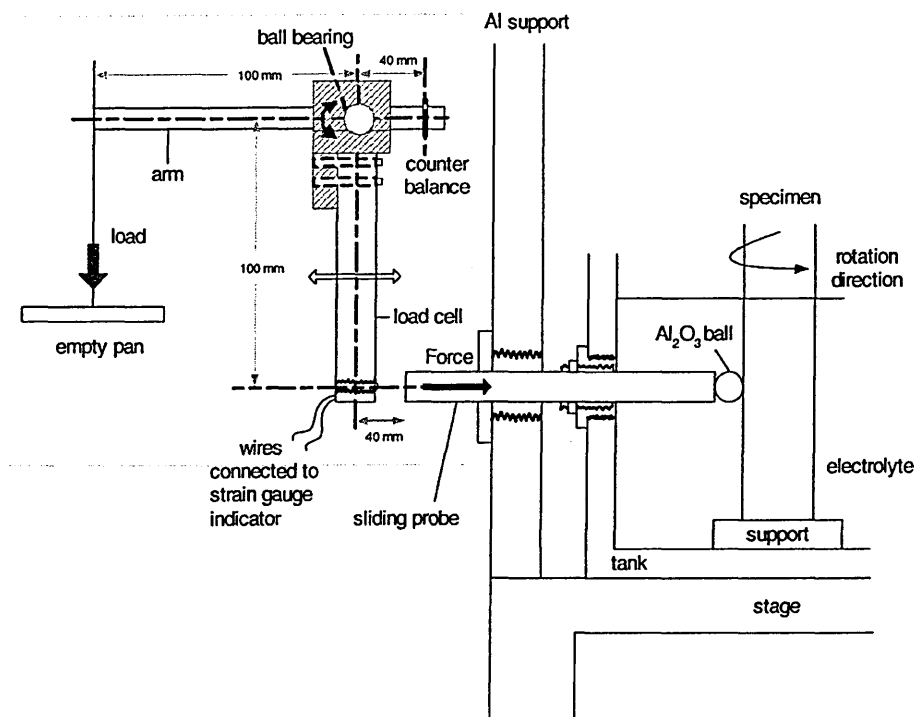


Fig. 2. Design and schematic diagram of modified SRET (not to scale).

screwed to a ball bearing which is attached to the cantilever arm. The main purpose of the load cell is to allow the system to be calibrated, in which a strain gauge indicator provides an output signal ($\mu\epsilon$) when a load is applied. The output signal is then plotted versus the applied load and a calibration factor obtained. Assuming no plastic deformation of the ball or sample, a linear graph is expected. When a load (weight) is placed on the empty pan, it will exert a force causing the sliding probe to make contact with the sample. Negligible frictional forces exist on movement of the sliding probe towards the specimen, thereby ensuring that the load applied on the empty pan is proportional to the load applied on the sample. This has been confirmed by system calibration.

2.3. Experimental setup and tribocorrosion calibration

Fig. 1 presents a schematic of the experimental setup for conducting tribocorrosion tests using the modified SRET, where the sliding contact system highlighted within the box is given in Fig. 2. Here, the sliding probe comprises of a changeable 6 mm alumina ball, being positioned diametrically opposite a pseudo (Pt) reference electrode probe which is located 100–150 μm away from the surface of a cylindrical specimen which rotates at 100 rpm. The SRET probe consists of two Pt wires separated as shown in Fig. 1. The wires are sharpened to increase their sensitivity and measure respectively the local and bulk isopotential field associated with the surface corrosion activity. By convention the SRET activity is defined as follows; negative values (anodic) and positive values (cathodic). The contact probe, specimen and

reference probe are immersed within a chosen electrolyte, for this study, being aqueous 0.01% NaCl. The dynamic corrosion activity is monitored via the Pt probe by recording variations in ionic flux emanating at the surface of the corroding sample. The probe can operate in three modes, namely line scan (current versus specimen displacement and current versus time), in which corrosion activity along a single position on the circumference of the specimen is measured, or map scan in which a 2D corrosion activity area map of the surface of the specimen is obtained.

Calibration of the system was carried out using both uncoated 316 SS and a PVDSS test specimens, which were rotated in air and in tap water (which has a very similar conductivity and viscosity to that 0.01% NaCl solution). The use of coated and uncoated samples for calibration was aimed at assessing any effects of the coating on the calibration factor. The load cell was connected to a P3500 strain gauge indicator, and the output reading was recorded each time a load was applied from 0 to 6 N. The empty pan (weight ~ 0.2 N) was located at a constant position on the arm.

2.4. Experiments

The following tribocorrosion tests were carried out using the same experimental conditions as that used for the calibration. Further details are given in Table 2.

1. Calibration of the system.
2. Effect of load on electrochemical potential (E_{corr}).
3. Effect of load (0–6 N) on localised corrosion activity.

Table 2
Test conditions for tribocorrosion tests using the modified SRET

Experiment	Sample ^a	Load, N	Loading mode	Test duration	Potential, (mV)	Environment	Results
1 Calibration of system	SS & PVDSS	0–6	Increasing	N/A	N/A	Tap water	Output strain via load cell as a function of applied load
2 Effect on E_{corr}	SS	1 and 3	Loading and unloading	Up to 6 h	E_{corr}	0.01% NaCl	E_{corr} as a function of applied load and time
3 Effect of applied load	SS	0–4	Increasing	30 s per load	E_{corr}	0.01 % NaCl	SRET current density line scan (real-time tribocorrosion activity), line displacement scan and calculated active anodic area
	PVDSS	0–6	Increasing and unloading				
4 Effect of loading and unloading	PVDSS	0.5, 1, 3, 5	Loading and unloading (on same area)	1 h per mode	E_{corr}	0.01% NaCl	SRET current density line scan and measured worn area
5 Effect of coating on TC ^b response in different environments	SS & PVDSS	1 N	Constant	1 h	(a) N/A (b) E_{corr} (c) Cathodic potential (–500 mV below E_{corr})	Air 0.01% NaCl	Measured worn area, wear coefficient, E_{corr} versus time, SRET current density line scan, and microstructure

^a 316 Stainless steel was used as the substrate material.

^b TC: tribocorrosion.

- Effect of loading and unloading on sample recovery (repassivation).
- Effect of coating on tribocorrosion damage in different environments.

3. Results and discussion

3.1. Experiment 1: calibration of system

The results of the tribocorrosion calibration test carried out in air and tap water are presented in Fig. 3. As observed with the air calibration test, the output signal was very consistent and linear, with output signal increasing linearly with increasing applied load. A linear response was obtained regardless of whether the sample was coated or uncoated. Thus, it was concluded that the load applied on the arm (via the pan) is proportional to the load applied on the sample. Note that the equation obtained in Fig. 3 is based upon the SS steel substrate. Different substrate materials may, subject to their deformation behaviour, produce different calibration curves.

3.2. Experiment 2: effects of applied load on E_{corr}

Variation of the open circuit potential (OCP or E_{corr}), as a function of applied load, is shown in Fig. 4. E_{corr} was measured under loading and no loading conditions. The E_{corr} recorded during the tests is a mixed potential reflecting the activity of the unworn material and the activity of the material in the wear track. Thus, a galvanic coupling between damaged and undamaged sites on the sample surface takes place.

An applied normal force was found to cause a change in the free corrosion potential of the samples. The initial part of the graph (Fig. 4), from 0 to 5 min, shows the E_{corr} of the freshly ground 316 SS sample at zero load. After 5 min, when a 1 N load was applied on the rotating sample, an instantaneous decrease of the E_{corr} (similar behaviour was observed when a 3 N load was applied) was observed. A similar poten-

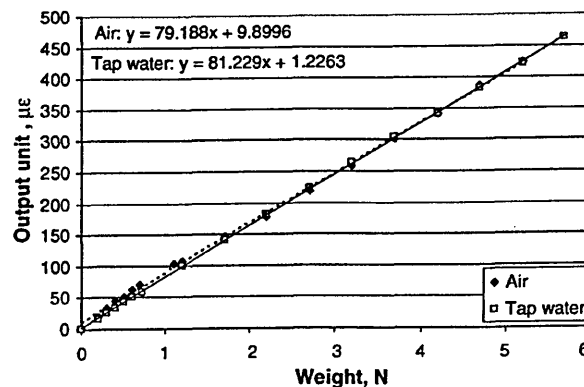


Fig. 3. Tribocorrosion calibration results in air and tap water.

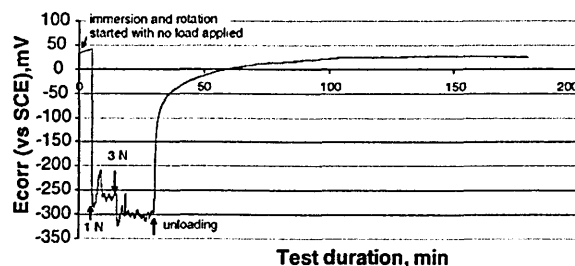


Fig. 4. Influence of loading and unloading on the open circuit potential of SS in 0.01% NaCl.

tial trend has been observed by Ponthiaux et. al. [17]. When the sliding counterface is applied on the surface, the corrosion potential suddenly decreases, this potential shift is associated with the surface damage suffered by the sample. Here the surface passes from a passive to (i) active state induced by wear [18], followed by (ii) local dissolution of the base material as a consequence of the galvanic coupling between the passive surface layer and the bare base material, and (iii) a larger area of active material in the wear track due to increase normal load [17]. On unloading, E_{corr} increases and approaches the initial E_{corr} value (prior to loading).

Fig. 5 shows the variation in the free corrosion potential of C/Cr coated sample under tribocorrosion conducted in 0.01% NaCl at 1 N load. E_{corr} , at the onset of the test, decreases from -23 to -170 mV after ~ 20 min of sliding. Some recovery/stabilisation of the surface occurs as E_{corr} increases gradually to -140 mV. The sudden change in the potential to above 0 mV occurred when the sliding contact was removed. The shift in corrosion potential, which occurs on loading, may be the result of (i) deterioration of the passive film due to mechanical interaction between the counterbody, the sample and corrosion of the exposed area, and (ii) continuous metal removal (caused by the contact with counter body) and reformation (contact with the electrolyte) of the chromium passive oxide layer on the sample surface [18].

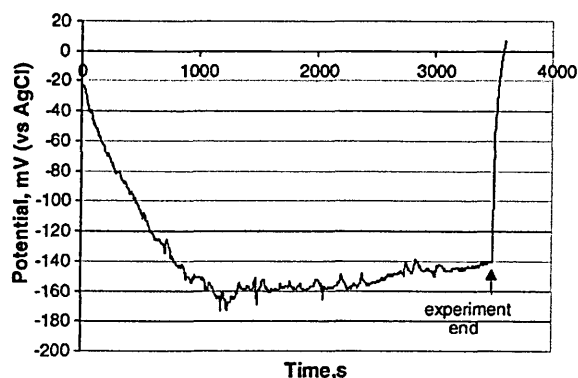


Fig. 5. E_{corr} vs. time for PVDSS at a load of 1 N in 0.01% NaCl.

3.3. Experiment 3: effects of applied load on localised corrosion activity

The initial tribocorrosion test was conducted under open circuit conditions. Abrasion between the alumina ball and the rotating sample led to an increase in current density, see Fig. 6a, indicating an increase in corrosion activity due to the activation of the anodic reaction. Note that the SS sample experiences about one order of magnitude higher anodic activity than the PVDSS sample. In-situ monitoring of the sample using the line scan mode revealed the active sites as ‘movable anodes’, where the anodic areas varied in magnitude and location with applied load and exposure time. Increasing the load caused an increase in the number and magnitude of the local active sites. During tribocorrosion, material removal takes place simultaneously by mechanical wear and corrosion. Most corrosion resistant metallic materials such as stainless steels are protected by a thin 1–2 nm thick oxide passive film, which forms on the surface by spontaneous reaction with oxygen in the environment [19]. Abrasion leads to local removal of the passive film resulting in exposure of bare metal to the aggressive environment, which subsequently, may or may not, repair itself by oxidation of the metal. Passive film breakdown therefore leads to a substantial increase in the anodic partial current [1], and to an increase in local corrosion rate. The effect of abrasion by the alumina ball was obtained by monitoring the SRET activity during contact and non-contact conditions. Fig. 6b shows the line displacement map scan (versus time) of the tribocorrosion activity of the coated sample under these conditions. The real-time local tribocorrosion activity can be detected under contact mode (when load is applied), and is observed to decrease upon unloading (note the darkest region), which then stopped due to surface repassivation, immediately upon removal of the contact component (e.g. zero load). However, upon immediate contact of a load (5 N), the sample experienced increased damage. Sample recovery time is depended on the repassivation rate of the bulk substrate or coating. Fig. 6c presents the damage area, mC/cm^2 , after loading for uncoated (SS) and PVDSS samples. The area under the anodic portion of the SRET line scan curve in Fig. 6a (shaded area) was determined using Simpson’s rule, being equivalent to the total volume of metal loss (mC/cm^2). This value was observed to increase with increasing load, being particularly obvious for the SS sample. Furthermore, this analysis clearly shows that the C/Cr coating has protected the substrate from severe damage at various applied loads. This may be attributed to the chemical inertness and self-lubricating characteristic of the graphite resulting in a reduction in the overall friction between the two rubbing surfaces.

3.4. Experiment 4: effects of loading and unloading on sample recovery

Fig. 7 shows the results of the effect of different loads, namely 0.5, 3, and 5 N on the changes in local corrosion ac-

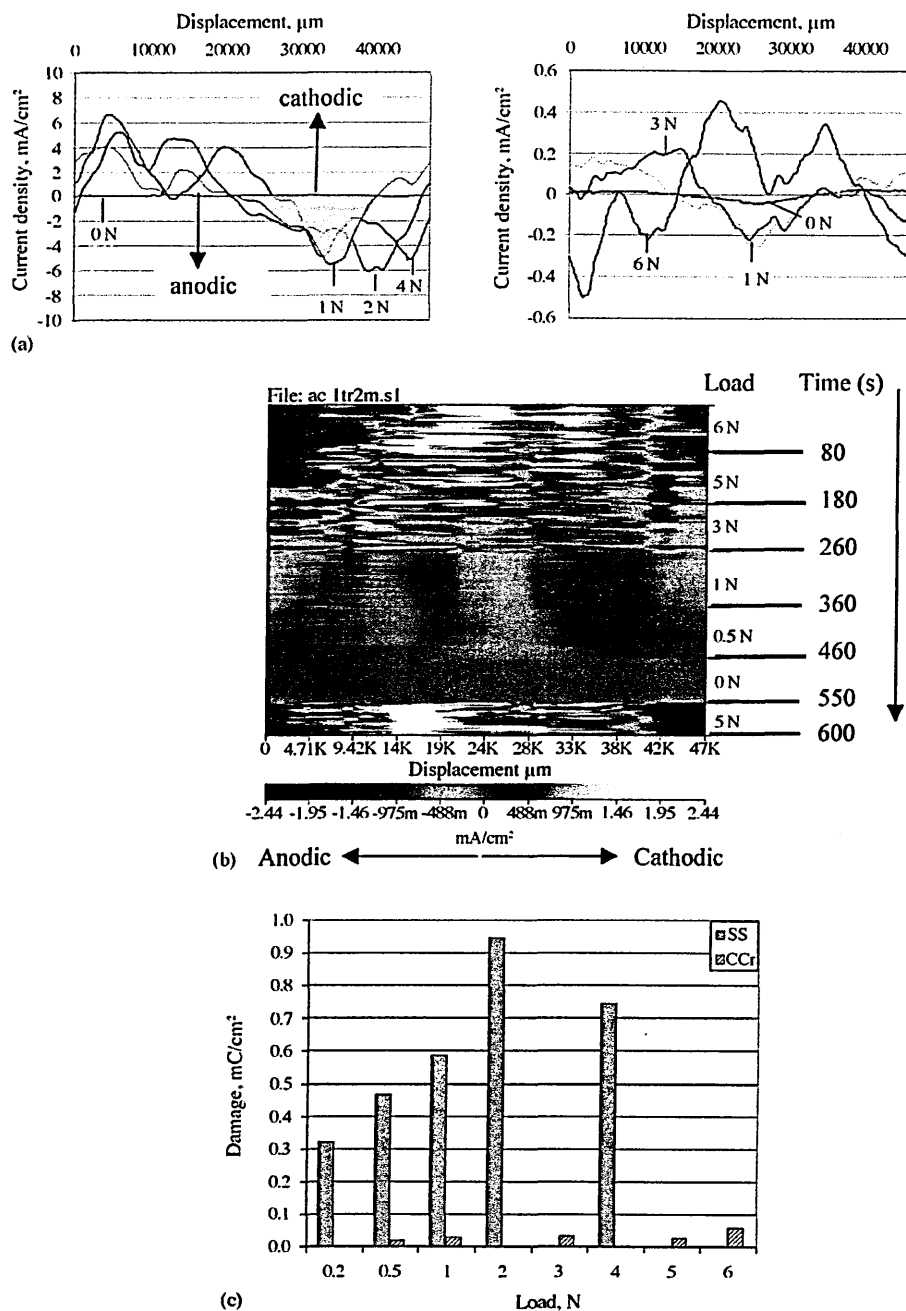


Fig. 6. (a) SRET line scan under various applied loads for identical contact times for uncoated SS (left) and PVDSS (right) samples, (b) line displacement versus time scan upon unloading and loading and (c) equivalent total volume of metal loss (mC/cm^2) calculated from SRET line scan.

tivity at OCP. Loads were applied at the same position on the sample. The sample was unloaded after each applied load to see whether or not the sample recovers after 1 h sliding. Theoretically, above this 'threshold' load, the sample experiences permanent damage caused by the interaction of electrochemical and mechanical processes. Fig. 7a shows the results obtained. Here 5 s represents the curve immediately after 5 s a load was applied, while the curve labelled 1 h represents ac-

tivity after sliding contact for 1 h. At each load, after testing for 1 h, the sample was unloaded and the signal was monitored. It was noted that the current density during loading increased due to damage of the passive film [20]. As abrasion ceases, the current density decreases dramatically to a negligible value. The unloading line scan after 1 h sliding at 3 N presented in Fig. 7b shows recovery after 90 s of unloading (note: lines were obtained at 15 s interval). Unfortunately,

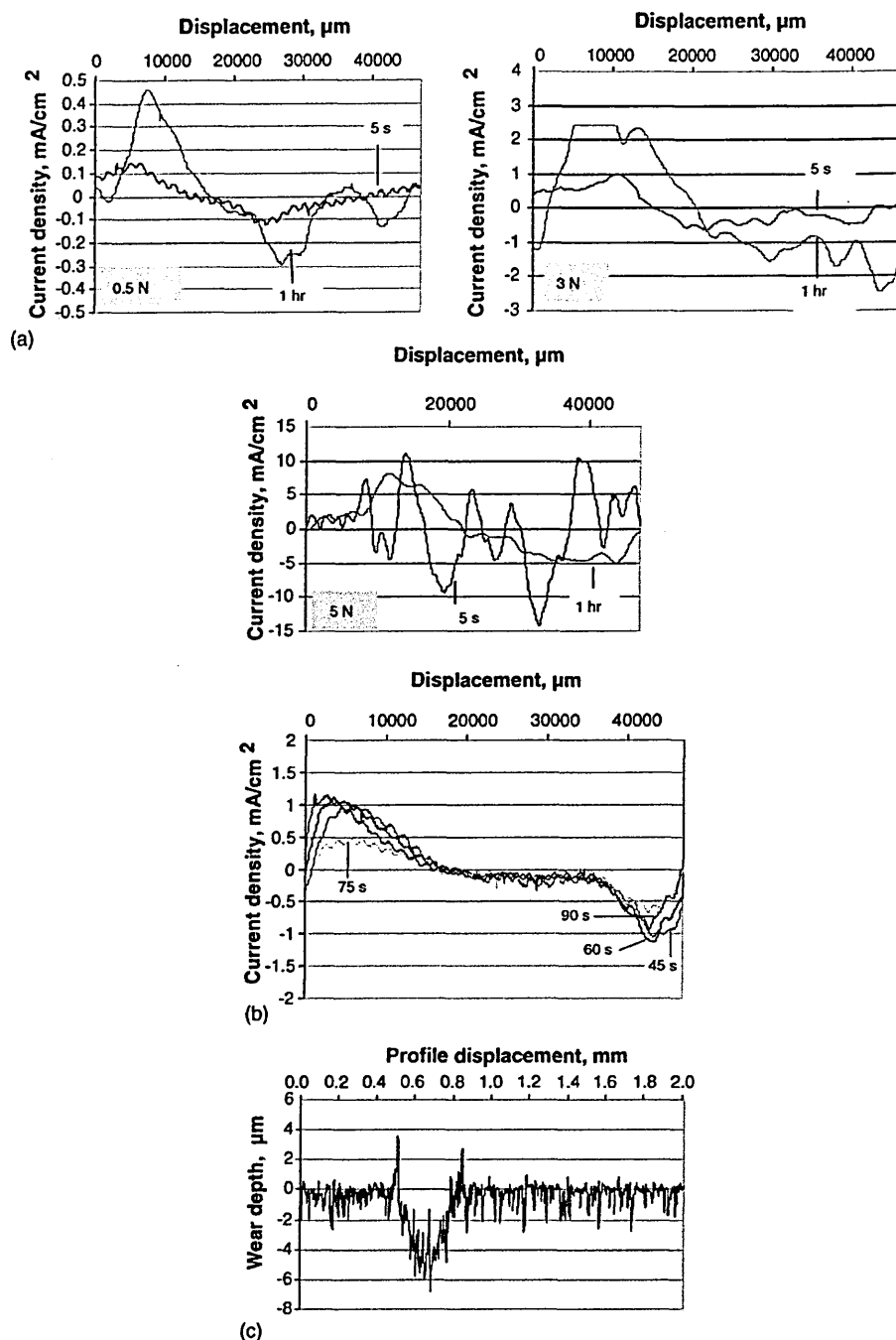


Fig. 7. SRET line scan for PVDSS sample subjected to (a) repeated loading, (b) unloading sequence and (c) wear track in PVDSS sample after test.

it is extremely difficult to determine the exact recovery time of the sample, because the sample recovers (significant reduction in current density) almost immediately after the load was removed due to repair of the passive film. Although no exact recovery time could be obtained upon unloading from various loads, we suppose the applied load could slightly affect the recovery time, where the higher the load, the longer

the time it takes to recover upon unloading. This could be due to larger contact area and damage generated at higher load. The results proved that the current density measured during sliding contact is indeed due to mechanical loading, as a permanent wear scar appeared on the sample. Fig. 7c shows the wear track profiles of the PVDSS sample at the end of the test. The wave peaks on the outer edge of the wear track (Fig. 7c)

are probably due to plastic flow of the indented metal around the sliding ball [21].

3.5. Experiment 5: effect of coating on tribocorrosion damage in different environments

These tests were carried out by applying a 1 N load for a duration of 1 h in three different test environments (refer to Table 2 for details), namely:

- Air (i.e. sliding wear test),
- 0.01% NaCl solution at E_{corr} (i.e. tribocorrosion),
- 0.01% NaCl solution under cathodic protection.

From these experiments, it was found that the testing environment affects:

- amount of wear,
- wear coefficient,
- wear morphology.

The wear volumes on the samples were determined by measuring the wear track cross-sectional area using laser profilometry, and multiplying it by the length of the wear track [21,22]. At least four positions along the length of the wear track were measured to obtain the average area. Even though there was material loss in the wear track during mechanical interaction between the ball and the sample, for ease of calculating the sliding distance, we take the circumference of the sample instead of the circumference of the wear track. Therefore, by using the radius of 7.5 mm, the circumference of the sample was calculated to be 47.12 mm, and the total sliding distance for 1 h at 100 rpm sliding speed was 282.72 m. The wear coefficient was calculated based on Archard's law [21], but taking no account of the hardness of the sample in this study:

Wear coefficient,

$$K = \frac{\text{wear volume}}{\text{applied force} \times \text{sliding distance}} \text{ m}^3 \text{ N}^{-1} \text{ m}^{-1}$$

Fig. 8a shows the wear track profiles of the SS and PVDSS samples developed in 0.01% NaCl, compared with the SS sample wear track generated in air. Here, it can be seen that the PVDSS sample exhibits a shallower and reduced wear track than that of the bare substrate. Fig. 8b presents the wear coefficient of uncoated and C/Cr coated samples tested under various test environments. Uncoated SS samples show the highest wear coefficient of $1.08 \times 10^{-13} \text{ m}^3 \text{ N}^{-1} \text{ m}^{-1}$ while the PVDSS sample exhibited a lower wear coefficient of $8.44 \times 10^{-16} \text{ m}^3 \text{ N}^{-1} \text{ m}^{-1}$ when tested in air. Under test environments (b) and (c), the uncoated sample shows a substantial reduction in the wear coefficient by nearly two order of magnitude; but C/Cr coated sample showed a slight increase in the wear coefficient to $1.86 \times 10^{-15} \text{ m}^3 \text{ N}^{-1} \text{ m}^{-1}$ as compared to the sample tested in air. This could be due to the synergistic effect of wear and corrosion when the coated sample is immersed in the solution. However, in the case of

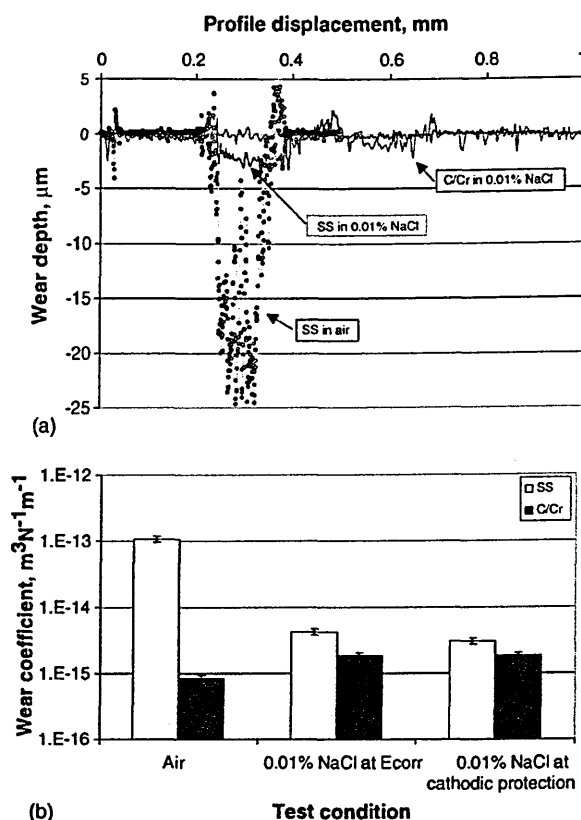


Fig. 8. (a) wear track profiles and (b) wear coefficients within various test environments.

the SS sample, the solution may act as a lubricant between rubbing surfaces thereby reducing the mechanical wear component substantially.

Fig. 9 shows the optical images of the alumina ball and the wear track on an uncoated SS sample. Severe ploughing was observed on both the sample and the ball after testing in air (Fig. 9a and b, respectively), leading to substantial material loss and thus the formation of wear debris which accumulates in the wear track and promotes third-body sliding, leading to the highest observed wear coefficient. When tested under cathodic polarisation (test environment c), both the ball and the sample exhibited different wear behaviour with less material loss (see Fig. 9c and d). García et al. [23] reported that the corrosive-wear of AISI 316 tested in aggressive environments consists of two processes; (i) mechanical delamination of the passive layer in the wear track, followed by (ii) a progressive electrochemical re-passivation of that active wear track area (representing that part of the wear track that temporarily loses its passive character due to the mechanical interaction during sliding). Passive materials such as stainless steel generally resist corrosion by the formation of a thin, dense, passive oxide film. However, mechanical loading interaction by sliding contact between two rubbing surfaces can deteriorate and remove part of the passive film. The extent of combined corrosion/wear depends on the type of materials

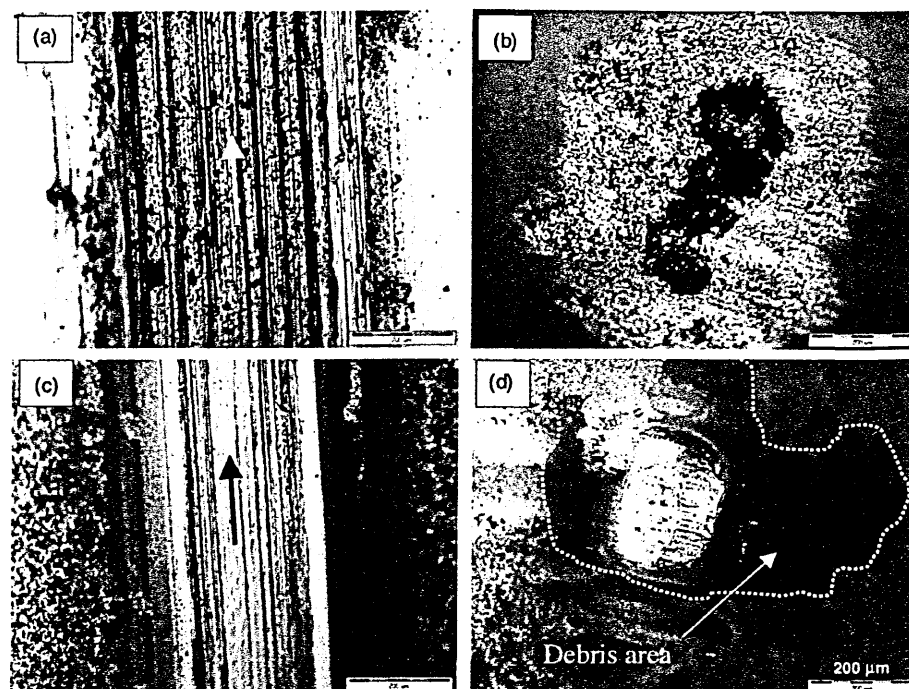


Fig. 9. Optical images of the wear scar (arrow shows the sliding direction) of uncoated sample and the counter part tested in (a and b) air and (c and d) under cathodic polarisation. All markers: 200 μm .

in contact, the composition of the environment, the applied load, and the electrode potential of the substrate [23].

4. Conclusions

In this study, a conventional SRET has been successfully modified to provide a novel method for characterising the real-time localised tribocorrosion behaviour of uncoated and PVD C/Cr coated samples. The load applied via a cantilever arm arrangement is proportional to the load applied at the sample surface, assuming no loss in the system. The influences of various testing conditions involving contact load and test environments have been demonstrated, and have been found to affect the following parameters:

- local anodic current activity,
- the number of active anodic areas,
- sample (repassivation) recovery time,
- free corrosion potential,
- amount of wear,
- wear coefficient,
- wear morphology.

In dry air, PVDSS samples exhibited 2–3 orders of magnitude improved wear resistance compared to the uncoated SS. In both 0.01% NaCl at OCP and -500 mV (versus Ag/AgCl), PVDSS samples also out-performed the uncoated SS by 2–3 times.

Acknowledgement

Authors are grateful to Mr. Gary Robinson for constructing the tribocorrosion test rig and technical support.

References

- [1] D. Landolt, S. Mischler, M. Stemp, Electrochemical methods in tribocorrosion: a critical appraisal, *Electrochim. Acta* 46 (24–25) (2001) 3913.
- [2] H.N. McMurray, D.A. Worsley, Scanning electrochemical techniques for the study of localised metallic corrosion, in: *Res. Chem. Kinet.*, vol. 4, Blackwell Science Ltd., 1997, pp. 149–202.
- [3] R. Akid, Localised Corrosion: a new evaluation approach, *Mater. World* (1995) 522–525.
- [4] H.S. Isaacs, V. Brijesh, scanning reference electrode techniques in localised corrosion, in: F. Mansfeld, U. Bertocci (Eds.), *Electrochemical Corrosion Testing*, American Society for Testing and Materials, ASTM STP 727, 1981, pp. 3–33.
- [5] K.R. Trethewey, D.A. Sargeant, D.J. Marsh, A.A. Tamimi, Applications of the scanning reference electrode technique to localized corrosion, *Corros. Sci.* 35 (1–4) (1993) 127.
- [6] K. R. Trethewey, D.A. Sargeant, D.J. Marsh, S. Haines, New methods of quantitative analysis of localised corrosion using scanning electrochemical probes, in: K.R. Trethewey, P.R. Roberge (Eds.), *Modelling Aqueous Corrosion*, British Crown, Printed in the Netherlands, 1994, pp. 417–442.
- [7] H.N. McMurray, S.R. Magill, B.D. Jeffs, Scanning reference electrode technique as tool for investigating localised corrosion phenomena in galvanised steels, *Ironmak. Steelmak.* 23 (2) (1996) 183.

- [8] R. Akid, D.J. Mills, A comparison between conventional macroscopic and novel microscopic scanning electrochemical methods to evaluate galvanic corrosion, *Corros. Sci.* 43 (2001) 1203.
- [9] H.N. McMurray, Localised corrosion behaviour in aluminium-zinc alloy coatings investigated using the scanning reference electrode technique, *Corrosion* 57 (4) (2001) 313.
- [10] N. Cui, H.Y. Ma, J.L. Luo, S. Chiovelli, Use of scanning reference electrode technique for characterizing pitting and general corrosion of carbon steel in neutral media, *Electrochem. Commun.* 3 (2001) 716.
- [11] R. Akid, G.M. Treacy, D.J. Mills, M. Toff, Application of the rotational scanning reference electrode technique to assess the anti-corrosion performance of organic and metallic coatings, *EuroCorr* 2000. 10–14th September, 2000. Queen Mary & Westfield College, University of London, UK.
- [12] I. Petrov, P. Losbichler, D. Bergstrom, J.E. Greene, W.-D. Münz, T. Hurkmans, T. Trinh, Ion-assisted growth of $Ti_{1-x}Al_xN/Ti_{1-y}Nb_yN$ multilayers by combined cathodic-arc/magnetron-sputter deposition, *Thin Solid Films* 302 (1997) 179.
- [13] C. Schönljahn, L.A. Donohue, D.B. Lewis, W.-D. Münz, I. Petrov, Enhanced adhesion through local epitaxy of transition-metal nitride coatings on ferritic steel promoted by metal ion etching in a combined cathodic arc/unbalanced magnetron deposition system, *J. Vac. Sci. Technol. A* 18 (4) (2000) 1718.
- [14] W.-D. Münz, I.J. Smith, D.B. Lewis, S. Creasey, Droplet formation on steel substrates during cathodic steered arc metal ion etching, *Vacuum* 48 (5) (1997) 473.
- [15] P.Eh. Hovsepian, Y.N. Kok, A.P. Ehasarian, A. Erdemir, J.-G. Wen, I. Petrov, Structure and tribological behaviour of nanoscale multilayer C/Cr coatings deposited by the combined steered cathodic arc/unbalanced magnetron sputtering, *Thin Solid Films* 447–448 (2004) 7.
- [16] Y.N. Kok, P.Eh. Hovsepian, Q. Luo, D.B. Lewis, J.G. Wen, I. Petrov, Influence of the bias voltage on the structure and the tribological performance of nanoscale multilayer C/Cr PVD coatings, *Thin Solid Films* 475 (1–2) (2005) 219.
- [17] P. Ponthiaux, F. Wenger, D. Drees, J.P. Celis, Electrochemical techniques for studying tribocorrosion processes, *Wear* 256 (5) (2004) 459.
- [18] L. Fedrizzi, S. Rossi, F. Bellei, F. Deflorian, Wear-corrosion mechanism of hard chromium coatings, *Wear* 253 (2002) 1173–1181.
- [19] S. Mischler, A. Spiegel, D. Landolt, The role of passive oxide films on the degradation of steel in tribocorrosion systems, *Wear* 225–229 (1999) 1078.
- [20] M. Stemp, S. Mischler, D. Landolt, The effect of contact configuration on the tribocorrosion of stainless steel in reciprocating sliding under potentiostatic control, *Corr. Sci.* 45 (2003) 625.
- [21] S. Mischler, P. Ponthiaux, Commission Tribocorrosion du CEFRA-COR Centre Français de l'Anticorrosion, F - 75007 Paris, France, A round robin on combined electrochemical and friction tests on alumina/stainless steel contacts in sulphuric acid, *Wear* 248 (2001) 211.
- [22] S. Mischler, A. Spiegel, M. Stemp, D. Landolt, Influence of passivity on the tribocorrosion of carbon steel in aqueous solutions, *Wear* 251 (2001) 1295.
- [23] I. Garcia, D. Drees, J.P. Celis, Corrosion-wear of passivating materials in sliding contacts based on a concept of active wear track area, *Wear* 249 (2001) 452.